International Committee for Future Accelerators

Sponsored by the Particles and Fields Commission of IUPAP

Beam Dynamics Newsletter

No. 74

Issue Editor:
Eliana Gianfelice-Wendt

Editor in Chief:
Y. H. Chin

August 2018

Contents

1 Foreword

1.1 From the Chair

Yong Ho Chin, KEK
Mail to: yongho.chin@kek.jp

We have an announcement. Swapan Chattopadhyay and Toshiyuki Okugi have stepped down from the ICFA Beam Dynamics Panel (BDP) members, leaving their long standing achievements on beam dynamics studies. We have now two new ICFA BDP members who succeded them, Ji Qiang of LBNL and Yoshihiro Shobuda of JAEA. Their memberships were officially approved by ICFA. I would like to express my sincere gratitude to Swapan and Toshiyuki for their long-term contributions to our panel and the accelerator community. It has been a great privilege for me to work with them in this panel.

The 61st ICFA Advanced Beam Dynamics Workshop on High-Intensity and High Brightness Hadron Beams (HB2018) was held very successfully on June 17-22, 2018, in Daejeon, Korea. About 150 participants from all over the world gathered together to exchange ideas and best practices about hadron machines, their new development trend and related key technologies. The proceedings will be published soon on the JACoW website (http://www.jacow.org/index.php?n=Main.Proceedings). For more details of HB2018, the workshop report is available in the Section 3. This year, we will have another ICFA Advanced Beam Dynamics Workshop:

- The 62nd ICFA Advanced Beam Dynamics Workshop on High Luminosity Circular e+e- Colliders 2018 (eeFACT2018), September 24-27, 2018 at Institute for Advanced Studies (IAS), Hong Kong University of Science and Technology (HKUST), Hong Kong. http://eefact2018.ust.hk/

ICFA has approved another ICFA Advanced Beam Dynamics Workshop next year:

- The 63rd ICFA Advanced Beam Dynamics Workshop on Energy Recovery Linacs, ERL2019, September 16-20, 2019, at Helmholtz Zentrum Berlin, Germany.

The preparation of all these workshop is under way and this and the next year will be a very productive year for the ICFA Beam Dynamic Panel activities. Following the endorsement of ILC operating at 250 GeV by ICFA, the Japanese Ministry of Education, Culture, Sports, Science and Technology (MEXT) renewed its activities with the ILC working groups to discuss physical merits of ILC at 250GeV and the technical and cost aspects. The final reports were already made and sent to the Japanese government.

The editor of this issue are Dr. Eliana Gianfelice-Wendt, a senior scientist at Fermilab. The theme is the electron-ion colliders (EIC). I want to thank Eliana for editing a valuable and formidable newsletter of high quality for the accelerator community.

1.2 From the Editor

Eliana Gianfelice-Wendt, Fermilab
Mail to: mailto:eliana@fnal.gov

Dear readers! I am relatively new to the ICFA panel for Beam Dynamics and this is the first Newsletter I am editing. I thank the Chair for giving me this opportunity.
Thinking on interesting topics to be proposed, my choice fell on electron/hadron colliders with polarized beams (EIC), which realization has been recognized by the 2015 US Nuclear Science Advisory Committee (NSAC) as the highest priority for nuclear science following the completion of the Facility for Rare Isotope Beams (FRIB).

Particle spin was introduced in the 20s for explaining the result of the Stern-Gerlach experiment. Spin precession equation was first derived by Thomas in 1927 and reformulated in covariant 4-vector form by Bargmann, Michel and Telegdi in 1959.
In 1959 Froissart and Stora studied the effect of resonance crossing of polarized protons.
In the early 60s Sokolov and Ternov discovered the self-polarization mechanism.
The very first observation of beam self-polarization followed in 1968 at
ACO in Orsay and was confirmed at Novosibirsk VEPP-2 in 1970 and VEPP-2M where the technique of high precision beam energy measurement by using resonant depolarization was invented.

Owing to the added complexity of providing longitudinal polarization for the experiments, at high energy e+- circular colliders priority has been given to luminosity. LEP used beam polarization solely for high precision energy measurement. Besides e+e- collisions, SLC at SLAC provided collisions of ~46 GeV longitudinally polarized electrons against polarized nuclear targets. The polarized electron beam was supplied by a polarized source. Research with polarized electrons at low energy is pursued at VEPP-4 in Novosibirsk (radiative polarization, energy calibration), ELSA and MAMI (polarized sources) in Germany, and CEBAF (recirculating linacs) at JLab.
Self-polarization mechanism being useless for heavy particles, polarized hadrons must be produced by polarized sources and accelerated through resonances. Polarized hadrons became available in the 60s thanks to the steady steps forward of polarized ion sources. The Argonne ZGS (1963-1979), the first synchrotron to accelerate spin polarized protons, demonstrated the possibility of crossing 29 resonances with negligible loss of polarization. Since then much progress has been done in spin manipulation techniques at AGS, IUCF, where the Siberian Snakes concept was proven, and in particular at RHIC, the world's only polarized proton collider.

Polarization is considered extremely important for the physics program of lepton-hadron colliders. The only ring colliding protons with (longitudinally) polarized leptons has been HERA (DESY). The lepton energy was about 27.5 GeV while protons were accelerated to 820 GeV, and later to 920 GeV. Polarized leptons were delivered to the HERMES internal target experiment and, after the machine upgrade, to the collider experiments H1 and ZEUS. Transverse lepton polarization was obtained through Sokolov-Ternov effect and, for the first time in a high energy ring, polarization was brought into the longitudinal direction at the experiments by means of spin-rotators.

The possibility of getting polarized protons in addition was extensively studied. The studies showed that this would have been a daunting task, however they gave the opportunity of consolidating the theory of acceleration and storage of proton beams at very high energy.

The idea of an electron/hadron collider with eventually both beams polarized, has been carried out since on both sides of the Atlantic.
Two studies in the US have survived infancy, namely BNL eRHIC and JLab JLEIC.
In this Newsletter the primary aspects of these two studies are presented.

I take the opportunity for warmly thanking all contributors for their effort.

2 THE ELECTRON-ION COLLIDER (EIC)

2.1 The Electron Ion Collider Science

Elke C. Aschenauer (*) and Markus Diefenthaler (**)

Mail to: elke@bnl.gov
mdiefent@jlab.gov

(*) Brookhaven National Laboratory, Upton, NY 11973, USA
(**) Thomas Jefferson National Accelerator Facility, Newport News, Virginia, USA

2.1.1 **Introduction**

Quantum Chromodynamics (QCD), the theory of the strong interaction, is a cornerstone of the Standard Model of modern physics. It explains all nuclear matter as bound states of point-like fermions, known as quarks, and gauge bosons, known as gluons. The gluons bind not only quarks but also interact with themselves. Unlike with the more familiar atomic and molecular matter, the interactions and structures are inextricably mixed up, and the observed properties of nucleons and nuclei, such as mass and spin, emerge out of this complex system. The mass of the nucleon e.g. is not due to its nearly massless quarks (and massless gluons) but originates from the self-generating gluon field and the quark-gluon interactions. The similarity of mass between the proton and neutron arises from the fact that their internal gluon dynamics are the same. The key aspects of QCD, asymptotic freedom, chiral symmetry breaking, and color confinement, are driven by gluons. Despite the fundamental role of gluons, and the many successes in our understanding of QCD, the properties and dynamics of gluons remain largely unexplored.

To precisely image the quarks and gluons and their interactions and to explore the new QCD frontier of strong color fields in nuclei, the Nuclear Physics community proposes an US-based Electron Ion collider (EIC) with high-energy and high-luminosity, capable of a versatile range of beam energies, polarizations, and ion species. The community is convinced that the EIC is the right tool to understand how matter at its most fundamental level is made. In recognition of this, the Nuclear Science Advisory Committee advising the Department of Energy and the National Science Foundation, recommended in its Long Range Plan in 2015 an EIC as the highest priority for new facility construction [1].

Subsequently, a National Academy of Sciences panel was charged to review both the scientific opportunities enabled by a U.S. based EIC and the benefits to other fields of science and society [2]. The National Academy of Sciences report strongly articulates the merit of an EIC: *"In summary, the committee finds a compelling scientific case for such a facility. The science questions [How does the mass of the nucleon arise? How does the spin of the nucleon arise? What are the emergent properties of dense systems of gluons?] that an EIC will answer are central to completing an understanding of atoms as well as being integral to the agenda of nuclear physics today. In addition, the*

development of an EIC would advance accelerator science and technology in nuclear science; it would as well benefit other fields of accelerator-based science and society, from medicine through materials science to elementary particle physics."
This positive report could be the basis for a Critical Decision-0 or Mission Need approval for the Department of Energy Office of Science, setting in motion the process towards formal project R&D, engineering and design, and construction. The DOE Office of Nuclear Physics is already supporting increased efforts towards the most critical generic EIC-related accelerator research and design.

2.1.2 **The Secrets of Nucleons and Nuclei**

Deep-inelastic scattering (DIS), the basic process at the EIC, is because of its unmatched precision the ideal tool to study the inner structure of nuclear matter. The distribution of partons insight nucleons and nuclei depends on the scale, Q^2, which specifies the resolution at which partons are resolved, and the momentum fraction, x, carried by the parton relative to the momentum of the nucleon. Both variables (x, Q^2) define the kinematics and regime probed in a DIS measurement and can be controlled event-by-event. Figure 1 shows schematically how going from high x (~1) to small x ($\sim 10^{-4\text{-}5}$) at a resolution scale Q^2 of a few GeV^2 reveals a more and more complicated structure of quarks and gluons inside the proton. The proton goes from a few-body regime with its structure dominated by the valence quarks to a many-body regime dominated by the quark-gluons dynamics responsible for hadron structure, to a collective regime dominated by gluons generated through QCD radiation and at last to the saturation regime where the parton densities are so large that the gluon radiation is balanced by gluon recombination leading to non-linear effects.
Understanding the observed properties of nucleons or nuclei, such as mass or spin, requires to be able to probe all regimes and the transition from one regime to the other and to explore how the observed properties emerge from the complex, strongly-interacting many-body systems of nuclear matter. The EIC with versatile beam energies and species and a broad range in x and Q^2 will be the right tool to unravel the QCD structures and dynamics of matter.

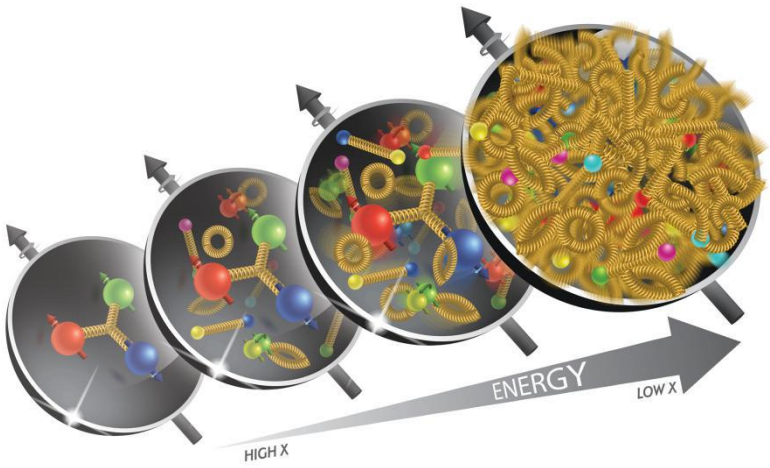

Figure 1: The development of the internal quark and gluon structure of the proton going from high to low x. Decreasing x corresponds to increasing the center-of-mass energy.

Till today the consolidated understanding of the nucleon structure is basically one-dimensional. In inclusive DIS, the nucleon appears as a bunch of fast-moving quarks, antiquarks and gluons, whose transverse positions and momenta are not resolved. EIC will open up the unique opportunity to go far beyond this one-dimensional picture of the nucleon. It will enable parton femtoscopy by imaging quarks and gluons in transverse position and momentum space for all kinematic regimes. Such "tomographic images" will provide insight into the QCD dynamics inside hadrons, such as the interplay between sea quarks and gluons and the role of pion degrees of freedom at large transverse distances.

Hadron structure cannot be understood without unraveling spin structure. While past or existing DIS experiments were and are very successful in determining the polarized quark structure of the nucleon and of some light nuclei, none matches the unique capabilities of an EIC by being able to change at the same machine between longitudinal, transverse, and (for deuteron only) tensor polarization states and with being able to collide polarized electron beams with polarized protons, deuteron, and Helium-3 beams over a broad kinematic range.

The capability of electron-ion collision with a wide range in A at the EIC will allow to extend the "tomographic images" to nuclei to gain insight into the short-range structure of nuclei. Nuclei are made out of nucleons, which in turn, are bound states of the fundamental constituents, quarks and gluons, probed in high-energy scattering. The binding of nucleons into a nucleus must be sensitive to how these quarks and gluons are confined into nucleons and must influence how they are distributed inside the bound nucleons. EMC at CERN [3] and many follow-up experiments revealed a peculiar pattern of nuclear modification of the DIS cross-section as a function of Bjorken x, giving us clear evidence that the momentum distributions of quarks in a fast-moving nucleus are strongly affected by the binding and the nuclear environment. With much wider kinematic reach in both x and Q^2, and unprecedented high luminosity, experiments at EIC not only can explore the influence of the binding on the momentum distribution of sea quarks and gluons, but also, study how quark-gluon interactions create nuclear binding.

Both nucleons and nuclei, when viewed at high energies, appear as dense systems of gluons creating fields whose intensity may be the strongest in nature. These high densities will possibly lead to the phenomenon of parton (gluon) saturation [4,5]. The transition from the collective to saturation regime is characterized by the saturation momentum, Q_S, which can be large for heavy ions. By studying the collisions of high energy nuclei with energetic electrons, one might be able to probe the strong gluon fields beyond the collective regime as suggested by HERA, RHIC, and the LHC data and identify the saturation regime and its parameters.

The unique kinematic reach of the EIC for polarized electron-proton and electron-ion collisions is illustrated in Figure 2.

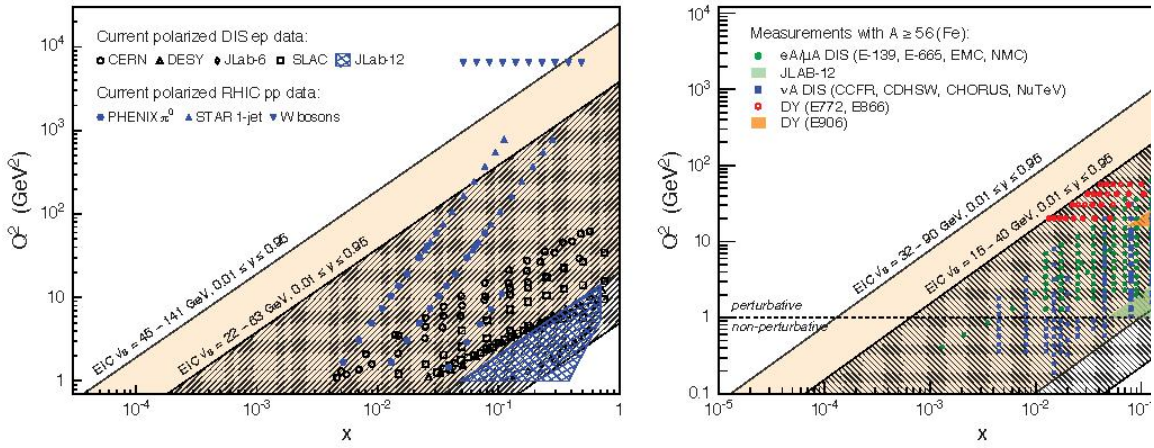

Figure 2: *Left*: The range in parton momentum fraction *x* vs. the square of the momentum transferred by the electron to the proton Q^2 accessible with EIC in polarized ep collisions for two different center-of-mass regions ($\sqrt{s} = 22 - 63$ **GeV and** $45 - 141$ **GeV**) compared to past (CERN, DESY, SLAC) and existing (JLAB, COMPASS) facilities as well to polarized pp collisions at RHIC. *Right*: The kinematic acceptance in *x* and Q^2 of completed lepton-nucleus (DIS) and Drell-Yan (DY) experiments (all fixed target) compared to the EIC acceptance for two different center-of-mass regions ($\sqrt{s} = 15 - 40$ **GeV and** $32 - 90$ **GeV**). The acceptance bands for EIC are defined by $Q^2 = xsy$ with $0.01 \leq y \leq 0.95$.

2.1.3 The Spin of the Nucleon

Helicity-dependent parton densities encode the information to what extent quarks and gluons with a given momentum fraction *x* tend to have their spins (anti-)aligned with the spin direction of a nucleon. The most precise knowledge about these non-perturbative quantities, along with estimates of their uncertainties, is gathered from comprehensive global QCD analyses [6,7] to all available data taken in spin-dependent DIS and proton-proton collisions, with and without additional identified hadrons in the final state.

Apart from being essential for a comprehensive understanding of the partonic structure of hadronic matter, helicity PDFs draw much their relevance from their relation to one of the most fundamental and basic but yet not satisfactorily answered questions in hadronic physics, namely how the spin of a nucleon is composed of the spins and orbital angular momenta of quarks and gluons. The integrals of helicity PDFs over all momentum fractions *x* (first moments) at a resolution scale Q^2, $\Delta f(Q^2) \equiv \int_0^1 \Delta f(x,Q^2)dx$, provide information about the contribution of a given parton flavor *f* to the spin of the nucleon. A precise determination of the polarized quark $\Delta q(x,Q^2)$ and gluon $\Delta g(x,Q^2)$ distribution functions in a broad kinematic regime is a primary goal of the EIC.

Several channels are sensitive to Δg in ep scattering at collider energies such as DIS jet or charm production, but QCD scaling violations in inclusive polarized DIS have been identified as the golden measurement. Scaling violations are a key prediction of QCD

for PDFs and have been used successfully at HERA to determine the unpolarized gluon distribution with high precision. The inclusive DIS structure function $g_1(x,Q^2)$ is the most straightforward probe in spin physics and has been determined at various fixed-target experiments at medium-to-large values of x in the last two decades. It is also the best-understood spin-dependent quantity from a theoretical point of view.
For studying DIS scaling violations, i.e., $dg_1(x,Q^2)/dlogQ^2$, efficiently, it is not only essential to have good precision but also to cover the largest possible range in Q^2 for any given fixed value of x. The accessible range in Q^2 is again linked to the capabilities of detecting electrons in an as wide as possible range of momenta and scattering angles.
Figure 3 (left) illustrates the simulated data sets for inclusive polarized DIS at the EIC for three different choices of center of mass energies. The error bars reflect the expected statistical accuracy for an integrated luminosity of 10 fb^{-1} and assuming 70% beam polarizations. The uncertainties of the DSSV14 theoretical prediction [7] are shown by the blue bands.

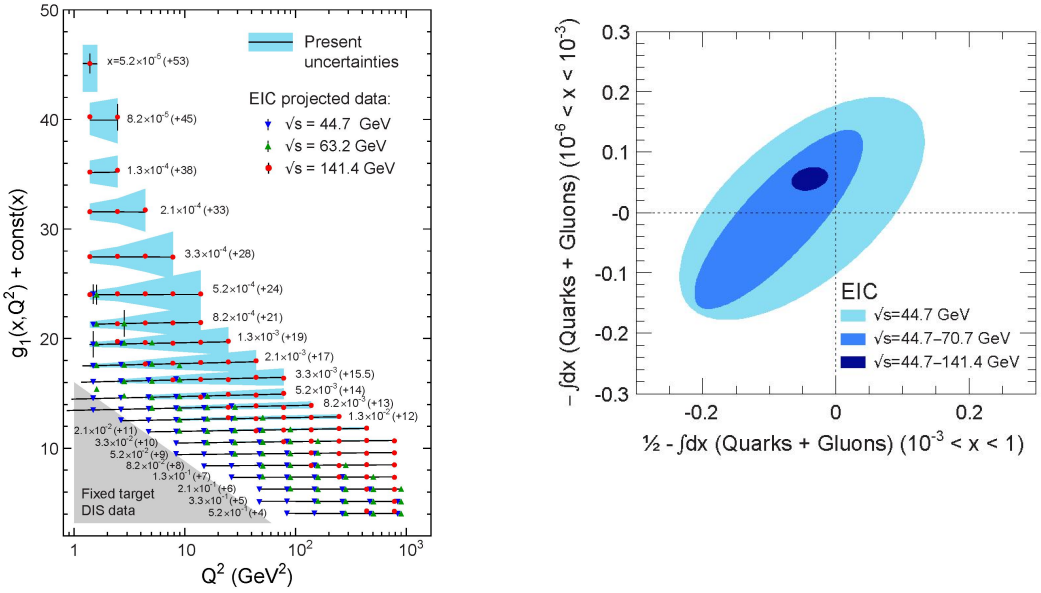

Figure 3: *Left:* Projections for the structure function $g_1(x,Q^2)$ at different center of mass energies, compared with a model extrapolation and its uncertainties [8]. The curves correspond to different values of x that are specified next to each curve. For clarity, constants are added to g_1 to separate different x bins; moreover, multiple data points in the same x-Q^2 bin are displaced horizontally. The gray area marks the phase space currently covered by fixed target experiments.
Right: The EIC's impact on the knowledge of the integral of the quark and gluon spin contribution in the range $10^{-6}<x<10^{-3}$ (y-axis) versus the contribution from the orbital angular momentum in the range $10^{-3}<x<1$ (x-axis).

Figure 3 uses simulated data to clearly demonstrate the EIC's impact on the knowledge of the integral of the proton's quark and gluon spin contributions for $10^{-6}<x<10^{-3}$ versus the contribution to the orbital angular momentum for the range $10^{-3}<x<1$. A dramatic shrinkage of the uncertainties in the parton helicities is seen with the largest energy reach. The underlying reason for this rapid shrinkage can be traced to the completely unknown behavior of $g_1(x,Q^2)$ due to the lack of data at small x.

The full understanding of the flavor separated of the spin structure of protons and neutrons will require measurements of transverse spin asymmetries to measure the transversity distribution and deuteron and/or Helium-3 beams.

Machine Requirements for Polarized Deep Inelastic Scattering:
The measurement of spin asymmetries requires longitudinally polarized electrons off longitudinally (or transversely) polarized light hadron beams (proton, Deuterium and/or He-3) with high polarization values (> 70%). Experimental systematic uncertainties, coming from polarization measurements and other (time dependent, detector related) false asymmetries in measurements have to be constrained to a few percent [8]. High energy beams will allow to probe the missing spin contributions of quarks and gluons at lox-*x*.

2.1.4 Nucleons and Nuclei in 3-Dimensions

From inclusive DIS measurements we can only learn about the longitudinal motion, *x*, of partons (see Figure 4) in a fast-moving nucleon but no information about the transverse positions or momenta of partons can be obtained. Even though a fast-moving nucleon is Lorentz-contracted, its transverse size is still about 1 fm, which is the typical scale of non-perturbative interactions, where phenomena such as confinement occur. This leads to fundamental questions such as:

- How are quarks spatially distributed inside the nucleon?
- How do they move in the transverse plane?
- Is there a correlation between orbital motion of quarks, their spin, and the spin of the nucleon?
- How can we access information on such spin-orbit correlations, and what will this tell us about the nucleon?

The above questions address two complementary aspects of the nucleon structure: the distribution of quarks and gluons in the transverse plane in momentum space and in coordinate space. We still lack quantitative answers to these questions, but in recent years we have obtained a much better idea on how to answer them due to recent theoretical progress [8]. Generalized parton Distributions (GPDs) and transverse momentum dependent parton distributions (TMDs) are the novel tools in QCD that allow us to study the inner structure in three dimensions. In addition to the longitudinal momentum fraction x, GPDs provide information about the transverse position b_T (see Figure 5). TMDs describe the inner structure in momentum space as a function of x and the transverse momentum k_T (see Figure 6). They encode information about spin-orbit correlations in nuclear matter.
To precisely image the momentum and spatial structure of quarks and gluons is one of the key goals of an EIC.

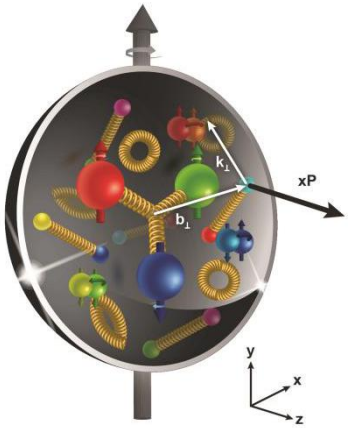

Figure 4: Schematic view of a parton inside the proton with longitudinal momentum fraction x, transverse position b_T and transverse momentum k_T in the proton.

The EIC will probe TMDs in the few-body, many-body and collective regime. The high luminosity and broad kinematic coverage of the EIC will allow for a high-precision measurement of TMDs for quarks taking all kinematic correlations into account in a multi-dimensional analysis in x, Q^2, Φ_S, p_T, z, and Φ. The kinematic reach of the EIC will provide not only a broad coverage in x, $0.01 < x < 0.9$ and a sufficiently high Q^2 to suppress higher twist contributions but will enable the first measurement of TMDs for sea quarks and the first measurement of TMDs for gluons by tagging the photo-gluon fusion process. The coverage of the few-body, many-body and collective regimes is ideal for systematic studies of TMD evolution and stringent tests of the underlying theory of TMDs.

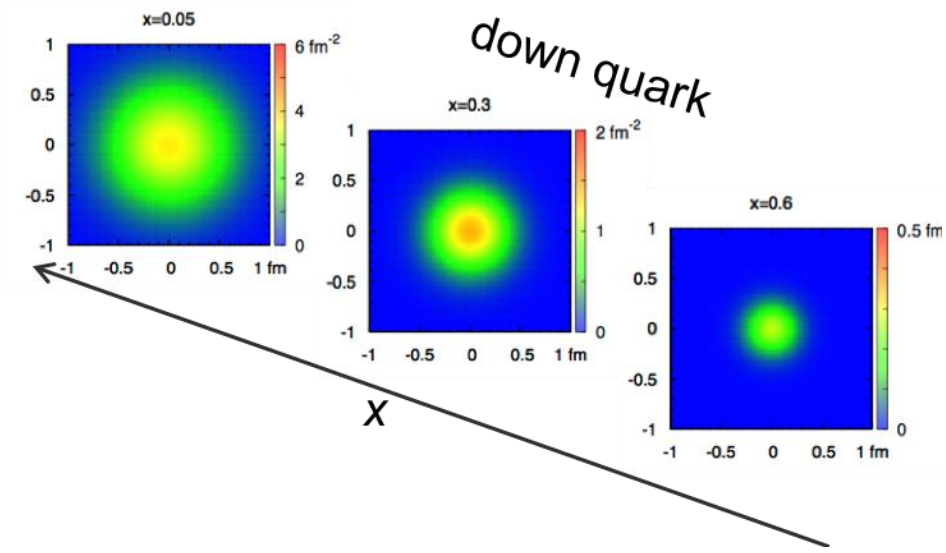

Figure 5: Transverse position snapshots of a down quarks in an unpolarized nucleon for three values in x. The color coding of the three panels indicates the probability of finding the down quark.

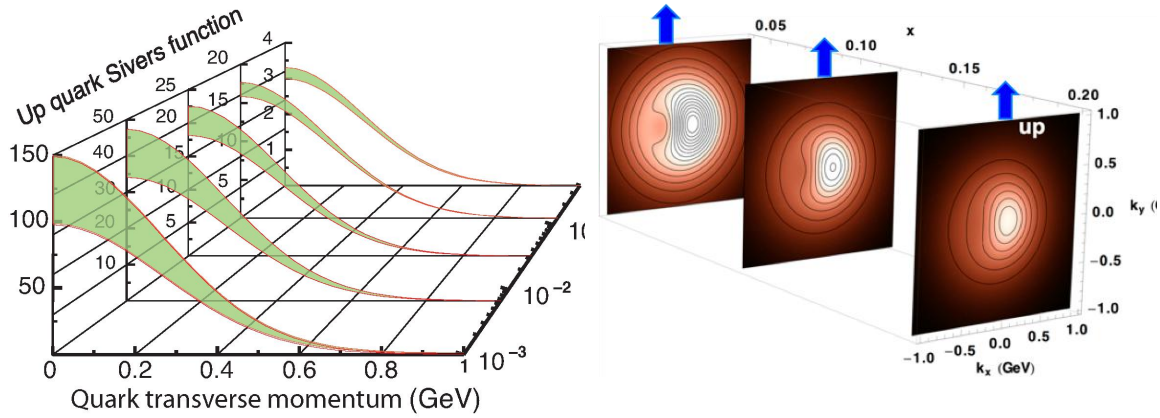

Figure 6: *Left:* The transverse momentum profile of the Sivers TMD for up quarks for five x values accessible at the EIC, and corresponding statisistical uncertainties. *Right:* Transverse momentum snapshots of a transversely polarized nucleon (polarization direction indicated in blue) for three values in x. The color coding of the three panels indicates the probability of finding the up quark.

The EIC will allow to study GPD in various processes in the few-body, many-body and collective regime. The flavor decomposition of GPDs and their dependence on the polarization can be studied for valence and sea quarks in measurements of electro-production of π^+, $K^{+/-}$, ρ, and K^*. Measurements of deeply virtual Compton scattering [9] and the exclusive production of J/Ψ, ρ and φ mesons will allow to constrain transverse position distributions of sea quarks and gluons and their spin-orbit correlations.
An unique opportunity of the EIC is to study GPDs and TMDs in nuclei and learn about their nuclear dependence.

Machine Requirements for Nucleons and Nuclei in 3-Dimensions:
Measurements of GPDs and TMDs require longitudinally polarized electrons off longitudinally and transversely polarized light hadron beams (proton, Deuterium and/or He-3) with high polarization values (> 70%). High luminosity ($10^{33\text{-}34}$ cm^{-2}s^{-1}) is required for a multidimensional analysis taking all the kinematic correlations into account. Versatile beam energies are required to probe the few-body, many-body and collective regime and for a broad coverage in Q^2.

2.1.5 Physics at high Parton Densities

DIS experiments with nuclei have established that PDFs (or structure functions) in nuclei compared to the ones of a free proton exhibit various nuclear effects, not surprisingly most prominent for gluons: a strong suppression of the gluon distribution function in nuclei compared to that in nucleons for $x < 0.01$ (shadowing), and slight enhancement around $x \sim 0.1$ (anti-shadowing), followed again by a suppression (EMC effect [3]) at large x. In sharp contrast to the proton, the gluonic structure of nuclei is not known for $x < 0.01$. Measurements of the inclusive cross section with and without

charm tagging in the final state will considerably constrain these distributions down to $x = 10^{-4}$. To emphasize the precision achievable at an EIC, two examples of the reduced cross-section as a function of x at the Q^2 values of 4.4 GeV^2 and 139 GeV^2 are shown in Figure 7 for inclusive (left) and charm (right) production. It is clear from Figure 7 that at large values of x, the uncertainties are small. It is only at $x < 10^{-2}$ and small Q^2 that the expected experimental errors on the EIC measurements become much smaller than the uncertainties from the EPPS16 parametrization that are largest at the smallest x values; these will clearly be significantly constrained by data at these x values.

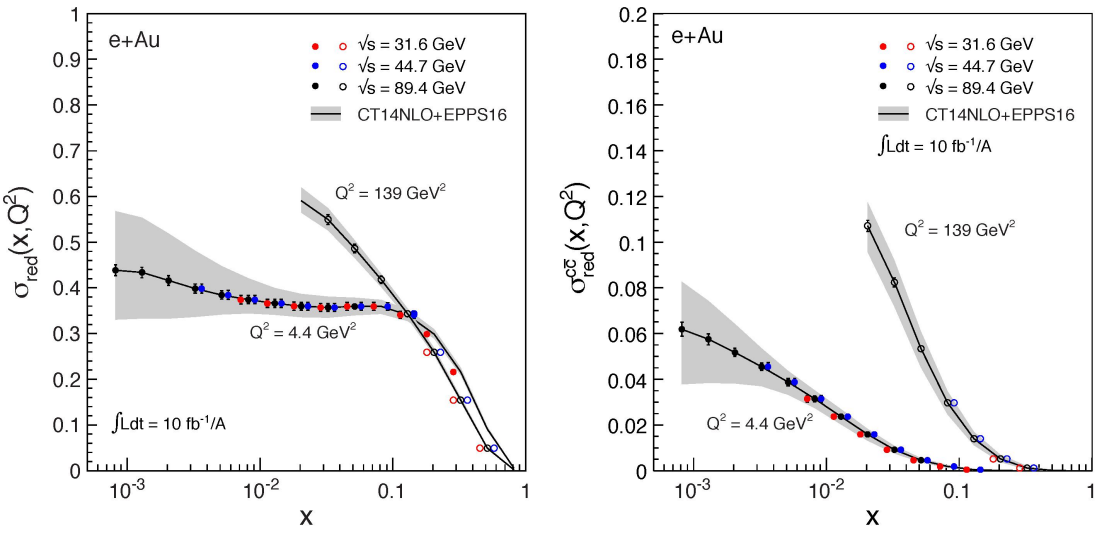

Figure 7: Inclusive (left) and charm (right) reduced cross-sections as a function of x at the Q^2 values of 4.4 GeV^2 (solid circles) and 139 GeV^2 (open circles) at three different center-of-mass energies.

The modification introduced by the nuclear environment can be quantified in terms of the ratio between the nucleus A and the free proton PDF (R_f^A , $f = q; g$) for quarks and gluons, with deviations from unity being manifestations of nuclear effects. A depletion of this ratio relative to unity is often called shadowing. The impact study of EIC simulated data shown in Figure 7 was done by incorporating these data into the EPPS16 fit [10]. However, as the parameterization is too stiff in the as yet unexplored low x region, additional free parameters for the gluons have been added to the functional form (EPPS16* [11]). The corresponding R_g^{Pb} from EPPS16* is shown in Figure 8.

The grey band represents the EPPS16* theoretical uncertainty. The orange band is the result of including the EIC simulated inclusive reduced cross-section data in the fit. The lower panel of each plot shows the reduction factor in the uncertainty (orange curve) with respect to the baseline fit (gray band). It is clear that the higher center-of-mass energy has a larger impact in the whole kinematical range with the relative uncertainty roughly a factor of 2 smaller than for the lower center-of-mass energy. The blue hatched bands show the simulated charm quark reduced cross-section for which no data currently exist. While it brings no additional constraint on the low-x region, its impact at high-x is remarkable providing up to a factor 8 reduction in uncertainty (blue curve).

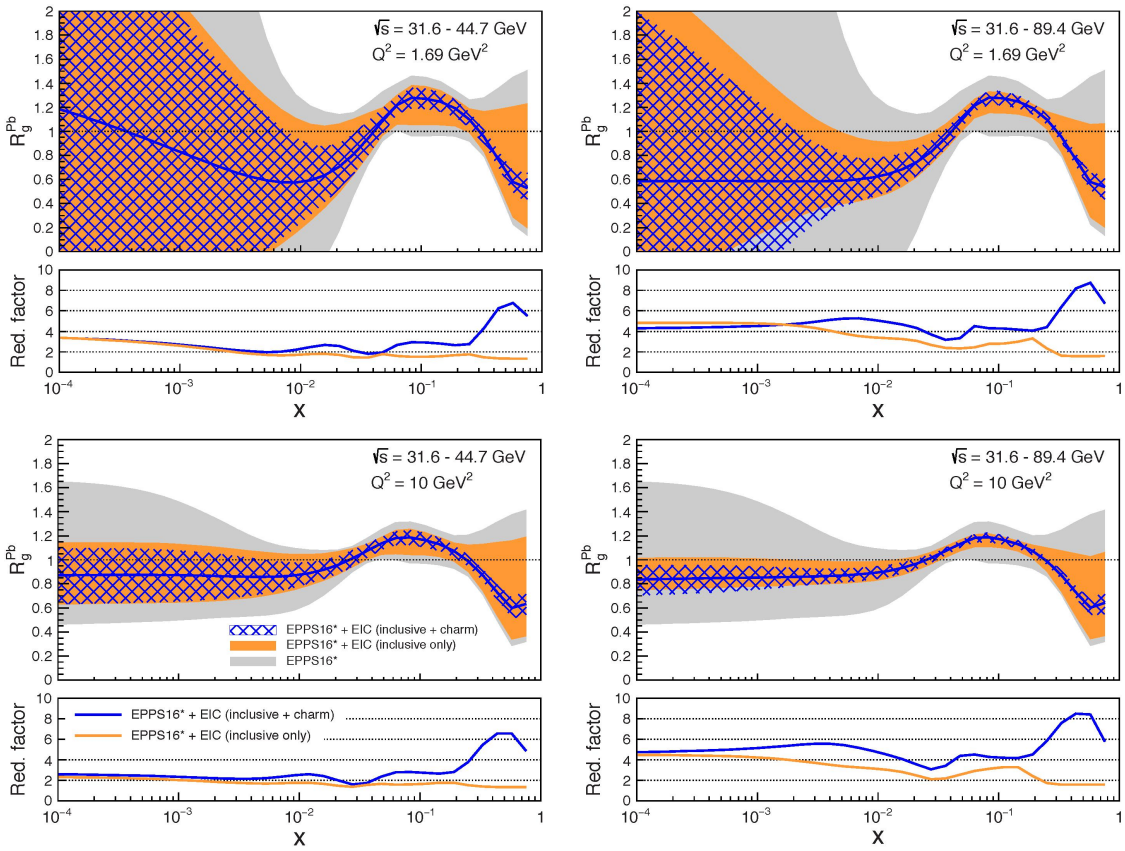

Figure 8: The ratio R_g^{Pb}, from EPPS16*, of gluon distributions in a lead nucleus relative to the proton, for the low (left) and high (right) $\sqrt{s}$, at Q^2 = 1.69 GeV^2 and Q^2 = 10 GeV^2 (upper and lower plots, respectively). The grey band represents the EPPS16* theoretical uncertainty. The orange (blue hatched) band includes the EIC simulated inclusive (charm quark) reduced cross-section data. The lower panel in each plot shows the reduction factor in the uncertainty with respect to the baseline fit.

The nucleon is a complex system of strongly interacting quarks and gluons. In addition to the valence quarks dominating the nucleon structure at large values of x, there is a "sea" of quarks, antiquark, and gluons popping in and out of existence and defining the nucleon structure in the many-body and collective regimes for intermediate and small x. While the nucleon sea originates from various contributions, it is dominated in the collective regime by gluons radiating off quark-antiquark pairs and other gluons.
However, gluon and quark densities cannot grow without limit at small-x. While there is no strict bound on the number density of gluons in QCD, there is a bound on the scattering cross-sections stemming from unitarity [12]. A nucleon or nucleus with a lot of "sea" gluons is more likely to interact in high-energy scattering, which leads to larger scattering cross-sections. Gluon saturation is a mechanism to tame this growth: When the gluon density becomes large, softer gluons can recombine into harder gluons. The competition between linear QCD radiation and non-linear gluon recombination causes the gluon distributions to saturate at small x. The onset of saturation and the properties of the saturated phase are characterized by a dynamical scale, the saturation scale [13,14,15], Q_S^2, which grows with increasing energy (smaller x). The saturation regime is terra incognita in QCD and can only be studied in high-energy collisions.

The advantage of using nuclei to explore this regime is the enhancement of the saturation phenomena with increasing A, making it easier to observe and study experimentally. This dependence is justified by any probe interacting over the distance $L \sim (2m_N x)^{-1}$ being unable to distinguish between nucleons in the front or back of the Lorentz contracted nuclei once $L > 2\,RA \sim A^{1/3}$; the probe then interacts *coherently* with all nucleons. These considerations suggest that $Q_S^2 \propto (A/x)^{1/3}$. DIS with large nuclei probes the same universal physics as seen in DIS with protons at x's at least two orders of magnitude lower (or equivalently an order of magnitude larger $\sqrt{s}$). When $Q^2 \gg Q_S^2$, one is in the well understood "linear" regime of QCD, while we have little theoretical control over the non-perturbative regime at $Q^2 \lesssim \Lambda_{QCD}^2$. For large nuclei, there is a significant regime at small x where $Q_S^2 \gg Q^2 \gg \Lambda_{QCD}^2$. This is identified as the saturation regime of strong non-linear gluon fields.
Quite generically, multi-parton correlations are more sensitive to the detailed dynamics of the probed objects than single parton distributions. One of the most captivating measurements in e+A is that of the azimuthal correlations between two hadrons h_1 and h_2 in $e + A \rightarrow e' + h_1 + h_2 + X$ processes. These correlations are not only sensitive to the transverse momentum dependence of the gluon distribution, but also to that of gluon correlations for which CGC computations are now available. The precise measurements of these di-hadron correlations at EIC would allow one to extract the spatial multi-gluon correlations and study their non-linear evolution.

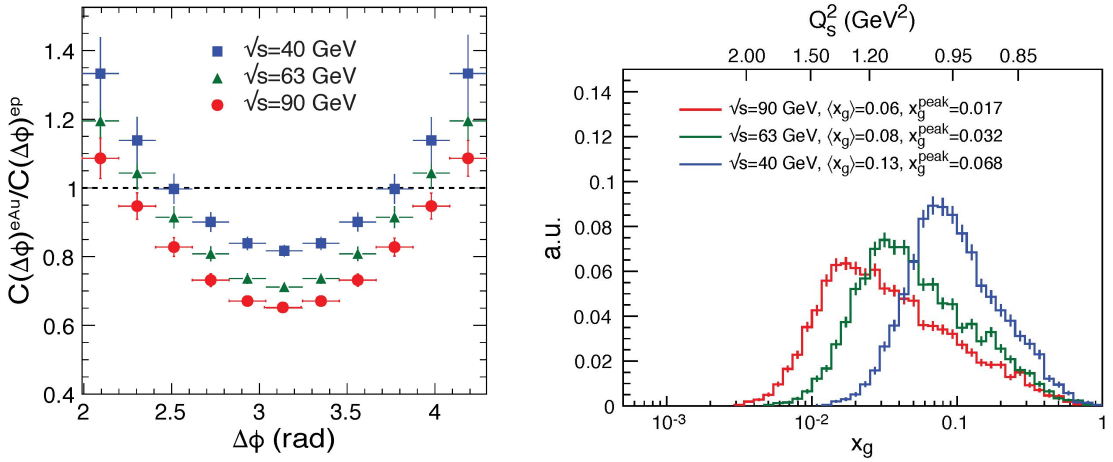

Figure 9: *Left:* Ratio of the dihadron correlation functions in e +Au collisions over those in e +p for the three center-of-mass energies. *Right:* x_g distributions probed by the correlated hadron pairs for different center-of-mass energies, √s= 40, 63, and 90 GeV in e+Au collisions. The average and peak values for the distributions are shown. The gluon saturation scales $\boldsymbol{Q_s^2}$ corresponding to xg values are displayed on top of the plot.

Experimentally, di-hadron correlations are relatively simple to study at EIC. They are usually measured in the plane transverse to the beam axis and are plotted as a function of the azimuthal angle $\Delta\varphi$ between the momenta of the produced hadrons in that plane. Back-to-back correlations are manifested by a peak at $\Delta\varphi = \pi$. Saturation effects in this channel correspond to a progressive disappearance of the back-to-back correlations of hadrons with increasing atomic number A. In the conventional linear QCD picture, one expects from momentum conservation that the back-to-back peak will persist as one

goes from e+p to e+A. In the saturation framework, due to multiple re-scatterings and multiple gluon emissions, the large transverse momentum of one hadron is balanced by the momenta of several other hadrons, effectively washing out the correlation [16]. A comparison of the heights and widths of the di-hadron azimuthal distributions in e+A and e+p collisions respectively would clearly mark out experimentally such an effect. An analogous phenomenon has already been observed at RHIC for di-hadrons produced at forward rapidity in comparing central d+Au with p+p collisions at RHIC [17]. In that case, di-hadron production originates from valence quarks in the deuteron scattering on small-x gluons in the target Au nucleons.
To better illustrate the energy dependence, the ratio of the correlation functions in e+Au over those in e+p is shown in Figure 9 (left) for three center-of-mass energies. Note the suppression is a factor of 2 at √s = 90 GeV. Measuring a suppression greater than 20% relative to e+p will be crucial in the comparison of data with saturation model calculations that typically carry uncertainties of at least in this order [18]. The ability to study dihadron suppression over a wide range of x_g is of the utmost importance for this observable. Figure 9 (right) shows the corresponding x_g distributions for dihadrons produced at the three different center-of-mass energies. The corresponding Q_s^2 values are provided at the top of the plot. Only a sufficiently wide lever arm will allow one to study the non-linear evolution in x_g and Q^2 and extract the saturation scale with high precision.

Machine Requirements for Physics with Nuclei:
The measurement of nuclear PDFs and observables to establish saturation need both nuclear beams with the highest nuclear mass and center of mass energy to reach into a regime to study the onset of saturation and the evolution of its effects with x and Q_s^2 to reach lowest x at highest Q_s^2.

2.1.6 Summary and Conclusions

The EIC will explore how nuclear matter at its most fundamental level is made. The facility will allow to precisely image the quarks and gluons and their interactions and to explore the new QCD frontier of strong color fields in nuclei. The science program described in this overview and in detail in [1,2,19] addresses directly and with high precision the following questions that relate to our fundamental understanding of QCD:

- How are the sea quarks and gluons, and their spins, distributed in space and momentum inside the nucleon? How do the nucleon properties emerge from them and their interactions?
- How do color-charged quarks and gluons, and colorless jets, interact with a nuclear medium?
  How do the confined hadronic states emerge from these quarks and gluons?
  How do the quark-gluon interactions create nuclear binding?
- How does a dense nuclear environment affect the quarks and gluons, their correlations, and their interactions? What happens to the gluon density in nuclei? Does it saturate at high energy, giving rise to a gluonic matter with universal properties in all nuclei, even the proton

The parameters for an EIC can be derived from the above questions and have been used to guide the eRHIC and JLEIC pre-conceptual designs being discussed in the following sections:

Contrary to hadron-hadron collisions, **deep inelastic scattering** of electrons off hadrons is a process that allows to the study the inner structure of nuclear matter with unmatched precision. A **high-energy** (20 -- 100 GeV, upgradable to 140 GeV) electron-ion collider is needed to reach from the many-body regime dominated by quark-gluon dynamics to the collective and saturation regimes dominated by gluon effects.

A **versatile range of** electron and ion **beam energies** is required for full coverage of the many-body, collective, and saturation regimes as well as for a broad coverage in Q^2 for studying QCD evolution, disentangling the non-perturbative and perturbative regimes of QCD, and make connection to the kinematic regimes with existing experiments.

Longitudinal polarized lepton and longitudinal and transversely polarized hadron beams are required to investigate how the different partons make up the spin of the nucleon and to map the 3-dimensional structure of nuclear matter.

A **versatile range of ion species** is required to study nuclear dependence and saturation effects. A wide range of ion beams from light to heaviest mass offers, e.g., a precise dial in the study of propagation-length for color charges in nuclear matter. Ion beams with heaviest mass are required to possibly identify the saturation regime.
High luminosity ($10^{33\text{-}34}$ cm^{-2}s^{-1}) is required for high precision measurements in various configurations (beam, polarization, ion species), in particular to unravel the multidimensional dependencies of the different physics processes on the kinematic variables (x, Q^2, Φ_S, p_T, z, and Φ).

2.1.7 References

[1] A. Aprahamian et al., “Reaching for the horizon: The 2015 Long Range Plan for Nuclear Science”, INSPIRE-1398831 https://science.energy.gov/~/media/np/nsac/pdf/2015LRP/2015_LRPNS_091815.pdf
[2] The National Academy of Sciences Report, https://www.nap.edu/catalog/25171/an-assessment-of-us-based-electron ion-collider-science
[3] J. J. Aubert et al., Phys. Lett. B123, 275 (1983). J. Ashman et al., Nucl. Phys. B328, 1 (1989).
[4] E. Iancu, A. Leonidov, and L. D. McLerran, Phys. Lett. B510, 133 (2001).
[5] H. Weigert, Prog. Part. Nucl. Phys., 55:461–565, 2005, hep-ph/0501087.
[6] D. de Florian, R. Sassot, M. Stratmann, and W. Vogelsang, Phys. Rev. Lett. 101, 072001 (2008).
D. de Florian, R. Sassot, M. Stratmann, and W. Vogelsang, Phys. Rev. D 80, 034030 (2009).
[7] D. de Florian, R. Sassot, M. Stratmann, and W. Vogelsang, Phys. Rev. Lett. 113 , 012001 (2014).
[8] The 3-D Structure of the Nucleon, M. Anselmino, et al. Eur. Phys. J. A (2016) 52. 164.
[9] E.C. Aschenauer, S. Fazio, K. Kumericki, and D. Mueller, JHEP09(2013)093.

[10] K. J. Eskola, P. Paakkinen, H. Paukkunen, and C. A. Salgado, Eur. Phys. J. C77 , 163 (2017).
[11] E. C. Aschenauer et al. , Phys. Rev. D 96, 114005 (2017).
[12] M. Froissart, Phys. Rev. 123, 1053 (1961).
[13] L. V. Gribov, E. M. Levin, and M. G. Ryskin, Phys. Rept. 100, 1 (1983).
[14] E. Iancu, K. Itakura, and L. McLerran, Nucl. Phys. A708, 327 (2002).
[15] A. H. Mueller and D. N. Triantafyllopoulos, Nucl. Phys. B640, 331 (2002).
[16] D. Kharzeev, E. Levin, and L. McLerran, Nucl. Phys. A748, 627 (2005).
[17] A. Adare et al. [PHENIX Collaboration], Phys. Rev. Lett. 107, 172301 (2011).
[18] L. Zheng, E.C. Aschenauer, J. H. Lee, and B.-W. Xiao, Phys. Rev. D89 , 074037 (2014).
[19] A. Accardi et al., Electron Ion Collider: The Next QCD Frontier, Eur. Phys. J. A52, 2016.

2.2 eRHIC

Christoph Montag and Vadim Ptitsyn
(for the eRHIC study group)
Mail to: montag@bnl.gov
Brookhaven National Laboratory, Upton, NY 11973, USA

2.2.1 Introduction

Brookhaven National Laboratory (BNL) is proposing eRHIC as a cost-effective implementation of the EIC which meets all the requirements on the accelerator formulated in the White Paper. The EIC eRHIC takes advantage of the entire existing Relativistic Heavy Ion Collider (RHIC) facility with only a few modifications, with only modest cost implications. The well-established beam parameters of the present RHIC facility are close to what is required for the highest performance of eRHIC. The addition of an electron storage ring inside the present RHIC tunnel will provide polarized electron beams for collisions with the polarized protons or heavy ions of RHIC.

The eRHIC design must satisfy the requirements of the science program, while having acceptable technical risk, reasonable cost, and a clear path to achieving design performance after a short period of initial operating time. The strategy for arriving at an optimum design that meets these requirements led to an eRHIC design based on an electron storage ring, referred to as Ring-Ring (R-R) design.

The storage ring based design meets or even exceeds the requirements referenced in the Long Range Plan including the upgraded energy reach:

Center-of-mass energy (E_{CM}) of 29 to 140 GeV. The upper limit can only be extended by a significant additional investment in RF equipment; the lower limit is softer and is given by the ability to detect low energy deep inelastic scattered electrons; there is no hard restriction from the accelerator other than reduction in luminosity. The long range plan requires approx. 20 to 100 GeV;

- A luminosity of up to $10^{34}\mathrm{cm}^{-2}\mathrm{sec}^{-1}$; the long range plan requires 10^{33} to $10^{34}\mathrm{cm}^{-2}\mathrm{sec}^{-1}$;

- High polarization of electron and ion beams in arbitrary spin patterns with polarizations well above 50%; the long range plan requires polarizations up to 70%;
- Beam divergences at the interaction point and apertures of the interaction region magnets that are compatible with the acceptance requirements of the colliding beam detector;
- Collisions of electrons with a large range of light to heavy ions (protons to gold ions); the long range plan requires ions as heavy as lead;
- Two interaction regions.

The RHIC tunnel complex incorporates two large experimental halls, with full infrastructure for two major collider detectors. These are at the 6 o'clock position, where the RHIC STAR detector is currently operating, and the 8 o'clock position, home of the RHIC PHENIX detector; see Fig. 1. The design described here allows for eRHIC detectors in each of these areas. In this report we describe in detail the IR configuration for a large general purpose detector in one of these areas (6 o'clock) that could fulfill the requirements for the full range of EIC science questions described above. Our plans for eRHIC include the capability for two such detectors.

The scientific requirements, calling for high luminosity and near-complete angular coverage by the detector, result in an IR lattice that produces a significant degree of chromaticity (energy sensitivity of the beam optics). The non-linear sextupole fields needed to compensate for this effect then limit the dynamic aperture. Calculations motivated by experience at HERA indicate that adding an identical second IR can be achieved without further reduction of the dynamic aperture. We thus plan for detectors at both the IR6 and IR8 positions. In order to avoid unacceptably large beam-beam effects in the case of two experiments, the collider would be operated in a mode where each of the two experiments sees one-half of the bunch crossings; i.e., each experiment receives ½ of the total luminosity.

Highest luminosities can only be achieved by implementing strong cooling of the ion and proton beams to counteract emittance growth by intrabeam scattering (IBS) associated with the corresponding small beam emittances. Cooling of hadron beams with beam energies up to 275 GeV requires novel cooling techniques which are currently being developed and tested in an R&D program at BNL [1].

The design satisfies all requirements and takes into account that beam dynamics limits are not exceeded. In particular, the design parameters remain within the limits for maximum beam-beam tune-shift parameters (hadrons: $\xi_p \leq 0.015$; electrons: $\xi_e \leq 0.1$) and space charge parameter (≤ 0.06), as well as beam intensity limitations. The outline for the eRHIC electron ion collider is shown in Figure 1.

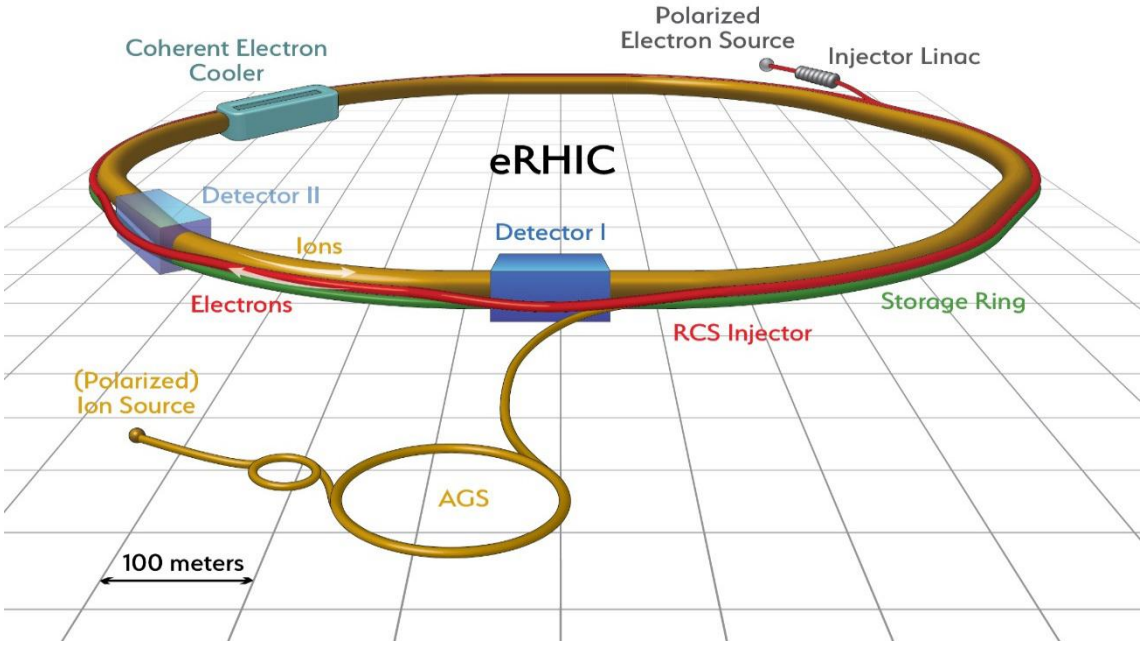

Figure 1: Schematic diagram of the eRHIC layout

Polarized electron bunches carrying a charge of 10 nC are generated in a state-of-the-art polarized electron source. The beam is then accelerated to 400 MeV by a linear accelerator (LINAC). Once per second, an electron bunch is accelerated in a rapid cycling synchrotron (RCS), which is also located in the RHIC tunnel, to a beam energy of up to 18 GeV and is then injected into the electron storage ring, where it is brought into collisions with the hadron beam. The polarization orientation of half of the bunches is anti-parallel to the magnetic guide field. The other half of the bunches have polarization which is parallel to the guide field in the arcs. The Sokolov-Ternov effect [2] will depolarize these electron bunches, in particular at 18 GeV where the (nominal) polarization time constant is smaller, namely 30 min. In order to maintain high spin polarization, each of the bunches with their spins parallel to the main dipole field (of which there are 165 at 18 GeV) is replaced every 6 min. The polarization lifetime is larger at lower beam energies and bunch replacements are less frequent.

The highest luminosity of $10^{34}\mathrm{cm}^{-2}\mathrm{sec}^{-1}$ is achieved with 10 GeV electrons colliding with 275 GeV protons ($E_{\mathrm{CM}} = 105$ GeV). The high luminosity is achieved due to ambitious beam-beam parameters, a flat shape (or large aspect ratio $\frac{\sigma_x}{\sigma_y}$) of the electron and hadron bunches at the collision point, and the large circulating electron and proton currents distributed over as many as 1320 bunches. Table 1 lists the main design parameters for the beam energies with the highest peak luminosity.

Table 1: Maximum Luminosity Parameters

Parameter	***hadron***	***electron***
Center-of-Mass Energy [GeV]	104.9	
Energy [GeV]	275	10
Number of Bunches	1320	
Particles per Bunch [10^{10}]	6.0	15.1
Beam Current [A]	1.0	2.5
Horizontal Emittance [nm]	9.2	20.0
Vertical Emittance [nm]	1.3	1.0
Hor. β-function at IP β_x^* [cm]	90	42
Vert. β-function at IPβ_y^* [cm]	4.0	5.0
Hor./Vert. Fractional Betatron Tunes	0.3/0.31	0.08/0.06
Horizontal Divergence at IP [mrad]	0.101	0.219
Vertical Divergence at IP [mrad]	0.179	0.143
Horizontal Beam-Beam Parameter ξ_x	0.013	0.064
Vertical Beam-Beam Parameter ξ_y	0.007	0.1
IBS Growth Time longitudinal/horizontal [hours]	2.2/2.1	-
Synchrotron Radiation Power [MW]	-	9.18
Bunch Length [cm]	5	1.9
Hourglass and Crab Reduction Factor	0.87	
Luminosity [10^{34}cm-2sec-1]	1.05	

At the lower center-of-mass energies, the beam sizes need to be increased and/or the beam intensities have to be decreased to keep the beam-beam tune shift below the maximum allowed value. At a higher center-of-mass energy, which is achieved by increasing the electron energy to 18 GeV the electron beam intensity has to be reduced to limit the synchrotron radiation power loss to 10 MW. Figure 2 shows the peak luminosity versus center-of-mass energy which will be achieved in eRHIC. In the case of collisions between electrons and ions, the electron-nucleon luminosity is lower, but event rates comparable to the e- p case are achieved.

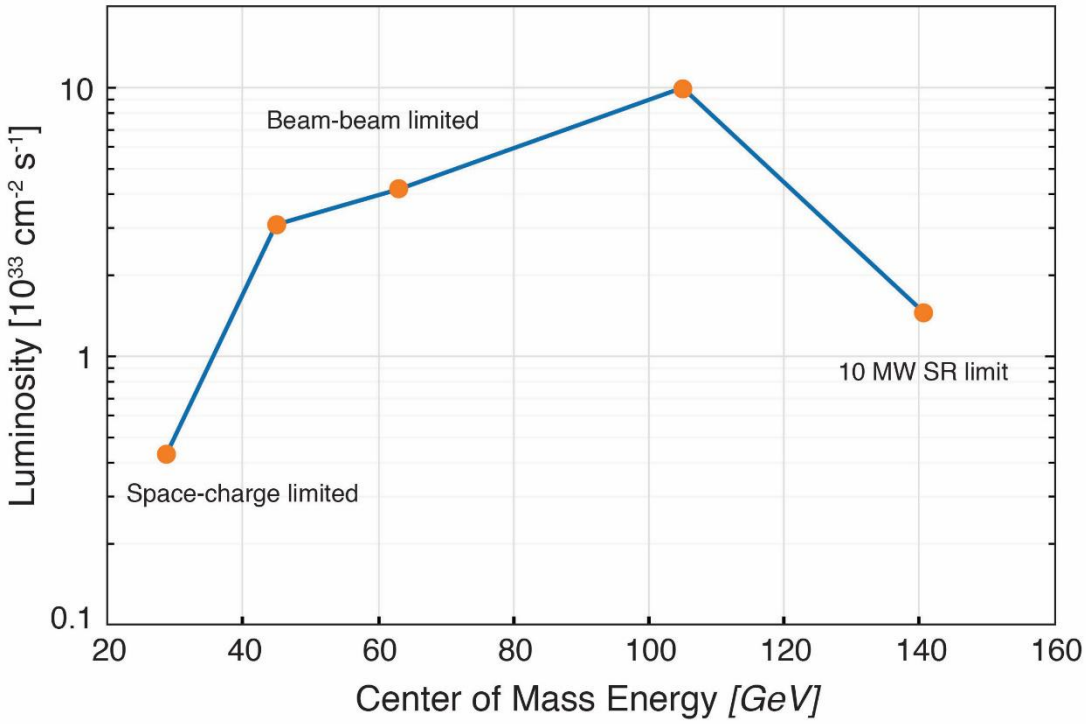

Figure 2: The eRHIC peak luminosity calculation versus center-of-mass energy E_{CM}. The luminosity for low E_{CM} is limited by the beam-beam interaction; at high E_{CM}, the luminosity is limited by the electron beam intensity and the total synchrotron radiation power. A maximum power of 10 MW is chosen to limit the operational costs. This is not a technical limit but a design choice. Solid lines connecting the dots are inserted to guide the eye.

We need to separate the electron and hadron beams quickly after collisions. In order to avoid parasitic crossings without introducing separator magnets and the associated generation of synchrotron radiation, the beams collide under a crossing angle of 22 mrad. Collisions with a crossing angle increase the effective cross section of the beams thereby reducing the luminosity by an order of magnitude. In addition, with a crossing angle, the transverse beam-beam forces depend strongly on the longitudinal position of the particles which generates strong synchro-betatron resonances that affect the beam lifetime and stability. These crossing angle effects are avoided by employing crab crossing using crab cavities. Compensation of the crossing angle by crab cavities is a proven technology that has been demonstrated routinely in the electron-positron collider KEKB, and crab crossing is planned for the high luminosity upgrade of the large hadron collider LHC.

The main elements of eRHIC which have to be added to the existing RHIC complex are:

- A low frequency photocathode gun delivering 10 nC polarized electrons at 1 Hz;
- A 400 MeV normal-conducting S-band injector LINAC;
- A 5 to 18 GeV rapid cycling synchrotron (RCS) in the RHIC tunnel;

- A high intensity, spin-transparent 5 to 18 GeV electron storage ring in the RHIC tunnel with superconducting RF cavities;
- A high luminosity interaction region with 22 mrad crossing angle, crab cavities and spin rotators that allows for a full acceptance detector; a second interaction region is possible and feasible;
- A 150 MeV energy recovery LINAC which provides continuous electron beams for strong hadron cooling;
- A small number of additional buildings which house additional RF power stations and the electron injector.

The eRHIC electron storage ring design is using established and existing technologies from high intensity electron storage rings such as the B-factories of KEK and SLAC, as well as from modern synchrotron light sources.

Other pre-conceptual eRHIC designs, based on the LINAC-Ring (L-R) concept have been presented in the past [3]. As the Ring-Ring design is our chosen solution, the L-R design is presently not further developed and it is not discussed in the body of this report.

2.2.2 **eRHIC Design Concept**

The eRHIC pre-conceptual design provides a path towards a machine with a nominal luminosity of up to $10^{34}\mathrm{cm}^{-2}\mathrm{sec}^{-1}$. The overall concept is to base the design to a large extent on existing technologies, which will greatly reduce the technical risk. This is expected to result in reduced project costs, rapid commissioning, and will provide usable physics data soon after project completion. A design version with somewhat reduced luminosity ("moderate luminosity") is discussed as well in the context of design risk mitigation.

As already mentioned, the eRHIC pre-conceptual design meets the requirements as formulated in the EIC White Paper [4]:

- The design peak luminosity reaches $10^{34}\mathrm{cm}^{-2}\mathrm{sec}^{-1}$ (depending on center-of-mass energy). The electron energy and the luminosity at energies $E_e \geq 10$ GeV is limited by the power of the synchrotron radiation. A total synchrotron radiation power of 10 MW is considered a reasonable upper limit. This allows a beam energy of 18 GeV together with a luminosity which is still 15% of the maximum luminosity at 10 GeV. For center-of-mass energies of 29 GeV and above the electron energy is at least 5 GeV.

- The center-of-mass energy from 29 to140 GeV is realized by proton energies that range from 41 to 275 GeV, and by electron energies that range from 5 GeV to 18 GeV. RHIC magnets will allow to exceed the present maximum operational energy of 255 GeV since some magnets which presently limit the beam energy will no longer be needed in eRHIC. The lowest eRHIC proton energy is 41 GeV. It is limited by the need to maintain the revolution time for low energy protons. The lowest electron energy is 5 GeV. This is not a hard

limit, but the luminosity will drop below $10^{33}\mathrm{cm}^{-2}\mathrm{sec}^{-1}$ at electron energies below 5 GeV.

- Both electron and hadron beams will be spin polarized with flexible spin patterns. Proton polarization is part of the present RHIC program and can be carried over as-is to eRHIC. The capability of ion polarization (helium and deuterons) will be added by upgrading the Siberian snakes and ion sources, and by improved polarimetry. The electron beam polarization will be enabled by full-energy injection of polarized electron bunches with the desired spin direction (up or down) and frequent electron bunch replacement to ensure a high degree of polarization.

- A transverse momentum detection acceptance for scattered protons from 200 MeV/*c* to 1.3 GeV/c in at least one transverse plane is realized by limiting the divergence angle of the proton beam at the interaction point (IP). Proton β-functions at the IP are chosen such that 50% of all scattered protons with a transverse momentum of 200 MeV/*c* can be detected by forward detectors close to the beam ("Roman Pots"), which limits the achievable luminosity in this configuration. Increasing this lower limit of detectable transverse momentum allows us to decrease the horizontal β-function at the IP substantially, thus increasing the maximum luminosity by a factor of two or more. As the cross section increases steeply with decreasing scattering angle, it is sufficient to operate in this mode for only a small amount of time ($\cong 10\%$), which then has only a correspondingly small impact on integrated luminosity.

The basic assumptions of this design are:

- The electron ring is installed in the existing RHIC tunnel to minimize civil engineering efforts and has the same circumference as RHIC.

- The layout described here admits two interaction regions (IR) and two interaction points (IP). However, the second IR has not yet been integrated into the lattice design and the dynamic aperture assessment is yet to be completed. In case of operation with two collision points, the luminosity is maximized if half of the electron and hadron bunches collide in one of the two interaction points and the other half of the particles collide in the second IP. Luminosities and beam-beam parameters quoted are based on a single beam-beam interaction per turn. In operations with two detectors, each will receive half of the luminosity.

- Electron and hadron beams have identical beam sizes at the interaction point. The beams are flat and the horizontal beam size is larger than the vertical one. At the interaction point, the two beams intersect at a full crossing angle of 22 .in the horizontal plane. The resulting luminosity loss will be largely restored by tilting the bunches around the vertical axis in the IP (perpendicular to the crossing plane) by half the crossing angle using transversely deflecting RF resonators, so-called crab cavities, in the hadron ring. This is mandatory for hadron bunches. Crab cavities in the electron ring

are needed as well to avoid synchro-betatron resonances excited by the collision crossing angle in the electron beam, though their pure geometric effect is negligible.

- Hadron beam parameters are a moderate extrapolation of what has been achieved at RHIC, with the exception that the number of bunches is increased from 110 to up to 1320. The total proton current, however, is increased only by a factor of three. Injection and acceleration will be done with 330 bunches. At the maximum beam energy, in storage mode, the bunches will be adiabatically split in two steps into 1320 bunches. Note that in the absence of strong hadron cooling, a maximum luminosity of $0.4 * 10^{34} cm^{-2} sec^{-1}$ is achievable with 660 bunches.

- A rapid cycling synchrotron (RCS) located inside the RHIC tunnel serves as a polarized full-energy injector for the electron storage ring.

- The maximum electron beam-beam parameter does not exceed $\xi_e = 0.1$, a level that has been routinely achieved at the B-factories KEKB [5][6]. The electron ring will be operated near the integer betatron resonance to mitigate the beam-beam effect while simultaneously minimizing the impact of systematic depolarizing spin resonances.

- The RF power required to replace the power of the synchrotron radiation emitted by the beam is 10 MW. This corresponds to a linear synchrotron radiation power load of 4 kW/m, which is equivalent to $37\ \mathrm{W/mm^2}$ in the arcs. This linear load is less than half of the corresponding value for KEKB [5] and PEP-II [6]. There is no principle hard limit of the RF power but 10 MW is considered a practical upper limit.

2.2.3 **Beam Parameters and Luminosity**

The luminosity of an electron-proton collider is given by:

$$L = H f_b N_p N_e / 4\pi\sigma_x\sigma_y \qquad (1)$$

where N_p and N_e are the number of hadrons and electrons per bunch, respectively, f_b is the bunch frequency, σ_x and σ_y are the RMS beam sizes (assuming they are the same for both beams) given by their beam emittances $\epsilon_{x,y}$ and β-functions at the interaction point (IP) $\beta^*_{x,y}$ as $\sigma_{\{x,y\}} = \sqrt{\epsilon_{x,y}\beta^*_{x,y}}$.
H is a factor reflecting the impact of the hourglass effect (the impact of the variation of the beam cross section along the length of the bunch in collisions) and residual effects of the compensated crossing angle. With the bunch length being close to the vertical beta function at the IP, the factor *H* remains above 0.8.

For eRHIC, the current limits are taken as 1.0 A for the protons and 2.5 A for the electrons, based on the PEP-II [6] operation with 2.1 A at 9 GeV and 3.2 A at 3 GeV.

The numbers of particles per bunch $N_{e,p}$ are constrained by the beam-beam tune shift parameters induced by the bunches upon each other:

$$\xi_{x,y,e,p} = \frac{r_{e,p}}{2\pi}\frac{N_{p,e}}{\gamma_{e,p}\varepsilon_{e,p}}\frac{1}{1+K_{y,x}} \quad (2)$$

where $r_{e,p}$ are the classical radii of the electrons or protons, respectively, and $K_y = \frac{\sigma_y}{\sigma_x} = \frac{1}{K_x}$.

Combining these two equations and thereby eliminating the emittances yields:

$$L = \frac{1}{e^2\sqrt{r_e r_p}}\frac{1+K_y}{\sqrt{K_y}}(\gamma_e\gamma_p I_e I_p)^{1/2}\left(\frac{\xi_{e,x}\xi_{e,y}\xi_{p,x}\xi_{p,y}}{\beta^*_{e,x}\beta^*_{e,y}\beta^*_{p,x}\beta^*_{p,y}}\right)^{1/4} \quad (3)$$

In this form, the luminosity is expressed by the limiting factors, the beam currents I_e and I_p, the beam-beam tune-shift parameters $\xi_{x,y,e,p}$, the β-functions at the IP, and the beam size ratio K_y. We see that for flat beams, $K_y \ll 1$, one gets a significant enhancement factor of the luminosity as compared to round beams ($K_y = 1$). For this reason, the beam parameters are optimized around a value of $K_y = 0.13$ which enhances the luminosity by a factor of $\cong 1.5$ as compared to a round beam scenario.

Colliding beam experience at RHIC suggests the beam-beam parameters ξ_p for the protons are bounded by beam stability considerations at values of $\xi_p \cong 0.015$, while the electrons in a ring-ring collider can, with sufficient synchrotron radiation damping, reach $\xi_e \leq 0.1$ according to experience at the B-factories. Beam currents are assumed to be limited by the values achieved in RHIC (1.2 A) and in KEKB (3.2 A).

High luminosity obviously requires small values of the β-function at the IP. There are a number of constraints which limit the β-function:

- For flat beams, the vertical β-function at the IP is smaller than the horizontal one. The vertical β-function is limited by the length of the proton bunch via the hourglass effect. The proton bunch length in turn is limited by intra-beam scattering. The minimum value is about 5 cm for the highest luminosity case with 1320 bunches.

- An important part of the EIC physics program is the measurement of the spatial distribution of the gluon density of the hadrons. This requires detection of protons which are scattered under a small angle. The acceptance for such low transverse momentum scattered protons (low- p_t) depends strongly on the

horizontal divergence of the beam at the IP and gives rise to another limitation for the horizontal β-function and K_y. The horizontal divergence is proportional to $\frac{1}{\left(\beta_{xp}^*\right)^{1/2}}$. In order to accept scattered particles with $p_t = 200\,\mathrm{MeV}/c$, the horizontal β-function of the hadron beam should be about 1 m. The design values of are$\beta_{xp}^* = 90$ cm and $\beta_{yp}^* = 5$ cm.

- Small β-functions at the IP imply large β-functions in the strong final focus quadrupoles. Very large β-functions in quadrupoles cause a strong effect on the tune and the optics for off-energy particles, referred to as chromaticity. Chromaticity needs to be compensated to provide sufficient space for a stable working point for the beam in-between nonlinear resonances. Chromaticity correction is accomplished by nonlinear sextupole fields in the accelerator arcs. This in turn introduces a dynamic aperture limit and increases the width of nonlinear resonances to be avoided by reducing the tune footprint. Sufficient beam lifetime requires a minimum dynamic aperture which equals 10 times the transverse RMS beam size. Beyond a certain value of chromaticity the stability requirements for the beam cannot be fulfilled. This threshold value depends on other parameters such as phase advance per arc FODO cell and number of sextupole families. An approximate rule is that the IR chromaticity should not contribute more than about one third to the total natural chromaticity.

In summary, the general concept of achieving high luminosity is the same as that for e^+e^--colliders:

Luminosity is increased by running with the highest beam currents, using flat beams, low emittances, and low β functions at the IP. Focusing magnets are installed as close as possible to the IP. The beam current is distributed over many, shortly spaced bunches, while the charge per bunch is relatively low. These choices mandate a crossing angle collision geometry.

Table 1 shows the beam parameters for the highest luminosity. Highest luminosity is achieved for an electron beam energy of 10 GeV and for a hadron energy of 275 GeV. Both the β^* and emittances, of both protons and electrons, are larger in the horizontal than in the vertical plane, resulting in flat beam profiles at the IP. Unequal emittances are natural for the electrons in a storage ring. For protons, however, the beam first needs to be pre-cooled at low energies, using electron cooling. Subsequently, kicker noise is applied in the horizontal plane to increase the horizontal emittance to its desired value. Experimentally, it is known that such emittance asymmetries will be stable in RHIC for long storage times.

Maximum luminosity is achieved with an electron beam energy of 10 GeV and a proton energy of 275 GeV which corresponds to a center-of-mass energy of 105 GeV. For larger electron energies, the rapidly increasing synchrotron radiation power scales with the electron energy to the 4^{th} power, $P \sim E_e^4$. This requires reducing the electron current by the same factor to keep the total synchrotron radiation power below the design limit of 10 MW. At the highest energy, the electron current is only 0.26 A, nine times smaller than the maximum value. The loss in luminosity is mitigated by

decreasing the number of bunches by a factor of four and adjusting the transverse beam parameters. The increase of electron beam emittance, which scales as E_e^2 , is compensated by increasing the phase advance in the arcs from 60 degrees per FODO cell to 90 degrees per FODO cell. The overall result is that the luminosity is reduced by a factor of seven as compared to the maximum value achieved at 10 GeV.

These considerations result in the luminosity versus center-of-mass energy as shown in Figure 2.

The parameters shown in Table 1 are derived with the assumption that the proton beam emittance will remain at the very small values of $\varepsilon_x = 9.3$ nm and $\varepsilon_y = 1.3$ nm. However, the dense hadron beam is subject to substantial emittance growth due to intrabeam scattering (IBS). IBS must be counterbalanced by strong cooling of the hadron beam to maintain emittance and bunch length over a reasonable amount of time. This time needs to be much larger than the time it takes to replace a depleted hadron beam. Several schemes for strong cooling are considered that promise to yield sufficiently fast cooling rates to balance emittance growth at the operational parameters of eRHIC. One of these schemes called "Coherent Electron Cooling" [7] is being tested experimentally.

As already mentioned the design must enable detection of scattered protons with a minimum transverse momentum of $p_t = 200\ \mathrm{MeV}/c$, which at a hadron beam energy of 275 GeV corresponds to a scattering angle of $730\ \mu\mathrm{rad}$. The RMS divergence of the proton beam at the IP must not exceed one tenth of this minimum scattering angle, $\sigma' \leq 73\ \mu\mathrm{rad}$. This requirement, however, may be violated in the vertical plane, provided the beam divergence in the horizontal plane meets the requirement. A horizontal RMS beam divergence of $56\ \mu\mathrm{rad}$ allows detection of 50% of all scattered protons with a transverse momentum of 200 MeV/*c*. In order to improve low p_t acceptance eRHIC may be operated for a short time, say 10% of the time, with larger β^* and lower divergence and thus full acceptance. Because of the large cross section for small p_t, in a short amount of time a large amount of data can be collected so that there is eventually an equal amount of data at all p_t values. This scenario substantially increases the effective luminosity of the facility.

So far we have only discussed electron-proton collisions. Most of the considerations discussed in this section apply to ions with only a few exceptions that are addressed below.

Ions are characterized by the number of nucleons, *A*, and the electrical charge *Ze,* with $A \cong 2Z$. The beam-beam tune shift of the electrons, assumed to be at the maximum tolerable value for the collision parameters with protons, is proportional to *Z,* which for protons is equal to one. In order to maintain the electron tune shift value in collisions with ions, the number of ions per bunch, N_i has to be reduced by a factor *Z*. The beam-beam tune shift for the hadrons is also proportional to *Z* but is inversely proportional to *A*. Thus the ion beam-beam tune shift is reduced approximately by a factor of two for a constant number of electrons. In principle, we could benefit from the reduced tune shift and increase the number of particles in the electron bunch by a factor of two. However, this would increase the electron beam current by a factor of two, which is not possible. In conclusion, the electron-ion luminosity is reduced by a factor of *Z*. However, most of

the cross sections in electron-ion collisions will increase by a factor of A compared to e-p cross sections. Therefore, the event rate of electron-ion collisions is expected to increase by a factor of approximately two in electron-ion collisions as compared to electron-proton collisions in eRHIC.

2.2.4 **Moderate Luminosity without Strong Hadron Cooling**

The highest luminosity of the electron-ion collider depends on the feasibility of strong hadron cooling. The eRHIC approach to strong hadron cooling is coherent electron cooling. This is a novel approach which has never been tested experimentally. However, a proof-of-principle experiment is underway which aims to demonstrate this technique using a free electron laser (FEL) as an amplification mechanism. This experiment is scheduled to produce results by the end of FY18. Nevertheless, the feasibility of this approach cannot be guaranteed at this point, which constitutes a high technical risk for achieving the highest luminosity goal of eRHIC. In the following, we discuss how this risk is mitigated.

There are three ways this mitigation could be achieved:

- Coherent electron cooling with R_{56} enabled micro-bunching as an alternative coherent electron cooling amplification mechanism;
- Magnetized bunched beam electron cooling as an alternative hadron cooling scheme;
- An eRHIC design solution with a somewhat reduced peak luminosity.

The micro-bunching based coherent electron cooling might suffer from the same principle uncertainties as the FEL based scheme. It is nevertheless an attractive option that promises to need less current for the cooling electron beam. While we are pursuing this very promising approach, we do not consider it to be the primary way to mitigate the CeC performance risk.

Magnetized bunched beam electron cooling is a novel technique as well that has not yet been demonstrated. However, non-magnetized bunched beam cooling is being implemented for the RHIC low energy run in FY19 and FY20. There is no known reason why the fact that the beam is bunched would affect the otherwise well proven electron cooling mechanism. However, magnetized bunched beam cooling for 275 GeV hadron beams requires a complicated, expensive, and very challenging setup which, even though it might technically work, is considered prohibitive from a cost point of view. Independent of cost, the required beam current of the electron cooler is in the order of 1 A. This exceeds by far the present capability of CW high brightness electron sources. Furthermore, such currents require an energy recovery LINAC (ERL). However, the virtual beam power in the ERL would extend into the 100 MW regime, a factor 100 above state-of-the-art.

Our preferred solution is to consider a scheme with a more moderate but still more than sufficient peak luminosity which does not require strong hadron cooling as a realistic and credible way to mitigate the risk associated with a very high luminosity solution. The parameters of this solution will be discussed in this section.

The main difference between the high and moderate luminosity version is reducing the number of bunches by a factor of two, from 1320 to 660 bunches, which is still 6 times larger than the number of bunches in present RHIC. IBS is reduced by an increase of the vertical emittance of the protons by a factor 6.5 compared to the version with strong hadron cooling. Re-optimization of the beam optical parameters at the collision point and lengthening the proton bunches from 5 cm to 7 cm leads to the parameters as shown in Table 2. These hadron beam parameters imply IBS emittance growth times of more than nine hours in both the horizontal and the longitudinal plane which eliminates the need for strong hadron cooling.

The electron bunch current is more critical for this solution. The product of average current and bunch current, which is the figure-of-merit for heating of the vacuum system, increases by a factor of 1.5 but remains still within the margins given by the cooling of the RF shielded bellows, the temperature limit of the RF buttons, and other sensitive vacuum equipment. The resulting luminosity is still $4.4 * 10^{33}\mathrm{cm}^{-2}\mathrm{sec}^{-1}$. The full set of parameters is shown in Table 2.

Table 2: Moderate Luminosity Parameters for 10 GeV electrons on 275 GeV hadrons.

Parameter	***hadron***	***electron***
Center-of-Mass Energy [GeV]	104.9	
Energy [GeV]	275	10
Number of Bunches	660	
Particles per bunch [10^{11}]	1.05	3.0
Beam Current [A]	0.87	2.48
Horizontal Emittance [nm]	13.9	20
Vertical Emittance [nm]	8.5	4.9
Horizontal β_x^* at IP [cm]	90	63
Vertical β_y^* at IP [cm]	5.9	10.4
Horizontal Divergence at IP [mrad]	0.124	0.179
Vertical Divergence at IP [mrad]	0.380	0.216
Horizontal Beam-Beam Parameter ξ_x	0.015	0.1
Vertical Beam-Beam Parameter ξ_y	0.005	0.083
IBS Growth Time long/hor [hours]	10.1/9.2	-
Synchrotron Radiation Power [MW]	-	9.1
Bunch Length [cm]	7	1.9
Luminosity [10^{33}cm^{-2}sec^{-1}]	4.4	

The luminosities for different center-of-mass energies are obtained using the same considerations as the ones outlined for the high luminosity solution. The electron beam

current for energies larger than 10 GeV is reduced to limit the total energy loss of the beam to 10 MW. At lower energies, the parameters are optimized for the reduced beam-beam tune shift limits for the electrons. Figure 3 shows how the luminosity varies with center-of-mass energy.

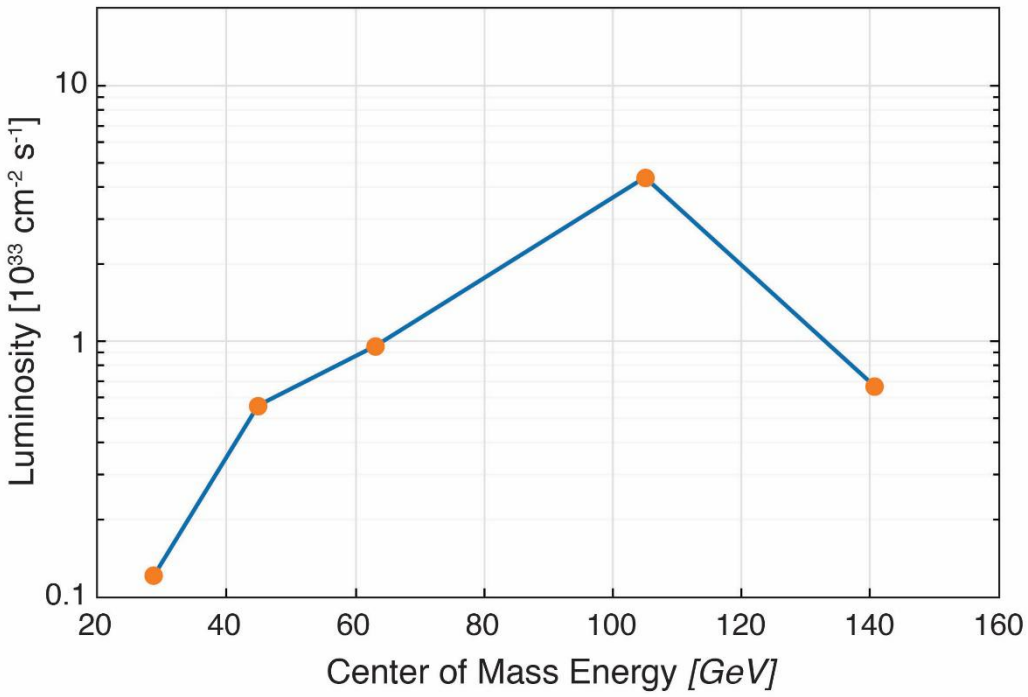

Figure 3: Moderate eRHIC peak luminosity versus center-of-mass (CM) energy. The luminosity for low CM energy is limited by the beam-beam interaction; at high CM energy, the luminosity is limited by the electron beam intensity and the total synchrotron radiation power, the limit of which has been set to 10 MW for cost reasons.

The luminosity without strong cooling is within a factor of 3 of the high luminosity goal of eRHIC. This luminosity satisfies the requirements on the performance of an EIC formulated in the Nuclear Physics White Paper and thus this more moderate eRHIC performance still provides access to the entire EIC physics program. The moderate luminosity solution has been reviewed and characterized as realistic and implementable without major technical risk. We conclude that this performance would, at least initially, fully satisfy the needs of the physics program. This would provide more time to develop, implement and optimize strong hadron cooling, thereby greatly reducing the technical risk associated with strong hadron cooling. In addition, this solution would lead to a substantial initial cost saving.

In summary, we conclude that the solution with moderate luminosity not only mitigates the risk of strong hadron cooling falling short of expectations but offers in addition initial substantial construction cost savings.

2.2.5 **Beam-Beam Dynamics**

The eRHIC approach to achieving stable beam-beam interactions is similar to the HERA approach:

Each beam is assumed to achieve the same beam-beam tune shift values as they did when colliding with a beam of the same species. The beam-beam tune shift is an established measure of characterizing the strength of the highly nonlinear interaction of the two beams.

However, for eRHIC, this approach is applied on a much higher level of beam-beam strength than HERA. For this reason, comprehensive simulation studies have been performed to ensure that the beams remain stable in collisions and that the hadron beam does not suffer from strong emittance growth when colliding with the electron beam. Long-term slow emittance growth is investigated by so-called weak-strong beam-beam simulations. With this method one beam is considered static in its transverse and longitudinal dimensions. This is the equivalent of treating it as a static external field. The other beam is described by single particles which are launched in phase space and whose trajectories are tracked in a complete dynamic model over a large number of turns. This study did not reveal any strong hadron beam emittance growth for the operational parameters of eRHIC.

The other effect which might compromise the performance of an electron-ion collider is a strong coherent interaction between the two beams. Such interactions have been observed occasionally in HERA, but could not be studied systematically. If such a coherent beam-beam instability occurs, the hadron beam transverse phase space will filament quickly, which corresponds to a strong effective emittance growth. This renders the hadron beam completely useless for high luminosity collision operations.

This issue was investigated for eRHIC parameters using so-called strong-strong beam-beam simulations. Both beams are described by super-particles in a complete dynamical model. The particle distributions at the collision point are used to generate a realistic beam-beam force. Much mathematical finesse is required to suppress artificial noise due to the fact that the number of super-particles is much smaller than the number of particles in a real beam. These methods are not well suited to investigate long term stability of the beam but are designed to describe short term strong dynamic effects.

The simulations for eRHIC performed with the computer codes BBSS [8] and BeamBeam3D [9] indeed revealed a coherent instability such as observed in HERA. A clear instability threshold has been found for beam-beam tune shift values of the hadron beam which are twice as large as the eRHIC design parameters. Figure 4 shows the result of this simulation.

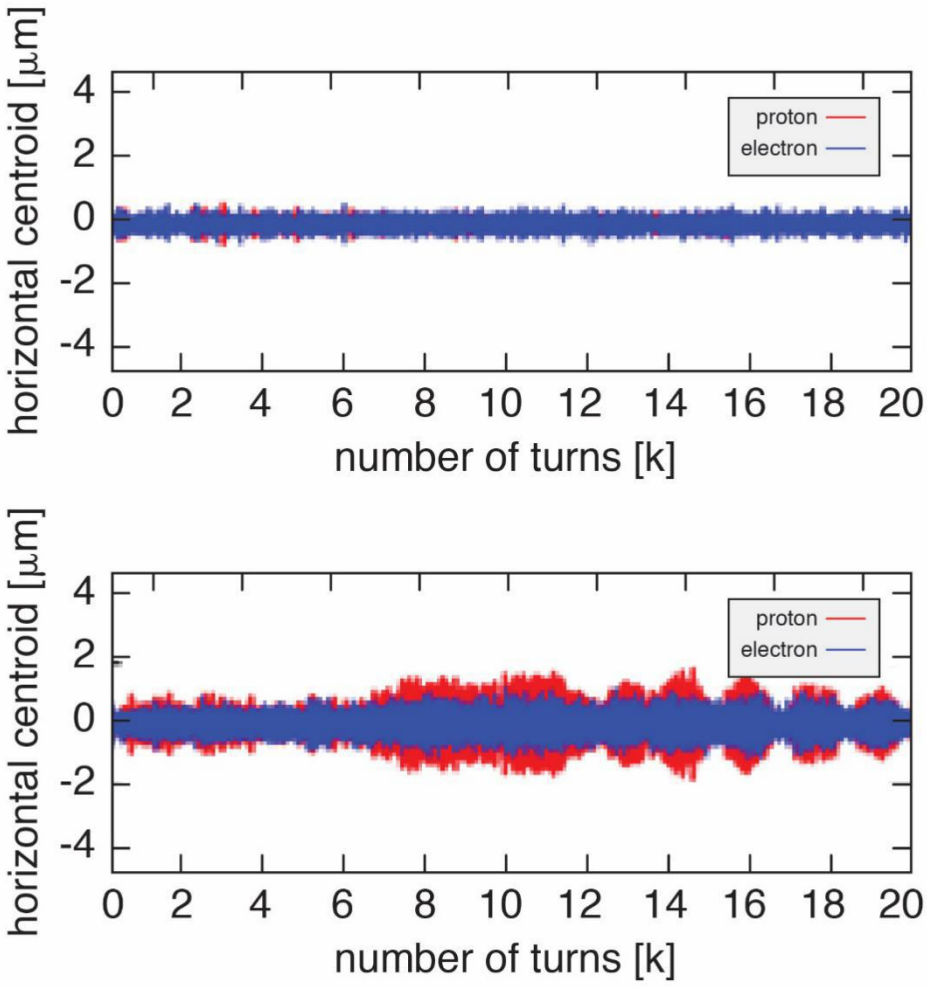

Figure 4: Coherent beam-beam instability as seen by strong-strong beam-beam simulations using the code BBSS. The number of protons in the upper plot is at 1.6 times the eRHIC design value of 10^{11}. In the lower plot, the number of protons is increased to twice the design value. In this case both beams perform unstable betatron oscillations. Such oscillations will blow up the hadron beam emittance

The conclusion of the beam-beam dynamics study is that while the eRHIC beam-beam parameters are fairly aggressive, the simulations predict stable beams in collisions with only small long-term emittance growth. Further studies are still in progress at this stage of the eRHIC design. Additional detrimental effects could still arise due to the imperfect compensation of the crossing angle and residual dynamic effects such as synchro-betatron resonances as well as due to imperfection and spurious dispersion in the crab cavities.

2.2.6 **Layout of the Interaction Region**

The layout of the interaction region (IR) fulfills the following requirements:

- To achieve small beam cross sections and high luminosity, the beams are strongly focused at the interaction point (small β^*) by low-β quadrupole magnets, also referred to as final focus quadrupoles.
- The final focus quadrupoles must have sufficient aperture for the large beam size at their location.

- Large contributions to the chromaticity, which is a set of parameters characterizing the energy sensitivity of the beam optics, are generated in the low-β quadrupoles. Chromaticity needs to be compensated by sextupole fields which, in turn, limit the dynamic aperture. The IR design balances small β^* and tolerable values of chromaticity.

- The colliding beam detector requires a large acceptance of protons scattered off the collision point. Therefore, we do not place accelerator components inside the detector within 4.5 m from the IP. The low-β quadrupoles have a large aperture so that scattered protons and neutrons can be detected by detector elements placed further downstream.

- The beam divergence and therefore the minimum β^* is restricted to enable detection of forward scattered protons with transverse momenta as small as $p_t = 200\ \mathrm{MeV}/c$ These particles are then outside the 10σ proton beam envelope and are detectable by near-beam detectors, so-called "Roman Pots", which are placed on the forward hadron beam pipe.

- The beams collide under a crossing angle of 22 mrad to separate the electron and proton beams quickly, to avoid parasitic collisions, and to provide space for a neutron detector in the forward direction and the luminosity detector in the forward electron direction. An important factor is the large bunch frequency of up to 112 MHz, which corresponds to only 9 nsec bunch spacing, required for high luminosity. The crossing angle effects, in particular enlarged transverse beam size and excitation of synchro-betatron resonances, must be compensated for by using so-called crab cavities, transverse RF resonators which kick the head and the tail of the proton and electron bunches in opposite directions in the plane of the crossing angle. These cavities are placed at a horizontal betatron phase advance of $\pi/2$ from the interaction point (IP) on both the rear and the forward side, forming a 180 degree bump. This causes the bunches to be tilted in the horizontal plane by exactly half the crossing angle at the IP, and provides (ideally) the same collision geometry as head-on collisions, thereby avoiding synchro-betatron coupling.

- Strong synchrotron radiation which might be generated by the electron beam can destroy sensitive detector equipment and make data-taking impossible. Therefore, we argue that the electron beam must not experience dipole fields in the interaction region (IR), certainly not on the forward side upstream of the IP. This is another strong reason why the two beams must collide at a crossing angle. Synchrotron radiation generated in the low-β quadrupoles on the rear-electron side should be absorbed on the rear side of the IR as far as possible from the detector in order to minimize backscattered photons. This requires an extra large

aperture for the electron low-β quadrupole magnets on the downstream side of the IP.

- Both the hadron and electron beams are spin polarized. Polarization is only stable if the polarization direction coincides with the direction of the guide field in the arcs. In collisions, the polarization is oriented longitudinally. Thus the IR design accommodates pairs of spin rotators which accomplish longitudinal spin at the IP and vertical spin in the arcs. The spin rotators in the hadron ring already exist and are unchanged in this design.
  The electron beam spin rotators are based on a sequence of strong solenoids and horizontally bending dipoles interleaved with quadrupoles which are tuned for canceling the *x*-*y* coupling introduced by the solenoids. While the dipole bending angle is fixed, a proper setting of the solenoids allows the correct spin rotation at all energies between 5 and 18 GeV.
  One of such rotators is required on each side of the IP. The beam transport between the rotators is "spin transparent". This means that the magnetic fields in quadrupole magnets experienced by a particle performing betatron and synchrotron oscillations cancel between the spin rotators. This translates into beam optics spin matching conditions.

- The IR layout must provide room for a luminosity monitor on the rear side. This monitor detects hard γ-rays that are generated in the Bethe-Heitler process and exploited for luminosity measurement. The dipole magnet bending the electrons away from the path of the γ beam is at the same time a spectrometer magnet for the off-momentum electrons generated by the Bethe-Heitler process.

- On the forward proton side, a neutron spectrometer is required. A dipole magnet bends the hadron beam away from the collision axis to provide space for this element. It also generates dispersion which helps to detect forward scattered protons in detectors that are integrated into the hadron beam pipe, called "Roman Pots".

Figure 5 shows a schematic of the top-view of the IR with 22 mrad beam crossing angle which satisfies all these conditions. For high luminosities, the β-functions at the IP are required to be as small as possible. In the case of 10 GeV electrons colliding with 275 GeV hadrons, the β-functions are $\beta^*_{x,e} = 42$ cm, $\beta^*_{y.e} = 5$ cm, $\beta^*_{x,p} = 90$ cm, and $\beta^*_{y,p} = 4$ cm (see Table 1).

To avoid generation of an excessive amount of chromaticity in the low-β quadrupoles, these magnets should be placed as close as possible to the interaction point. Special quadrupole magnets are needed to focus the two beams with the conditions and constraints mentioned above.

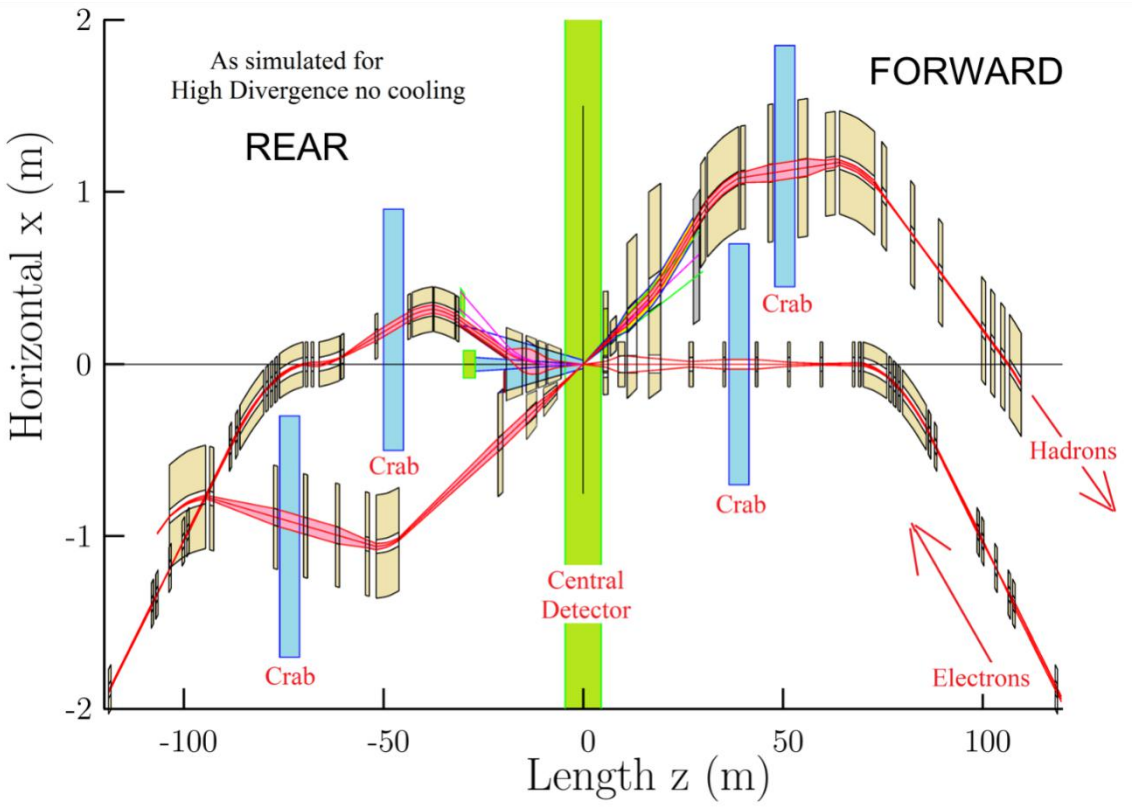

Figure 5: Schematic layout of the interaction region (top view). Beams cross at an angle of 22 mrad. Note that the length scales for the horizontal and vertical axis are very different. The IR design integrates focusing magnets for both beams, luminosity and neutron detectors, electron taggers, spectrometer magnets, near-beam detectors (Roman pots for hadrons), crab cavities, and spin rotators for both beams. The two beams are focused by quadrupole doublets. On the hadron-forward side, there are separate focusing magnets which are longitudinally interleaved. The first quadrupole magnet for electrons is integrated into a hadron spectrometer dipole. On the rear side, hadrons and electrons are focused by quadrupoles which are installed side-by-side in the same cryostat. The maximum β-functions in the IR for hadrons of 1600 m remain within the operating range of RHIC, while the maximum β-functions for electrons remain below 400m.

On the forward side, electron and hadron quadrupole magnets are interleaved. The first magnet is a room temperature spectrometer magnet with a very large aperture which is large enough for the first quadrupoles for the electron beam. The electron beam is shielded from the strong fields of the superconducting hadron quadrupoles by either active shielding coils (1st hadron quadrupole) or by a strong return yoke with a cut-out for the electron beam (2nd hadron quadrupole). A strong dipole magnet is required on this side of the IP to steer the hadron beam away from the path of neutrons that are detected in the downstream neutron detector placed in this area as well.

On the rear side, the superconducting focusing magnets for electrons and protons are installed side-by-side in the same cryostat. A steel return yoke shields the electron beam from the field of the hadron quadrupole magnets. Electron quadrupoles have an extra large aperture to provide sufficient space for the synchrotron radiation fan which is generated by the forward-side quadrupoles and must be absorbed further downstream,

far away from sensitive detector components. The electron beam is steered away from the path of γ-radiation created by electron-hadron scattering (Bethe-Heitler), which is used to measure luminosity. The bending magnet acts as a spectrometer magnet for the electrons which lost energy in the Bethe-Heitler process. These are tagged as part of the luminosity measurement.

The positions of all these IR-magnets are shown in Figure 5. The cross-section of the first quadrupoles on the hadron-rear side is shown in Figure 6. The properties of the IR quadrupoles are summarized in Table 3.

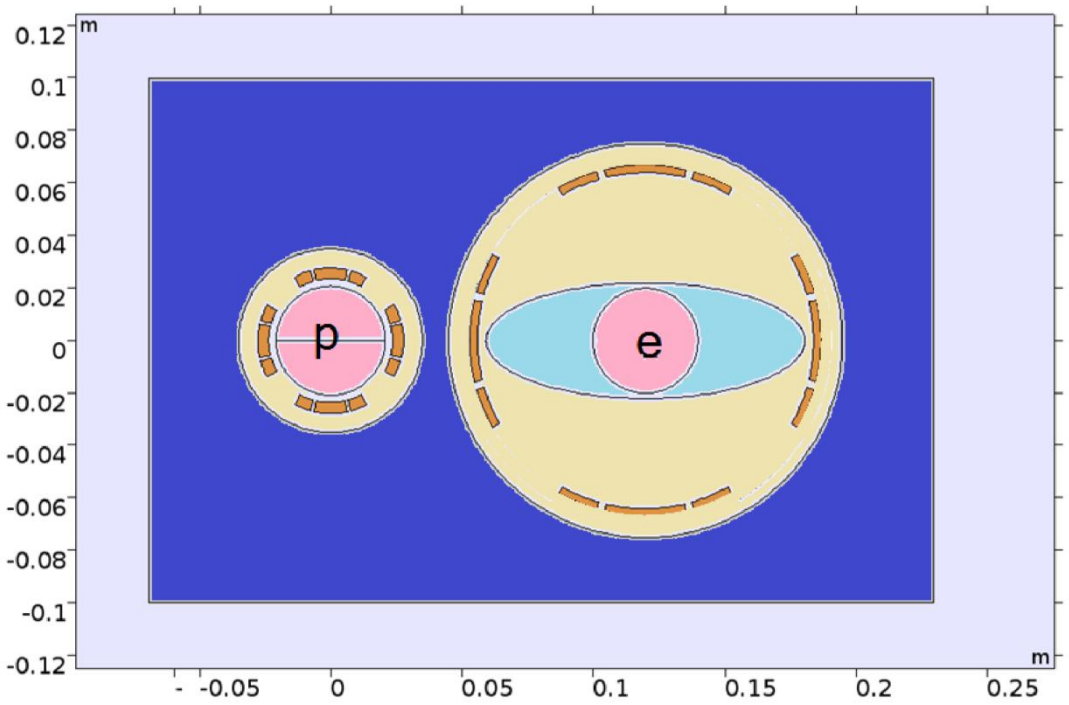

Figure 6: Cross section through the first low-β quadrupole cryostat on the hadron rear side (electron forward side). The two superconducting magnets, one for hadrons (left) and one for electrons (right) are separated by a common return yoke structure

Table 3: Summary of IR superconducting (s.c.) and normal-conducting (n.c.) magnets.

Hadron Forward Side

Name	*Beam*	*Position entrance [m]*	*Length [m]*	*Strength*	*Aperture entrance [mm]*	*Aperture exit [mm]*	*Coil*
B0	hadrons	5.0	1.2	1.3 T	500x240	500x240	s.c. NbTi
Q0FE	electrons	5.0	1.2	14.6 T/m	22	22	s.c. NbTi
Q1FP	hadrons	6.8	1.5	131 T/m	84	84	s.c. Nb_3Sn
Q1FP shield	electrons	6.8	1.5	N/A	N/A	N/A	s.c. NbTi
Q1FE	electrons	8.74	1.72	6.0 T/m	48.5	48.5	s.c. NbTi
Q2FE	hadrons	11.1	2.4	45 T/m	210	210	s.c. NbTi
B1	hadrons	13.9	3.0	4.47 T	270	1270	s.c. NbTi

Hadron Rear Side

Name	*Beam*	*Position [m]*	*Length [m]*	*Strength*	*Aperture entrance [mm]*	*Aperture exit [mm]*	*Coil*
Q1RE	electrons	5.5	3.42	5.1 T/m	135	186	s.c. NbTi
Q1RP	hadrons	5.5	3.42	82.9 T/m	42	86	s.c. NbTi
Q2RE	electrons	11.67	2.57	4.23 T/m	228	266	s.c. NbTi
Q2RP	hadrons	11.67	2.57	54.86 T/m	90	110	s.c. NbTi
BER1	electrons	19.2	4.0	0.09 T	281	338	s.c. NbTi

The maximum β in the low-β quadrupoles for protons are $\beta_{xp} = 1600$ m and $\beta_{yp} = 1200$ m, respectively. For electrons the corresponding numbers are $\beta_{xe} = 1000$ m and $\beta_{ye} = 200$ m.

The two beam lines are relatively close, so the early magnets of both beams need to have limited outside radial dimensions, outside of which the fields must be low. The magnets on the forward side use active shielding as demonstrated at BNL for an ILC IR application [10], or in the case of the dipole B1, a yoke with a hole in it for electrons. The apertures for the hadron magnets are considerably larger than required by the circulating hadron beam to provide sufficient clearance for scattered hadrons from the IP to be detected further downstream.

2.2.7 **Spin Rotators**

Spin polarization of the electron beam is preserved in beam storage if the spin orientation in the arcs of the accelerator is vertical. In collision, both electron and proton spins are required to be in the longitudinal direction. In order to rotate the electron spin from the vertical direction in the arcs to the longitudinal direction, a set of magnets called spin rotators are required and need to be integrated into the interaction region. A second spin rotator which rotates the spin back into the vertical direction is required after the beam passes the interaction point. Spin rotators are an integral part of the interaction region and are associated with a number of beam optics conditions which are discussed below.

The proton spin rotators are identical to the ones presently used in RHIC, which are based on helical dipole magnets. Spin rotators based on helical magnets have been successfully used for polarized protons in RHIC [11][12].

A helical magnet design leads to smaller orbit excursion compared with a design based on regular dipoles. The eRHIC electron spin rotators must operate over a large energy range, from 5 GeV to 18 GeV. Since the orbit excursion in the dipole magnets (either regular or helical) scales inversely with the beam energy, a HERA-type rotator leads to 1 m orbit excursions of 5 GeV electrons [13].

Furthermore, the synchrotron radiation power per meter produced by 18 GeV eRHIC electrons is considerably larger than that generated by the 27.5 GeV electrons in HERA due to the much larger electron current. Reducing the linear power load requires further increasing the rotator length and, correspondingly, the orbit excursion. Therefore, the most practical solution consists of a spin rotator based on strong solenoid magnets. Solenoidal Siberian Snakes have been used in electron accelerators operating in the 0.5 GeV to 1 GeV range [14].

The spin rotators for electrons are based on interleaved solenoids and bending magnets. Figure 7 depicts a schematic of the locations of all components around the interaction region. Light green boxes represent solenoidal magnets of the spin rotators. Blue lines and blue boxes are normal quadrupoles and dipole bending magnets, respectively. Each of the long and short solenoid modules contains a solenoid (split into two half-sections), and seven normal quadrupoles that compensate the impact of the strong solenoidal fields on beam optics and transverse coupling and satisfy the required spin matching conditions. The lengths of the solenoids are chosen such that the maximum magnetic field required is 7 T. The settings for the magnetic fields of the solenoids to achieve longitudinal polarization of the electron beam depend on the beam energy. Optimization of the solenoidal spin integrals led to the parameters listed in Table 4.

The optics functions through the IR are shown in Figure 8. The set of β-functions describing this coupled case is given in Mais-Ripken parameterization [15]. Betatron coupling functions are limited to the rotator insertions, which are also dispersion-free.

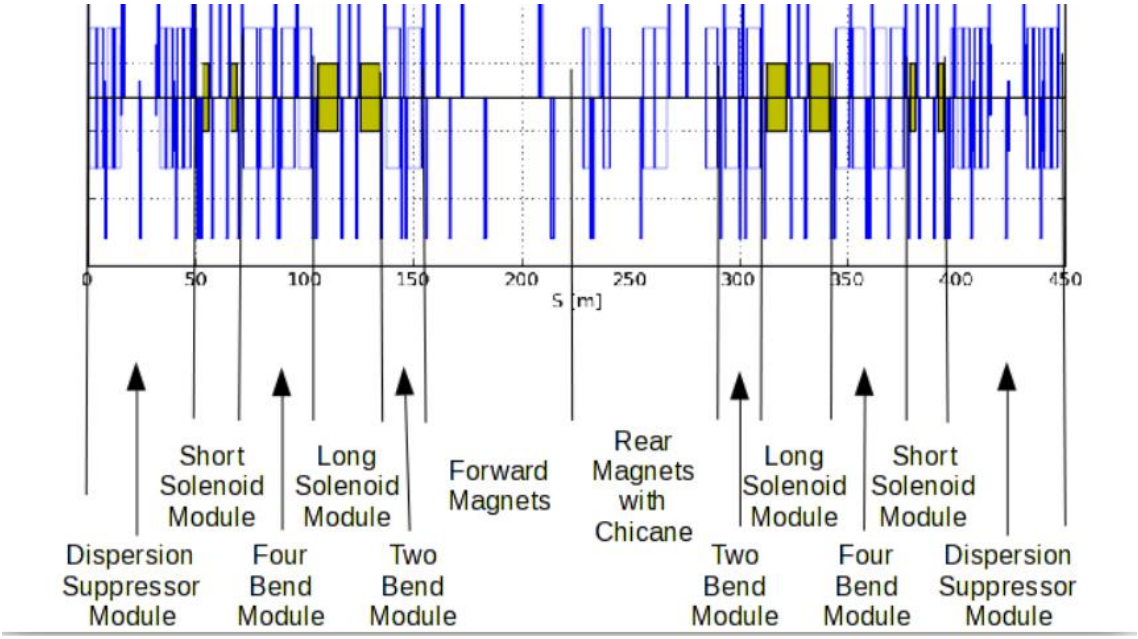

Figure 7: Major components of the electron lattice around the interaction region. Spin rotator magnets are shown as green boxes. The blue boxes indicate quadrupole and dipole magnets

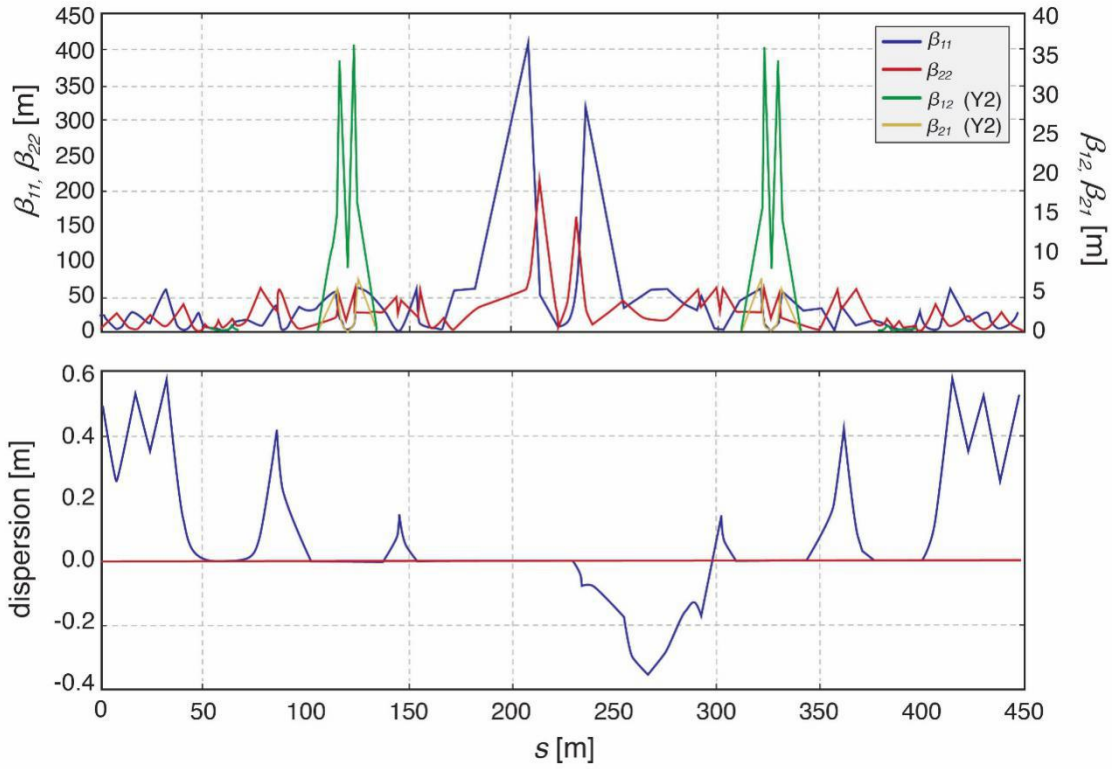

Figure 8: 18 GeV electron beam optics in the colliding straight section with the interaction region, the matching sections, the spin rotators, and dispersion suppressors. In the center of the plot is the interaction point (IP) with large values of the β-functions on both sides. The additional β peaks, denoted by $\beta_{1,2}$ and $\beta_{2,1}$ in this plot are caused by the coupled β-functions which vanish outside the rotator. These are drawn on a different scale shown on the right-hand side of the plot

Table 4: Spin rotator parameters.

Parameter	*Short solenoid module*	*Long solenoid module*
Field integral range [T-m]	20-34	4-122
Solenoid length [m]	5.4	18.
Solenoid spin rotation angle (at 18 GeV)	32°	116°
Location in the RHIC tunnel	D9-D10	D6-Q8

2.2.8 Electron Storage Ring

2.2.8.1 *Electron Storage Ring Overview*

The electron storage ring is located in the existing RHIC tunnel, in the same plane as the ion ring, and has a circumference of 3833.940 m which matches the proton revolution time at 133 GeV, an energy that balances the orbit offsets required for maintaining the revolution time at 100 GeV and 275 GeV. Like the ion ring, it consists of alternating inner and outer arcs in order to have the same revolution time as the ion ring. With the existing Yellow Ring of RHIC being used as the eRHIC ion ring, the

electron ring will be placed on the opposite side, the side of the Blue ring, as illustrated in Figure 9.

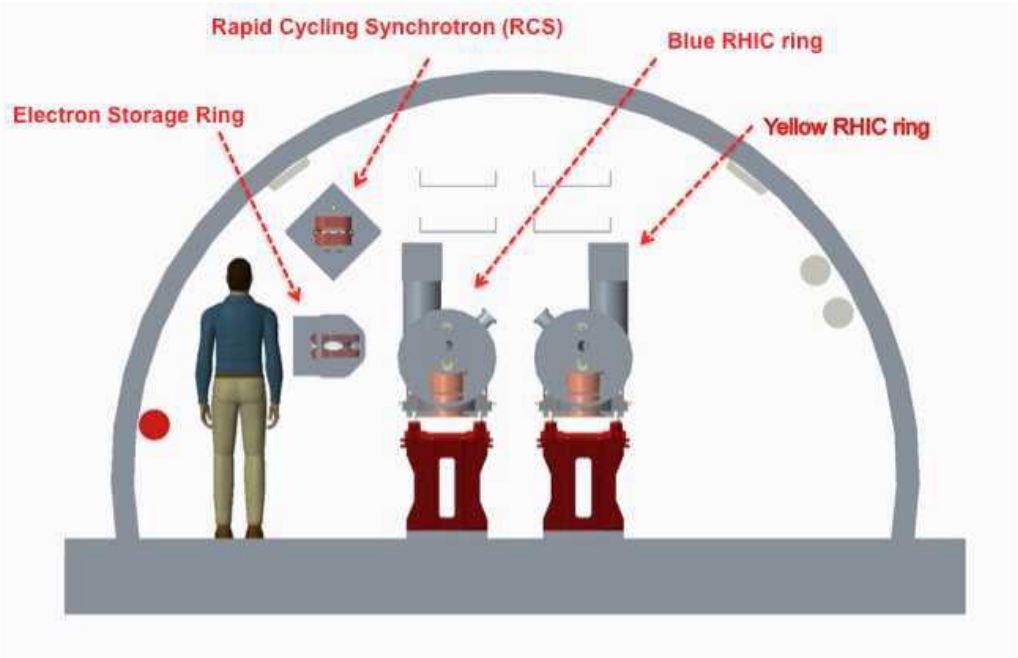

Figure 9: Location of the electron storage ring in the tunnel arcs, on the opposite side of the Blue ring. The Rapid Cycling Synchrotron injector is mounted above the collider ring plane

As in the present RHIC, there are six arcs separated by six ~200 m long straight sections with a potential interaction point (IP) in the middle. The IPs are denoted by their geographical positions as 2 o'clock to 12 o'clock, with 12 o'clock being in the North.

The ring is organized as follows:

Straight section IR6: colliding beam detector with hadron/electron low-β section, spin rotators and crab cavities;

Straight section IR10: superconducting RF systems, strong hadron cooler facility, hadron beam abort;

Straight section IR12: damper systems, special instrumentation, electron injection/extraction;

Straight section IR2: electron source and pre-injector LINAC;

Straight section IR4: half of the superconducting RF systems, hadron injection, hadron RF;

Straight section IR8: 2nd colliding beam detector, spin rotators and crab cavities.

The average arc radius is 381 m, while the actual dipole bending radius is $\rho = 242$ m. The lattice in the arcs and the non-colliding utility straights is composed of FODO cells.

Each of the main dipoles in the arcs consists of three individual bending magnets, a short, 0.445 m long magnet in the center between two longer (l = 2.66 m) magnets.

In this configuration, the amount of synchrotron radiation can be controlled to ensure sufficient radiation damping for all beam energies between 5 and 18 GeV, thereby providing sufficient damping decrements in support of strong beam-beam parameters of

$\xi_{x,y} \leq 0.1$ (see below).

Simultaneously, the split magnets produce the desired beam emittance at the 5 GeV beam energy. Each arc of the electron ring is composed of 16 identical FODO cells. Each half cell consists of a 0.6 m long quadrupole, a 0.5 m long sextupole, a 6.06 m long dipole triplet, and a 0.25 m long dipole corrector. The drift spaces between the individual magnets are slightly different for the inner and outer arcs to account for the difference in the average bending radius. Figure 10 shows the layout of one arc FODO cell.

At both ends of each arc, two additional FODO cells with individually powered quadrupoles are used to match the optical functions between the straights and the arc, and to suppress the dispersion in the straight sections. A missing-magnet scheme eases the dispersion matching.

The specific horizontal emittances required at different energies are realized by a combination of FODO cell phase advances in the arc, and utilizing the super-bends, while the vertical emittance is controlled by applying a vertical dispersion bump. At a beam energy of 18 GeV, the phase advance per arc FODO cell is set to 90 degrees, while at 5 and 10 GeV it is reduced to 60 degrees. The vertical phase advance is set to the same value in order to maximize the dynamic aperture. These different phase advances require a flexible chromaticity correction scheme, based on four families for a FODO cell phase advance of 90 degrees, and 6 families for a 60 degree phase advance. The parameters of the beam optics of the arcs for different beam energies are shown in Table 5.

Table 5: Parameters of the electron beam optics in the arcs for different beam energies. At the lowest energies $E < 10$ GeV, the short dipole in each half-cell is reversed, thus creating a super-bend. This increases radiation damping and damping decrement, provides the required beam emittances, and avoids the bunch length becoming too short.

Energy [GeV]	***5***	***10***	***18***
Phase advance per cell [degrees]	60	60	90
Horizontal emittance [nm]	20	20	22
Relative energy spread [10^{-4}]	5.8	5.5	10.0
Transverse damping time [turns]	7750	5450	940
Natural chromaticity x/y [turns]	-96.2/-89.5	-96.2/-89.5	-101.2/-99.6
Momentum compaction factor [10^{-3}]	1.03	1.04	0.53
Quadrupole strength k_{QF} [m^{-2}]	0.215	0.215	0.283
Quadrupole strength k_{QD} [m^{-2}]	0.216	0.216	0.279
Number of sextupole families	6×2×3	6×2×3	6×2×2
Arc β_{xmax} [m]	27.7	27.7	26.5
Arc β_{ymax} [m]	27.4	27.4	26.8
Arc maximum dispersion [m]	0.95	0.95	0.57
Quadrupole aperture requirement x/y [mm]	30/30	30/30	30/30

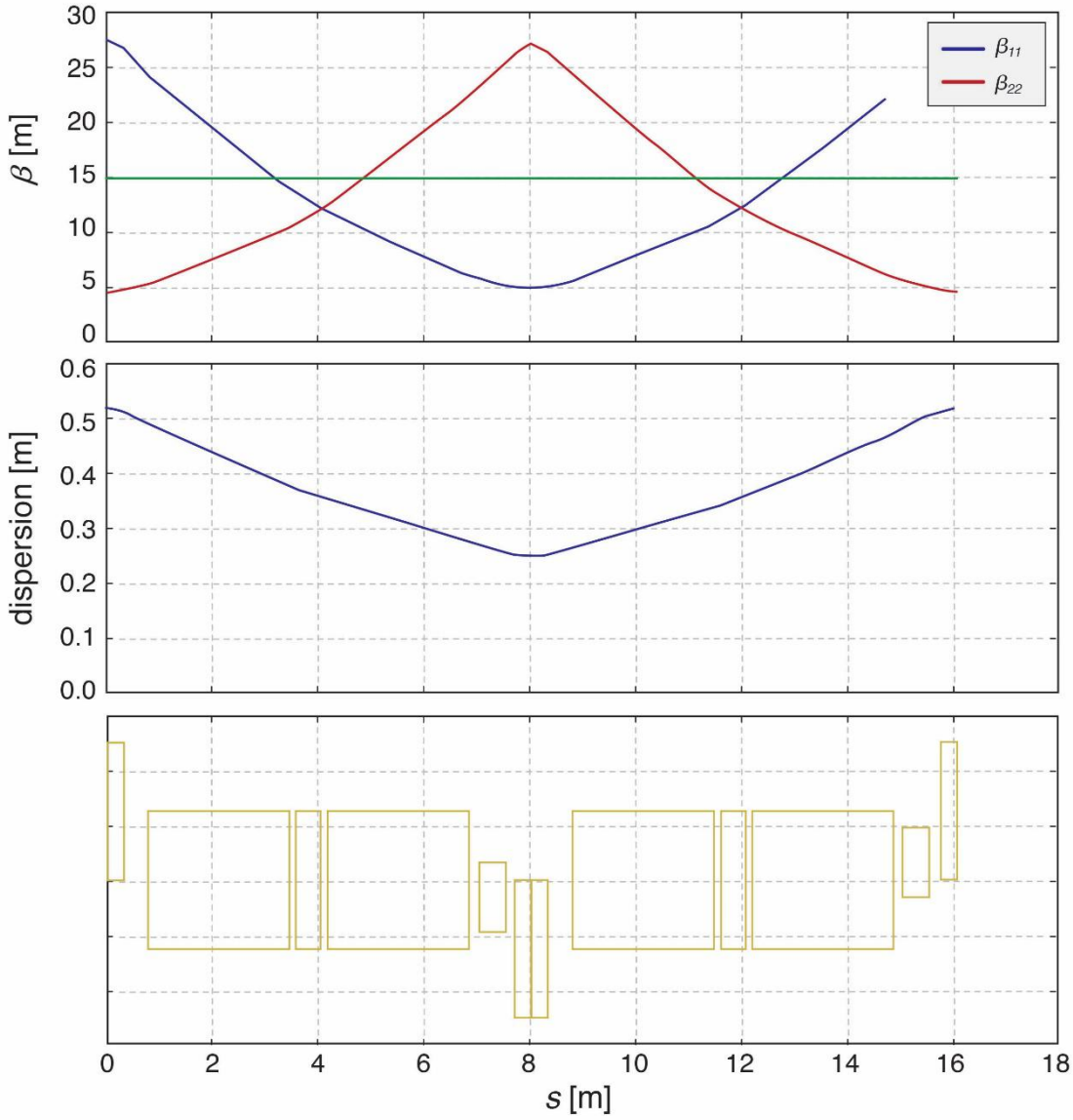

Figure 10: One arc FODO cell for an outer arc cell. The lengths of individual components are to scale.

the arcs. The small β-functions at the IP result in large β-functions in the low-β quadrupoles.

The horizontal β-functions are intentionally large at the crab cavities in order to lower the required cavity voltage. Together with the large β-functions in the final focus quadrupoles, these contribute significantly to the chromaticity. The solenoid spin rotators induce betatron coupling. This coupling is compensated by splitting each solenoid into two individual magnets with a system of five individually powered quadrupoles between them. Spin matching is accomplished by adjusting 40 independent quadrupole circuits in the interaction region. Figure 7 shows the colliding straight section with the interaction region, matching section, dispersion suppressors, and spin rotators.

2.2.8.2 *Maintaining Radiation Damping and Emittance Control for 5 GeV Electron Beams*

Radiation damping allows the electron beam to have a large beam-beam tune shift. While sufficient radiation to allow a large beam-beam tune shift is produced at higher energies, simply scaling down the dipole fields for lower energies does not result in sufficient radiation damping to allow for the same large beam-beam tune shift. The radiation damping for 11 GeV still corresponds to the damping decrement $\delta = 1/(f_c \tau_{x,y})$ of KEKB, where $\tau_{x,y}$ denotes the horizontal and vertical damping time, while f_c is the revolution frequency.

The solution to this is to place three dipoles, instead of a single dipole, between the arc quadrupoles. At high energies (18 GeV), all three dipoles have the same field. At the lowest energy (5 GeV), the central dipole will have a higher field (0.46 T) and reversed polarity. This will increase synchrotron radiation sufficiently to reduce the transverse damping times to 50 ms which gives a damping decrement comparable to that realized in KEKB. This arrangement will also increase the beam emittance close to the 10 GeV value whereas the total synchrotron radiation power is less than half the 10 GeV value (3.2 MW). Figure 11 shows schematically the dipole configuration and orbits at different energies.

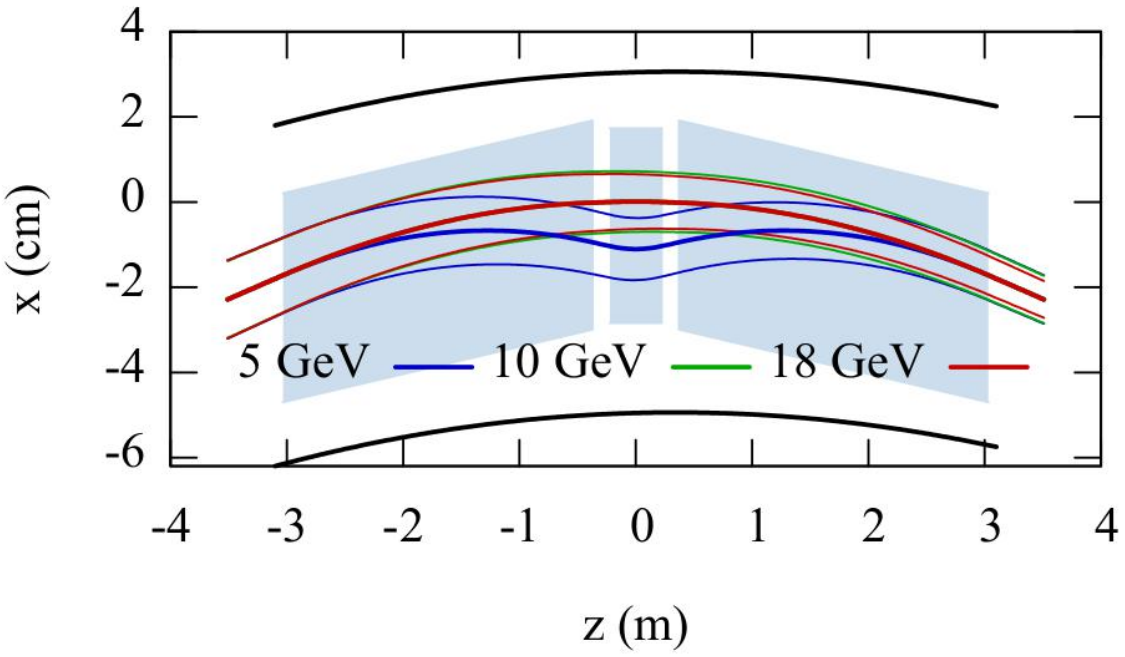

Figure 11: Schematic view of beam orbits in the split dipole magnets for various beam energies

There are three impacts associated with this scheme:

- Higher dipole fields are required;
- The orbits are different for each energy, requiring wider dipoles and a wider vacuum chamber;
- The additional drifts between dipoles reduce the dipole packing fraction, leading to unwanted higher synchrotron radiation losses at higher energies.

The parameters of the electron storage ring are summarized in Table 6.

Table 6: Parameters of the Electron Ring Lattice.

Parameter	*Value*
Path length in dipoles per half-cell [m]	6.06
Bend angle [mrad]	23.8
Number of split dipoles in the entire ring	252
Drift space between split dipoles [m]	0.15
Transverse Damping decrement	$(1.3 - 10.6) \times 10^{-4}$
Minimum Beam Energy [GeV]	5
Length of strong center dipole [m]	0.45
Field strength of center dipole [T] at 5GeV, 18GeV	-0.456, 0.248
Max. Difference between 5GeV and 18GeV orbits [mm]	14
Length of weak and long dipole [m]	2.66
Field strength of center dipole [T] at 5GeV, 18GeV	0.113, 0.248

2.2.8.3 *Electron Spin Polarization in the Storage Ring*

The collision of longitudinally polarized electrons and ions is a key requirement of an electron-ion collider, and a large effort has been undertaken to ensure good polarization of the electron beam during the store. The evolution of beam polarization in electron storage rings is defined by two processes related to synchrotron radiation: Sokolov-Ternov self-polarization [2], and depolarization caused by stochastic photon emission [17]. The self-polarization process leads to a build-up of electron polarization in the direction opposite to the vertical guiding field, up to a maximum level of 92.4% in a perfectly planar storage ring without spin rotators. Stochastic photon emission leads to a randomization of the particle spin directions (spin diffusion) and reduces the equilibrium polarization level.

Because experimenters call for the simultaneous storage of electron bunches with both spin helicities, the Sokolov-Ternov effect is not an option for eRHIC as it tends to polarize
all bunches in the same direction. A full energy polarized electron injector is needed instead, so that the electron bunches are injected into the storage ring with high transverse
polarization (~85%) and the desired spin direction.

In the storage ring the polarization is then brought into the longitudinal direction at the IP
by a pair of solenoidal spin rotators.

The self-polarization rate has a strong dependence on beam energy (as γ^5) and dipole bending radius (as $<1/|\rho|^3>$). The self-polarization time for the eRHIC storage ring placed in the present RHIC tunnel is shown in Figure 12. It takes into account the split dipole structure which enhances the synchrotron radiation at energies below 10 GeV. The self-polarization time is quite long over the entire energy range, except when approaching 18 GeV where it drops to about 30 minutes.

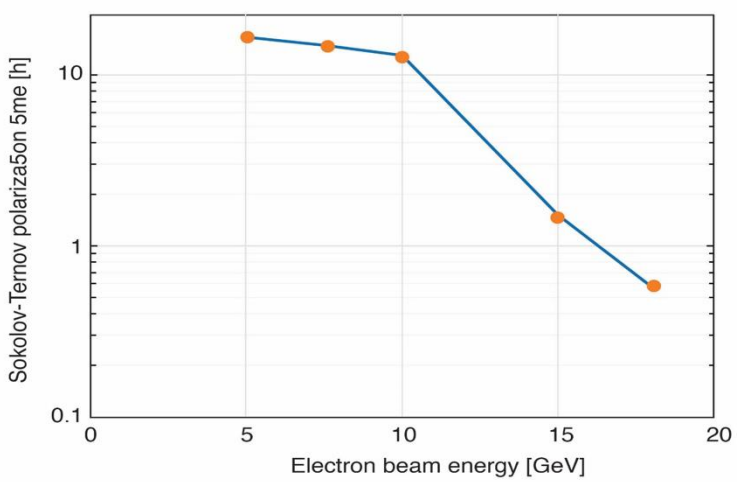

Figure 12: Sokolov-Ternov electron spin polarization time as a function of electron beam energy. The depolarization for spin parallel to the magnetic guide field due to the Sokolov-Ternov effect becomes important for beam energies well above 10 GeV.

While the Sokolov-Ternov effect is a slow process, stochastic photon emission in the storage ring in the presence of misalignments and spin rotators may quickly destroy the polarization of the injected beam, thus requiring a continuous replacement of the depolarized bunches. Spin matching is needed in order to minimize the spin diffusion introduced by the rotators. For the eRHIC storage ring, as the vertical dispersion vanishes at all bending magnets, it is sufficient and necessary to provide spin matching only for horizontal and synchrotron motion between the rotator pairs, by using the quadrupoles interleaved with the rotator solenoids.
We may assess the requirement on polarization in the eRHIC storage ring by considering that polarization varies with time as

$$P(t) = P_{\infty}\,[1 - \exp\,(-t/\tau_p)\,] + P(0)\,\exp\,(-t/\tau_p) \qquad (4)$$

where $P(0)$ is the starting polarization and P_{∞} and $1/\tau_p$ are the actual asymptotic polarization and polarization rate respectively.
It holds

$$P_{\infty} \cong \frac{\tau_p}{\tau_{BKS}}\ P_{BKS} \qquad \frac{1}{\tau_p} \cong \frac{1}{\tau_{BKS}} + \frac{1}{\tau_d} \qquad (5)$$

where $1/\tau_d$ is the spin diffusion rate, P_{BKS} and $1/\tau_{BKS}$ are respectively the asymptotic polarization and the polarization rate for the ideal machine in absence of spin diffusion (the Baier-Katkov-Strakhovenko [26] generalization of Sokolov-Ternov quantities for a lattice where the magnetic field is not homogenously vertical). Equations (4) and (5) can be used for evaluating the polarization evolution with time for bunches polarized

parallel or anti-parallel to the bending field. Fig.12a shows the polarization evolution for eRHIC storage ring at 18 GeV for $P(0)$=+85% (anti-parallel) and -85% (parallel) with P_∞ =30% and 50%.

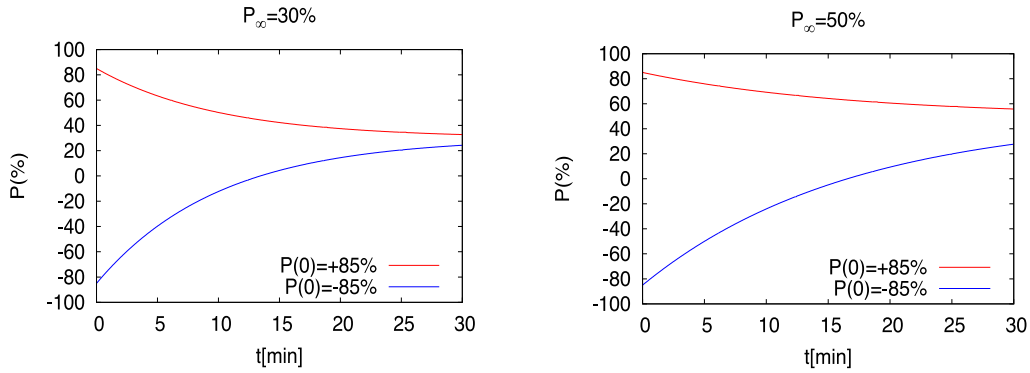

Figure 12a: Polarization vs. time for bunches with starting polarization anti-parallel to the bending field ($P(0)$=+85%) and parallel to it ($P(0)$=-85%) when the ring asymptotic polarization is 30% (left) and 50% (right).

Fig.12b shows polarization after 5 minutes from injection and the 5 minutes average polarization vs. P_∞ with $P(0)$=-85%. The benefit of increasing P_∞ saturates above ≈50% for the bunches with initial polarization parallel to the guiding field.

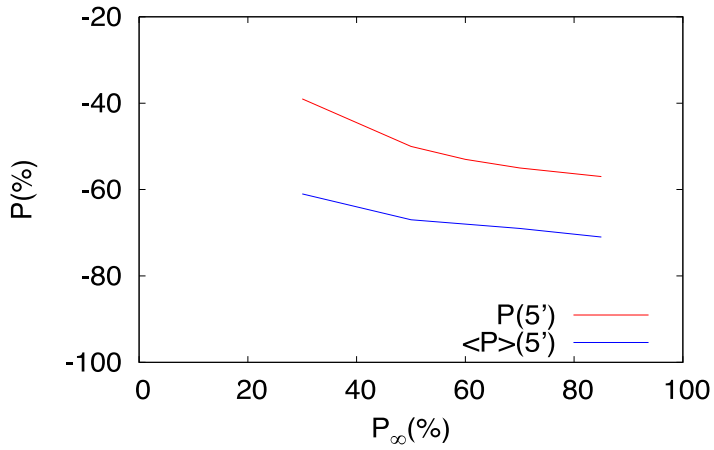

Figure 12b: Polarization after 5 minutes vs. P_∞ for bunches with starting polarization parallel to the guiding field ($P(0)$=-85%) (red). Its average over 5 minutes vs. P_∞ .

For polarization computations in the eRHIC storage ring we rely at the moment on the SITROS package [27]. SITROS includes a module, SITF, where orbit and spin motion are linearized, and a Monte-Carlo tracking module with 2nd order orbital motion and non-linear spin motion in the presence of quantum excitation and radiation damping.

Once the 6D equilibrium distribution is reached, to each particle a spin is added aligned to the stable polarization direction, namely the periodic solution of the Thomas-BMT equation [28][29], and tracking is pursued over an additional number of turns chosen by the user. Depolarization rate and asymptotic polarization are evaluated from the fit of $P(t)$. The fully 6D code SITF reads the same input file allowing preliminary checks before embarking on time consuming tracking. SITROS has been developed for PETRA and HERA-e and improved in view of the HERA luminosity upgrade. SITROS results for HERA-e were in good agreement with observations, with the exception of the evaluation of beam-beam interaction effects which appeared to be somewhat pessimistic. For the moment the polarization studies have been limited to the 18 GeV case, which is expected to be the most challenging one. The machine tunes are set to Q_x =0.12, Q_y =0.10 and Q_s =0.046 for luminosity operation. It is important to show that an asymptotic polarization ≥50% can be achieved also in presence of misalignments.

2.2.8.4 *Polarization in the unperturbed ring*

Fig.12c shows the asymptotic polarization vs. the "naive" spin tune $a\gamma$, a = 0.0011596 being the electron gyromagnetic anomaly, for the unperturbed ring in linear spin motion approximation and as results from the tracking. It can be expected that, manifesting the presence of higher order resonances and synchrotron side-bands, tracking calculations give lower polarization than calculations with linearized spin motion. However the discrepancy seems exceedingly large in this case. This may be related to the fact that the vertical emittance as computed by the tracking is about 8 times larger than expected, or to the fact that the IR optics is not yet fully spin matched.

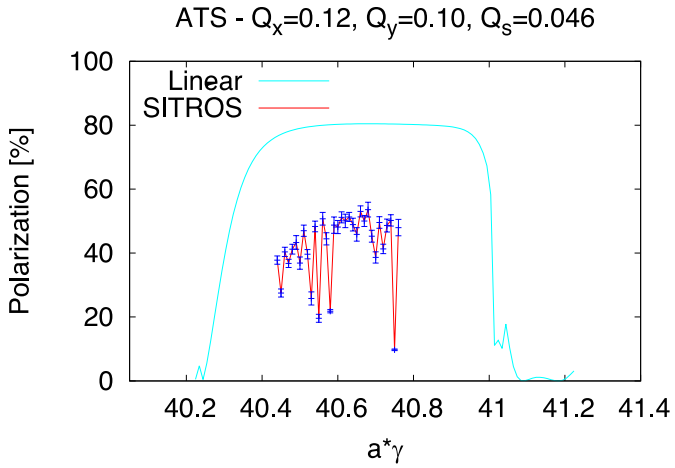

Figure 12c: Polarization vs. $a\gamma$ for the unperturbed ring in linear spin motion approximation (cyan) and as results from the tracking (red).

Fig.12d shows the RMS deviation from the vertical direction in the machine arcs of the

periodic solution to the Thomas-BMT equation, $\hat{n}_0$, which is vertical in the arcs and longitudinal between the rotator pair.

Although the solenoid strength is kept fixed, the deviation is small in the energy range considered.

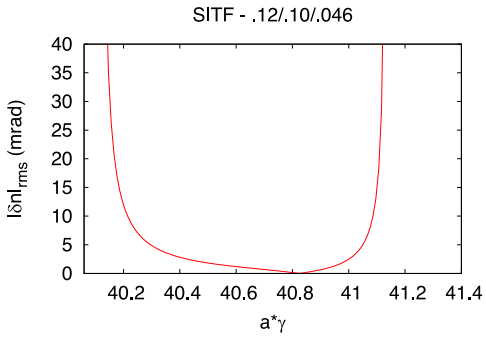

Figure 12d: RMS $|\delta\hat{n}_0|$ vs. $a\gamma$ for the unperturbed ring.

2.2.8.5 *Polarization in presence of misalignments*

Key points to achieve high polarization are the optimization of the betatron tunes, a well corrected closed orbit and a dedicated correction of $|\delta\hat{n}_0|$.
Following simulations are based on the MAD-X misalignment/correction tool kit. The resulting optics is dumped into a file which can be read by the SITROS package. 494 Beam Position Monitors (BPMs), measuring the beam position in both planes, have been added close to each quadrupole together with 494 vertical and 494 horizontal correctors. The RMS values of the quadrupole misalignment assumed are δx=δy=200 μm and a roll angle $\delta\Psi$=200 μrad. BPMs errors have not been included yet. It turns out that due to the large coupling in the solenoid sections, the orbit cannot be corrected in a satisfactory manner in the two planes separately in the whole machine as done by the MAD-X correction module. One way out was correcting both planes simultaneously with an “external" code and reading back the corrections with MAD-X. 46 independently powered skew quadrupoles, inserted at high D_x β_y and β_x β_y locations, are used for correcting spurious vertical dispersion and betatron coupling which are large due to the vicinity of the working point to the linear coupling difference resonance. Figs.12e and 12f show polarization for a particular error realization after closed orbit correction and with vertical dispersion and betatron coupling correction in addition respectively.

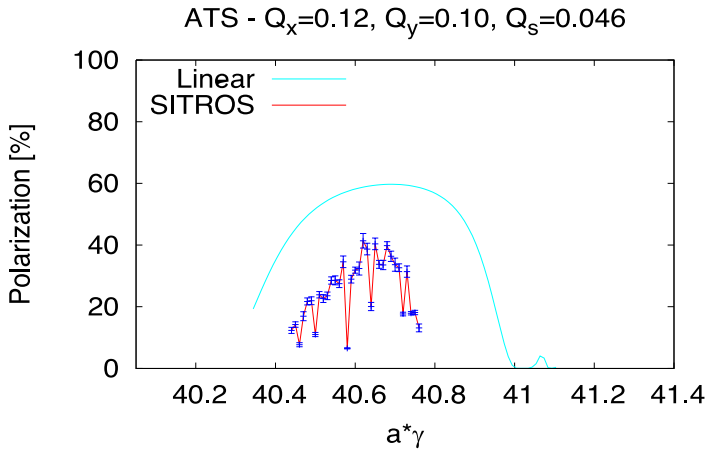

Figure 12e: Polarization vs. $a\gamma$ for the perturbed ring after closed orbit correction in linear spin motion approximation (cyan) and from tracking (red).

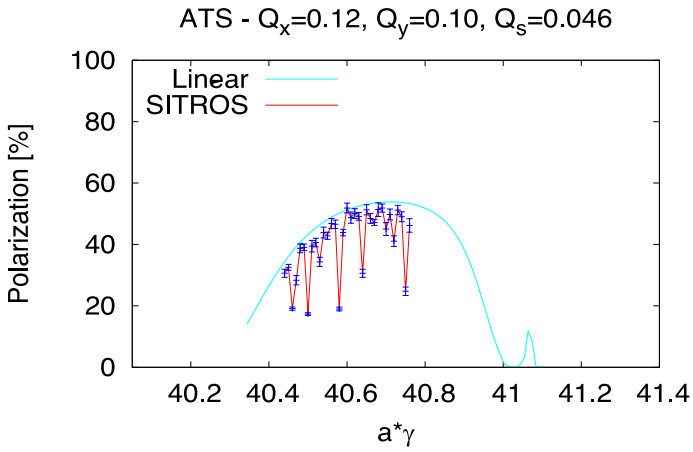

Figure 12f: Polarization vs. $a\gamma$ for the perturbed ring after closed orbit correction and skew quadrupoles optimization, linear spin motion approximation (cyan) and from tracking (red).

The deviation of the actual $\hat{n}_0$ on the perturbed orbit wrt to the nominal direction can be corrected resorting to *harmonic bumps* as done at HERAe [30] and LEP [18]. Fig.12g shows the RMS value of $|\delta\hat{n}_0|$ vs. $a\gamma$ before and after correction by harmonic bumps. Fig.12h shows the resulting polarization.

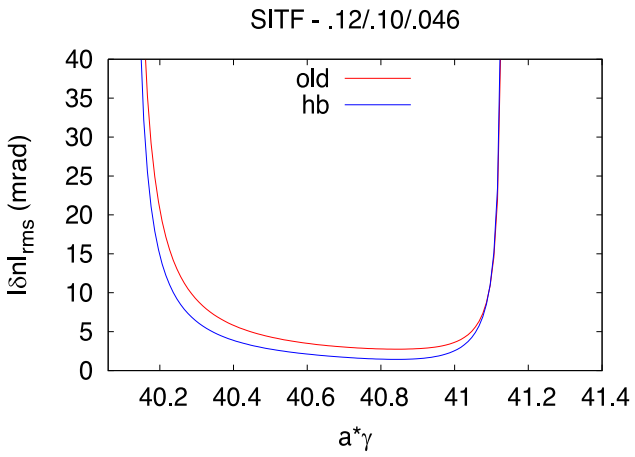

Figure 12g: RMS $|\delta \hat{n}_0|$ vs. $a\gamma$ for the the perturbed ring before (red) and after (blue) harmonic bumps optimization.

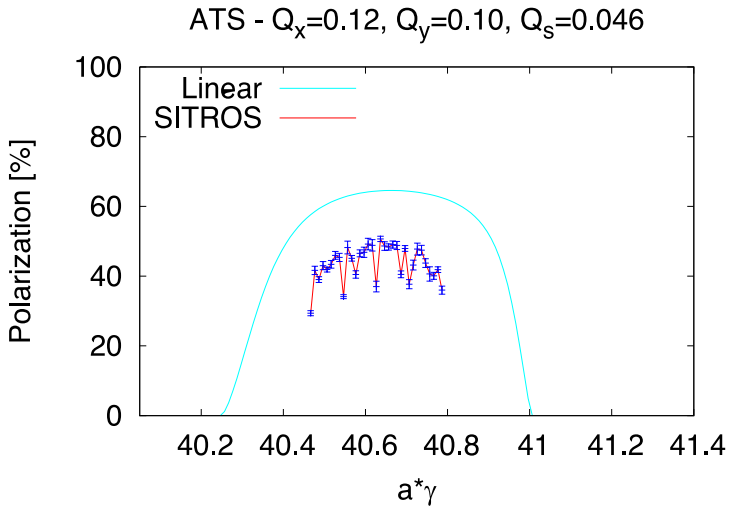

Figure 12h: Polarization vs. $a\gamma$ for the perturbed ring after closed orbit correction, skew quadrupoles optimization and $|\delta \hat{n}_0|$ correction. Cyan: linear spin motion approximation; red: tracking.

2.2.8.6 *Further considerations*

As discussed above, the eRHIC storage ring uses split dipoles to increase the damping decrement at lower energies. Such enhanced synchrotron radiation increases the spin diffusion rate. Thus, attention must be paid to the possibility of enhanced depolarization at lower energies too.

Similarly, the effect of beam-beam interactions on polarization requires consideration. The counter-rotating proton beam perturbs the electrons orbital and spin motion and acts as a non-linear focusing lens which shifts the beam tune and increases the tune spread, in particular in the vertical plane. The shift can be obviously compensated by the tuning quadrupoles; however the increased spread may affect the lifetime of the beam tails and restrict the tuning range. Running below the integer (*mirror tunes*) could ease the problem.

In HERA-I with one pair of spin rotators and $\xi_y^e \approx 0.06$ for two IPs, the effect of beam-beam interactions on polarization was not critical and with careful tuning beam polarization between 50% and 60% was delivered. Beam-beam effects however were clearly visible. For instance it was observed that non-colliding positron bunches could have a smaller polarization in collision mode because the tunes were optimized for colliding bunches. As a consequence of the removal of the experiment solenoid compensators and the introduction of 2 more spin rotators, in HERA-II the expected polarization was about 60% [16], w/o beam-beam effects. In addition ξ_y^e increased up to about 0.09. With positrons, for which the proton beam acts as a defocusing lens, the delivered polarization during collision was between 40% and 50%. With electrons however polarization reached only 30%-40% which increased to 40%-50% as for positrons, by operating the machine with mirror tunes.

The beam-beam tune spread might push a significant part of the eRHIC electrons away from ideal tunes for good polarization. However a state of the art orbit correction and a more efficient polarimeter are expected to increase the achievable polarization also in presence of beam-beam.

2.2.8.7 *Electron Storage Ring Dynamic Aperture*

The dynamic aperture of the electron storage ring is critical; the interaction regions contribute with maximum functions of ~400 m approximately 30% per IP to the natural chromaticity. A phase advance of 90 degrees per FODO cell is required to achieve the desired horizontal beam emittance of 20 nm for *18* GeV beam energy. At 10 GeV, where the highest luminosity is achieved, the optimum betatron phase advance in the arcs is 60 degrees per FODO cell. The total natural chromaticity including one IR is $\xi_{x,y} \cong -97.3, -92.4$. At 18 *GeV*, the interaction region contributes chromaticities of $\xi_{x,y}^{IR} \cong -33, -25$.

The dynamic aperture for particles with an ideal value of momentum is maximized by using a two-family sextupole correction scheme to control $\xi_{x,y} = +1$. However, the large off-momentum β-beat generated by the low-β quadrupole magnets causes a large nonlinear chromaticity which deteriorates the off-momentum dynamic aperture.

The strategy to recover off momentum dynamic aperture is two-fold:

- Achieve as much intrinsic compensation of $(\Delta\beta_{x,y}/\beta_{x,y})/(\Delta p/p)$ by optimized betatron phase advances between the sources of chromaticity. However, this is constrained by the spin matching conditions and the special phase advances between crab cavities and IP.
- Arrange the sextupoles in the arcs in families tuned in order to create an off-momentum β-beat that cancels the off-momentum β-beat from the IR, while avoiding the generation of nonlinear resonance driving terms.

In addition, sextupoles in the dispersion-free straight sections, called "geometric sextupoles", may be used to minimize residual contributions to driving terms of nonlinear resonances.

The 6 eRHIC arcs, however, consist of 16 regular periodic FODO cells and have at each end three FODO cells for dispersion matching which are not identical to the regular cells.

For the 60 degree optics for a beam energy of 10 GeV, a scheme with a structure of 32 sextupole magnets (16 horizontally focusing and 16 vertically focusing ones) per arc is applied. These are powered in three horizontal and three vertical families, labelled by $A_{h,v}$, $B_{h,v}$, and $C_{h,v}$. Some of the possible sextupole positions are left empty (denoted by "*E*") which is the result of optimization. The scheme is:

A-B-E-A-B-A-B-C-A-B-C-A-B-E-A-B

Note that only horizontally focusing sextupoles are shown in this scheme. Vertically focusing sextupoles are interleaved with the horizontal ones; the scheme is the same. Sextupoles belonging to the same family are always spaced by 180 degrees. This implies that driving terms for off-momentum β-beat accumulate over the sextupoles of the same family and thereby maximize the potential for compensation of the β-beat from the IR. The contributions to nonlinear driving terms from sextupoles of the same family, however, cancel, so that non-linear effects are only created in higher orders. Since the β-beat generated in the IR arrives at each arc with a different phase, the sextupole families need to be re-optimized in each arc.

This scheme produces a dynamic aperture of $\pm 20\,\sigma_x$ and provides a momentum aperture of $\pm 7\ \sigma_E$. These values are believed to provide sufficient margin to accommodate magnetic imperfections and effects of misalignment.

An additional margin is provided by geometric sextupoles in the straight section, which have not yet been optimized. Figure 13 shows the on-momentum dynamic aperture in the x-y plane. The variation of tunes on a trajectory with a given starting point in phase space is used as a figure-of-merit for the stability of each point in phase space. The plot of such a frequency map [19] shows a clear border between stable and unstable motion.

The color code refers to the tune fluctuation $dQ = \log\left(\sqrt{\Delta Q_x^2 + \Delta Q_y^2}\right)$, where $\Delta Q_{x,y}$ are the differences in tune obtained by FFT over two successive periods of 1024 turns. Figure 14 shows the frequency map in the $x - \Delta p/p$-plane.

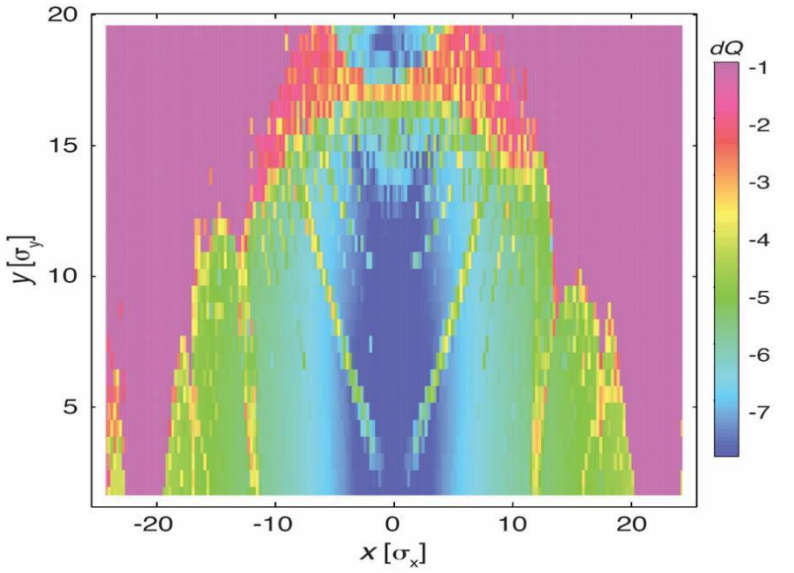

Figure 13: Frequency map of dynamic aperture in the *x-y* plane. The axis is plotted in units of RMS beam size at the starting point. The color scale (shown on the right-hand side) indicates the logarithm of tune fluctuations which are a measure for the stability of the motion

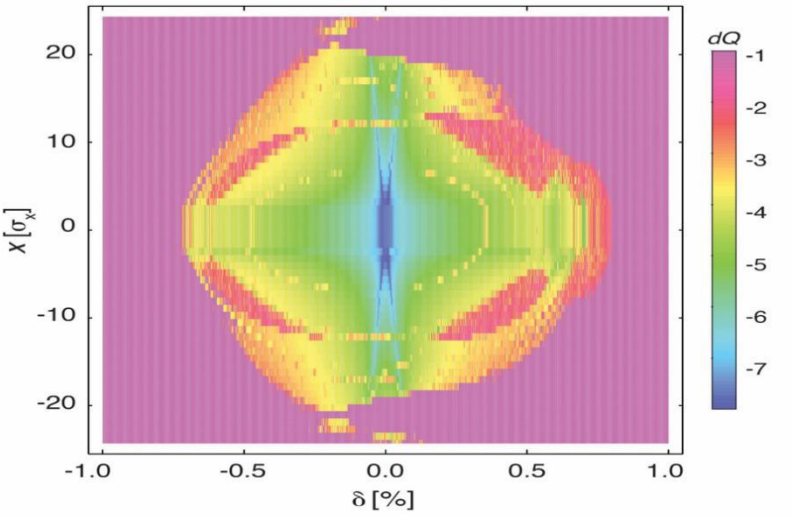

Figure 14: Frequency map of dynamic aperture in the *x-Δp/p* plane.

The beam optics for 18 GeV with a phase advance of 90 degrees requires a different strategy. With a phase advance of 90 degrees, two sextupoles in neighboring cells (horizontally focusing or vertically focusing, respectively) will generate an off-momentum β-beat if the two strengths are different. Sextupoles in successive cells with the same strength will add to this β-beat. However, there is no control over the phase of that β-beat. For this reason, the phase of the beat that originates at the IR needs to arrive with the correct phase at the first sextupole in the regular arc.

This requires the design of an appropriate betatron phase advance between the IP and the first sextupole in the arc. The betatron phase needs to be optimized between the 6 arcs in order to enable all sextupoles for correction of 2nd order chromaticity. Alternatively, one can arrange that the first arc corrects only the cosine-like part of the β-beat and the next arc, which would be spaced by a horizontal and vertical betatron phase difference from the first arc of $2(k+1)\pi/4$ (k integer), to correct the sine-like component of the β-beat (phase referring always to the first regular sextupole in the arc adjacent to the IR). The 18 GeV lattice is not fully optimized yet and is not further discussed. In case of unexpected difficulties, it will be possible to run with a 60 degree lattice at this energy which would result in some luminosity loss.

2.2.8.8 *Collective Effects in the eRHIC Electron Storage Ring*

We have considered coherent instabilities, intrabeam scattering and Touschek scattering.

Intrabeam scattering times in the electron storage ring are in the order of minutes, much longer than the 50 ms radiation damping times. Touschek lifetimes are hours, which is much longer than the bunch replacement time. We have considered coherent instabilities, intrabeam scattering and Touschek scattering.

Intrabeam scattering times in the electron storage ring are in the order of minutes, much longer than the 50 ms radiation damping times.

Touschek lifetimes are hours, which is much longer than the bunch replacement time based on polarization loss.

Coherent instabilities in the electron ring have been studied using a modified version of the computer code TRANFT [20], which was used during the design of the National Synchrotron Light Source II (NSLS-II) and evolved into the stochastic cooling simulation code. The code has evolved and now can simulate both single bunch and coupled bunch instabilities, by tracking of up to 5 bunches and assuming a uniform fill. This allows one to use a few times 10^5 simulation particles per bunch when doing coupled bunch calculations.

Simulations were done for 5, 10, and 18 GeV, and the results are summarized in Tables 7 and 8. The code tracks the longitudinal and a single transverse dimension. The four impedance values in Table 8 along with the short range resistive wall and Coherent Synchrotron Radiation (CSR) impedance were included. The beam-beam force was enough to damp transverse coupled bunch modes and a longitudinal damper with a gain of $g_z = 5 * 10^{-3}$ damped the coupled bunch longitudinal oscillations. The damper was applied once per turn and the gain was defined such that

$$\Delta E = - g_z \langle E \rangle$$

where ΔE is the energy kick given to each electron and $\langle E \rangle$ is the average energy error of the electron bunch. It is envisioned that one would use a transverse pickup in a dispersive region with closed orbit subtraction and a filter to notch out the betatron oscillations. The beam-beam parameter was set to 0.1 initially, but values as low as 0.075 were found to be sufficient to stabilize the electrons.

Table 7: Electron Beam Parameters for $|Z/n| = 0.1\Omega$. A uniform fill of 720 bunches was assumed for coupled bunch effects.

Parameter	*5GeV*	*10GeV*	*18GeV*
RF voltage ($h = 7200$) [MV]	20	20	62
RF voltage ($h = 3 * 7200$) [MV]	6.6	6.4	0
γ_T	31	31	41
V_{synch} [MV]	1.3	5.0	38
N_e $[10^{10}]$	31	31	6.3
$\sigma(p)/p$ (Z/n=0) $[10^{-4}]$	8.2	5.5	10
$\sigma(p)/p$ (Z/n=0.1) $[10^{-4}]$	8.6	6.4	10
σ_s (Z/n =0.1) [mm]	22.5	23	8.8

Table 8: Impedances assumed for calculations in Table 7.

Impedance Type	*Rsh*	*Q*	*Fres*
BB longitudinal	51 kΩ	2	20 GHz
BB transverse	1.4 MΩ/m	2	20 GHz
NB longitudinal	360 kΩ	80	856 MHz
NB transverse	10.8 MΩ/m	80	1.0 GHz

After dealing with the coupled bunch modes the main problem was the longitudinal microwave instability which manifested in the classic saw tooth pattern shown in Figure 15. With this impedance and full current we will need to have $\frac{\sigma(p)}{p} = 8.2 * 10^{-4}$. This is within the specifications of the narrow dipoles, but may not be necessary.

In Table 7 the quantity σ(p)/p(Z/n=0.1Ω) is the minimum momentum spread for which the nominal intensity has negligible bunch length oscillations. The bunch length $\sigma_s(\frac{Z}{n} = 0.1\Omega)$ is the corresponding RMS bunch length.

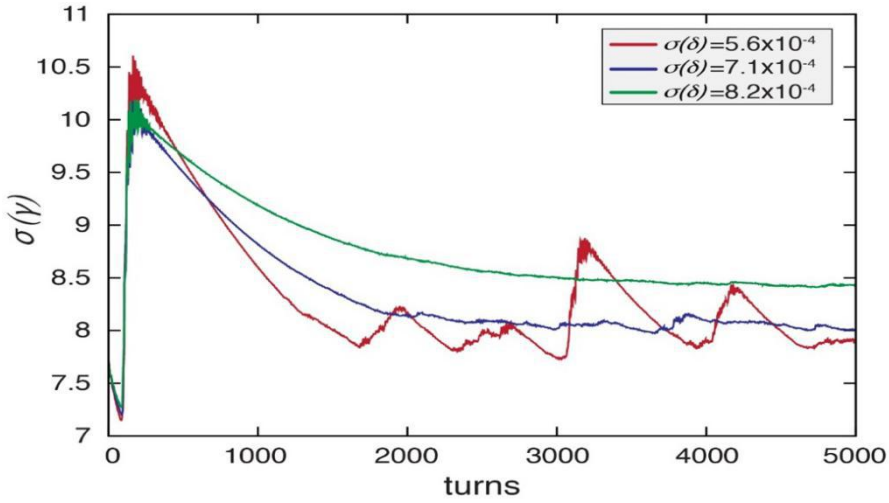

Figure 15: Energy spread in units of rest mass versus turn for 5 GeV electrons with the nominal lattice and various low current σ(p)/p.

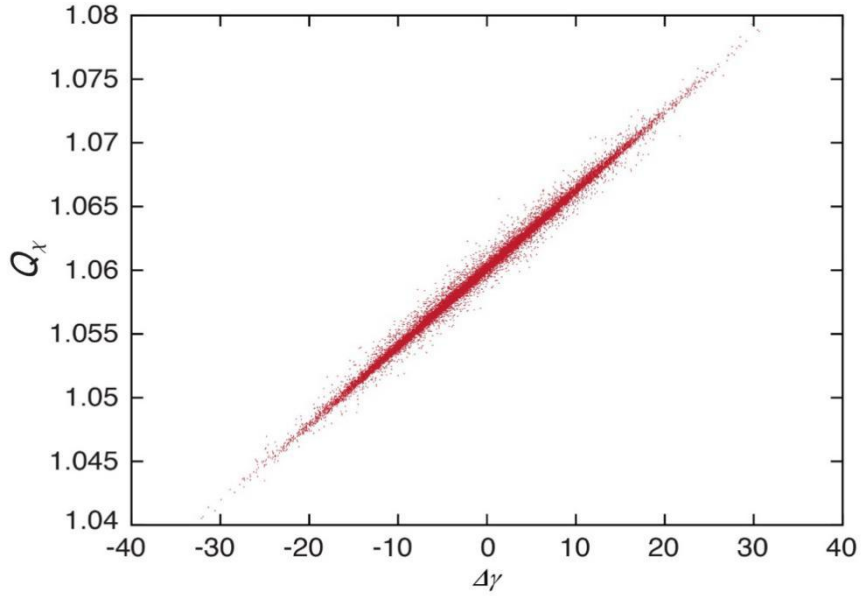

Figure 16: Betatron tune distribution for 5 GeV electrons with an intrinsic momentum spread of σ(p)/p=8.2*10^{-4}.

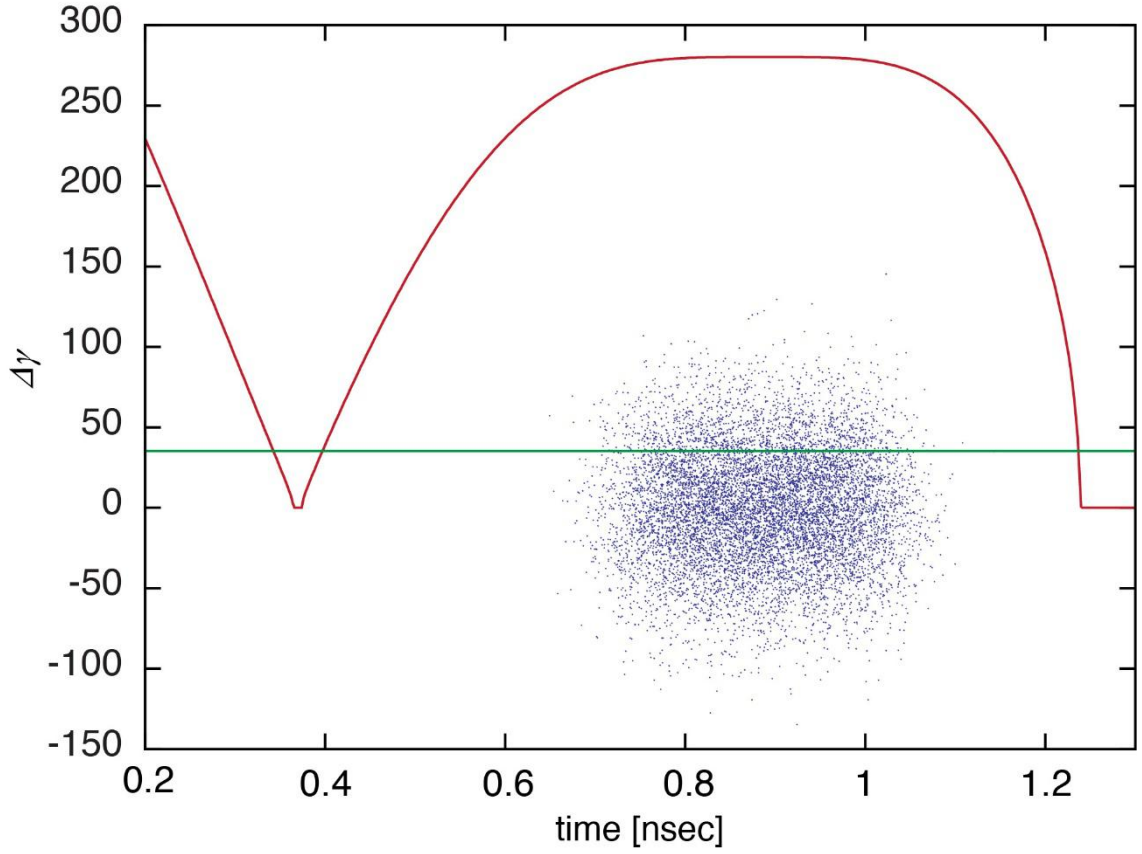

Figure 17: Bunch and bucket for 18 GeV electrons. The horizontal line is at 1.0σ. The full height is 10.5σ

Figure 15 shows the energy spread oscillations for the nominal intensity and various intrinsic momentum spreads at 5 GeV. Figure 16 shows the tune spread for stable beam. Figure 17 shows a nominal 18 GeV bunch within its bucket.

2.2.9 **Hadron Ring**

2.2.9.1 ***Lattice Design***

The present RHIC and its injector complex remain for the most part unchanged when becoming a part of eRHIC. In particular, the arcs with their superconducting magnet structure will remain the same as the present RHIC. Some modifications are necessary or desirable. eRHIC hadrons will circulate in the "Yellow" ring, while the "Blue" ring will remain in place as well. The sextant between IR6 and IR4 of the Blue ring will serve as a transfer line and the beam will be injected in IR4. Some modification of the RF system is necessary to accommodate the 330 bunches at injection and to accomplish the splitting into 1320 bunches. Space for more RF cavities will be provided in IR4 and IR10. The non-colliding straight sections (utility straights) will be simplified by removing the DX separator dipoles in order to simplify the geometry and provide space for the electron ring cross-over from inner to outer arcs and vice-versa.

Studies are underway to investigate whether the D0 magnet can be removed as well. The sextant between IR2 and IR12 of the Blue ring will be used to circulate low energy hadrons which then have the same revolution time as electrons despite their reduced velocity.

2.2.9.2 *Keeping the Hadron Revolution Frequency Constant for all Beam Energies*

Proton and ion beams are not ultra-relativistic in the energy range of an electron-ion collider. In eRHIC, the hadron beam energy is chosen to vary between 41 GeV and 275 GeV. If the beam orbit was the same, the revolution time would vary by 3.3 nsec between these two beam energies. In order to maintain synchronization with the ultra-relativistic electrons, the hadron orbit will be shortened by up to 94 cm for the lowest hadron energy of 41 GeV.

This is accomplished in the following way:

The hadrons circulate counterclockwise in the Yellow ring.

In the arc between IR2 and IR12 the high energy beam (in the 100-275 GeV energy range) travels in the outer arc (a part of the Yellow ring), while the 41 GeV beam passes through the inner arc (a part of the Blue ring).

The inner and outer arc radii differ by 88 cm, and an inner sextant is 94.2 cm shorter than an outer one. This path length difference allows for synchronizing 41 GeV hadron beams with the electrons. When synchronizing higher energies, using the outer arc between IR2 and IR12, the central orbit, passing through quadrupole magnet centers, is used for a proton beam of 133 GeV. For the beam energies 275 GeV and 100 GeV the synchronization can be accomplished by +14 mm and -14 mm radial shifts, correspondingly, which is well within the acceptance of the 80 millimeter diameter vacuum chamber.

The corresponding modifications to the RHIC lattice are only relatively minor. This requires some rearrangement of the bus system. The Blue ring sextants used for injection and low energy running must be powered with reversed polarity. The superconducting magnets of RHIC are protected by cold diodes which in principle must be reversed. However, quench analysis shows that at less than 20% of maximum excitation, this protection is not required.

Thus, modifications of the RHIC lattice and magnet system for eRHIC are fully reversible and are accomplished with relatively little effort.

2.2.9.3 *Hadron Ring Dynamic Aperture*

The strong focusing of the hadrons at the collision point causes maximum β-functions in the low-β quadrupoles to exceed $\beta_x = 1600\,m$ and $\beta_y = 1300\,m$. The contribution to the natural chromaticity generated in one IR amounts to $\xi_x = -30$ and $\xi_y = -40$, which is 20% of the contributions from the 90 degree arcs. This implies a large contribution of the chromaticity generated in the interaction region that must be compensated by sextupoles in the arcs in order to confine the tune footprint of the hadron beam to remain within the space between nonlinear resonance lines.

As discussed above, the strength of these resonances is enhanced by the nonlinear field, and the resonance free space in the tune diagram is shrinking. Obviously, there is a maximum amount of IR chromaticity and corresponding tune footprint which can be accepted. This chromaticity limit is determined by numerical particle tracking to verify that the dynamic aperture is sufficiently large. The numerical simulations also include the impact of field errors of the superconducting magnets, the magnets in the interaction regions, and imperfections such as magnet misalignment.

The dynamic aperture is defined as the maximum betatron amplitude within which particles are not lost in a given number of turns of single particle tracking. The long-term dynamic aperture converges to the boundary between regular and chaotic motion. Experience with RHIC operations indicates that relevant dynamic aperture figures require tracking over 10^6 turns. The stability of a particle is assessed by the analysis of the trajectories over 10^6 turns which allows one to characterize a trajectory as stable or unstable.

The results of such simulations show that the dynamic aperture of the eRHIC hadron ringm amounts to 10σ at injection and 6σ at high luminosity operation. The simulation includes the beam-beam effect in weak-strong approximation. This is the same value as obtained for present RHIC.

2.2.9.4 *Electron Cloud Effects*

Electron clouds are a serious concern for the ion ring with 1320 bunches and $0.6 * 10^{11}$ particles per bunch. Electrons which are produced in the beam vacuum chamber by ionization of the residual gas by the beam may get accelerated by the following bunches and may hit the vacuum chamber wall with high energy, thereby releasing more electrons from the wall. This mechanism may create an electron avalanche that builds up rapidly as the entire bunch train passes by. The consequence could be high cryogenic losses and beam instabilities. Next to beam current and bunch parameters,

the key parameter that determines the seriousness of the electron cloud effect is the secondary emission yield (SEY, number of emitted electrons from the surface per incident electron) coefficient of the vacuum chamber material.

We assume that the stainless steel beam pipe of RHIC will be coated with copper and that we will be able to improve the secondary emission coefficient by scrubbing the surface by beam operation to the level achieved in the LHC [21].

An initial simulation using the computer code CSEC [22] and a model for the wall parameters in the scrubbed LHC showed dangerous electron clouds both for the LHC and for eRHIC, with LHC being slightly worse. For both machines the average dose to the wall was in the tens of watts per meter range but this value depends critically on the assumed secondary emission yield, which was inferred for the LHC using the measured energy deposition.

eRHIC requires a stronger suppression of the electron cloud mechanism in order to keep the cryogenic load within tolerable limits of $P_{load} \leq \frac{1W}{m}$. This is planned to be achieved by an additional layer of coating consisting of amorphous carbon. For electron clouds we are collaborating with CERN in understanding and reproducing their results. In the end we know that electron clouds in the LHC are difficult but tractable. There is currently no reason to believe otherwise for eRHIC.

2.2.9.5 *Intra-Beam Scattering*

The effect of multiple Coulomb scattering of charged particles inside a bunched beam upon each other taking into account the Lorentz boost is known as Intra-Beam Scattering (IBS) [23] This causes emittance growth in all oscillation planes of the beam. This effect limits the high beam density needed for high luminosities, and it affects the luminosity lifetime and the average luminosity. Beam parameters thus must be chosen to achieve an IBS growth time of several hours given the beam set-up time of typically 1 hour, unless the emittance growth can be overcome by strong active cooling of the beam emittances. Table 9 lists the beam parameters and calculated IBS growth times for the eRHIC design parameters of protons at 41 GeV, 100 GeV, and 275 GeV.

Table 9: eRHIC Proton Beam Parameters.

Parameter	***Moderate luminosity without cooling***			***High luminosity with cooling***		
Beam energy [GeV]	41	100	275	41	100	275
Bunch intensity [10^{11}]	0.6	1.1	1.1	0.11	0.6	0.6
RMS Horizontal normalized emittance [mmmrad]	3.3	4.5	4.1	2.0	3.6	2.7
RMS Vertical normalized emittance [mmmrad]	2.5	2.5	2.5	0.11	0.19	0.4
Longitudinal bunch area [eVsec]	0.5	0.6	0.8	0.2	0.4	0.4
RF frequency [MHz]	225	225	563	563	563	563
RF voltage [MV]	8	11	24	8	16	18
RMS momentum spread [10^{-4}]	15	8.7	6.6	10.3	9.1	4.6
RMS bunch length [cm]	13	11	7	7.5	7	5
Longitudinal Emittance IBS growth time [hours]	10.3	8.	10.1	3.2	2.4	2.2
Horizontal Emittance IBS growth time [hours] (without coupling)	8.0	13.7	9.2	2 0	2.0	2.1

For the high luminosity parameters as listed in Table 9, beam growth due to IBS is significant and strong cooling is required to maintain the beam density and the luminosity over a reasonable store time of at least several hours. These parameters are based on new 225 MHz and 563 MHz RF systems for the hadron ring that would have to be added to the present RHIC. The results are based on complete decoupling of horizontal and vertical betatron motion. This is also essential to maintain unequal emittances in the horizontal and vertical plane. Very good vertical orbit control is also mandatory to avoid any significant vertical dispersion. With strongly suppressed vertical dispersion there will be no significant emittance growth due to IBS in the vertical plane.

2.2.9.6 *Hadron Ring Strong Beam Cooling*

Highest luminosity in an electron-ion collider can only be achieved by introducing a strong beam cooling mechanism that counteracts IBS, which would otherwise cause rapid increase of emittance and reduction of luminosity. Moreover, the hadrons which gained large transverse and longitudinal amplitudes by IBS experience a strong nonlinear force due to the beam-beam force imposed by the electron beam that would enhance halo formation and experimental backgrounds. Thus, with the parameters required for high luminosity, the hadron beam would become unusable quickly without cooling and would have to be replaced frequently.

As the turnaround time of superconducting RHIC is about 1 h, based on slow magnetic cycle of RHIC main magnets and spin rotators and the filling time at injection, the increase of peak luminosity above a certain level of performance would lead to a reduction of average luminosity. The eRHIC High Luminosity parameters (see parameter Tables 1 and 9) were selected to have an IBS growth time $\varepsilon/(d\varepsilon/dt)$ of no less than two hours in order to ease requirements on the hadron cooler.

Stochastic cooling is a well-established cooling mechanism for hadrons which has been pioneered at RHIC for bunched ion beams. It is used very successfully for cooling of gold beams in RHIC operations and has enhanced the luminosity significantly. It would work in principle for protons at high energies, but the cooling rates at typical intensities of eRHIC proton bunches fall short of the need by *orders* of magnitude because of bandwidth limitations of beam pick-up and kicker magnets.

Electron cooling with a DC electron beam is a standard cooling mechanism for hadron beams that works well at low hadron energies up to a few GeV. For large hadron energies of multi-GeV, however, this cooling method becomes quite unfeasible as the cooling time scales strongly with the beam energy as $\gamma^{5/2}$, with γ being the relativistic factor of the hadrons. Furthermore, the electrons have to have the same relativistic factor as the hadrons and DC electron energies of tens of MeV are not available.

Using bunched electron beams accelerated by an RF LINAC would mitigate this somewhat. However, the cooling of 275 GeV hadron beams is still extremely challenging with incoherent electron cooling and the effort in cooling installation becomes unrealistically large because of large required electron beam currents on the order of amperes.

We are also looking into more recent approaches for strong hadron cooling. A novel method of hadron cooling which promises to work at very high hadron beam energies has been proposed [7]. This method, which is called "coherent electron cooling", uses an electron beam to pick up the longitudinal Schottky noise of the hadron beam, and subsequently amplifies the signal by sending the electron beam through a free electron laser. The strongly micro-bunched electron beam is then merged with the hadron beam with proper timing. The electron beam then acts as a kicker to reduce the energy spread of the hadron beam.

Recently, a variant of this method has been proposed [24] which achieves the micro-bunching by sending the beam through a chicane or a series of chicanes with optimized R_{56}. This method has limited amplification of the signal but reaches extremely large bandwidth.

A proof-of-principle experiment on a low energy RHIC ion beam is underway that aims at demonstrating coherent electron cooling with FEL amplification. This experiment is expected to provide results in 2018 [1].

Figure 18 shows a sketch with the layout of the proposed coherent electron cooling system for eRHIC which is laid out to support the storage of hadron beams required for luminosities in the range of $10^{34}\text{cm}^{-2}\text{sec}^{-1}$. An electron beam generated by a superconducting RF gun is injected into a three-turn energy-recovery superconducting LINAC that provides an energy gain of 50 MeV per passage. The fully accelerated electron beam of up to 150 MeV is injected onto an orbit which overlaps with the orbit of the eRHIC hadron beam in the straight section of IR10 over a distance of 50 m, which is called the modulator section. After this first common section, the hadron beam propagates through a section with an appropriately tuned $R_{56} = \lambda_{FEL}/(\Delta p/p)_{RMS}$ which separates particles with positive and negative energy deviation by a longitudinal distance corresponding to the width of the micro-bunch peak of the electron beam.

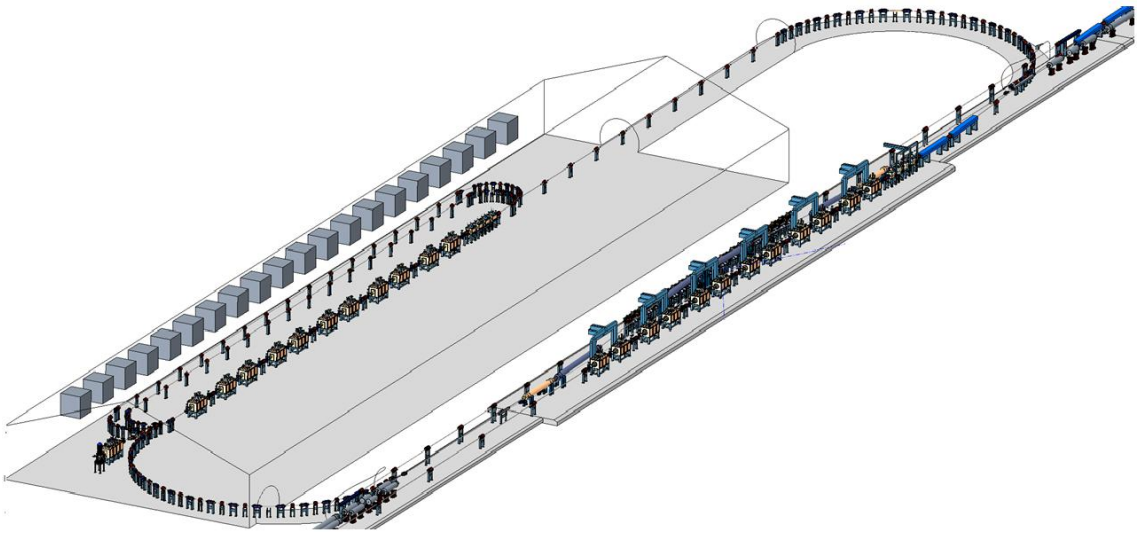

Figure 18: Rendering of the proposed layout for coherent electron cooling at eRHIC

The electron beam is energy-modulated due to residual fluctuating space charge forces from the proton beam. The electron beam passes through a chicane where the energy spread caused by the hadron beam density fluctuation is transformed into a micro bunching of the electron beam. The density modulation of the electron beam is then amplified by a mechanism exploiting plasma oscillations:

After one quarter plasma oscillation wavelength, the density modulation is transformed into a now even larger energy modulation, which after a second chicane is turned into a stronger density modulation.

The present stage of the development proposes two amplification stages to produce a sufficiently strong electron density modulation. The electron beam is again launched onto the hadron orbit thereby overlapping with the hadron beam with carefully adjusted phase.

Hadrons with higher energy will be ahead of the electron micro-bunch and will be decelerated. Hadrons with lower energy will trail behind the electron micro-bunch and will be accelerated. The energy spread of the hadrons will be reduced after this `kicker' section. Cooling times of 100 min are envisioned. Table 10 summarizes the parameters of eRHIC coherent cooling.

Table 10: Parameters of the eRHIC coherent electron cooling.

Parameter	***Value***
Hadron Energy Range [GeV]	41-275
Electron Beam Energy [MeV]	22-150
Electron Beam Current [mA]	100
Electron Peak Current [A]	10
Electron Charge per bunch [nC]	0.75
Primary R_{56} [m]	3×0.04
Plasma Amplification stages	2
Secondary R_{56} [m]	0.05
Length of the modulator section [m]	50
Length of the kicker section [m]	50
Cooling Time [hour]	.5

2.2.10 **Electron Injection Complex**

2.2.10.1 ***General Considerations***

The requirements on the electron injector complex are driven by the need for polarized electrons in electron-ion collisions. The electron polarization should be close to 80%. It is also necessary to have two electron spin polarization directions simultaneously present in the same store. This is important to discriminate against systematic errors in the detection. We already discussed the consequences for the injection system but summarize here the chain of arguments:

In principle, electron polarization in a storage ring builds up by the so-called Sokolov-Ternov effect: Spin flips are induced in the process of emitting synchrotron light photons.

Spin flips from spin which is parallel to the magnetic dipole field to spin which is antiparallel when emitting photons are slightly more likely than the opposite spin flip. The differential flip rate leads to a slow build-up of polarization antiparallel to the magnetic dipole field. Unfortunately, the polarization build-up time is much too slow to be of practical use at eRHIC electron energies. Consequently, the spin polarization for eRHIC electron beams must be produced at the source and must be preserved during the acceleration process.

The bunches which are polarized parallel to the magnetic guide field are subject to slow depolarization by the Sokolov-Ternov effect in the storage ring. At 18 GeV operation, a bunch replacement rate of once per 6 *min* for each individual bunch in the storage ring is required to keep the time-averaged level of polarization larger than approximately 84% of the injected polarization. Thus the injector has to provide a new bunch about every second to maintain good polarization of all 330 bunches. At 10 GeV and 5 GeV, the depolarization time is much longer, and the bunch replacement rate can be reduced by a factor of at least five.

The injector will deliver electron bunches which are 85% spin polarized at beam energies of 5 GeV, 10 GeV, and 18 GeV. In the storage ring the highest bunch charge of 50 nC is required for operation at 10 GeV and 5 GeV without hadron cooling whereas for 18 GeV operation a bunch charge of 10 nC is more than sufficient. In order to reach the storage ring bunch intensity of 50 nC at 10 GeV five bunches from the injector need to be accumulated in one storage ring bucket. Thus the injector has to deliver 10 nC at a 1 Hz rate. These bunch charge and rate requirements are sufficient for operation at all energies with and without hadron cooling, as shown in Table 11.

The electron injection complex consists of the following elements:

- Electron gun with a Ga-As photo-cathode;}
- Low energy transfer line (0.4 *MeV*);
- Electron S-band LINAC (400 *MeV*);
- Medium energy transfer line (400 *MeV*);
- Rapid cycling electron synchrotron (0.4-18 *GeV*) in the RHIC tunnel;
- High energy transfer line (5-18 *GeV*).

Table 11: Requirements for the electron injector.

Parameter	*Moderate luminosity without cooling*			*High luminosity with cooling*		
Energy E [GeV]	5	10	18	5	10	18
Ext. E_k from Source ($\gamma = 1.27$) [keV]		350			350	
LINAC energy gain [MeV]		400			400	
Normalized electron emittance after LINAC [μm]	125	95	115	20	20	115
Beam emittance at RCS extraction [x/y, nm]	20/13	20/4.9	22/3.3	20/2	20/1	22/3.3
Bunch Charge in Storage Ring [nC]	50	50	10	25	25	10
Number of Bunches in Storage Ring	660	660	330	1320	1320	330
Bunch Charge in Source and RCS [nC]	10	10	10	5	5	10
Ramp Rate [Hz]		1			1	
Bunch Replacement Period [min]	55	55	5.5	110	110	5.5
Bunch replacement period (polar. req.) [min]	149	118	6.6	149	118	6.2

2.2.10.2 *Polarized Electron Source*

The requirement for the polarized eRHIC source is a charge of 3-10 nC of 85% polarized electrons at a rate of 1 Hz and a normalized transverse emittance of 10-30 μm This requirement satisfies the needs for all operation modes of the storage ring.

Polarized electron beams are obtained from special photo-cathodes. The most common material which has been used successfully in the last 30 years is Ga-As alloy. Strained Ga-As cathodes which are irradiated with UV laser light of 780 nm yield high polarization of the extracted electron beam and a high quantum efficiency (QE $\geq$ 1%) when coated with a mono-layer of Cs.

The polarized electron gun of the Stanford Linear Collider (SLC) which was developed in the 1980's provided a reliable performance delivering 16 nC of polarized electrons (70-75% polarization) at 120 Hz repetition rate. In principle, the eRHIC injector could be based on the SLC gun. However, to exploit the technical development which has occurred in the last three decades, a dedicated eRHIC gun has been designed which promises larger beam energy, longer cathode lifetime, higher reliability, and larger polarization ($\geq$ 80%). A comparison of gun parameters is shown in Table 12.

Table 12: Electron source parameters.

Project	*RF Frequency [GHz]*	σ_s *[ps]*	*Bunch Charge [nC]*	*Energy [MeV]*	*Emittance [μm]*	$\Delta\gamma/\gamma$ [%]	*Cathode Material*
SLC 5mJ,845nm Laser	DC	2000	$9-16$	0.12	15	1.5	Ga-As
eRHIC 5mJ,780nm Laser	DC	2000	$3-10$	0.35	$10-30$	2	Ga-As super lattice

A new gun geometry based on the "inverted gun"-scheme has been designed. The design is optimized for a high extraction voltage of 350 keV and low electron beam loss. For good cathode lifetime and high reliability, excellent vacuum conditions are needed in the gun, the extraction line, and the tune-up beam dump. A prototype of this beam line has been built and tested. A load lock system for installation of prepared and activated cathodes into the gun has been designed. A prototype of this system is available and has been tested.

2.2.10.3 *Rapid Cycling Synchroton*

Full energy injection of polarized electron bunches is accomplished by a Rapid Cycling Synchrotron (RCS) in the RHIC tunnel which accelerates the electrons from the 400 MeV LINAC to up to 18 GeV for injection into the storage ring. The synchrotron has a repetition rate of 1 Hz and a total ramping time of 200 msec. The most important design feature of the synchrotron is spin transparency up to the full energy of 18 GeV. This is accomplished by high lattice periodicity P. The RHIC tunnel, however, only allows a lattice symmetry of 6 as it is composed of 6 arcs separated by 6 straight sections. This design overcomes this limitation by configuring the straight section beam optics such that the transformation of beam coordinates through the straight section is an identity transformation. This also includes the electron spin. In order to suppress intrinsic depolarizing resonances, the periodicity P and the vertical betatron tune $Q_{y,\,arc}$,

calculated by accounting betatron phase advance in the arcs only, must fulfill the conditions:

$$P - Q_{y,\,arc} > a\gamma$$

And

$$Q_{y,arc} > a\gamma \qquad (6)$$

where $a\gamma = 40.849$ is the spin tune with $a = 1.16 * 10^{-3}$ being the anomalous magnetic moment of the electrons. This leads to the choice of $Q_{y,\,arc}$~50 and P = 96 which is readily accomplished given the large arcs of RHIC. The lattice in the arcs is thus composed of $6 * 32$ FODO cells with a betatron phase advance of π/2. A super-period consists of two FODO cells as there are two sextupole families per plane to compensate linear and nonlinear chromaticity. A special feature of one of the straight sections is that the synchrotron orbit must pass around the colliding beam detector with a spin transparent chicane.

At the peak energy of 18 GeV, the electrons suffer from an energy loss of 36 MeV/turn due to synchrotron radiation. The acceleration and radiation loss compensation is done by 13 eight-cell 563 MHz RF cavities powered by IOT amplifiers.

The synchrotron accelerates single bunches with a charge of 10 nC. With this amount of bunch charge, the electron beam remains below any collective instability threshold. A third harmonic system is being studied which could provide additional stability margin.

The concept of spin transparent acceleration was tested extensively by comprehensive simulation studies. The amount of depolarization during the acceleration was found to be only in the order of two percent. These simulations take into account an imperfect machine lattice. In order to obtain realistic estimates on the preservation of electron spin polarization, imperfections of quadrupole fields, typical betatron coupling, misalignment and closed orbit errors as well as sextupole fields for chromaticity corrections have been introduced in the machine model.

Correction algorithms have been applied to adjust correction elements such as dipole correctors, tune correction quadrupoles and skew quadrupoles. It is assumed that orbit excursions can be kept below 0.5 mm. It is further assumed that the betatron tunes during the ramp are kept within $|\Delta Q| \leq 0.01$ by applying tune feedback or pre-programmed time-dependent tune corrections.

With this realistic machine model, simulations show that the polarization is robust and resilient against residual imperfections (see Figure 19). These good polarization results are consistently obtained for a number of statistical error seeds.

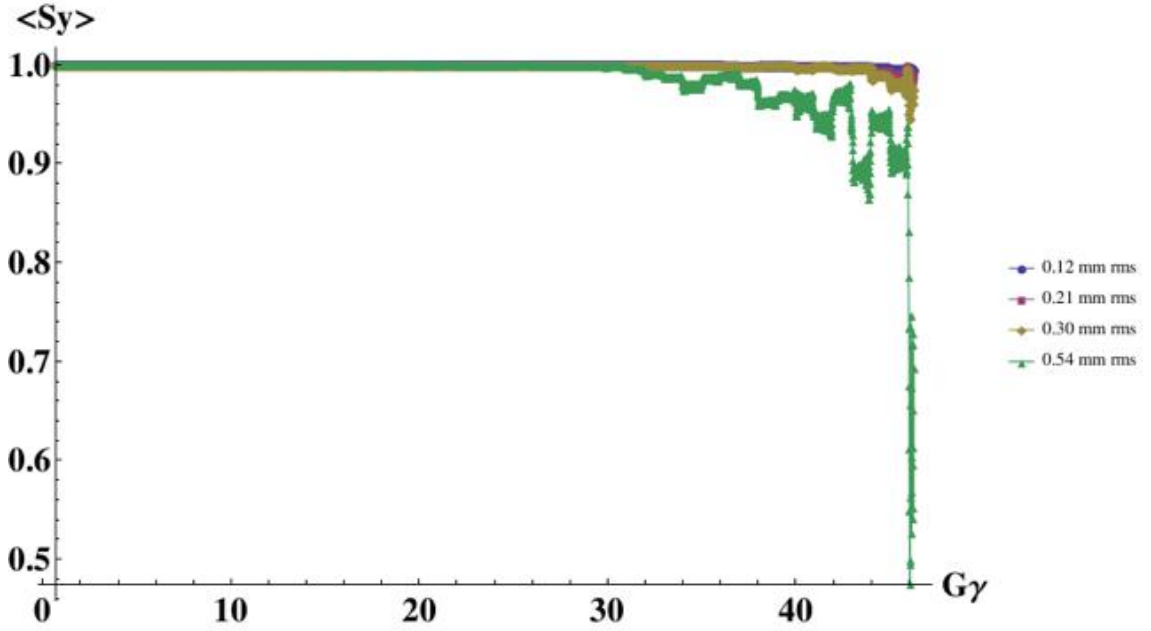

Figure 19: Electron spin polarization in the Rapid Cycling Synchrotron as a function of beam energy expressed in terms of spin tune $a\gamma$ during the ramp. Different color curves indicate different RMS values of residual orbit distortions. Note the suppressed zero of the vertical scale

2.2.10.4 *Electron Injection*

The requirement of arbitrary spin patterns in the electron ring coupled with radiative polarization necessitates regular bunch replacement. At an electron beam energy of 18 GeV, we plan to replace electron bunches every 6 min. With 330 bunches this corresponds to 1 sec between injections. The electron injection is accomplished by a combination of fast and slow kickers and a pulsed eddy current injection septum in the horizontal plane. The slow kickers form two closed three-bumps. The first one is used to extract a bunch with depleted polarization to create an empty bucket for the fresh bunch. It kicks a large fraction of the stored beam to transverse amplitudes close to the extraction septum. A fast kicker magnet right next to the first slow bump kicker kicks only the bunch that will be extracted and is going to be replaced by a fresh, injected bunch. The additional kick allows the selected bunch to enter the extraction septum.

The second slow bump is for injection. The storage ring beam optics has a dispersion at the injection septum where the second slow bump has its maximum spatial excursion. The new bunch is extracted from the RCS with a slight energy offset with respect to the energy of the circulating beam in the storage ring. The energy offset times the dispersion equals the distance of the bunch to be injected from the orbit of the circulating beam. This scheme results in injection without a transverse oscillation amplitude, but with a longitudinal oscillation amplitude. The offset of the injected beam with respect to the closed orbit vanishes at locations where the dispersion is zero which is in particular the case in the IR. The longitudinal injection oscillation will be eventually removed by radiation damping. The scheme is illustrated in Figure 20.

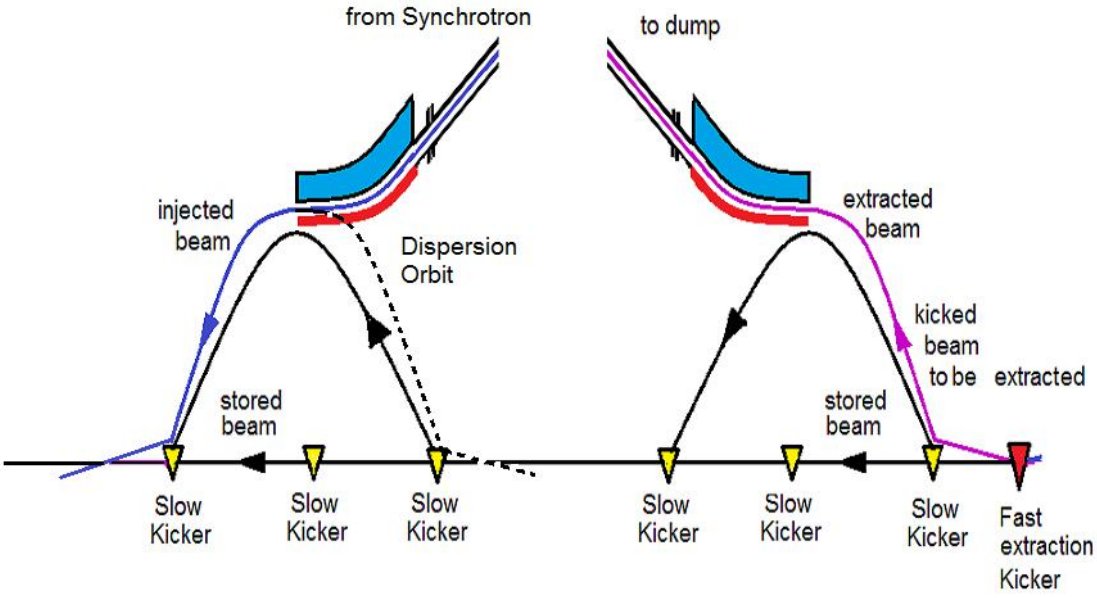

Figure 20: Electron injection and extraction scheme, based on two slow 180 degree kicker bumps, one for extraction (right hand side) and one for injection (left hand side) which bring the stored beam within three horizontal RMS beam sizes ($\sigma_x = \sqrt{(\varepsilon_x \beta_x + D_x^2 \sigma_E^2)}$ to the injection and extraction septum, respectively. The bumps rise in $13\mu sec$ (one turn around the accelerator) and return to zero during the following 13μsec. The dispersion at the injection septum is non-zero. The beam to be injected has a slightly different energy than the stored beam and the distance between the center of the stored beam and the beam to be injected equals the dispersion times the relative energy difference between stored and injected beam. This way the beam is injected in the center of horizontal phase space but off-center in the longitudinal phase space. For extraction, a fast kick is required on top of the slow bump to kick the beam into the extraction septum

2.2.11 **Hardware Systems of the eRHIC EIC**

By far the largest fraction of present day RHIC will remain unchanged for eRHIC. There are only very few technical components of the hadron storage ring which need some upgrade for eRHIC operation. These will be discussed in the following sections.

2.2.11.1 ***Hadron RF Systems***

The largest modification concerns the RF system. The hadron bunches from AGS with a bucket area of $1.6\text{eV} * \text{sec}$ will be received by the existing 28 MHz RF system which will also be used to accelerate the beam to full energy. The existing 197 MHz system is no longer needed. For maximum luminosity operation, each hadron bunch will be adiabatically split into four bunches by a two-stage beam splitting scheme. This requires two new 112.6 MHz RF cavities.

The split bunches need to be pre-compressed by a 225 MHz RF system (4 cavities) before they can be accepted in a storage cavity system with 563 MHz. These cavities will be superconducting and are identical to the electron storage ring cavities. Three 2-cell cavities will be required to squeeze the bunches to 7 cm bunch length, which requires 8 MV of RF voltage per cavity.

2.2.11.2 *Hadron Injection Kicker*

Another modification that is required is a new kicker system that is re-designed for a shorter rise time. The 28 MHz bunch frequency (bunch spacing $T_s = 35.5$ nsec) is three times larger than the present RHIC bunch frequency which requires new, faster injection kickers. The new kickers have a rise time which is three times shorter than the present injection kicker system, less than 12 nsec. The 20 kicker units have a total length of $\cong 25$ m. The new injection kickers will be placed in the straight section of IR4. The corresponding updates of the magnetic elements in IR4 are only minor.

2.2.11.3 *Hadron Collimation*

The present RHIC collimation system needs to be improved for the needs of an electron-ion collider. A two-stage system with optimized phase advance between the primary and secondary collimators like in HERA is planned. In addition, a system with non-zero dispersion for momentum collimations is foreseen. The hadron collimation system is planned to be installed in IR12.

2.2.11.4 *Copper Coating of the RHIC Beam Pipe for Hadrons*

The high peak current of the eRHIC proton beam ($\cong 200$ mA) with its large number of short, high intensity bunches results in unacceptably high heat load of the cold stainless steel beam pipes in the superconducting RHIC magnets. To reduce this heat load to levels below 1W/m, which can be compensated by the RHIC cryogenic system, the conductivity of the beam pipe has to be increased. This will be accomplished by in-situ copper coating of the entire RHIC ring.

To prevent electron cloud build-up due to the short bunch spacing the secondary electron yield (SEY) of the beam pipe surface has to be reduced below 1.2. Thorough "scrubbing" of the newly applied copper coating using a plasma discharge cleaning technique might accomplish that, but in order to reduce risk, it is also planned to apply a layer of amorphous carbon to safely reduce the SEY below the critical value.

2.2.11.5 *Electron Storage Ring Magnets*

The magnet system of the electron storage ring consists of conventional iron-dominated room temperature electro-magnets. They have hollow, water cooled conductors. The current density is below $5\mathrm{A/mm}^2$ and the magnetization of the yoke does not exceed 1.4 T. High quality magnetic steel (AISI 1006) is assumed. It is not decided at this point whether to machine yokes from solid blocks or build the yokes from fine blanked laminations.

The bending magnets in the regular FODO structure are split into three magnets, two 2.66 m long ones with field strength of up to 0.248 T and a short magnet in-between which is 0.45 m long with a maximum strength of 0.7 T. There are 252 of such triplets. Figure 21 shows a rendering of these magnets.

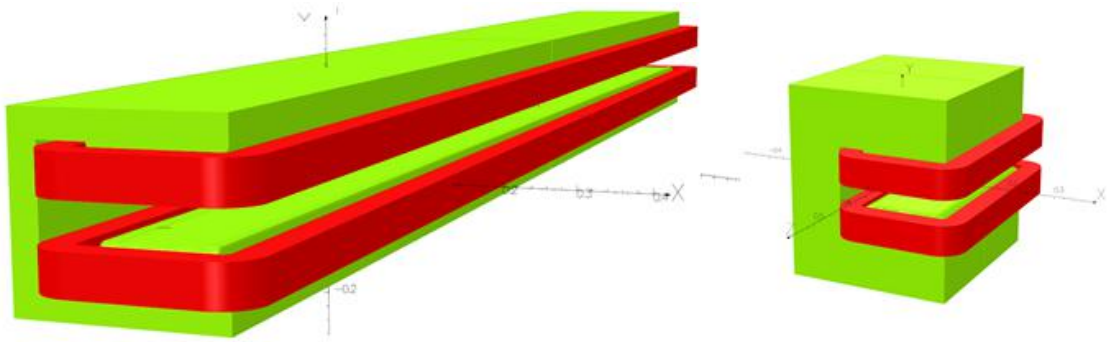

Figure 21: Short and long units of the dipole magnet triplet of the electron storage ring

The field quality of the dipoles is controlled by chamfering of the yokes which reduces the largest field harmonic (sextupole) to -1.4 units of 10^{-4} relative field error at 25 mm. This is subject to further optimization.

There are 494 conventional quadrupole magnets with a maximum field gradient of 18.4 T/m. The quadrupole magnet is 0.6 m long and its outer dimensions are 0.42 m*0.42 m. The cross section of the quadrupole is shown in Figure 22 and the cross section of the sextupole magnet is shown in Figure 23.

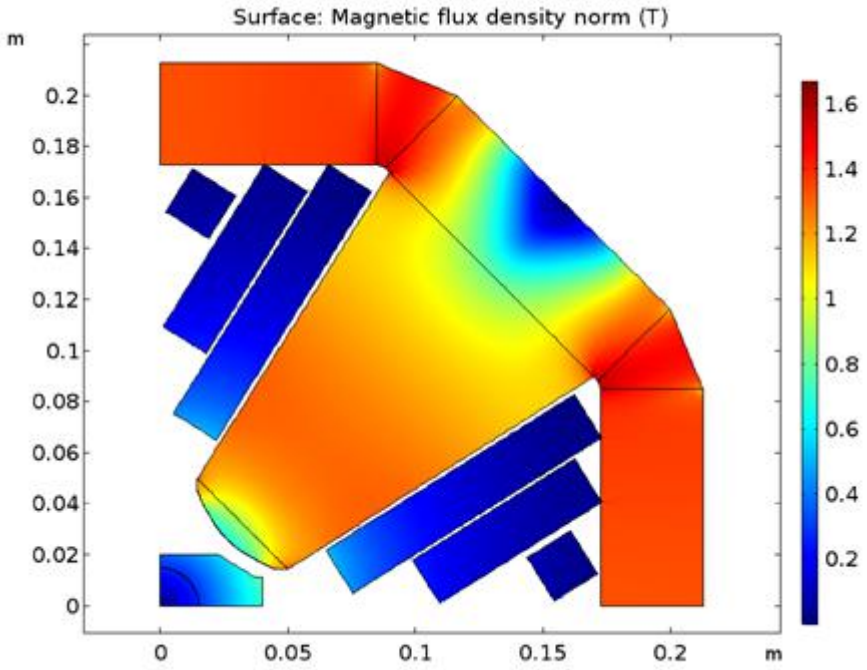

Figure 22: Cross sections of the quadrupole magnet; the color code indicates the field strength in tesla. The largest harmonic is a 12-pole component of $1.8 * 10^{-4}$ at 25 mm referring to the integrated gradient field at 25 mm which is 0.276 Tm.

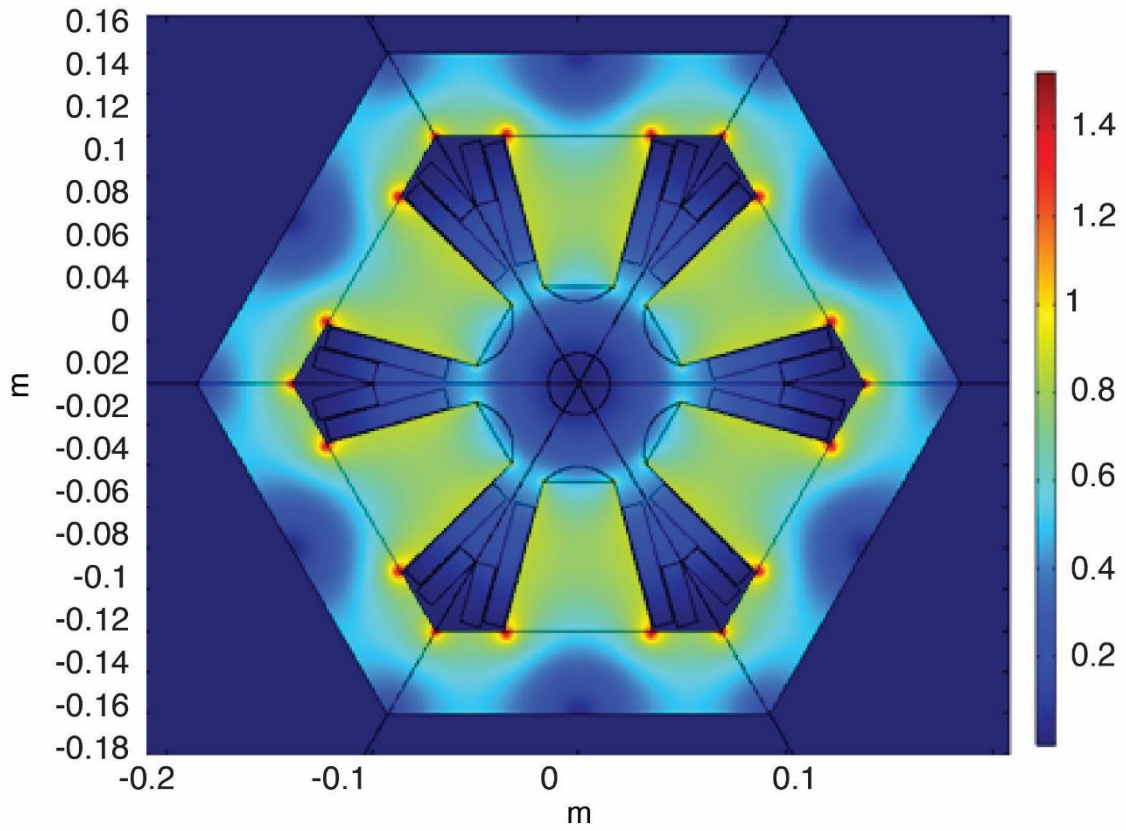

Figure 23: Cross section of the sextupole magnet; the color code indicates the field strength in tesla.

The total power consumption at the highest beam energy of 18 GeV is 3.3 MW. Figure 24 depicts the power consumption for each type of magnet versus the electron beam energy.

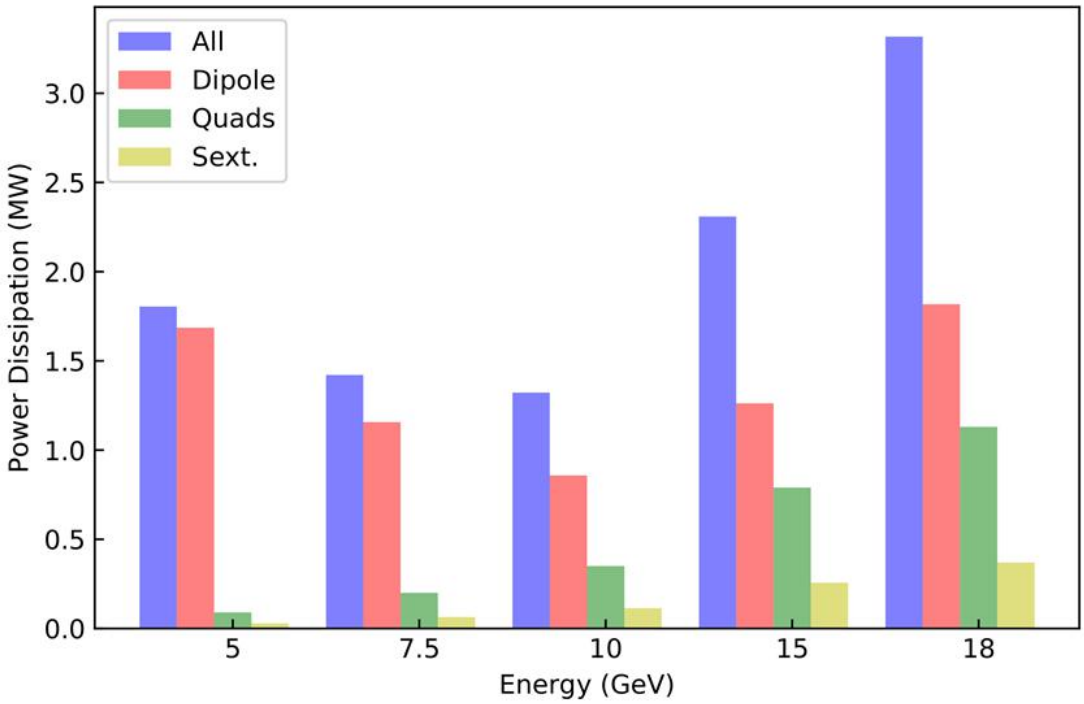

Figure 24: Power dissipation of storage ring magnets for operation energies 5 GeV to 18 GeV.

2.2.11.6 *Vacuum System of the Electron Storage Ring*

The eRHIC Storage Ring vacuum system consists of 3.8 km of vacuum chamber separated into 36 vacuum sections. Each of the arc vacuum sections is comprised of eight arc FODO cells. Each FODO cell has two 6.2 m long dipoles which are split in three parts each with a common vacuum chamber and two 1.7 m long quadrupole chambers. The quadrupole chambers accommodate the quadrupole, sextupole and corrector magnets, the beam position monitors, synchrotron radiation masks, and pump ports. The chambers are separated by RF shielded bellows.

There are also twelve vacuum sections for the 1.2 km of straight section and in addition twelve sections with specialized equipment such as interaction region, RF-sections, and beam injection/extraction. The sections are separated by gate-valves which allow one to isolate the vacuum sections from each other. The vacuum chambers are pumped by NEG-strips, NEG cartridges, titanium sublimation pumps and ion getter pumps. The vacuum system is designed for a pressure of 10 nTorr with full beam current of 2.7 *A*. The lifetime due to bremsstrahlung from scattering off the rest gas is larger than 20 hours for all beam energies from 5 to 18 GeV.

The thermal load from synchrotron radiation hitting the beam pipe is considerable. A total synchrotron radiation power of up to 10 MW is accommodated by the water cooled vacuum chamber. On average, the vacuum chamber is exposed to a linear power density of 6 kW/m if the beam energy is between 10 and 18 GeV. With the horizontal aperture of 80 mm, the emitted synchrotron radiation travels on average 5 m before it hits the vacuum chamber. With a horizontal beam emittance of ε=24 nm and an emittance ratio of $\kappa = \frac{\varepsilon_y}{\varepsilon_x} = 0.02$, the synchrotron radiation spot of the 18 GeV beam has

a beam height of 128 μm when it hits the vacuum chamber. This corresponds to an average power density of $37\frac{\mathrm{W}}{\mathrm{mm}^2}$.

A material with good heat conductivity properties has to be chosen which has at the same time good vacuum properties, good mechanical stability and will allow standard manufacturing processes such as extrusion, welding or brazing. Such a material is the Cu-Cr-Zr alloy which has a heat conductance close to that of copper and excellent manufacturability. In addition this material has excellent yield strength and is less costly than materials with comparable properties. Figure 25 shows a cross section of the vacuum chamber.

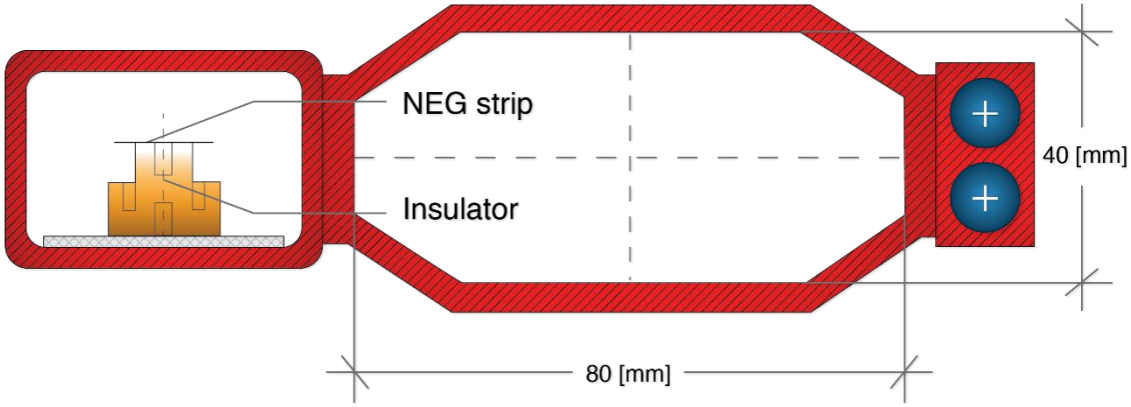

Figure 25: Cross section of storage ring vacuum chamber in dipole magnets

With a cooling water velocity of 2 m/sec, the maximum temperature on the inner surface of the dipole chamber is about 100^{o}C. Figure 26 shows the temperature distribution on the dipole chamber inner surface.

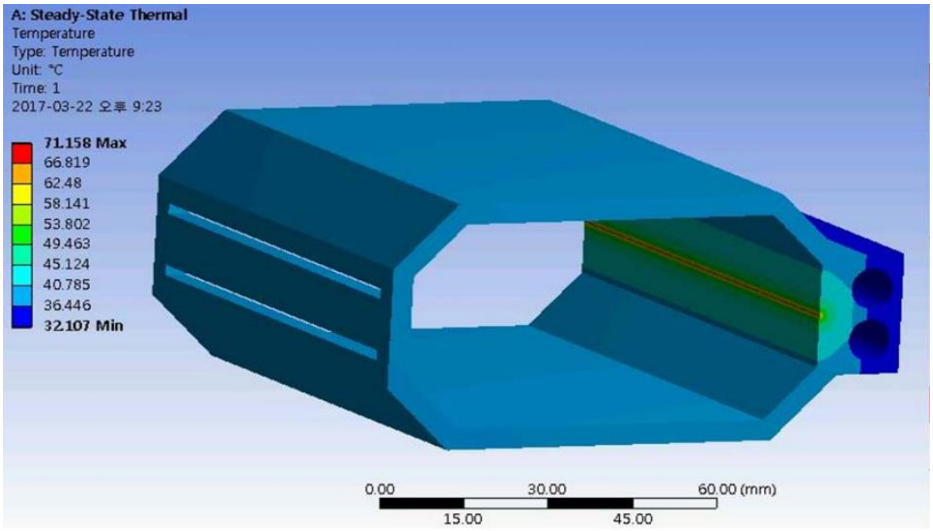

Figure 26: Analysis of the temperature distribution of the dipole chamber which is exposed to the full synchrotron radiation power

The chamber can be fabricated by extrusion. The pumping screen, flanges, and pump port will be attached to the chamber by tag welding without loss of the mechanical stability of the chamber material. The highest surface temperature is obtained at 5 GeV operation, when the center dipole is reversed in field direction and the field is increased to about twice the value for 18 GeV operation. In this case, the synchrotron radiation reaches the inside of the vacuum chamber inside the quadrupoles where the pump screen is located and where there is no cooling. The temperature reaches up to $210^{o}\mathrm{C}$ at this point.

The gas load in the vacuum chamber is dominated by desorption of molecules from the chamber wall by synchrotron radiation photons (PSD). The photon flux at 10 GeV with a beam current of 2.7 A (worst case) is $8.1 * 10^{17} * \frac{E}{\mathrm{GeV}} * \frac{I}{\mathrm{mA}} = 2 * 10^{22}\mathrm{torr} * l * \mathrm{m}^{-1} * \mathrm{s}^{-1}$. A desorption coefficient in the order of η=$1 * 10^{-6} molecules/photon$ is assumed to be achieved after some conditioning. The desorbed gas load is then $1.3 * 10^{13} molecules/(\mathrm{sec} * \mathrm{m})$ or $4 * 10^{-7}\mathrm{torr} * \frac{l}{\mathrm{sec}*\mathrm{m}}$. The linear pumping speed is designed to be $100\, l/(\mathrm{sec} * \mathrm{m})$ which results in a pressure of 4 nTorr. This capacity is achieved by pumping slots which cover 10% of the surface of the pump screen corresponding to a conductance of $200\frac{l}{\mathrm{sec}*\mathrm{m}}$. Near the location of the quadrupole magnets, large lumped NEG cartridges and ion getter pumps are foreseen.

Due to the large beam currents, the RF-shielded bellows are a very critical element of the vacuum system design. The eRHIC design adapts the design which has been produced for the NSLS-II storage ring. The thermal contact of the sleeves is accomplished by fingers on the outside (see Figure 27). The NSLS-II design has shorter and wider fingers compared to the bellows designed for the Advanced Photon Source which minimizes the gaps in-between fingers and therefore avoids heating of the fingers by RF power leaking through the gaps.

Another critical element of the vacuum design is the RF seal of flange connections. The pre-conceptual design choice is to use soft RF springs. These require careful assembly and alignment to avoid steps and discontinuities in the vacuum chamber which would lead to considerable impedance and beam heating.

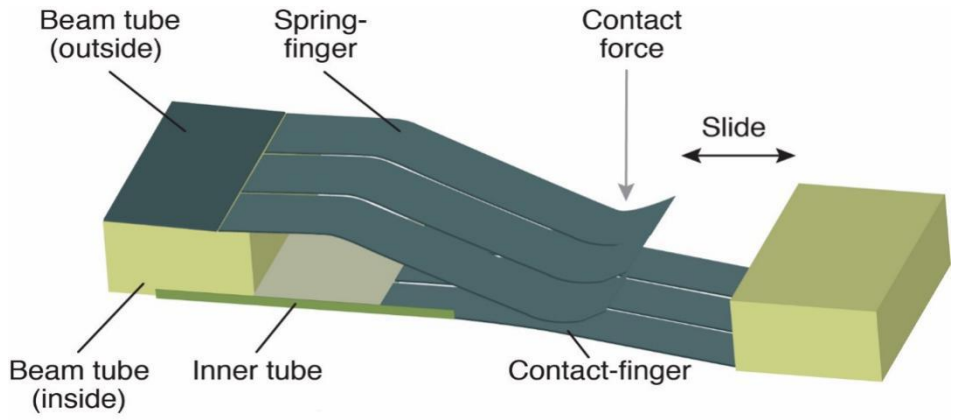

Figure 27: Schematic view of the bellow-finger concept

2.2.11.7 *RF System of Electron Storage Ring-Overview*

One limitation of the luminosity of the eRHIC electron-ion collider is the synchrotron radiation loss in the electron storage ring. The RF power needed to replace the synchrotron radiation losses of the high current electron beam with beam currents of up to 2.7 *A* and a beam energy of 10 GeV is 10 MW and requires an RF voltage of about 72 MV. The RF system is also the most costly hardware sub-system of the electron complex of eRHIC and its components need to be carefully optimized from both performance and cost point of view in the earliest stage of the design. Table 13 summarizes some relevant input parameters which determine the RF System.

Table 13: Summary of the eRHIC RF system requirements for 10GeV and 18GeV operations.

Parameter	*10GeV*	*18GeV*
Beam current [A]	2.7	0.27
Energy loss per turn [MeV]	3.7	37
Synchrotron radiation power [MW]	10	10
Required RF voltage [MV]	41	63

The choice of the electron cavities is based on superconducting RF resonators. The reasons for choosing superconducting RF cavities are as follow:

- Operational cost saving. For 18 GeV operation, the total power which would be required to generate the voltage of 63 MV in a normal-conducting cavity with typically $10\ \mathrm{M\Omega/m}$ shunt impedance and a maximum voltage of 2 MV/m would be approximately 12 MW. This is a large additional RF power which would have to be installed and operated. The additional power is much larger than the cryogenic power of 240 kW required to keep the cavities at 4 K. The additional RF installation would cost significantly more than the difference in cost for normal- and superconducting cavities.
- Superconducting cavities have a much higher (factor 9) stored field energy and are much better suited to handle heavy beam loading conditions.
- The impedances which drive coupled bunch instabilities are much lower than they would be for a normal-conducting cavity system with the same RF voltage.
- Because of the high gradient of superconducting cavities (8 MV/m vs. 2 MV/m for normal-conducting cavities), the superconducting cavities require less longitudinal space than normal conducting cavities.
- The disadvantage of superconducting cavities is their dependence on liquid He cooling and a more intricate protection system.

Superconducting RF systems are used in most light sources, as well as in KEKB and SuperKEKB. Technical solutions for such cavity systems based on single-cell 500 MHz resonators exist. The designs are mature and the systems are in principle commercially available. The available systems are, however, not optimized for high energy beam applications such as eRHIC. While the systems would work technically, the solution would not be optimum from a cost point of view. The eRHIC storage ring RF system is based on a dedicated and optimized concept of superconducting cavities:

- 2-cell 563 MHz cavities are designed for a more compact and cost effective RF structure.
- We developed a variable coupling, high power input coupler to run the system in various scenarios with optimized parameters for each beam energy and beam current.
- Novel RF power stations based on multiple IOT RF tubes lead to a cost effective design and require a relatively small footprint.

These design concepts lead to the parameters referenced in Table 14.

Table 14: Parameters of the eRHIC RF system.

Parameter	*Value*
RF frequency [MHz]	563
Number of cavity-cells per cryostat	2
Number of cryostats	16
Accelerating gradient [MV/m]	8
Maximum RF voltage [MV]	63
Maximum power per input coupler [kW]	500
Number of input couplers per cryomodule	2
Maximum RF output power [MW]	14
Number of RF transmitter stations	32
HOM power per cryomodule [kW]	28
HOM coupler type	Beam-pipe SiC
Beam pipe absorbers per cryostat	4

2.2.11.8 *Superconducting RF Cavities*

One 2-cell 563 MHz cavity is installed in each cryostat. The cavity shape has been optimized to suppress parasitic modes to the extent that the coupled bunch instabilities which are associated with the residual higher order modes (HOMs) can be safely controlled by a multi-bunch damper system. The broad-band impedance of the cavity structure is sufficiently low so there is no issue with single bunch instabilities. The cavity shape is depicted in Figure 28 and the higher order mode structure is shown in Figure 29.

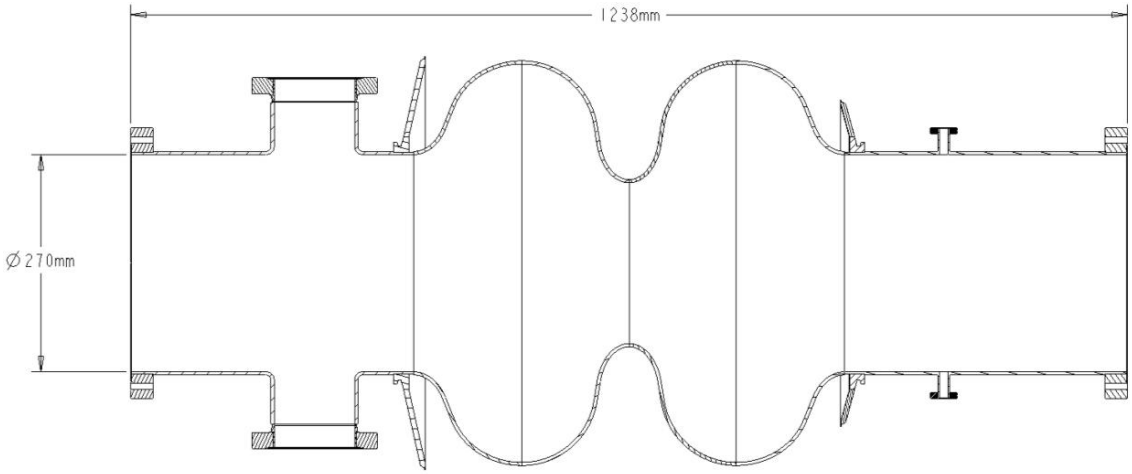

Figure 28: Optimized shape of the 2-cell 563 MHz superconducting cavity for eRHIC

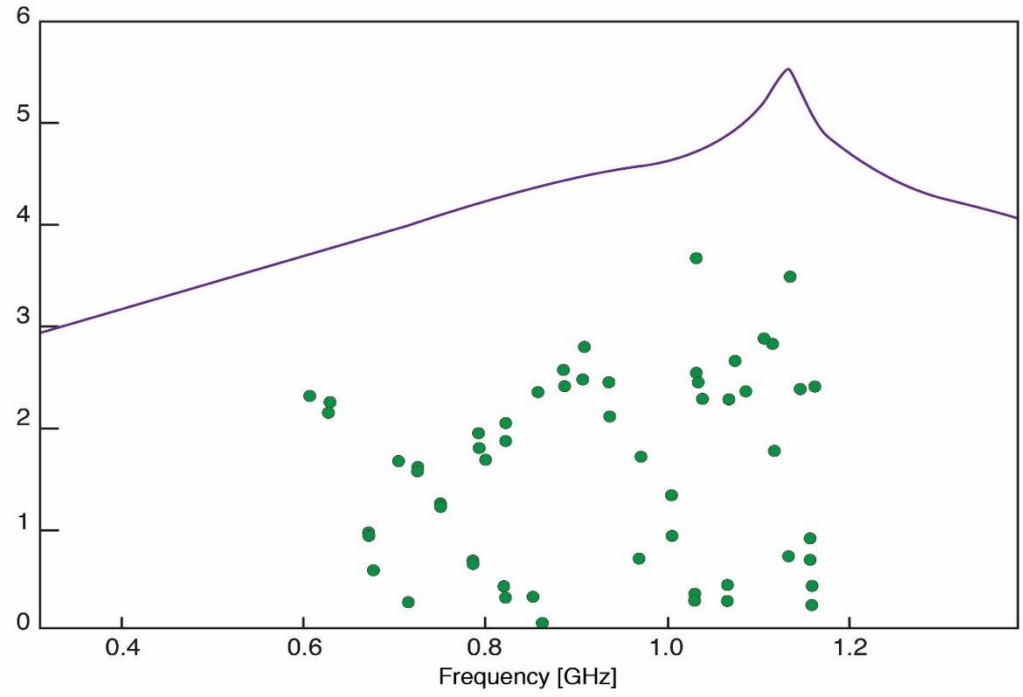

Figure 29: Longitudinal impedance of a single 2-cell cavity. The solid line is a Lorentzian fit of the envelope function; the dots are calculated using the code URMEL [25]. The vertical axis is impedance in units of kΩ .

Strong damping of higher order parasitic modes is important to achieve robust beam stability and to limit the required power of the broad-band damper system which actively stabilizes the beam. The choice made in the design of the eRHIC RF design is

to use beam-pipe type HOM dampers consisting of three well-cooled SiC sections of beam pipe
adjacent to each cavity. The SuperKEKB design [26] is adapted. Figure 30 depicts the RHIC SiC damper. Figure 31 shows a rendering of the new RF cavity design.

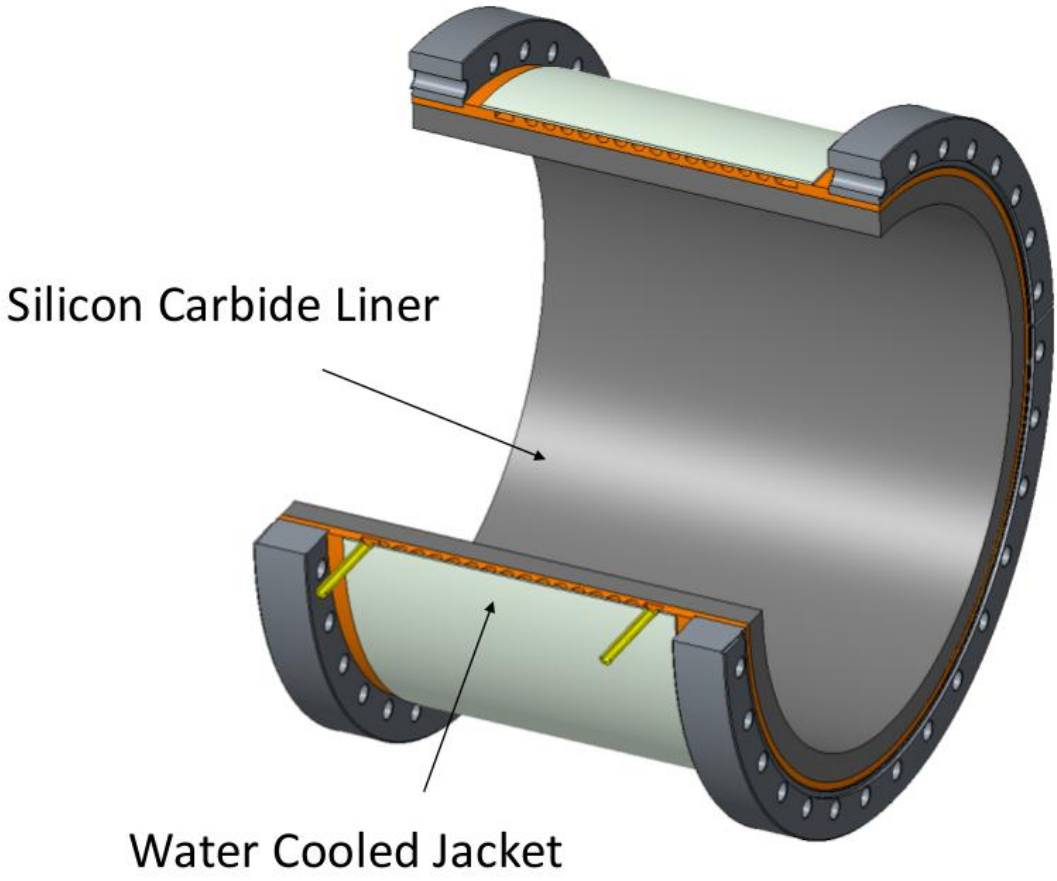

Figure 30: CAD model of the eRHIC SiC HOM damper (KEKB design)

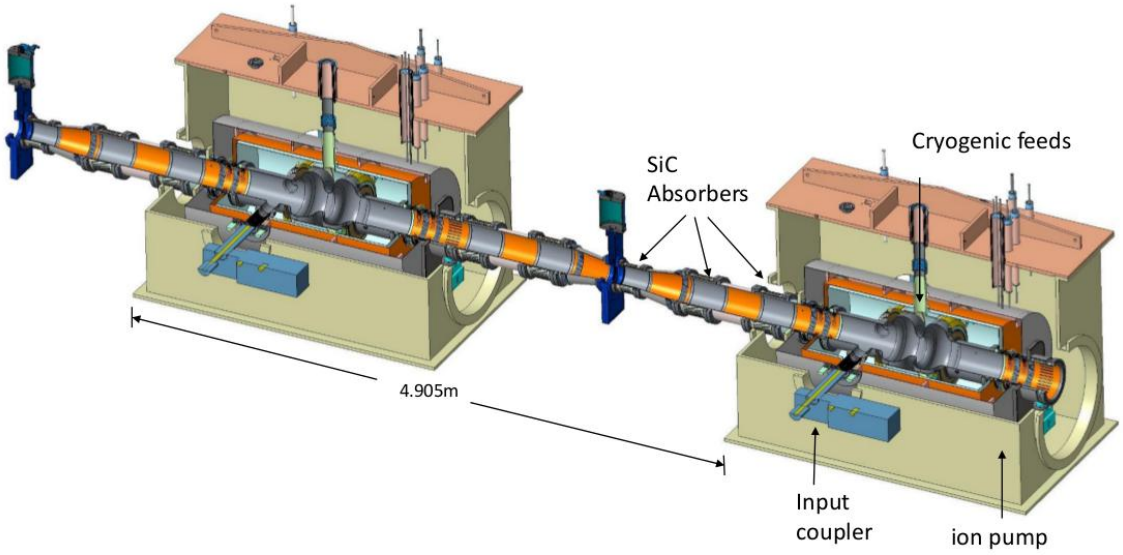

Figure 31: Rendering of the eRHIC two-cell superconducting cavity in a string of cryostats. Shown are two cryostats, each with a length of 4.0 m including the adjacent drift spaces with three SiC beam pipe absorbers, a taper and gate valves. Also shown are the cryogenic feeds and the RF input coupler. The cavity is enclosed in its liquid He tank

2.2.11.9 *High Power RF Input Complex*

The power capability of the fundamental power input coupler (FPC) is an important parameter for the layout of the RF system, since it determines the minimum number of cryomodules needed to feed 10 MW RF power to the beam. The choice was made to employ two 500 kW power couplers in each cryostat. Such a coupler had been designed and successfully tested with 500 kW for the superconducting photon gun developed at BNL. The eRHIC fundamental power coupler with two 500 kW arms is a development of this high power FPC.

The operation at different electron beam current and beam energies requires an optimized coupling of the superconducting cavities to their power source in order to avoid a large amount of reflected RF power. The optimum coupling is a function of the beam current, the synchronous phase, the shunt impedance, the power loss of the beam, and the cavity voltage. Figure 32 shows a CAD model of the eRHIC variable coupling high power input coupler.

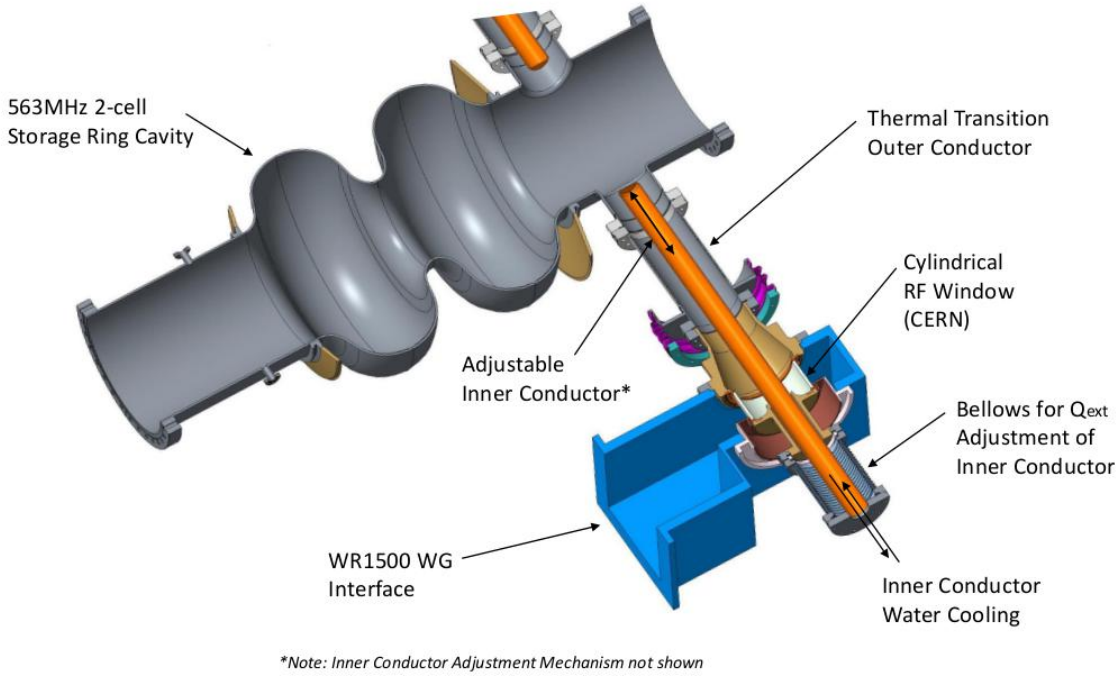

Figure 32: CAD model of the eRHIC 1 MW variable coupling double forward power coupler. Note that only one of the two 500 kW couplers is shown

2.2.11.10 *Electron Storage Ring RF Power Supply*

The RF power source of the eRHIC electron storage ring which has to deliver 10 MW of power to the beam is based on multi-IOT transmitters that can each generate 1 MW of RF power. The very large beam currents of the eRHIC electron storage ring with ion-clearing gaps in the bunch train cause substantial transient beam loading effects. The RF system has to provide a power margin of 15% to be able to control the RF voltage. The eRHIC collider will be operated with multi-purpose FPGA based cavity controller electronics which are designed to handle the large beam loading.

2.2.11.11 *Crab Cavities*

The eRHIC crab cavities, designed to operate at a frequency of 338 MHz, will be realized as superconducting Double Quarter Wave Crab Cavities (DQWCC). This cavity type, designed and developed at BNL for the LHC luminosity upgrade, has gone through a rigorous development program. The frequency of the LHC DQWCC devices is 400 MHz, conveniently close to the eRHIC DQWCC frequency, and thus serving to validate the expected performance of the eRHIC DQWCC.

At this time, a total of five LHC-style DQWCC have been built and tested with exceptionally good results: A proof-of-principle cavity built by Niowave Inc. for the BNL team and tested at BNL, two prototype cavities, designed by BNL, built by Niowave through a LARP program and tested at Jefferson Laboratory, and two prototype cavities of the same design built and tested at CERN. The BNL crab cavity team has been an active contributor to all the tests at JLab and CERN.

While the superconducting crab cavity is the most critical element of the crabbing system, there are many other auxiliary subsystems which are challenging and critical for

the proper crabbing of the beam. These subsystems, which will be described in detail in this document, include the liquid helium tank, HOM dampers, fundamental power and pickup couplers, mechanical cavity frequency tuner (comprising the dressed cavity, seen in Figure 33), as well as the crab cavity cryomodule. At this point all the subsystems mentioned have been built and successfully tested for the LHC DQWCC, and designed for the eRHIC DQWCC, using lessons learned from the LHC devices.

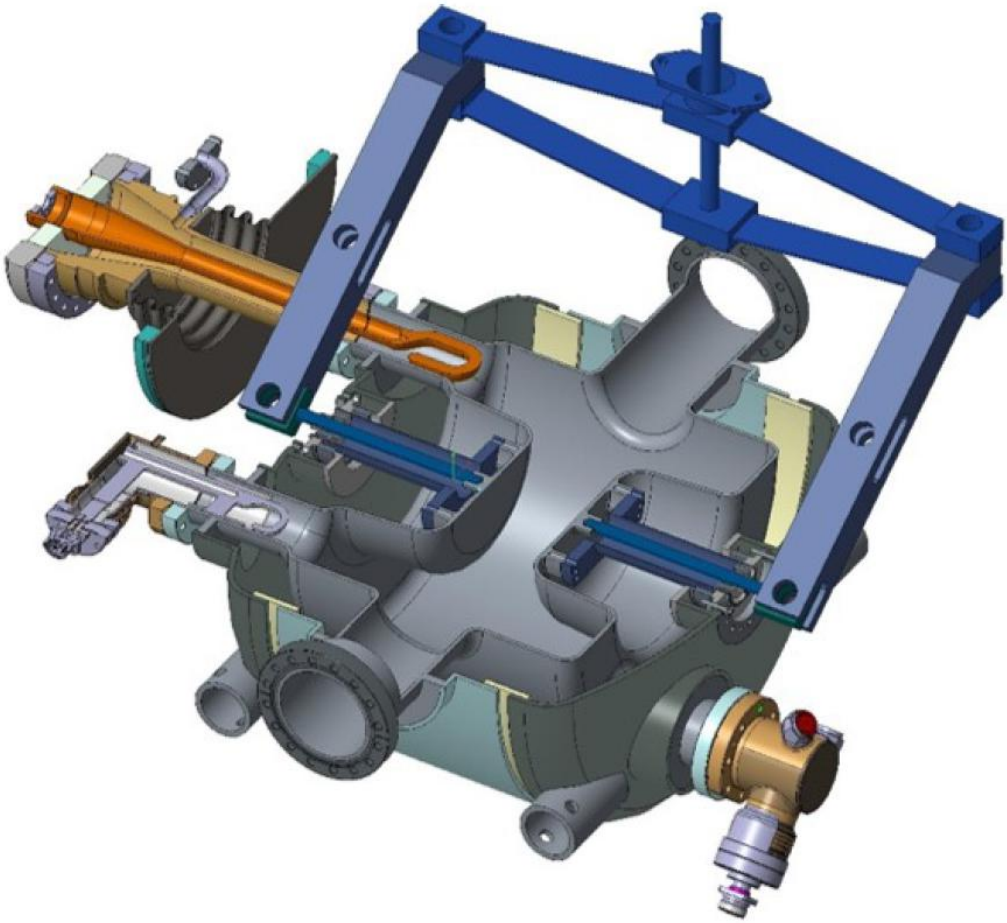

Figure 33: Cross section view of the eRHIC DQWCC showing the dressed cavity, with helium tank, couplers and tuner

The ultimate test of any accelerator cavity is its performance in the presence of beam. This is particularly true for hadron crab cavities, since there has never been any implementation of crab cavities in hadron accelerators. For this reason, a complete system, including two fully dressed DQWCC with all the couplers and tuners in a cryomodule, has been installed at CERN in the SPS accelerator, as can be seen in Figure 34 Beam tests are underway, with active participation of BNL staff.

Figure 34: The LHC prototype twin DQWCC cryomodule installed in the SPS tunnel for beam tests.

2.2.12 **Civil Construction and Infrastructure**

A major advantage of the eRHIC proposal is that only a modest amount of new buildings is required. At the present stage of the design, it is necessary to provide an industrial building at IR10 to house RF power sources for the electron storage ring and the rapid cycling synchrotron. A new building is also required for a 50 MeV superconducting LINAC which drives the electron cooling beam. The cryogenic capacity of the RHIC refrigerator is sufficient. However, at this point, the operation of the storage ring with 2 K liquid He is not excluded, which would allow a proton energy increase to 300 GeV. This choice would imply the necessity of a cold-compressor system in IR10 and IR4, respectively. The operation of RHIC does not require a large water cooling capacity whereas eRHIC operation requires cooling for the storage ring vacuum chamber with a capacity of 10 MW and for cooling room temperature magnets with a capacity of 7 MW.

The HVAC system in the RHIC tunnel requires a major upgrade in order to achieve thermal stability of stands and girders of the eRHIC magnet system.

2.2.13 **Summary**

The eRHIC collider as described provides collisions of electron and hadron beams stored in two storage rings, the Yellow ring of the Relativistic Heavy Ion Collider (RHIC) and a new electron storage ring, with high luminosity of $0 = 10^{34}\mathrm{cm}^{-2}\mathrm{sec}^{-1}$ over a center-of-mass energy range from 29 GeV to 140 GeV. The technical solution is based on accelerator physics and technology that is a moderate extrapolation of the state of the art. The required modifications of RHIC are few and relatively inexpensive on the scale of the entire project.

The challenge of the design lies in its implementation into an existing tunnel with existing infrastructure at a reasonable cost, which will require very detailed planning. The final factor of two to three in luminosity requires strong hadron cooling which will be realized by a novel scheme or by substantial extrapolation of existing technology. The main mitigation of the corresponding technical risk lies in the fact that a very respectable luminosity of up to $4.4 * 10^{33}\mathrm{cm}^{-2}\mathrm{sec}^{-1}$ can be achieved without strong hadron cooling, a performance which would provide full access to the entire EIC physics program.

The electron injector complex consists of a polarized electron gun and 400 MeV S-band LINAC which will provide polarized electron bunches of 10 nC to the rapid cycling synchrotron in the RHIC tunnel. This large synchrotron is to be constructed with normal-conducting magnets and normal-conducting RF systems. The critical requirement is high spin transparency for the polarized beam. This has been taken into account by special design features and has been tested by extensive simulations.

The anticipated performance of the collider has been addressed by a comprehensive accelerator physics design study. The design facilitates two large-solid-angle detectors utilizing the existing experimental areas now occupied by the RHIC detectors STAR and PHENIX/sPHENIX. Final parameters are chosen such that there is still a margin between the design values and values believed achievable. In that sense, the presented solution should be considered as robust and realistically achievable. While there are no components which require completely new technical concepts, several components are at state-of-the-art or slightly beyond present technology. The list of these components includes special superconducting magnets in the interaction regions with very large apertures and with active magnetic shielding. Other advanced components are 2-cell superconducting cavities with 1 MW of input power and variable coupling of the forward power couplers. Strong hadron cooling requires a CW electron source which can deliver reliably 100 mA of beam current.

2.2.14 **References**

1. D. Kayran et al., Proof-of-Principle Experiment for FEL-based Coherent Electron Cooling, Conf. Proc., C110328:2064-2066
2. A. A. Sokolov and I. M Ternov, Polarization and spin effects in the theory of synchrotron radiation, Doklady Akademii Nauk SSSr (USSR), English translation currently published in a number of subject-oriented journals, 153, 1963
3. E. C. Aschenauer et al., eRHIC Design Study: an Electron-Ion Collider at BNL, 2014. arXiv:1409.1633
4. A. Accardi et al., Electron Ion Collider: The Next QCD Frontier, Eur. Phys. J., A52(9):268, 2016. arXiv:1212.1701, doi:10.1140/epja/i2016-16268-9
5. N. Toge, KEK B-Factory Design Report, Technical report, 1995
6. PEP-II: An Asymmetric B-Factory. Conceptual Design Report. June 1993
7. V. N. Litvinenko and Y. S. Derbenev, Coherent Electron Cooling. Phys. Rev. Lett. 102:114801, 2009. Doi:10.1103/PhysRevlett.102.114801
8. K. Ohmi, Simulation of beam-beam effects in a circular e^+e^- collider. Phys. Rev. E62:7287-7294, 2000. Doi:10.1103/PhysRevE.62.7287
9. J. Qiang, M. A. Furman, and R. D. Ryne, A parallel particle-in-cell model for

beam-beam interacton in high energy ring colliders. J. Comput. Phys., 198:278-294, 2004. doi:10.1016/j.jcp.2004.01.008
10. B. Parker et al., Compact superconducting final focus magnet options for the ILC. Conf. Proc., C0505161:1569, 2005
11. V. Ptitsin and Yu. M. Shatunov, Helical spin rotators and snakes. Nucl. Instrum. Meth., A398:126-130, 1997. doi:10.1016/S0168-9002(97)00683-9
12. I. Alekseev et al., Polarized proton collider at RHIC. Nucl. Instrum. Meth., A499:392-414, 2003. doi:10.1016/So168-9002(02)01946-0
13. D. P. Barber et al., The first achievement of longitudinal spin polarization in a high-energy electron storage ring. Phys. Lett., B343:436-443, 1995. doi:10.1016/0370-2693(94)01465-0
14. Yuri Shatunov and Vadim Ptitsin, Siberian Snkes for electron Storage Rings. Conf. Proc., C970512:3500, 1997
15. I. Borchardt, E. Karantzoulis, H. Mais, and G. Ripken, Calculation of Beam Envelopes in Storage rings and Transport Systems in the Presence of Transverse Space Charge Effects and Coupling, Z. Phys., C39:339, 1988
16. D. P. Barber et al., Longitudinal Positron Polarisation in HERA-II. In 9th European Particle Accelerator Conference (EPAC2004), Lucerne, Switzerland, July 5-9, 2004. URL: http://accelconf.web.cern.ch/AccelConf/e04/PAPERS/MOPLT044.PDF
17. Y. S. Derbenev and A. M. Kondratenko, Diffusion of particle spins in storage elements. Sov. Phys. JETP,35:230, 1972
18. R. Assmann et al., Deterministic harmonic spin matching in LEP. Conf. Proc., C940627:932-934, 1994
19. J. Laskar et al., The measure of chaos by the numerical analysis of the fundamental frequencies. Application to the standard mapping. Physica, D56:253-269, 1992. doi:10.1016/0167-2789(92)90028-L
20. M. Blaskiewicz, A multipurpose coherent instability simulation code. In: particle Accelerator Conference (PAC 2007), p. 3690-3692, 2007
21. O. S. Bruning et al., Electron cloud and beam scrubbing in the LHC. In Proc. 1999 Particle Accelerator Conference (PAC'99), New York, New York, March 29-April 2, 1999. P. 2629-2631, 1999. URL: http://accelconf.web.cern.ch/AccelConf/p99/PAPERS/THA6.PDF
22. M. Blaskiewicz and U. Iriso, How to use CSEC. Technical report, Brookhaven National Laboratory (BNL) Relativistic Heavy Ion Collider, 2006
23. A. Piwinski, Intra-beam Scattering. In proc. 9th International Conference on High-Energy Accelerators (HEACC 1974), Stanford, CA, May 2-7, 1974, p. 405-409, 1974
24. D. Ratner, Microbunched Electron Cooling for High Energy Hadron Beams. Phys. Rev. Lett., 111(8):084802, 2013. doi:10.1103/PhysRevLett.111.084802
www.cst.com
25. T. Tajima et al., Development of HOM damper for B-Factory (KEKB) superconducting cavities. Conf. Proc., C950501:1620-1622, 1996
26. V.N. Baier, V.M. Katkov, V.M. Strakhovenko, Sov. Phys. JETP. 31 (1970) 908
27. J. Kewisch, Computation Of Electron Spin Polarization In Storag Rings, Proceedings, Europhysics Conference, Berlin, Germany, September 20-23, 1983, 249-254, 1985.
28. L. H. Thomas, "The Kinematics of an electron with an axis," Phil. Mag. 3, 1–21

(1927).
29. V. Bargmann, L. Michel, and V. L. Telegdi, Phys. Rev. Lett. 2, 435–436 (1959).
30. D.P. Barber et al., High spin polarization at the HERA Electron Storage Ring, Nucl. Instrum. Methods A **338**, 166-184 (1994).

2.3 JLEIC – A Polarized Electron-Ion Collider at Jefferson Lab

JLEIC Design Study Collaboration
(Edited by Todd Satogata and Yuhong Zhang)
Thomas Jefferson National Accelerator Facility, Newport News, Virginia, USA
Mail to: satogata@jlab.org and yzhang@jlab.org (editors)

2.3.1 Introduction

Todd Satogata and Yuhong Zhang
Thomas Jefferson National Accelerator Facility, Newport News, Virginia, USA
Mail to: satogata@jlab.org and yzhang@jlab.org

Modern nuclear physics has led to the development of Quantum Chromo-Dynamics (QCD), a theory describing strong interactions among quarks and leptons, and gluons as the carriers of the strong force. Understanding these interactions as well as the emergent properties of nucleons and nuclei from these interactions is the compelling goal of nuclear science. A polarized electron-ion collider (EIC) has long been envisioned as a gluon microscopy for exploring the QCD frontier. To meet this science need, Jefferson Lab has proposed JLEIC, a high luminosity high polarization EIC based on the CEBAF electron SRF linac. The JLEIC design was driven by the science program summarized in an EIC white paper [1], and significant design studies and accelerator R&D has been pursued and achieved over the last 16 years. In the following, a set of articles are collected to describe the JLEIC design and to report progress of the related accelerator R&D. The topics covered by these articles are ion sources, polarized electron source, polarization of electron and proton/light ion beams, electron cooling and high energy ERL cooler, beam-beam and other collective beam physics, ion ring magnets, interaction region design and special magnets.

During the last 6 years, two comprehensive reports [2,3] were produced on 2012 and 2015 respectively for summarizing the JLEIC design and accelerator R&D progress. It should also be mentioned that the JLEIC electron-ion collider design study was also reported and reviewed in the two early issues (April, 2003 and August, 2012) of the ICFA Beam Dynamics Newsletter. Presently, the JLEIC collaboration is writing a pre-Conceptual design report (CDR) [4] which is targeted for a public release at the end of October, 2018.

We would like to take this opportunity to acknowledge the valuable contributions by members of Jefferson Lab JLEIC accelerator design team and many external collaborators. These collaborators are from many US and international institutions which are listed below: Argonne National Laboratory, Brookhaven National Laboratory, Fermi National Laboratory, Lawrence Berkeley National Laboratory, SLAC National Accelerator Laboratory, Michigan State University, Northern Illinois University, Old Domino University, Texas A&M University, Muons Incorporated, Radiasoft LLC,

Tech-X Corporation, DESY, Sci. & Tech. Laboratory Zaryad, Moscow Institute of Physics and Technology, and Institute of Modern Physics of China.

1. A. Accardi, et al. "Electron-Ion Collider: The Next QCD frontier Understanding the glue that binds us all", Eur. Phys. J. A (2016) 52: 268
2. S. Abeyratne, et al. "Science Requirements and Conceptual Design for a Polarized Medium Energy Electron-Ion Collider at Jefferson Lab", edited by Y. Zhang and J. Bisognano (2012) https://arxiv.org/abs/1209.0757
3. S. Abeyratne, et al. "MEIC Design Summary", https://arxiv.org/abs/1504.07961 (2015)
4. "JLEIC Pre-CDR", edited by T. Satogata and R. Yoshida, (2018)

2.3.2 JLEIC Design Overview

Yaroslav Derbenev, Todd Satogata and Yuhong Zhang
Thomas Jefferson National Accelerator Facility, Newport News, Virginia, USA
Mail to: derbenev@jlab.org, satogata@jlab.org and yzhang@jlab.org

2.3.2.1 *JLEIC Baseline*

JLEIC is designed to meet the following requirements of the EIC science program [1]

- *Energy:* the range of CM energy is 20 to ~70 GeV; thus energies of the colliding beams range is 3 to 12 GeV for electrons, 30 to 100 GeV for protons, and up to 40 GeV per nucleon for ions.
- *Ion species:* polarized proton, deuteron, and helium-3; light to heavy ions up to lead ion are desirable but not polarized; all ions are fully stripped at collisions.
- *Detector:* JLEIC should be able to accommodate two detectors; both of them support full acceptance of particle detection;
- *Luminosity:* in a range of 10^{33} to above 10^{34} $cm^{-2}s^{-1}$ per IP for both *e-p* and *e-A* collisions; it should be optimized around 45 GeV CM energy.
- *Polarization:* JLEIC must deliver higher than 70% polarization in longitudinal direction at IPs for both electron and light-ion beams, and also in transverse direction at IPs for light ion beams only; spin-flip of both beams is extremely desirable.
- *Upgrade:* JLEIC accelerator design should include an option of future energy upgrade for reaching higher CM energy up to 140 GeV.

JLEIC is designed to take advantage of CEBAF at Jefferson Lab to provide an electron beam for JLEIC. This electron SRF linac was successfully upgraded recently to 12 GeV for driving a fixed target nuclear science program.

JLEIC will be a ring-ring collider, namely, both colliding electron and ion beams are stored in two figure-8 shaped rings as shown in Figure 1.2.1 [2,3,4]. The electron collider ring is made of normal conducting magnets and stores an electron beam of 3 to 12 GeV energy and up to 3 A averaged current. CEBAF SRF linac now serves as a full-energy injector into the electron ring, requires no upgrade for energy, beam current or polarization. The ion collider ring is made of SC magnets and stores a proton beam of 30 to 100 GeV energy or an all-striped light to heavy ion beam of up to 40 GeV/u energy. The two collider rings are stacked vertically and have nearly identical

circumferences of approximately 2.25 km, thus housed in the same tunnel next to CEBAF. The electrons execute a vertical excursion in the long straight of figure-8 ring to the plane of the ion ring to realize electron-ion collisions. The figure-8 crossing angle is 77.4º. The rings intersect at one point in each of two long straights and thus can accommodate two detectors. The two long straights also accommodate other machine components, among them, injection/ejection, RF system, electron cooler and polarimetry.

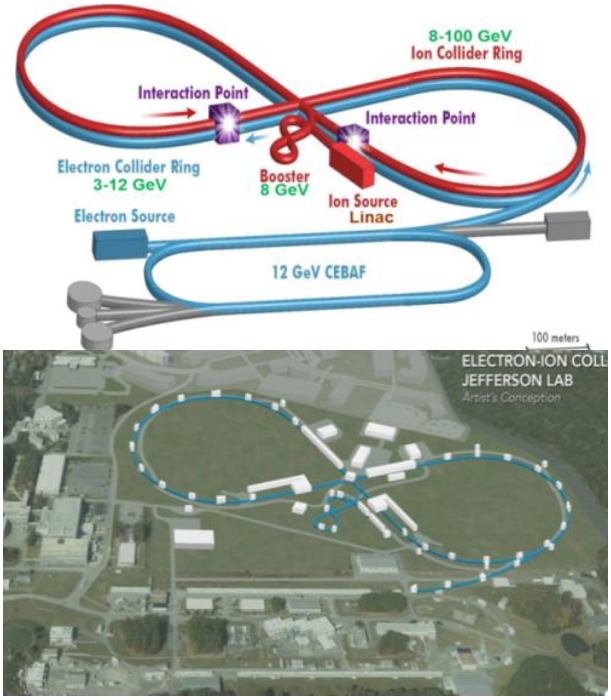

Figure 1.2.1: A schematic drawing of JLEIC (left) and JLEIC in the Jefferson Lab site

The unique figure-8 shape of the JLEIC collider rings was chosen for an optimization of preservation of ion polarization during acceleration in the booster and collider rings as well as during beam store. The idea behind a figure-8 ring design concept [6] is very simple: spin precessions in the left and right arc of a figure-8 ring are exactly cancelled, thus the net spin tune in the ring is zero which is energy independent. The spin tune can be further moved away from zero by spin rotators of very low magnetic field. A figure-8 ring design also provides the only practical solution in the medium energy range to accelerate and store a polarized deuteron beam given the present accelerator technology.

JLEIC takes advantage of two design features for delivering high luminosities: a highly polarized electron beam with up to 1.497 GHz bunch repetition rate from CEBAF and a new ion complex based on modern technology. In particular, this new green field ion complex which consist an ion injector and a collider ring can be designed to deliver colliding ion beams that match phase-space structure and high bunch repetition rate of the colliding electron beam for implementing a novel luminosity scheme. As shown in Figure 1.2.1, the ion injector consists of sources for polarized protons and light ions, and non-polarized light to heavy ions; a 285 MeV linac with a RFQ and a warm DTL-type apparatus followed by a SRF linac section; a compact booster ring also in a figure-8 shape and with an extraction energy of 7.9 GeV for proton and corresponding energies for partially stripped heavy ions.

By using CEBAF SRF linac as a full-energy injector, the filling time of the electron collider ring is short. Thus the stored beam in the electron ring can be quickly replaced whenever necessary, for example, when the beam emittance or polarization in particular becomes unsatisfactory to the science program. CEBAF can operate in a top-off mode to maintain current of the stored beam or continuously inject very small number of electrons into the ring to maintain high polarization. It should be noted the ring-ring collider design also enables collisions of polarized positrons to ions since the CEBAF linac can accelerate positrons as efficiently as electrons. The luminosity of positron-ion collisions may be relatively lower due to usually low current from a typical polarized positron source.

The JLEIC nominal parameters at representative low, medium and high CM energy design points are summarized in Table 1.2.1. The luminosity at these design points are all above 10^{33} $cm^{-2}s^{-1}$ for a full-acceptance detector, with the highest one reaching 2.1×10^{34} $cm^{-2}s^{-1}$ at the medium CM energy. To support such exceptional detection acceptance capability, the detector space (distance from an IP to the front face of the first final focusing quadrupole, FFQ) must be 7 m on the downstream side of the ion beam, however, the distance can be shortened to 3.5 m on the upstream side. For the electron beam, the FFQ magnets can be placed much closer to IPs, at 3.2 m and 3 m on the upstream and downstream respectively.

Table 1.2.1: JLEIC *e-p* design parameters

CM energy	GeV	21.9		44.7		63.3	
		p	E	P	e	P	E
Beam energy	GeV	40	3	100	5	100	10
Collision frequency	MHz	476		476		476	
Particles per bunch	10^{10}	0.98	3.7	0.98	3.7	0.98	0.93
Beam current	A	0.75	2.8	0.75	2.8	0.75	0.71
Polarization	%	>80	~80	>80	>80	>80	>80
RMS bunch length	cm	1	1	1	1	1	1
Normalized emittance	μm rad	0.3/0.3	24/24	0.5/0.1	54/11	0.9/0.18	432/86
Beta-star, hori./vert.	cm	8/8	13.5/13.5	6/1.2	5.1/1	10.5/2.1	4/0.8
Vertical beam-beam		0.015	0.092	0.015	0.068	0.002	0.009
Laslett tune-shift		0.06	Small	0.055	Small	0.03	Small
Detector space, up/dn	m	3.6/7	3.2/2	3.6/7	3.2/2	3.6/7	3.2/2
Hour glass		1		0.87		0.86	
Luminosity/IP, 10^{33}	$cm^{-2}s^{-1}$	2.5		21.4		1.7	

Presently, as a measure of the project cost reduction, JLEIC will reuse equipment of the decommissioned PEP-II *e*+*e*- collider including the RF power sources for the JLEIC electron collider ring and the magnets for transport beamline from CEBAF to the collider ring. This dictates the JLEIC bunch frequency to be 476 MHz, same as the frequency of the PEP-II RF system. As a result, the new RF systems for the ion collider ring must also have the same frequency or 952 MHz due to a consideration of future luminosity upgrade.

To derive these design parameters, certain limits were imposed on several key machine or beam parameters in order to improve robustness of the design and to reduce the cost and accelerator R&D challenges. These limits are based largely on previous lepton and hadron collider experiences and present state-of-the-art accelerator technologies and are listed below

- The stored beam currents are up to 0.75 A for protons or ions, up to 3 A for electrons.

- Electron synchrotron radiation power should not exceed 10 kW/m in arc
- The direct space-charge tune-shift of ion beams should not exceed 0.06
- The proton or ion beam-beam tune-shift at each IP should not exceed 0.015
- The electron beam-beam tune-shift at each IP could be a factor of 10 higher, namely, as high as 0.15, due to its synchrotron radiation damping.

The JLEIC luminosity as a function of CM energy is plotted in Figure 1.2.2. The luminosity performance is limited by the space charge effect at low proton energies (low CM energies) and by synchrotron radiation effect (both radiation power and induced emittance enlargement) at high electron energies (high CM energies). At the middle CM energy range, JLEIC luminosity is limited by the beam-beam effect.

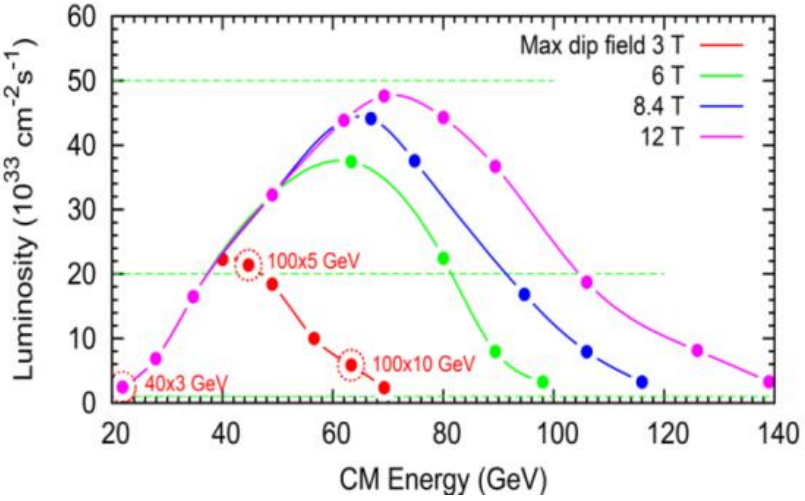

Figure 1.2.2: The JLEIC *e-p* luminosity

Since the equilibrium emittance of an electron beam in a storage ring depends on synchrotron radiation damping, its normalized value can vary up to 64 times from 3 to 12 GeV for a given lattice design. On the other hand, the ion beam emittance is largely determined by intra-beam scatterings and other beam effects and efficiency of beam cooling, and is assumed relatively stable. As a consequence, the emittances of the two JLEIC colliding beams are usually not matched in the entire energy range. In order to match beam spot sizes at an IP, the beta-star (the value of betatron function at an IP) must be adjusted accordingly for different energies, as shown in Table 1.2.1. Matching of spot sizes of colliding beams at an IP is critical in minimizing effects of the highly nonlinear beam-beam forces and maximizing the tolerable beam-beam tune-shift and therefore the luminosity.

In Table 1.2.1, the proton beta-star for the luminosity optimized design point (i.e., 100 GeV *p* x 5 GeV *e*) is 1.2 cm in vertical direction. This value is determined by having a sufficient beam-stay-clear at the FFQ magnets. On the other hand, at the lower CM energy design point (i.e., 40 GeV *p* x 3 GeV *e*) in Table 1.2.1, the proton beam geometry emittance at 40 GeV is 2.5 times large compared to the 100 GeV design point, the beta-star is thus relaxed (enlarged) substantially in order to fit the beam through the same physical aperture of the FFQ magnets. At the same time, the beta-star of the electron beam is also enlarged in order to achieve a match of beam spot sizes at IPs.

Collisions of electrons and ions can be arranged similarly to electron-proton collisions in JLEIC, and luminosities of *e-A* collisions should be comparable to *e-p* collisions. The ion energies are derived from the proton energy (100 GeV maximum) in

the ring by scaling of the charge-mass ratio Z/A, assuming the same maximum field strength of arc dipoles.

2.3.2.2 *JLEIC Luminosity Concept*

For ring-ring colliders involving hadron beams, there are traditionally small numbers of bunches per beam, therefore the bunch collision frequencies are small, for example, there are only 111 ion bunches in the RHIC collider ring so its bunch frequency is 9.2 MHz. With large bunch charges (usually 10^{11} protons or above) in order to maintain even a modest beam current, the bunch lengths are usually long (of the order of several tens cm) mainly due to limits of collective beam effects and also lack of damping. Long bunches inevitably prevent a small beta-star (namely, strong final focusing) due to the so-called hour-glass effect, and combined with large transverse emittance, lead to fairly large beam spots at collision points – and as a result, only delivering relative low luminosities.

It has been a primary design strategy of JLEIC, since the very beginning of the design study, to break away from the traditional approach of hadron colliders and to adopt a proved novel luminosity concept centered on high bunch collision frequency CW colliding beams. This design concept [5] can be summarized by the following list of key ingredients:

- High bunch repetition rate for both colliding beams
- Very small bunch charge
- Very short bunch lengths
- Very small transverse emittance
- Very strong final focusing (small beta-star)
- Large attainable beam-beam tune shift
- Crab crossing of colliding beams
- Strong synchrotron radiation damping for electron beam
- Strong cooling of proton and ion beams

In the above list, the first four items specify design principle of colliding beams in terms of their phase space structure (bunch length and emittance) and time structure (bunch frequency and CW). The next three items specify design strategy of interaction regions in order to take advantage of high-bunch-repetition CW colliding beams to achieve high luminosity. Crab crossing is required to eliminate parasitic collisions and associated long-range beam-beam effects. The last two items of the list, synchrotron radiation damping of the electron beam and strong cooling of proton and ion beams, are essential in preserving the stored electron beam, and for formation of the designed ion beams and reducing the beam emittance, respectively. This three-tier luminosity concept is illustrated in Figure 1.2.3.

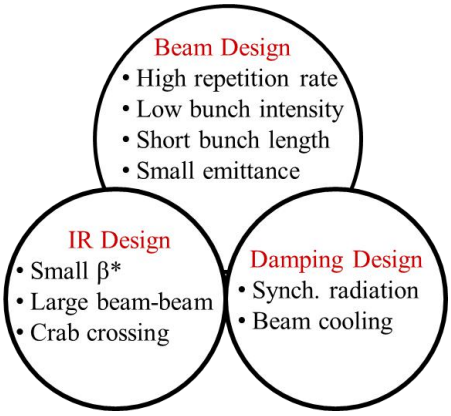

Figure 1.2.3: JLEIC luminosity concept

Briefly, JLEIC proton and ion beams are designed having very short bunch length and very small transverse emittance such that a strong final focusing can be applied to reduce the beam spot sizes as small as a few μm at collision points – hence, greatly boosting the collider luminosities. This can be seen from the standard luminosity formula [7] that it is inversely proportional to product of transverse beam spot sizes at IP. A high bunch repetition rate ensures a very small bunch charge (hence much weaker collective beam effects) of a colliding beam of nominal average current; therefore short bunch length and small transverse emittance could possibly be achieved. A detailed discussion of this novel luminosity concept can be found in [5].

This luminosity concept was proved by several lepton-lepton colliders worldwide and has led to the present world record of the highest achieved luminosity at the KEK-B factory. As a matter of fact, by adopting this luminosity concept, the JLEIC lepton-hadron collider is designed like a lepton-lepton collider in order to achieve ultra high luminosities.

The opportunity that JLEIC can adopt this novel luminosity concept is based on the following two advantages of an EIC at Jefferson Lab. The first advantage is that CEBAF delivers a CW beam at 1497 MHz bunch repetition rate, thus provides a half solution to the design concept. For the other half of solution, we need to produce and store high average current proton or ion beams with matched properties in terms of bunch repetition rates, length and emittance. Such ion beams do not exist yet at Jefferson Lab; however, they are technically feasible given advances in accelerator technologies over the last several decades, notably in ion sources, SRF liancs and cooling of ion beams. Therefore, a green field ion complex on the Jefferson Lab site is the other advantage. In fact, substantial studies have been devoted to the conceptual design of such a modern ion complex over the last sixteen years at Jefferson Lab.

In JLEIC, unlike the electron beam, the synchrotron radiation damping of the ion beams does not exist. Thus, an effective damping mechanism must be introduced into the ion complex for achieving reduction of the 3D emittance, up to an order of magnitude in all three directions, in order to deliver high luminosities. JLEIC has adopted a scheme of multi-phased electron cooling of the ion beam. It employs electron cooling first at the injection energy of the ion collider ring by a high current magnetized DC electron beam for initial emittance reduction; then at the top beam energy after boosting by a highly bunched magnetized electron beam from an ERL cooler with a circulator ring for conditioning the beams to the designed state for collisions. Most critically, JLEIC applies electron cooling continuously during collisions in order to

suppress IBS and other nonlinear collective effects and maintain the cooled small emittance. It has been estimated that, with a proper bunched cooling electron beam, cooling efficiency is good enough to achieve the design goal stated above.

1. A. Accardi, et al. "Electron-Ion Collider: The Next QCD frontier Understanding the glue that binds us all", Eur. Phys. J. A (2016) 52: 268
2. S. Abeyratne, et al. "Science Requirements and Conceptual Design for a Polarized Medium Energy Electron-Ion Collider at Jefferson Lab", edited by Y. Zhang and J. Bisognano (2012) https://arxiv.org/abs/1209.0757
3. S. Abeyratne, et al. "MEIC Design Summary", https://arxiv.org/abs/1504.07961 (2015)
4. "JLEIC Pre-CDR", edited by T. Satogata and R. Yoshida, (2018)
5. Ya. Derbenev, et. al. "Achieving High Luminosity in an Electron-Ion Collider", Proc. of. HB2010, MOPD06 (2010)
6. Ya. Derbenev, University of Michigan Report UM HE 96-05 (1996)
7. A. Chao and M. Tigner, Handbook of Accelerator Physics and Engineering, 3rd Print, P. 277, World Scientific (2009)

2.3.3 **Ion sources**

Amy Sy
Thomas Jefferson National Accelerator Facility, Newport News, Virginia, USA
Mail to: amysy@jlab.org

2.3.3.1 ***Introduction***

The physics program of a future electron-ion collider (EIC) calls for a variety of polarized and unpolarized ion species to explore a broad range of parameters in the quark-gluon plasma space. As Jefferson Lab is currently primarily a polarized electron facility, several ion source technologies are being explored to provide both polarized light ions and unpolarized light and heavy ions for the JLEIC physics program. Here we focus on the existing polarized ion source technologies that can provide polarized protons, deuterons, and ^{3}He ions to the JLEIC ion collider ring.

2.3.3.2 ***Polarized Ion Source Technologies***

Polarized ions are currently created by polarizing the electron in the atom of interest, and transferring the electron polarization to nuclear polarization through the hyperfine interaction. The polarized atom is then ionized through charge-exchange reactions, either with unpolarized ions or through electron pickup from an alkali-metal vapor. The two main types of polarized ion sources are the Atomic Beam Polarized Ion Source (ABPIS) and the Optically-Pumped Polarized Ion Source (OPPIS). Both generate polarized ions by the general procedure just described, but the details of the processes involved vary tremendously. We summarize the operation, performance, and future prospects for both types of polarized ion sources and their suitability as an injector for the JLEIC ion complex. We also discuss the prospects for polarized $^3He^{++}$ ion sources for a future electron-ion collider.

2.3.3.2.1 Atomic Beam Polarized Ion Source (ABPIS)

Atomic Beam Polarized Ion Sources (ABPIS) [1-4] utilize resonant charge-exchange reactions between polarized neutral atomic beams and unpolarized atomic ion species to obtain polarized atomic ions. Sources of this type have produced polarized H^+, H^-, D^+ and D^- ions, and may be able to produce polarized ^3He and Li ions with additional R&D [5]. For production of negatively-charged polarized hydrogen ions, the resonant charge-exchange reaction utilized is:

$$H^0 \uparrow + D^- \Rightarrow H^- \uparrow + D^0 \qquad (1)$$

The cross-section for reactions of this type, for production of both positive and negative polarized ions, is on the order of 10^{-14} cm^2 for collision energies on the order of 10 eV. Thus the ABPIS must produce cold polarized atomic neutrals and slow unpolarized ions to maximize the efficiency of the charge-exchange reaction. The cold atomic neutral species are produced in an RF gas dissociator and cryogenically-cooled nozzle, and are polarized by passage through Stern-Gerlach separating magnets (for electron spin selection) and through RF transition units (for electronic to nuclear polarization transfer). The slow unpolarized ions are provided by a plasma source. The polarized atoms and unpolarized ions react in a solenoid field, and the resultant polarized ions are extracted from the charge-exchange region for further experiments. A schematic of an ABPIS for polarized H^- production is shown in Figure 1.

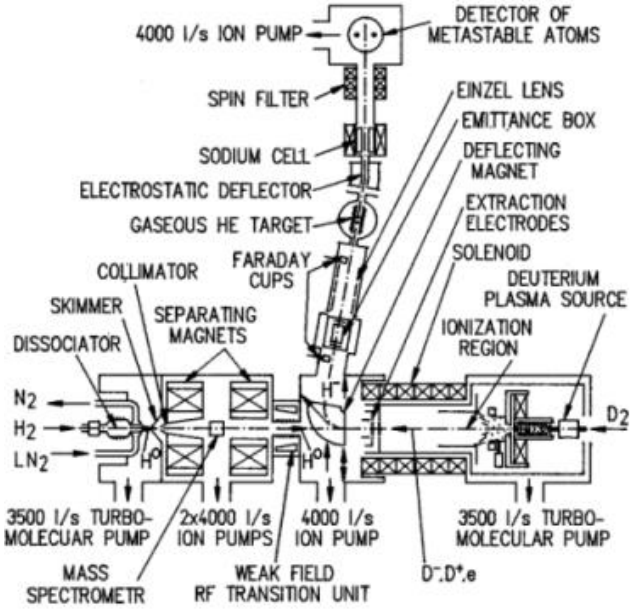

Figure 1: Schematic of ABPIS for polarized H- production [1].

2.3.3.2.2 Operation

An RF gas dissociator and cooled nozzle provide cold atomic beam species of the desired polarized ion (i.e. hydrogen atoms for polarized H^-, deuterium atoms for polarized D^-. The atomic beam is formed with a skimmer and collimator upstream of the Stern-Gerlach separating magnets for polarization selection. The separating magnets are sextupoles with physical dimensions matched to the velocity distribution of the atomic beam. Typical velocity for the atomic beam produced in these sources is on the order of

2000 m/s. The sextupole magnets for polarization selection have pole tip fields on the order of 1 T.

After spin selection with the sextupole magnets, the atoms in the beam are electron-spin polarized. The polarization is transferred from the electron spin to the nuclear spin of the atoms with RF transition units based on the "adiabatic passage" method. This method induces complete population transfer between neighboring quantum states using magnetic fields and RF fields at frequencies of the energy differences between states. The use of multiple RF transition units with different magnetic field magnitudes along the atomic beam direction, characterized as weak field transition units (WFT), medium field transition units (MFT), or strong field transition units (SFT) based on the relative magnetic field strength, allows for different vector or tensor polarization states to be accessed in the polarized atomic beam. This is particularly important for polarized atomic deuterium beams, where several RF transition units combined allow for the production of purely tensor-polarized deuterons.

Unpolarized ions for charge-exchange with polarized atoms are provided by a plasma source. Older iterations of ABPIS devices utilized fast (few keV) unpolarized ions extracted from electron cyclotron resonance (ECR) or other ion sources. Use of extracted ion beams limits the resultant polarized ion flux by increasing the relative collision energy of the charge-exchange reaction and thus reducing the cross-section for the reaction, as well as by limiting the density of unpolarized ions available for the reaction due to space charge effects. Recent iterations of ABPIS devices inject plasma species (both positive and negative ions, as well as electrons) directly into the charge-exchange region. Use of a plasma source provides slow unpolarized ions, and the quasi-neutrality of the plasma allows for ion densities much higher than the space charge limit in low energy ion beams. For the production of negative ions, care must be taken to minimize the electron current in the charge-exchange region, as these electrons will tend to destroy the slow polarized ions before they can be extracted.

The nuclear-spin polarized atoms and unpolarized plasma species are injected towards each other from opposite ends into a solenoid field region. The solenoid field prevents depolarization and acts to confine the polarized ions, but can also affect the emittance in the extracted polarized ion beam, particularly for solenoid fields above about 0.1 T, as mentioned in [3]. Polarized ions from the charge-exchange reactions are extracted from the charge-exchange region by pulsing the applied voltages to the extraction electrodes.

2.3.3.2.3 Performance

The polarized atomic beam intensity at the entrance of the charge-exchange region is on the order of 10^{17} atoms per second. Polarized beam currents of milliamps in pulses of hundreds of microseconds have been extracted from such sources, and even higher intensities, up to 11 mA in 200 μs pulses, have been reported for production of polarized protons [3]. Unpolarized ion currents of tens of milliamps have also been extracted. H^-/D^- ions from ABPIS have demonstrated polarization over 90%. The efficiency of the charge-exchange reaction is calculated as the ratio of the polarized ion current (ions per second) to the intensity of the atomic beam (atoms per second) and is reported to be on the order of 12% for polarized H^- production [2]. Demonstrated ABPIS performance compared to the desired JLEIC parameters is summarized in Table 1.

Table 1: JLEIC desired polarized ion source parameters compared with demonstrated parameters from ABPIS and OPPIS.

Parameter	Unit	JLEIC	ABPIS	OPPIS
Ion species	…	H^-	H^-	H^-
Pulse current	mA	2.0	3.8	1.0
Pulse length	ms	0.5	0.17	0.3
Charge per pulse	μC	1.0	0.65	0.3
Ions per pulse	10^{10}	624	403	187
Repetition rate	Hz	5-10	5	1
Emittance (norm.)	π mm-mrad	2.0	1.2	0.4
Polarization	…	0.9	0.91	0.85

2.3.3.2.4 Prospects

The high polarized ion current available from pulsed ABPIS devices make them suitable as injectors for high intensity machines. An ABPIS producing polarized D^+ ions is currently operating as an injector for the Nuclotron at JINR, and will operate as an injector for the future collider NICA [4]. For JLEIC, additional R&D is required to demonstrate the desired intensity for both polarized hydrogen and deuteron beams, as well as the feasibility of a modified ABPIS for polarized ^{3}He and Li production. Avenues for optimization of ABPIS devices include increasing both the atomic beam density and the unpolarized ion current density into the charge-exchange region. The polarized ion current available is proportional to the unpolarized ion current from the plasma source, and further optimization of the plasma source and extraction system can result in improved ABPIS performance. Limitations on the pulsed polarized atomic beam density in the ABPIS are not yet fully understood, and improved ABPIS performance may also be possible with optimization of atomic beam formation components.

2.3.3.3 *Optically-Pumped Polarized Ion Source (OPPIS)*

Optically-Pumped Polarized Ion Source (OPPIS) type sources, such as that used at RHIC [6-8], can also be used for the polarized H^- injection. The RHIC OPPIS utilizes laser pulses to polarize the electron spins of rubidium atoms, and the polarized electrons are transferred to relatively fast (few keV) protons, creating polarized neutral hydrogen atoms. The electron polarization of the neutral hydrogen atom is transferred to the proton by passage through the Sona transition region, where a fast magnetic field reversal facilitates the polarization transfer. The final step involves the ionization of the polarized atomic hydrogen beam by passage through a cell containing sodium vapor, producing polarized H^- ions. The RHIC OPPIS now utilizes the series of charge-exchange processes as follows:

$$H^+ \xrightarrow{H_2\ cell} H^0 \xrightarrow{He\ cell} H^+ \xrightarrow{Rb\ cell} H^0 \uparrow \xrightarrow{Na\ cell} H^- \uparrow \quad (2)$$

A schematic of the upgraded RHIC OPPIS is shown in Figure 2.

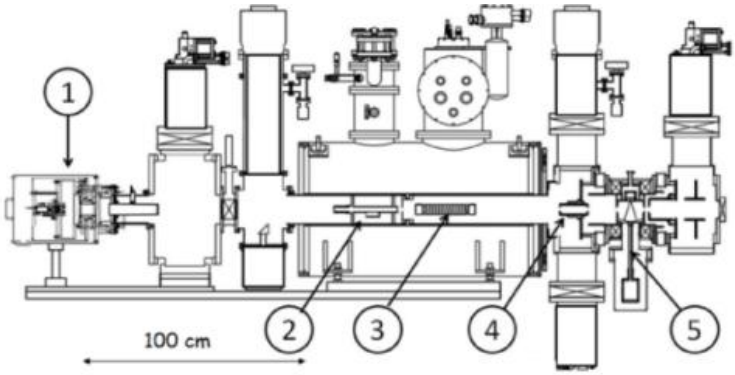

Figure 2: Schematic of OPPIS for polarized H^- production [7]. 1 – Fast atomic beam source; 2 – He cell; 3 – Optically-pumped Rb cell; 4 – Sona transition; 5 – Na cell.

2.3.3.3.1 Operation

OPPIS devices begin with protons that will pick up polarized electrons. Recent upgrades to the RHIC OPPIS include the replacement of its primary proton source (previously an ECR ion source) with a fast (few keV) atomic beam source and helium gas cell. The fast atomic beam source provides an intense atomic hydrogen beam that is ionized as it passes through the helium gas cell. The ionization efficiency is 60-80%, and the resultant proton beam has improved intensity and reduced emittance compared to the previous primary proton source. This intense proton beam continues through the OPPIS charge-exchange processes for polarized H^- production.

Optically-pumped alkali-metal vapor readily donates its polarized electron to incident protons. OPPIS devices use powerful lasers to produce electron-spin polarized alkali-metal vapor atoms, typically rubidium atoms, at a rate on the order of 10^{19} atoms/s. These optically-pumped atoms form a gas target with typical target thickness on the order of 10^{13}-10^{14} atoms/cm^2. For the RHIC OPPIS, with incident proton energy of 2.5 keV, the neutralization efficiency (polarized electron pickup) is about 50%.

The electron-spin polarized atoms are nuclear-spin polarized after passing through the Sona transition region. The Sona transition efficiency is nearly 100% and the magnetic fields in the region can be tuned to optimize the gradients and resultant polarization. The nuclear-spin polarized hydrogen atoms are ionized to H^- ions by picking up a second electron on passage through a second alkali-metal vapor cell. For incident polarized atom energy of 2.5 keV, the ionization efficiency in the RHIC sodium-jet cell is 8.4%.

2.3.3.3.2 Performance

The RHIC OPPIS has also demonstrated polarized H^- performance that is near the JLEIC requirements, with parameters also listed in Table 1. The source can produce over 100 mA equivalent beam current of atomic hydrogen, and is currently delivering polarized H^- pulse currents of 0.5-1.0 mA in 300 μs pulses for booster injection. The polarized H^- ion yield should increase with the recently completed source upgrades. Maximum measured polarization of 85% at beam energy of 200 MeV, at the linac exit, has been reported.

2.3.3.3.3 Prospects

The RHIC OPPIS has operated successfully since 2000, and continues to benefit from upgrades for increased intensity and improved beam quality.

The RHIC OPPIS is currently only capable of delivering polarized H^- and unpolarized H^-/H^+ beams. Significant modification is necessary to produced polarized D^- ions in an OPPIS type source. Feasibility of polarized D^- production was investigated with the first OPPIS source at KEK by utilizing a second optical pumping stage in the final gas cell (the ionization step) [9]. The second optical pumping stage polarizes the electron spins of the ionizing alkali species, and only those polarized deuterium atoms in a certain spin state are quantum-mechanically allowed to be ionized by picking up the polarized electrons. The method demonstrated 70% vector-polarized D^- ions, and tensor-polarized D^- ions may be accessible by utilizing an RF transition unit as in ABPIS devices.

2.3.3.4 *Polarized $^3He^{++}$ Source*

Significant progress has been made to develop a source of polarized $^3He^{++}$ ions for RHIC [7, 10]. ^3He atoms are polarized by the metastability-exchange optical pumping (MEOP) process [11] and will be ionized in an electron beam ion source. The polarized $^3He^{++}$ source for RHIC is expected to provide 2e11 ions per pulse in 20 μs pulses, an intensity orders of magnitude higher than previously achieved in existing sources. The source has demonstrated over 80% polarization of ^3He gas, and further development for ionization tests is ongoing.

Polarized $^3He^{++}$ ions could potentially be produced in an ABPIS-like device, as described in [5]. In this configuration, the polarized ^3He atoms are also produced in the MEOP process, and resonant charge-exchange reactions between the polarized ^3He atoms and unpolarized $^4He^{++}$ ions produce the polarized species of interest. This process has not been experimentally demonstrated, but many of the supporting techniques have been developed in the existing ABPIS devices, such as the use of a storage cell for production of polarized positive ions.

2.3.3.5 *Summary*

Existing technologies for the production of polarized light ions are currently or will be operational at several colliders worldwide and can be adapted to provide the desired polarized ions for the JLEIC physics program. The desired parameters for JLEIC have not yet been demonstrated by the existing polarized ion sources, but remain within reach for future R&D.

2.3.3.6 *References*

1. A.S. Belov et al., “High-intensity source of polarized negative hydrogen ions with a resonant charge-exchange plasma ionizer”, Rev. Sci. Instrum. 67 (3), 1293 (1996).
2. A.S. Belov et al., “Intensity improvements of pulsed source of polarized negative hydrogen ions”, Rev. Sci. Instrum. 77, 03A522 (2006).
3. A.S. Belov, “Production of Polarized Ions with Nearly Resonant Charge-Exchange Collisions in Plasma”, AIP. Conf. Proc. 980, 209 (2008).
4. A.S. Belov, et al., “Source of polarized ions for the JINR accelerator complex”, J.

Phys.: Conf. Ser. 938 012017 (2017).
5. A.S. Belov, "A scheme for a polarized ^{3}He ion source with a resonant charge-exchange plasma ionizer", NIM A 402 (1998) 205-207.
6. A. Zelenski et al., "The RHIC polarized H^- source", Rev. Sci. Instrum. 87, 02B705 (2016).
7. A. Zelenski et al., "Optically-Pumped Polarized H^- and $3He^{++}$ Ion Sources Development at RHIC", Proc. IPAC2018, Vancouver, BC, Canada, TUYGBE4 (2018).
8. A. Zelenski et al., "The RHIC polarized source upgrade", J. Phys. Conf. Ser. 295 (2011) 012147.
9. M. Kinsho et al, "Production of polarized negative deuterium ion beam with dual optical pumping", Rev. Sci. Instrum. 67, 1362 (1996).
10. J. Maxwell et al., "Development of a Polarized Helium-3 Source for RHIC and eRHIC", Int. J. Mod. Phys. Conf. Ser. 40, 1660102 (2016).
11. F. D. Colegrove, L. D. Schearer, and G. K. Walters, "Polarization of ^{3}He Gas by Optical Pumping", Phys. Rev. 132, 2561 (1963).

2.3.4 **Polarized Electron Source**

Matt Poelker
Thomas Jefferson National Accelerator Facility, Newport News, Virginia, USA
Mail to: poelker@jlab.org

Although the JLEIC polarized electron beam requirements are well within the present state-of-the-art, modifications to the CEBAF photoinjector will be required to address the comparatively high bunch charge requirement of 26 pC, which is more than 100 times higher than typically delivered to the CEBAF accelerator today. It may surprise some readers that 26 pC represents a challenge but the time structure of the JLIEC beam, with relatively high pulse repetition rate and short bunch length, combined with the necessity of incorporating beamline elements that serve important functions but also lengthen the keV beamline, likely necessitates operating the CEBAF dc high voltage polarized photogun at a bias voltage much higher than -130 kV employed at CEBAF today.

The CEBAF dc high voltage polarized electron source [1] feeds beam to an adjoining baked UHV beamline approximately 10 m long that includes a bend magnet to permit illumination of the photocathode at normal incidence (an important requirement for some types of physics experiments), a 4π spin manipulator composed of two Wein filters and two spin-rotating solenoids [2], and a sophisticated apparatus composed of two rf-deflecting cavities used to set the temporal acceptance of the electron bunches delivered to the first SRF accelerating cavities. En route to these SRF cavities, electron bunches experience significant space-charge induced blow up, in both spatial and temporal dimensions. At an electron bunch repetition rate of 31 MHz and 1.3 pC bunch charge, the highest bunch charge delivered to a physics experiment in CEBAF history [3], transmission through injector apertures was approximately 80%. At the JLEIC bunch charge of 26 pC, transmission would be significantly worse and likely deemed unacceptable. It is possible the CEBAF injector could be modified and shortened to improve beam transport for JLIEC, for example, by removing the rf-

deflecting cavities used to set the temporal acceptance of the bunches, but because some keV beamline features and components are essential for JLIEC operation (i.e., the bend magnet to permit illumination of the photocathode at normal incidence, and Wien filter spin manipulator), space charge induced beam blow-up will remain a problem. A relatively straightforward solution is to increase the bias voltage of the photogun, to generate a stiffer beam that is less susceptible to beam blow-up. Particle tracking codes simulations will inform the correct choice of bias voltage but based on past experience at CEBAF and also at the Jefferson Lab free electron laser, it is likely that a photogun operating at ~ -300kV will suffice.

A viable -300 kV dc high voltage photogun design is shown in Figure 1 (right), next to the -130 kV photogun used at CEBAF today. Both photoguns employ an inverted-insulator geometry [4], with the high voltage insulator extending into the photogun vacuum chamber and serving as the support structure for the cathode electrode. A slight variation of this -300 kV photogun design is now being used to generate unpolarized magnetized beam using alkali-antimonide photocathodes [5], but the same basic photogun design could be used to generate polarized electron beam using a GaAs photocathode.

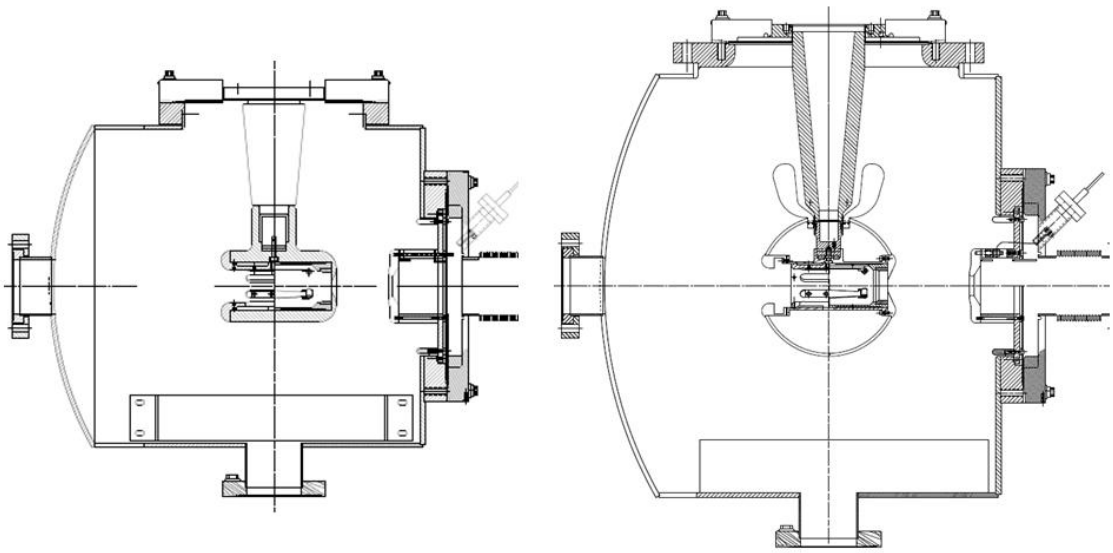

Figure 1: Jefferson Lab dc high voltage photoguns with inverted-insulator designs; (left) the CEBAF -130 kV dc high voltage photogun and, (right) the -300 kV dc high voltage photogun described here. For scale, the top flange on both photogun designs is 10" in diameter.

Perhaps a more versatile JLEIC injector design would leave the present CEBAF photogun and keV beamline unchanged to support an on-going fixed-target physics program at the four experiment halls, while adding a second photoinjector composed of a new photogun, spin manipulator and SRF booster to supply polarized electron beams to JLEIC. Collider and fixed-target physics programs could be conducted exclusively, one program at a time, but it is also worth imagining simultaneous CEBAF and JLEIC operation, with two polarized photoinjectors operating simultaneously, producing interleaved MeV beams of slightly different energy and combined at ~ 5 MeV using a dipole magnet, and then delivered to the injector full cryomodules before delivery to the recirculating linacs. Very preliminary considerations suggest there is enough room at

the CEBAF photoinjector to install a second polarized photoinjector without modification to the injector tunnel.

To deliver independent spin-polarized electron beams to multiple halls conducting experiments simultaneously, CEBAF employs versatile and reliable gain-switched diode laser master oscillators and power amplifiers, to create interleaved CW electron pulse trains at subharmonic frequencies of the SRF accelerating frequency [6]. Such a laser system can be used to generate the electron beam for JLEIC although a pulsed laser amplifier might be required to generate the required macropulse structure with 26 pC microbunches. Although not employed at CEBAF today, such a pulsed laser amplifier is within the present laser state-of-the-art.

To orient the electron spin in the vertical out-of-plane direction, as described in Section 1.5 below, a Wien filter spin manipulator will be required [1]. CEBAF employs two Wien filters that are part of a 4π spin manipulator, but these devices were designed for maximum electron beam energy of 130 keV. If JLEIC requires a -300 kV voltage photogun, the CEBAF Wien filter design will need to be scaled-up to provide the higher electric and magnetic fields required to rotate polarization 90 degrees out-of-plane. Although a magnet design seems relatively straightforward, the voltage applied to the capacitor plates will be +/- 33 kV for a 1.5 cm gap, and this corresponds to an electric-field strength of 4.5 MV/m. Although this represents a modest challenge compared to building a dc high voltage photogun, some hardware development will be required.

In summary, JLEIC polarized electron beam requirements are well within the present state-of-the-art but modifications to the present CEBAF photoinjector are envisioned. A dc high voltage photogun operating at higher voltage compared to CEBAF today will assist beam transport to the SRF accelerating cavities and the recirculating linacs and ensure adequate beam quality delivered to JLEIC. A viable -300 kV photogun design is operating today, and used to generate unpolarized magnetized beam, so very little photogun R&D would be required to support the JLIEC polarized beam program. If a ~ -300 kV polarized photogun is used, a new Wien filter would need to be developed to provide the required out-of-plane spin orientation. The CEBAF gain switched diode laser/power amplifier scheme could also be used to generate JLEIC polarized beam, although a different power amplifier would be needed to address the JLEIC macropulse time structure. Finally, it seems worthwhile to consider leaving the present CEBAF polarized photoinjector intact, to continue conducting a fixed-target physics program, while adding a second photoinjector composed of a dc high voltage photogun, Wien filter spin manipulator and SRF booster to provide polarized beam for JLIEC. It is even possible to consider interleaved polarized electron pulse trains, for simultaneous implementation of collider and fixed-target physics programs.

2.3.4.1 *References*

1. C. K. Sinclair, M. Poelker, P. A. Adderley, B. M. Dunham, J. C. Hansknecht, P. Hartmann, J. S. Price, P. M. Rutt, W. J. Schneider, and M. Steigerwald, "A High Average Current Polarized Electron Source with Long Cathode Operational Lifetime", Phys. Rev. ST Accel. Beams **10**, 023501 (2007)
2. J. Grames, P. Adderley, J. Benesch, J. Clark, J. Hansknecht, R. Kazimi, D. Machie, M. Poelker, M. Stutzman, R. Suleiman, Y. Zhang, “Two Wien Spin

Flipper," Proceedings of 2011 Particle Accelerator Conference, New York, NY, USA, contribution TUP025
3. Armstrong D. S., et al. Phys. Rev. Lett. 95:092001 (2005)
4. P. A. Adderley, J. Clark, J. Grames, J. Hansknecht, K. Surles-Law, D. Machie, M. Poelker, M. L. Stutzman, and R. Suleiman, "Load-locked dc high voltage GaAs photogun with an inverted-geometry ceramic insulator", Phys. Rev. ST Accel. Beams **13**, 010101 (2010)
5. Y.W. Wang, P.A. Adderley, J. F. Benesch, D.B. Bullard, J.M. Grames, F.E. Hannon, J. Hansknecht, C. Hernandez-Garcia, R. Kazimi, G.A. Krafft, G.A. Krafft, M.A. Mamun, G.G. Palacios Serrano, M. Poelker, R. Suleiman, M.G. Tiefenback, S. Zhang, G.A. Krafft, S.A.K. Wijethunga , "300 kV DC High Voltage Photogun with Inverted Insulator Geometry and CsK2sb Photocathode," Proceedings of 201 International Particle Accelerator Conference, Vancouver, British Columbia, Canada, contribution THPMK110
6. J. Hansknecht and M. Poelker, "Synchronous Photoinjection Using a Frequency-Doubled Gain-Switched Fiber-Coupled Seed Laser and ErYb-Doped Fiber Amplifier", Phys. Rev. ST Accel. Beams **9**, 063501 (2006)

2.3.5 **Electron Polarization with a Figure-8 Ring**

Fanglei Lin
Thomas Jefferson National Accelerator Facility, Newport News, Virginia, USA
Mail to: fanglei@jlab.org

2.3.5.1 ***Introduction***

An essential aspect of the JLEIC design strategy is the need to meet the expectation of the nuclear physics program, namely of preserving and manipulating a highly polarized electron beam with

- polarization of 70% or above,
- longitudinal polarization at collision points,
- polarization flipping at required frequencies.

To satisfy the requirements, various strategies have been carefully considered and investigated [1,2]. In this section, first, we will briefly describe the radiative polarization in an electron storage ring in general. Then we will focus on manipulation, preservation and numerical simulation of electron polarization in the JLEIC electron collider ring. In particular, the following issues will be discussed in detail: spin rotators, calculation of polarization lifetime, continuous injection, and spin tracking simulation.

2.3.5.2 ***Radiative Polarization Effects and Spin Matching***

In the rest frame of a moving charged particle, the motion of the spin vector under the external electromagnetic field is described by the Thomas-BMT equation [3, 4]

$$\frac{d\vec{S}}{dt} = \frac{e}{\gamma m}\vec{S} \times [(1+G\gamma)\vec{B}_{\perp} + (1+G)\vec{B}_{\parallel} + (G\gamma + \frac{\gamma}{\gamma+1})\frac{\vec{E}\times\vec{\beta}}{c}]. \qquad (1)$$

Here the spin vector $\vec{S}$, namely the normalized single particle spin expectation value, is in the particle rest frame, $\vec{B}_\perp$ and $\vec{B}_\parallel$ are the transverse and longitudinal components of the magnetic fields in the laboratory frame with respect to the particle's velocity $\vec{\beta}c$. γ is the Lorentz factor, $G = \frac{g-2}{2}$ is the anomalous gyromagnetic factor which has the value of 0.00115965 for electrons, and the vector $\vec{E}$ is for the electric field. The terms involving $\vec{E}$ are usually small comparing to those involving magnetic fields $\vec{B}_\perp$ and $\vec{B}_\parallel$, and are neglected from most discussion of spin motion in an accelerator. The polarization is then the average of $\vec{S}$ over an ensemble of particles in a bunch.

In contrast to the spin dynamics of ions in a storage ring, where the evolution of a spin vector just follows the above Thomas-BMT equation, synchrotron radiation from electrons causes spin flip from up to down and vice versa. The transition rates for the two initial spin orientations differ, building up the equilibrium polarization up to 92.4% in ideal circumstances. This is a purely quantum mechanical and called Sokolov-Ternov (S-T) effect [5]. The S-T polarizing process is usually slow on the time scale of other dynamical phenomena occurring in storage ring, and its inverse time constant in a dipole magnet is

$$\tau_{st}^{-1} = \frac{5\sqrt{3}}{8}\frac{r_e\gamma^5\hbar}{m_e|\rho|^3}, \qquad (2)$$

Where r_e is the classical radius of the electron, $\hbar$ is the Planck constant, m_e is the electron rest mass, and ρ is the dipole bending radius. τ_{st} depends strongly on γ and ρ and is typically minutes or hours.

However, the majority of the photons in the synchrotron radiation tend to randomize the electron orbital motion in the inhomogeneous magnetic fields in an accelerator. If the ring is not sufficiently well aligned and/or if it contains special magnet systems, like the spin rotators needed to rotate the polarization to the desired orientation at the collision point(s), the spin-orbit coupling embodied in the Thomas-BMT equation can cause spin diffusion, i.e. depolarization. Then the equilibrium polarization is less than 92.4%, and will depend on the polarization and depolarization processes and magnet layouts. Taking into account the radiative depolarization due to photo-induced longitudinal recoil, the equilibrium electron polarization is given by the Derbenev-Kondratenko formula [6, 7]

$$P_{dk} = -\frac{8}{5\sqrt{3}}\frac{\oint ds\left\langle\frac{1}{|\rho(s)|^3}\hat{b}\cdot\left(\hat{n}-\frac{\partial\hat{n}}{\partial\delta}\right)\right\rangle_s}{\oint ds\left\langle\frac{1}{|\rho(s)|^3}\left(1-\frac{2}{9}(\hat{n}\cdot\hat{s})^2+\frac{11}{18}\left(\frac{\partial\hat{n}}{\partial\delta}\right)^2\right)\right\rangle_s}, \qquad (3)$$

where $\langle\rangle_s$ denotes an average over phase space at azimuth s, $\hat{s}$ is the direction of motion, $\hat{b}$ is a unit vector along the magnetic field, $\hat{n}$, called invariant spin field [8, 9, 10], is a 1-turn periodic unit 3-vector field over the phase space satisfying the Thomas-BMT equation along particle trajectories $u(s)$, and $\delta = {}^{\Delta E}/_{E}$ is the relative energy deviation. The first two terms in the parenthesis in the denominator come from the generalization by Baier and Katkov [11, 12] of the original S-T expression to an arbitrary magnetic field. The third term contains the spin-orbit coupling function $(\frac{\partial\hat{n}}{\partial\delta})^2$, which quantifies the radiative depolarization. The beam polarization points along the unit vector $\hat{n}_0$. This is the 1-turn periodic solution of the Thomas-BMT equation on the closed orbit: $\hat{n}_0 = \hat{n}(u=0;s)$. For $e^{\pm}$ away from spin-orbit resonances in storage rings, $\hat{n}$ is normally at most a few mill-radians away from $\hat{n}_0$. To obtain high polarization, we need $\left|\frac{\partial\hat{n}}{\partial\delta}\right|^2 \ll 1$ in

dipole magnets where $1/|\rho(s)|^3$ is large. Correspondingly, the inverse polarization time constant for this build-up of equilibrium polarization in the presence of radiative depolarization is

$$\tau_{dk}^{-1} = \frac{5\sqrt{3}}{8}\frac{r_e\gamma^5\hbar}{m_eC}\oint ds\left\langle\frac{1-\frac{2}{9}(\hat{n}\cdot\hat{s})^2+\frac{11}{18}(\frac{\partial\hat{n}}{\partial\delta})^2}{|\rho(s)|^3}\right\rangle_s, \quad (4)$$

which implies that due to the self-polarization effect, the equilibrium polarization P_{dk}, will be achieved after several polarization lifetimes, τ_{dk}. Equation 4 can be written in terms of the spin-flip rate, τ_{bk}^{-1}, and the spin-coupling depolarization rate, τ_{dep}^{-1}, as

$$\tau_{dk}^{-1} = \tau_{bk}^{-1} + \tau_{dep}^{-1}. \quad (5)$$

Here

$$\tau_{bk}^{-1} = \frac{5\sqrt{3}}{8}\frac{r_e\gamma^5\hbar}{m_eC}\oint ds\left\langle\frac{1-\frac{2}{9}(\hat{n}\cdot\hat{s})^2}{|\rho(s)|^3}\right\rangle_s, \quad (6)$$

and

$$\tau_{dep}^{-1} = \frac{5\sqrt{3}}{8}\frac{r_e\gamma^5\hbar}{m_eC}\oint ds\left\langle\frac{\frac{11}{18}(\frac{\partial\hat{n}}{\partial\delta})^2}{|\rho(s)|^3}\right\rangle_s. \quad (7)$$

The time dependence for build-up from an initial polarization P_0 to equilibrium is

$$P(t) = P_{ens,dk}\left[1 - e^{-t/\tau_{dk}}\right] + P_0 e^{-t/\tau_{dk}}, \quad (8)$$

where $P_{ens,dk} = P_{dk}\langle\hat{n}\rangle_s$ is the ensemble average of the polarization.

In a perfectly aligned storage ring containing only horizontal bends, quadrupoles and RF cavities, there is no vertical betatron motion and $\hat{n}_0(s)$ is vertical. Since there are no radial quadrupole fields and electric fields in cavities are parallel to the particle motion, $\hat{n}(s)$ is vertical and parallel to $\hat{n}_0(s)$ at each location in the phase space. Then $(\frac{\partial\hat{n}}{\partial\delta})^2$ vanishes and there is no depolarization. However, misalignments complicate the spin dynamics in real accelerators. Due to the vertical betatron motion, the spins see the radial fields which tilt them from the vertical direction. $\hat{n}_0(s)$ is also tilted and spins couple to vertical quadrupole fields too. As a result, $\hat{n}(s)$ becomes dependent on u in the phase space and tilts away from $\hat{n}_0(s)$ by an amount that usually increases with the orbit amplitudes. Then $(\frac{\partial\hat{n}}{\partial\delta})^2$ does not vanish in the dipoles where $1/|\rho(s)|^3$ is large and depolarization occurs. In particular, $(\frac{\partial\hat{n}}{\partial\delta})^2$ is non-zero in dipoles even with a perfect alignment in the presence of spin rotators. The deviation of $\hat{n}(s)$ from $\hat{n}_0(s)$, resulting in depolarization, is enhanced near to the spin-orbit resonances condition

$$\nu_{spin} = k_0 + k_x\nu_x + k_y\nu_y + k_z\nu_z. \quad (9)$$

Here ν_{spin} is the spin tune on the closed orbit, k_0, k_x, k_y and k_z are integers, ν_x, ν_y and ν_z are horizontal, vertical and synchrotron tunes. This deviation is also increased with distance in phase space from the closed orbit. The spin-orbit coupling function $(\frac{\partial\hat{n}}{\partial\delta})^2$ quantifies the depolarization and can be so large, resulting in small or zero equilibrium polarization. Note that the ensemble average polarization is mainly influenced by the value of P_{dk} in Eq. 3, even very close to resonances.

In principle, depolarization can be suppressed by an optimization technique called spin matching. This involves adjusting the optics and layout to minimize $(\frac{\partial\hat{n}}{\partial\delta})^2$ in the

dipoles in the ring. So far it is only possible to do this within the linear approximation for spin motion. When successful, as for example at HERA [13], spin matching immediately reduces the strengths of the first order spin-orbit resonances and leads to a reduction of the strength of higher-order resonances.

Usually, spin matching takes place in stages. Strong synchrobeta spin matching is applied to the optics and layout of the perfectly aligned ring and then harmonic closed orbit spin matching is applied to soften the effect of misalignments by adjusting the closed orbit to reduce the tilt of $\hat{n}_0$ from the vertical in arcs. A section of the ring which is spin matched is said to be "spin transparent". For details of spin matching see [14].

2.3.5.3 *Universal Spin Rotator (USR)*

CEBAF serves as a full energy electron injector and polarization source of the JLEIC electron ring. Two Wien filters installed in the photo-injector can be set up carefully to ensure electron beams with a vertical polarization at the injection point of the collider ring. Such an injection has three advantages. First, it avoids spin decoherence caused by the energy variation during the acceleration in the CEBAF. Second, it simplifies polarization transport between CEBAF and collider ring. Third, electron beams with vertical polarization are injected in the arc section in the ring. Injection here can significantly reduce the background in the detector because dipole magnets in the arc sweep out incompletely injected electrons so that they have less chance to propagate through the chamber and hit the detectors.

The polarization in the electron collider ring is designed to be vertical in the arcs to minimize spin depolarization and longitudinal at the collision points for the physics experiments. Spin orientation is accomplished using spin rotators located at each end of two arcs. A USR has been developed for this purpose [15] and it performs correctly over the whole energy range of 3 to 12 GeV. A schematic drawing of such a spin rotator is shown in Fig. 1. In principle, a spin rotator can rotate a spin from the vertical direction to an arbitrary direction; for the case of the JLEIC electron ring, a 90^o rotation from the vertical to the longitudinal direction is desired. Implementing this concept requires allocating two arc dipoles (or two sets of arc dipoles) of bending angles $\hat{\alpha}_1$ and $\hat{\alpha}_2$ to the spin rotator (see Fig. 1). Each of two arc dipoles provides a spin rotation of $= G\gamma\hat{\alpha}$, where $G = 0.001159652$ is the gyromagnetic anomaly for electrons and γ is the Lorentz factor. The solenoid fields vary to make the net rotation of a spin rotator always equal to a fixed value (90^o for the JLEIC) regardless the beam energy; hence the name universal. The complete treatment of a USR can be found in [15]. The final analytic results are given in the following two equations:

$$\sin\phi_1 \sin\alpha_1 = \cos\alpha_2 \qquad (10)$$

$$\sin\phi_1 \sin\phi_2 \cos\alpha_1 = \cos\phi_1 \cos\phi_2 \qquad (11)$$

where ϕ_1, ϕ_2, α_1 and α_2 are angles of spin rotation in two solenoids and two bending dipoles, respectively, as shown in Fig. 1. Table 1 shows spin rotation angles for two solenoids and two bending dipoles in the USR for several representative electron beam energies, as well as the integrals of solenoid fields. Since the bending angles of the dipoles are fixed, the designed orbit in the spin rotator remains the same in the whole energy range. The transverse coupling induced by the solenoids in the USR is compensated using normal quadrupole families [16,17,18].

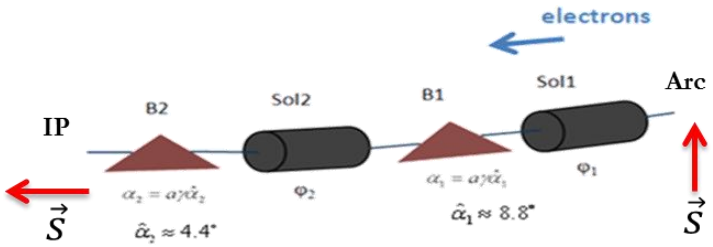

Figure 1: Schematic drawing of a USR. B1 and B2 are the two sets of arc dipole bends rotating the spin around the vertical by α_1 and α_2. Sol1 and Sol2 are the solenoids rotating the spins around the longitudinal by ϕ_1 and ϕ_2.

Table 1: Parameters of the USR in the JLEIC electron collider ring.

Energy	Solenoid 1		Dipole 1	Solenoid 2		Dipole 2
	Spin Rotation	BDL	Spin Rotation	Spin Rotation	BDL	Spin Rotation
GeV	rad	T.m	rad	Rad	T.m	rad
3	π/2	15.7	π/3	0	0	π/6
5	0.23π	11.9	0.56π	0.55π	28.7	0.28π
7	0.18π	13.1	0.78π	0.64π	47.1	0.39π
9	π/6	15.7	π	2π/3	62.8	π/2
12	0.19π	24.6	4π/3	0.61π	76.4	2π/3

2.3.5.4 *Electron Polarization Design*

Usually, Sokolov-Ternov effect is used to build up the electron or positron polarization, such as in the HERA machine [8]. However, this self-polarization becomes impractical at the low energy since the time constant for the build-up process is inversely proportional to the 5th power of the beam energy and takes place in hours up to a few tens of hours. The depolarization process caused by the imperfection of magnetic fields in the storage ring is usually much faster than the self-polarization process, resulting in a low equilibrium polarization.

Instead of relying on self-polarization, one can inject an electron beam with a polarization higher than the equilibrium value P_{dk}. Then the polarization will approach this value with the characteristic time τ_{dk}. Since the S-T polarization time is inversely proportional to the 5th power of the beam energy, injecting a pre-polarized beam is the only solution if the required energy of the stored beam is so low that is impractically large. It is also practical if the lifetime of the stored beam is small: full polarization is immediately available while the luminosity is still high. In the JLEIC electron polarization design, CEBAF provides a polarization, up to ~90%, higher than the equilibrium polarization, this is very important at high energy since the depolarization rate were high, as happens when $(\frac{\partial \hat{n}}{\partial \delta})^2$ in Eq. 4 is large compared to 1. To avoid an immediate loss of polarization in the electron ring, the vertical polarization, lying along the $\hat{n}_0$vector, is injected at the injection point in the collider ring arc.

The polarization configuration in the JLEIC electron collider ring, as shown in Fig. 2 is determined by the solenoid field directions in the pair of spin rotators in the same long straight [19, 20]. These were chosen to have the opposite solenoid polarities, blue arrows in cylinders shown in Fig. 2. Then the polarization is anti-parallel to the vertical guiding field in one arc and parallel to the guiding field in the other one, regardless of the choice of two possible opposite longitudinal polarizations (purple solid and dashed

arrows in Fig. 2) at the IPs. Therefore, the Sokolov-Ternov self-polarization process has a net depolarizing effect in the whole collider ring, and both polarization states from the polarized source will be equally affected.

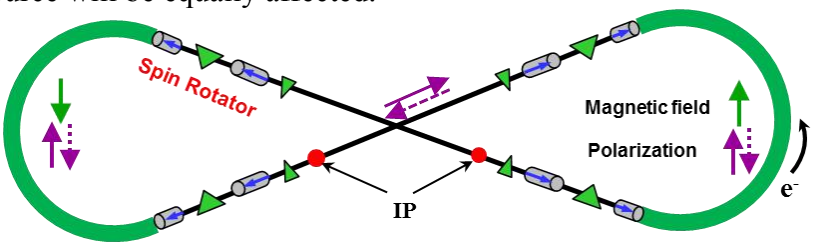

Figure 2: Polarization configuration in the JLEIC electron collider ring. Polarization (purple solid and dash arrows) directions remain same in two arcs by having opposite longitudinal solenoid field directions in the same long straight. The blue arrow in the solenoid represents the field direction.

In addition, with such opposite longitudinal solenoid fields in the pair of spin rotators in the same long straight, the net field integral is zero. As a result, the 1st order spin perturbation in the solenoids for off-momentum particles vanishes. This significantly extends the polarization lifetime and reduces the burden on the spin matching and ring-optics design. Though this polarization configuration has zero equilibrium polarization, with highly polarized injected beams, the polarization lifetime at low energies (< 9 GeV) is large enough (~half an hour to a couple hours) for detectors to collect data.

Such a polarization configuration, combined with a figure-8 geometry of collider ring, produces a net zero spin precession on the designed orbit. Hence the spin tune on the design orbit is zero and independent of beam energy. This significantly reduces the strengths of synchrotron sideband resonances [21]. In addition, since there is no preferred direction of the polarization, the polarization can be easily controlled and stabilized by using relatively small magnetic fields, for example a spin-tuning solenoid in the straights where the polarization is longitudinal. This spin-tuning solenoid introduces additional spin precession only, resulting in a non-zero spin tune that moves spin motion away from the harmful zero spin resonance, but has no effect on $\hat{n}_0$, i.e., the design polarization direction.

Desired spin flipping to reduce systematic uncertainties in the experiments in the JLEIC is implemented by alternating the helicity of the photo-injector driver laser at the source to provide oppositely polarized electron beams. Therefore, two polarization states coexist in the collider ring and have similar polarization degradation in the aforementioned polarization configuration. Figure 3 shows two long oppositely polarized bunch trains and polarization pattern in collider ring's arcs, with gaps in between for beam abortion, ion cleaning etc.. The injection time structure of two polarized electron bunch trains, considering synchronizing different RF frequencies in CEBAF and collider ring, is described in detail in [2].

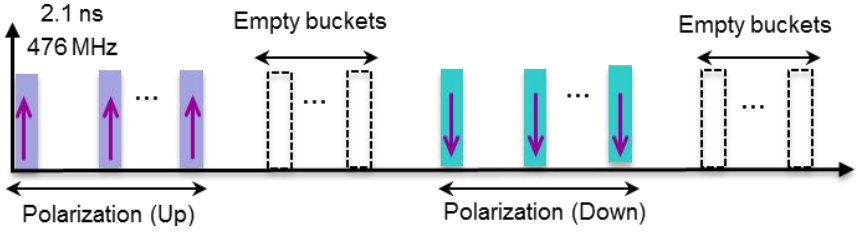

Figure 3: Bunch train and polarization pattern in collider ring's arcs.

2.3.5.5 *Polarization Lifetime and Continuous Injection*

Analytical estimation of the equilibrium polarization and lifetime, with inclusion of high order resonances, requires evaluating $\hat{n}$ and $(\frac{\partial \hat{n}}{\partial \delta})^2$ all over the orbital phase space and this can require large amounts of computer power. However, valuable first impressions can be obtained easily and quickly by linearizing the spin motion as in the SLIM [22] algorithm. This is implemented in the thick-lens code SLICK. For details of these matters see [14]. The linearization entails assuming that the angle between $\hat{n}$ and $\hat{n}_0$ is small all over phase space. The formalism only exhibits the first order spin-orbit resonances but that suffices in the first step.

Tracking simulations have been performed using the code SLICK/SLICKTRACK [14] to validate the developed spin manipulation scheme and study the spin dynamics. SLICK calculates the polarization lifetime analytically by evaluating the invariant spin field $\hat{n}$ and spin-orbit coupling function $(\frac{\partial \hat{n}}{\partial \delta})^2$ in the Derbenev-Kondratenko formula. SLICKTRACK is an extended version of the analytic code SLICK providing Monte-Carlo simulation of photo emission and allowing one to numerically track many particles' spins using full 3D spin motion. The depolarization time is measured and the polarization lifetime is calculated accordingly. Since the full 3D spin motion is considered, SLICKTRACK has the capability of capturing higher-order spin-orbit resonances.

The advantage of the figure-8 shape JLEIC collider rings is removal of the spin-tune energy dependence during acceleration and storage. Since the designed-orbit spin tune is zero, particles are sitting in the zero-integer spin resonance. To stabilize the spin motion, it is sufficient to use a weak magnet insertion to move the spin tune away from zero. In our electron polarization studies, a spin-tuning solenoid is placed in the straight section as shown in Fig. 4. Since the polarization is longitudinal in the straight, such a spin-tuning solenoid does not change the polarization direction in the whole ring but causes additional spin precession. Note that the electron beam is injected from CEBAF to the collider ring at a full energy. Therefore, the spin-tuning solenoid does not need to ramp.

The spin tune at a given energy can be adjusted by varying the strength of the spin-tuning solenoid. Such a procedure is called a spin-tune scan. By doing this, one can find an optimum spin tune that is large enough to avoid the zero-integer spin resonance and give a long polarization lifetime. A spin-tune scan has been performed for electrons at 5 GeV in the JLEIC electron collider ring. Figure 5 shows the simulation results where the Sokolov-Ternov time is in red, the spin-orbit coupling depolarization time in the linear approximation (SLICK) is in green and the spin-orbit coupling depolarization time of 500 particles from a Monte-Carlo simulation (SLICKTRACK) is in blue.

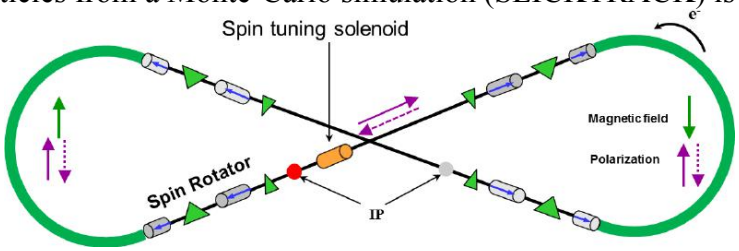

Figure 4: Polarization configuration in the electron collider ring, with a spin-tuning solenoid located in the straight where the polarization is longitudinal.

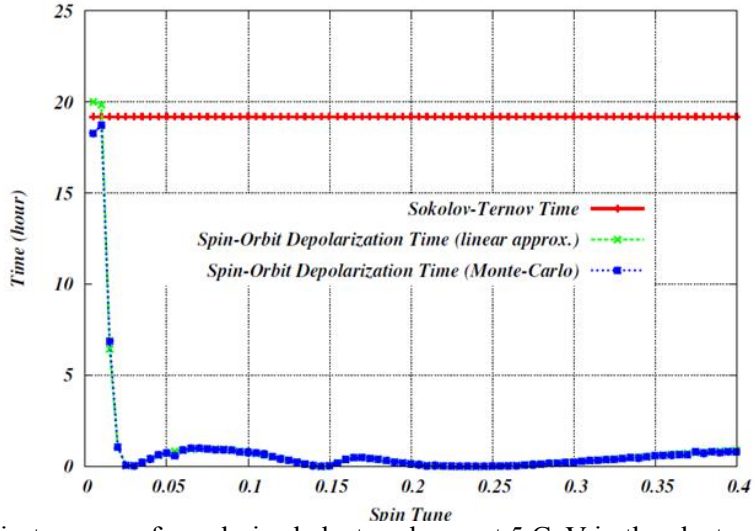

Figure 5: Spin-tune scan for polarized electron beam at 5 GeV in the electron collider ring.

The radial fields due to vertical quadrupole misalignments and dipole rolls tilt the spin from the vertical direction and are the two major contributors to the zero-integer resonance strength. To simplify the simulation and separate different depolarization mechanisms, quadrupoles are randomly shifted in the vertical direction only according to a Gaussian distribution with an rms width of 0.3 mm. The vertical closed orbit excursion shown in Fig. 6 is corrected with an rms orbit distortion of ~86 μm at quadrupoles.

As shown in Fig. 5, an optimum spin-orbit depolarization time of ~19 hours can be obtained when the spin tune is moved away from the integer by 0.01. The required field integral of the spin-tuning solenoid is ~1 T.m only. Then the optimum polarization lifetime τ_{dk} is ~9 hours as calculated through Eq. 5 with $\tau_{bk} = \tau_{st} = 19$ hours and $\tau_{dep} = 19$ hours given in Fig. 5.

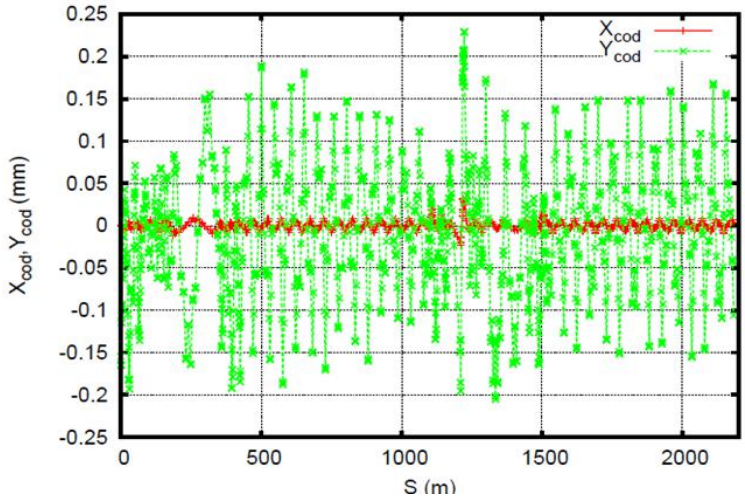

Figure 6: Corrected closed orbit distortions with quadrupoles vertically misaligned only.

The depolarization time of zero at spin tune 0.027 is due to the first order synchrotron resonance when the spin tune equals the synchrotron tune. It occurs due to breaking of the figure-8 symmetry by the spin-tuning solenoid. The dip depolarization times surrounding 0.15 and 0.24 are due to resonances occurring when the spin tune equals the fraction part of the horizontal and vertical betatron tunes. Short

depolarization times in the spin tune range between 0.03 and 0.33 are due to stronger breaking of the implemented first-order spin match when increasing the strength of the spin-tuning solenoid to obtain a larger spin tune.

The spin-tune scans obtained through the analytic calculation (the solid green line in Fig. 5) and the numerical simulation (the dotted blue line in Fig. 5) completely overlap. This demonstrates, as we predicted, that the figure-8 shaped JLEIC electron collider ring has only weak high-order synchrotron sideband resonances that narrow the range of polarization stability and are difficult to compensate due to slow synchrotron motion. The wiggles in the Monte-Carlo simulation (the dotted blue line in Fig. 5) come from the statistical fluctuation and can be suppressed by using more particles in the simulation.

Given the polarization lifetime at 5 GeV beam energy from the tracking simulation, polarization lifetimes listed in Table 2 at a few representative electron beam energies are obtained by scaling with the 5th power of the energy.

Table 2: Polarization lifetime in the electron collider ring.

Energy	GeV	3	5	7	9	12
Polarization lifetime	Hours	116	9	1.7	0.5	0.1

Note that solenoid fields in the spin rotator are not scaled with the beam energy, hence $\hat{n}_0$ in the spin rotator is different at different energies. Polarization lifetimes obtained by simply scaling with the energy may not be very precise. Tracking simulations will be performed for the polarized electron beam at other energies, with proper settings of USR, to obtain accurate polarization lifetimes. In addition, spin matching is under way to extend the depolarization time, i.e. polarization lifetime.

However, there is no doubt that the polarization lifetime decreases with the electron beam energy. In particular, in the JLEIC electron collider ring, the Sokolov-Ternov self-polarization has a net depolarizing effect. This becomes a challenge at higher energies where the polarization lifetime is mainly determined by the net Sokolov-Ternov depolarization effect and is inversely proportional to the 5th power of the Lorenz factor. Therefore, continuous injection of highly polarized electron beams from the CEBAF is being considered to compensate the polarization loss [19, 20]. Continuous injection, also called top-off injection, has already been successfully applied in the PEP-II at SLAC [23] to increase the integrated luminosity and in the NSLS-II at BNL [24] to maintain the beam current. With the current state of the art, it is not a technical problem. The function of continuous injection in the JLEIC electron collider is two-fold. First, by mixing the partially depolarized stored beam with a fresh highly polarized one through continuous injection, the relative equilibrium polarization at a constant stored beam current is given by

$$\frac{P_{equ}}{P_i} = \frac{\frac{I_{inj}}{I_{ring}} f_{rev}}{\frac{1}{\tau_{dk}} + \frac{I_{inj}}{I_{ring}} f_{rev}} \qquad (12)$$

where P_{equ} is the attained equilibrium polarization, P_i is the injected polarization, I_{inj} is the average injected beam current, I_{ring} is the stored beam current, f_{rev} is the revolution frequency, and τ_{dk} is the Derbenev-Kondratenko polarization lifetime that can be estimated using the code SLICK. The relative equilibrium polarization as a function of the average injected current at a few of representative energies is shown in Fig. 7 using the nominal JLEIC design parameters. At a reasonably low average beam

current at the nA level, one can achieve a relative equilibrium polarization above 85%. Second, the requirement on obtaining large momentum acceptance and dynamic aperture is not strict because the beam lifetime should be comparable to the polarization lifetime. Decent momentum acceptance and dynamic aperture can help particles' extraction. This will significantly reduce the burden of handling the nonlinear beam dynamics.

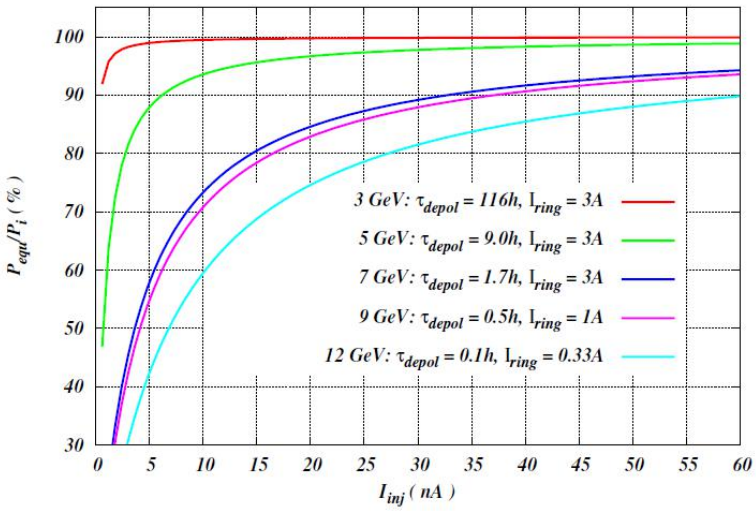

Figure 7: Relative equilibrium polarization as a function of average injected beam current at a few of representative energies.

2.3.5.6 *Numerical Analysis of Polarization Control Parameters*

Preliminary tracking simulations for a 5 GeV electron beam have also been carried out using ZGOUBI [25] to obtain two independent assessments of polarization. Note that ZGOUBI does not have the function to simulate the Sokolov-Ternov self-polarization process. Hence, tracking simulation performed using ZGOUBI only represents the polarization loss due to the imperfection of the magnetic fields and/or particle motions through the spin-orbit coupling effect. To have a fair comparison of simulation results, similar simulation conditions must be established in SLICK/SLICKTRACK and ZGOUBI. For these, only vertical misalignment is introduced to quadrupoles in the electron ring. This results in a rms vertical closed orbit excursion of ~87 μm at quadrupoles, close to its value in the tracking simulation using SLICK/SLICKTRACK discussed in the above section of polarization lifetime and continuous injection. The closed orbit excursion is shown in Fig. 8.

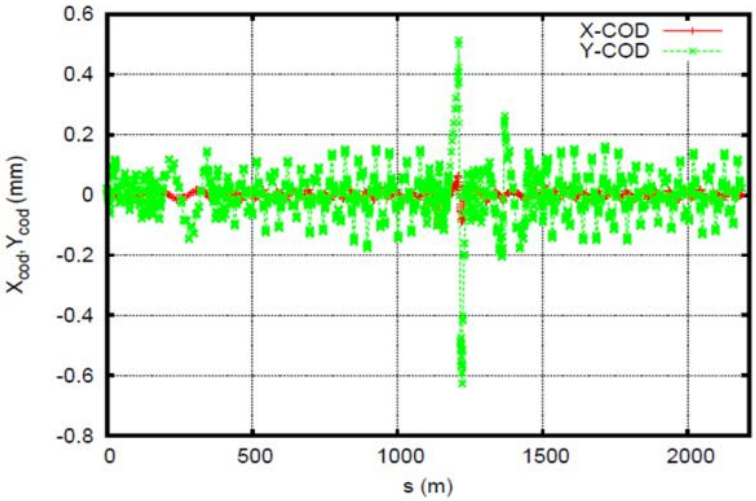

Figure 8: Closed orbit excursions with random quadrupole misalignments introduced in the vertical plan only.

In order to restrict the computing time, spin tracking simulations are performed using 20 particles with the two characteristic spin tunes, 0.01 and 0.027. According to the simulation results from SLICK/SLICKTRACK, a spin tune of 0.01 produces a long polarization lifetime and a spin tune of 0.027 gives zero polarization lifetime due to the first order synchrotron resonance. In order to balance the computing time consumption and time needed for electrons damped to the equilibrium condition caused by the synchrotron radiation, tracking simulations are performed for about 3 damping times (~ 40k turns) when the electron emittance is approaching to the equilibrium emittance.

Figure 9 presents the simulation result of polarization as a function of time with the spin tunes of 0.01. Here P is calculated by

$$P = \sqrt{{P_x}^2 + {P_y}^2 + {P_z}^2} \quad P_x = \frac{\sum_{n=1}^{m} S_x}{m} \quad P_y = \frac{\sum_{n=1}^{m} S_y}{m} \quad P_z = \frac{\sum_{n=1}^{m} S_z}{m} \tag{13}$$

Here S_x, S_y and S_z are three spin components in the radial, vertical and longitudinal directions, respectively. m = 20 is the number of particles in the simulation. Since only the spin-orbit coupling depolarization effect is represented in the tracking simulation, Equation 8 can be re-written as

$$P(t) = P_0 e^{-t/\tau_{dep}} \tag{14}$$

Then τ_{dep} can be obtained by

$$\tau_{dep} = -\frac{t}{\ln\left(\frac{P(t)}{P_0}\right)} \tag{15}$$

Using the tracking simulation result from Fig. 9, the depolarization time is ~11 hours with a spin tune of 0.01. However, the depolarization time is ~19 hours from the simulation using SLICK/SLICKTRACK. Such a factor of 2 difference in the depolarization time from simulations using two codes is questionable. It might be false because the depolarization time is calculated after 5 damping times in SLICK/SLICKTRACK when the particles are very much damped to the equilibrium emittance, while it is calculated in 3 damping times in ZGOUBI. A long computing time can help obtain more accurate depolarization time in simulations using ZGOUBI. However, this difference might also be real. The orbital motion is linearized in SLICK/SLICKTRACK, while nonlinear particle motion is included in ZGOUBI. More spin resonances may appear in ZGOUB only because of higher-order harmonics in the orbital motion, this results in more polarization loss comparing to the simulation result

from the SLICK/SLICKTRACK. Therefore, spin tracking simulations performed by using the code Bmad [26] are being considered to provide an additional assessment of electron polarization in the JLEIC.

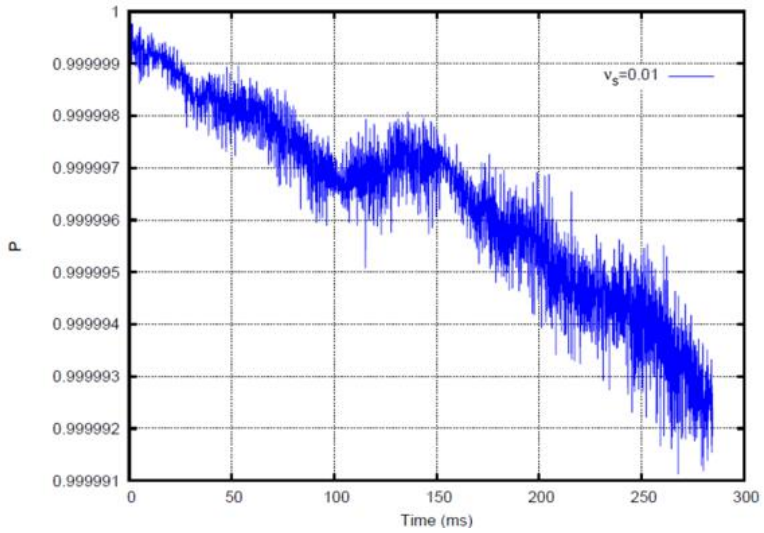

Figure 9: Polarization as a function of time with the spin tune of 0.01.

Spin tracking simulation with the spin tune of 0.027 is also performed using ZGOUBI. Figure 10 shows the simulation results with spin tunes of 0.01 and 0.027. Just as it is shown in the simulation using the code SLICK/SLICKTRACK, at the optimum spin tune of 0.01, the polarization decays much slower than the one at the spin tune of 0.027 where the first order synchrotron resonance occurs. The polarization lifetime with the spin tune of 0.027 is only about one minute. In a conclusion, tracking simulations using codes of SLICK/SLICKTRACK and ZGOUBI agree that spin tune of 0.01 is the optimum one to maintain a long polarization lifetime.

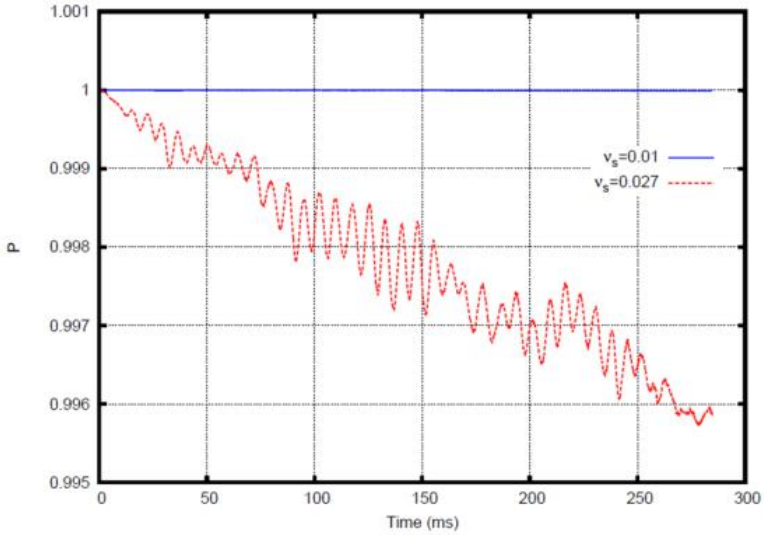

Figure 10: Polarization as a function of time with spin tunes of 0.01 and 0.027.

2.3.5.7 *References*

1. S. Abeyratne et al., "Science Requirements and Conceptual Design for a Polarized Medium Energy Electron-Ion Collider at Jefferson Lab", edited by Y. Zhang and J. Bisognano, arXiv:1209.0757 (2012).

2. S. Abeyratne et al., “MEIC Design Summary”, edited by G. Krafft, arXiv:1504.07961 (2015).
3. L.H. Thomas, “The Kinematics of an Electron with an Axis”, Phil. Mag. 3, 1 (1927) ; V. Bargmann, L. Michel, V.L. Telegdi, “Precession of the Polarization of Particles Moving in a Homogeneous Electromagnetic Field”, Phys. Rev. Lett. 2, 435 (1956).
4. S.Y.Lee, “Spin Dynamics and Snakes in Synchrotrons”, Singapore: World Scientific (1997).
5. A.A. Sokolov, I.M. Ternov, “On Polarization and Spin Effects in Synchrotron Radiation Theory”, Sov. Phys. Dokl. 8 N012, 1203 (1964) .
6. Ya.S. Derbenev, A.M. Kondratenko, “Polarization Kinetics of Particles in Storage Rings”, Sov. Phys. JETP 37, p.968 (1973).
7. S.R. Mane, “Electron-Spin Polarization in High-Energy Storage Rings. I and II”, Phys. Rev., A36, p.105, p.120 (1987).
8. D.P. Barber et al., five articles in proceedings of ICFA workshop “Quantum Aspects of Beam Physics”, Monterey, U.S.A., 1998, edited by P. Chen, World Scientific (1999).
9. K. Heinemann and G.H. Hoffstaetter, “Tracking Algorithm for the Stable Spin Polarization Field in Storage Rings using Stroboscopic Averaging”, Phys. Rev. E 54 (4), 4240 (1996).
10. G.H. Hoffstatter, M. Vogt, D.P. Barber, “Higher-Order Effects in Polarized Proton Dynamics”, Phys. Rev. ST Accel. Beams 11 (2) 114001 (1999).
11. V.N. Baier, V.M. Katkov, “Radiative Polarization of Electrons in a Magnetic Field”, Sov. Phys. JETP. 25, 944 (1967).
12. V.N. Baier, V.M. Katkov, V.M. Strakhovenko, “Kinetics of Radiative Polarization ”, Sov. Phys. JETP. 31, 908 (1970) .
13. D.P. Barber et al., “The First Achievement of Longitudinal Spin Polarization in a High Energy Electron Storage Ring”, Phys. Lett. 343B, 436 (1995).
14. D.P. Barber, G. Ripken, “Handbook of Accelerator Physics and Engineering”, edited by A.W. Chao and M. Tigner, World Scientific, 1st edition, 3rd printing (2006).
15. P. Chevtsov, Ya.S. Derbenev, G. Krafft, Y. Zhang, “Electron-Ion Collider Spin Manipulation System and its Mathematics”, Jlab-TN-10-026 (2010).
16. A. Zholents, V. Litvinenko, “On the Compensation of Solenoid Field Effects by Quadrupole Lenses”, BINP (Novosibirsk) Preprint 81-80 (1981). English translation: DESY Report L-Trans 289 (1984).
17. H. Sayed et al., “Spin Rotator Optics for MEIC”, in proceedings of 2010 International Particle Accelerator Conference (IPAC’10), Kyoto, Japan (2010), TUPEB044.
18. F. Lin, Y.S. Derbenev, A. Hutton, V.S. Morozov, F. Pilat, and Y. Zhang, “Towards a Small Emittance Design of the JLEIC Electron Collider Ring”, in proceedings of 2016 International Particle Accelerator Conference (IPAC’16), Busan, Korea (2016), WEPMW016.
19. F. Lin, D.P. Barber, Y.S. Derbenev, V.S. Morozov and Y. Zhang, “Polarized Electron Beams in the MEIC Collider Ring at JLab”, in proceedings of the 2013 International Workshop on Polarized Sources, Targets and Polarimetry (PSTP’13), PoS(PSTP2013)025 (2013).
20. F. Lin, D.P. Barber, Y.S. Derbenev, V.S. Morozov and Y. Zhang, “Preservation

of Electron Polarization in the MEIC Collider ring", in proceedings of 2014 International Particle Accelerator Conference (IPAC'14), Dresden, Hamburg, Germany (2014), MOPRO006.
21. S.Y. Lee and M. Berglund, "Overlapping Spin Synchrotron Sideband Resonances", Phys. Rev. E 54, 806 (1996).
22. A.W. Chao, "Evaluation of Radiative Spin Polarization in an Electron Storage Ring", Nuc. Ins. and Meth. 180, p.29-36 (1981).
23. J.L. Turner et al., "Trickle-Charge: a New Operational Mode for PEP-II", in proceedings of 9th European Particle Accelerator Conference (EPAC'04), Lucerne, Switzerland (2004).
24. T. Shaftan et al., "NSLS-II Injection Concept", in proceedings of 2005 Particle Accelerator Conference (PAC'05), Knoxville, Tennessee, USA (2005).
25. F. Meot, "The Ray-Tracking Code ZGOUBI", Nuc. Ins. and Meth., A427, 353 (1999).
26. D. Sagan, "Bmad: A Relativistic Charged Particle Simulation", Nuc. Ins. and Meth. Phys. Res. A, 558, p356-359 (2016)

2.3.6 **Ion Polarization in Figure-8 Ring**

Vasiliy Morozov
Thomas Jefferson National Accelerator Facility, Newport News, Virginia, USA
Mail to: morozov@jlab.org

2.3.6.1 ***Requirements and challenges***

The nuclear physics requirements to the JLEIC ion polarization design can be summarized as:

- High polarization (over 80%) for protons or light ions (d, $^3He^{++}$, and possibly $^6Li^{+++}$)
- Capability to adjust the polarization to both longitudinal and transverse directions at all collision points
- Sufficiently long polarization lifetime to maintain a high degree of the polarization during the store
- Frequent spin flipping

Ion polarization loss in accelerators is caused by spin resonances [1], i.e. periodic spin kicks correlated with the spin precession rate, or the spin tune. Due to the energy dependence of the spin tune in a conventional accelerator, an ion beam crosses an increasingly larger number of spin resonances during acceleration to a higher energy resulting in a partial or complete polarization loss [2]. An efficient technique to preserve the beam polarization is to make the spin tune equal to one half independent of the beam energy by inserting one or more Siberian snakes [3, 4] into the ring. A Siberian snake is a device that rotates the spin by $180°$ about an axis in the accelerator's plane. However, their use in the medium energy range of proton beams from a few to a few tens of GeV is complicated because longitudinal-field snakes become impractical due to their high required field integral [5] while transverse-field snakes still cause an unacceptably large orbit excursion [5, 6]. Moreover, any kind of a snake becomes impractical for deuterons above a few GeV due to their small anomalous magnetic moment ($G_d \approx -0.143$). Polarization control and spin flip may also be challenges in a

conventional ring. Adjusting the polarization direction requires large field integrals, which may affect the beam dynamics. Spin flipping in a conventional ring is usually done by sweeping an rf magnet's frequency through an induced spin resonance [7]. However, this technique causes a finite polarization loss during each spin flip [7]. Therefore, it may introduce a systematic error in an experiment and the polarization cannot be flipped many times.

2.3.6.2 *The figure-8 scheme*

An elegant solution for acceleration of any polarized ions including deuterons is to use an accelerator with a figure-8 ring configuration [8]. While beam polarization control schemes for conventional accelerators with Siberian snakes remain applicable to figure-8 accelerators, figure-8 accelerators offer new opportunities for manipulation of the beam polarization [9, 10] including spin flipping. In such an accelerator, rotation of the spin in one arc is completely cancelled by the other arc. The spin tune of an ideal figure-8 accelerator is zero for any beam energy, i.e. the particles are in the region of the zero-integer spin resonance. To stabilize the polarization direction, instead of strong snake fields, it is now sufficient to introduce a "weak" field to overcome the effect of the zero-integer spin resonance strength. For polarization stability, the spin tune ν induced by the weak field must significantly exceed the strength w of the zero-integer spin resonance: $\nu \gg w$. For example, a longitudinal field integral of about 1 T·m in the ion collider ring of JLEIC is sufficient to preserve the polarizations of both protons and deuterons during acceleration to 100 GeV [11]. To stabilize the spin tune during acceleration, the solenoid field should change proportionally to the beam momentum. To control the polarization direction at the collision point of any particle species including deuterons, a universal 3D spin rotator is inserted into the collider's experimental straight. As described below, it is based on "weak" solenoids and "forces" a given polarization direction $\vec{P} = \vec{n}$.

Both the booster and ion collider rings of JLEIC have the figure-8 design. Below we focus our discussion on the collider ring since its spin dynamics requirements are more demanding.

2.3.6.3 *Acceleration of polarized proton and deuteron beams in the JLEIC ion collider ring*

Polarizations of the proton and deuteron beams are preserved during acceleration from 8 GeV/c to 100 GeV/c in the ion collider ring using a week solenoid. To ensure the polarization stability, the spin tune ν induced by the solenoid must significantly exceed the strength of the zero-integer spin resonance $\vec{w}$: $\nu \gg w$. The resonance strength is the average spin field $\vec{w}$ (the zero-integer Fourier harmonic of the spin perturbation without a stabilizing solenoid) determined by deviation of the trajectory from the design orbit due to machine element errors and beam emittances. In the absence of a solenoid, the spin precesses by an angle of $2\pi w$ about the $\vec{w}$ direction in one particle turn. The resonance strength consists of two parts: a coherent part arising due to additional transverse and longitudinal fields along the closed orbit deviating from the design orbit and an incoherent part associated with the particles' betatron and synchrotron oscillations (beam emittances) [9]

$$\vec{w} = \vec{w}_{coh} + \vec{w}_{emitt}\,, \qquad w_{coh} \gg w_{emitt}\,. \tag{1}$$

In practice, the coherent part w_{coh} significantly exceeds the incoherent one w_{emitt}. The coherent part does not cause beam depolarization and only results in a simultaneous rotation of the polarization about the field determined by the strength and alignment errors of the collider elements. In principle, the direction and size of the coherent part of the resonance strength can be measured and taken into account for polarization control. To preserve the polarization, it is then sufficient to satisfy a weaker condition: $\nu \gg w_{emitt}$.

Figure 1 shows the β functions of the JLEIC collider lattice in the acceleration mode [12] used in our spin dynamics calculations. The origin of the coordinate frame is located at the collider's IP. Figure 1 also indicates the location of the solenoid stabilizing the spin during acceleration. The difference from the collision mode [13] where the β functions in the IP region reach 2.5 km is that, in the acceleration mode, the β functions in the detector section do not exceed 150 m.

Figure 2 shows the incoherent part of the proton resonance strength for the normalized emittance values of 1 mm·mrad in both the radial and vertical directions. As one can see, the value of the incoherent part does not exceed $2 \cdot 10^{-4}$ practically in the entire momentum range of the collider with the exception of the narrow "interference" peaks where the spin perturbations add up coherently in the arc magnets. The presented calculation indicates that a spin tune value of 10^{-2} induced by the solenoid field is sufficient to stabilize the spin with the normalized emittances of the betatron motion equal to 1 mm·mrad.

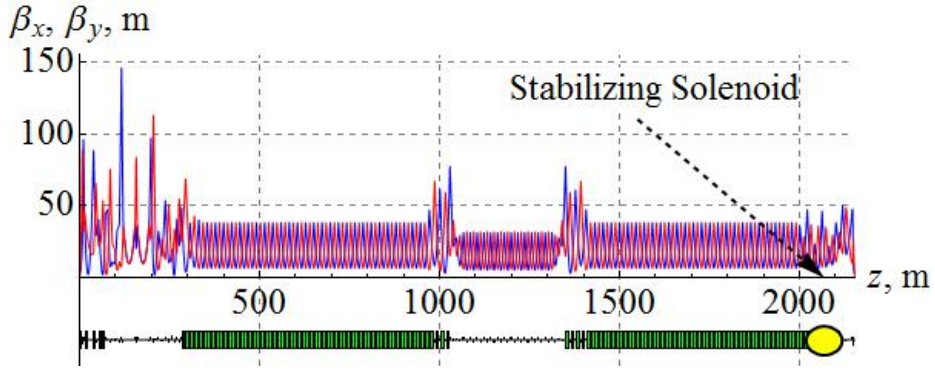

Figure 1: β functions of the ion collider ring in the injection mode.

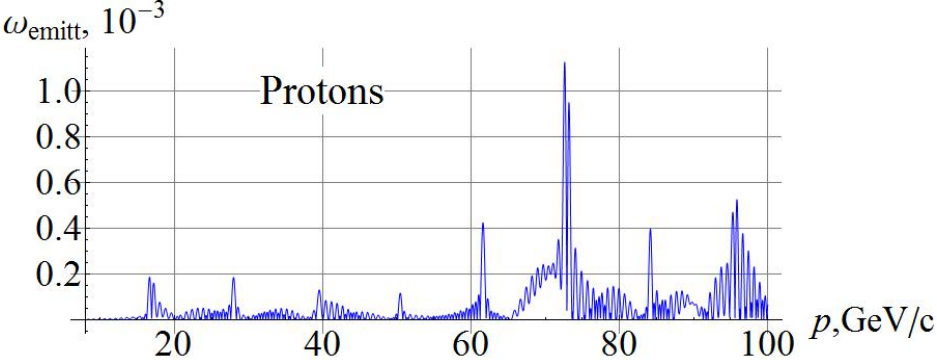

Figure 2: Incoherent part of the proton spin resonance strength for the injection mode optics of the JLEIC ion collider ring.

Figure 3 shows a similar graph of the dependence of the incoherent part of the deuteron spin resonance strength on the beam momentum. Our calculations assume that the transverse size of the deuteron beam is equal to the proton beam size, i.e. both of the

transverse normalized beam emittances are 0.5 μm. In contrast to protons, due to the small value of the deuteron anomalous magnetic moment, deuterons have only one interference peak at the momentum of 93 GeV/c whose value does not exceed $2 \cdot 10^{-8}$. Thus, a deuteron spin tune of $3 \cdot 10^{-3}$ induced by a solenoid significantly exceeds the incoherent part of the resonance strength.

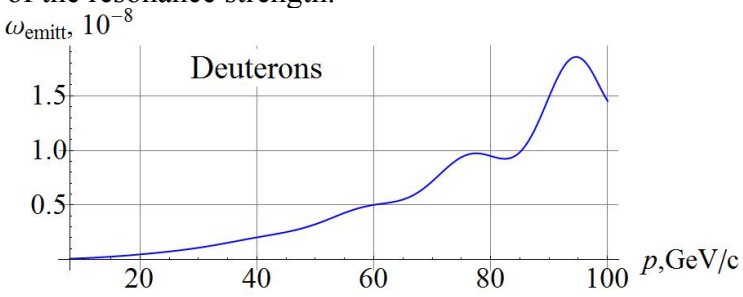

Figure 3: Incoherent part of the deuteron spin resonance strength for the injection mode optics of the JLEIC ion collider ring.

Let us now calculate the coherent part of the spin resonance strength using the statistical model with random shifts of all quadrupoles in the transverse directions. Figure 4 shows the coherent part of the proton resonance strength for the injection mode optics of the ion collider ring with random quadrupole misalignments resulting in a transverse closed orbit distortion of about 100 μm·rms. The statistical model calculates the most probable magnitude of the coherent part of the resonance strength not specifying its direction, which lies in the collider's plane. As in the case of the incoherent part, the coherent part of the resonance strength has interference peaks whose maximum values do not exceed $1 \cdot 10^{-2}$, which has an order of magnitude comparable to the field induced by the stabilizing solenoid. Figure 5 shows a graph of the coherent part of the deuteron spin resonance strength calculated using the statistical model of random quadrupole misalignments.

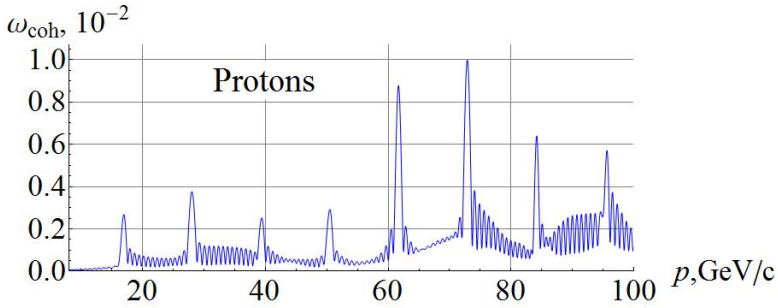

Figure 4: Coherent part of the proton spin resonance strength for the injection mode optics of the JLEIC ion collider ring.

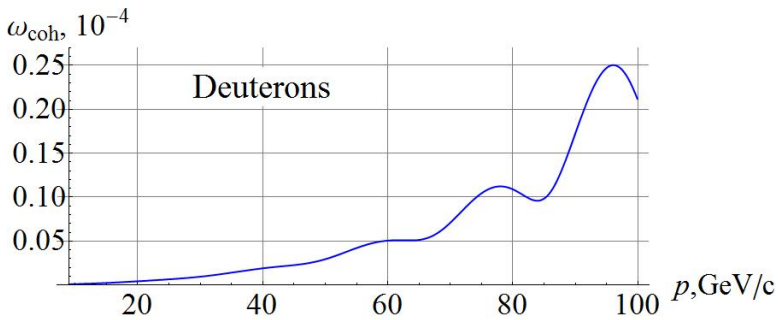

Figure 5: Coherent part of the deuteron spin resonance strength for the injection mode optics of the JLEIC ion collider ring.

The spin dynamics during acceleration in the ion collider ring is a precession about the spin field $\vec{h}$, which consists of the field $\vec{h}_{sol}$ induced by the stabilizing solenoid and the resonance strength $\vec{w}$: $\vec{h} = \vec{h}_{sol} + \vec{w}$ [9]. During acceleration the field $\vec{h}_{sol}$ is maintained constant while the resonance strength $\vec{w}(t)$ experiences significant changes in the regions of the interference peaks.

The beam polarization substantially depends on the field ramp rate in the arc magnets. When using superconducting magnets with a field ramp rate of ~3 T/min, acceleration happens adiabatically, which means that, in a characteristic time of change in the spin field, the spin makes a large number of turns. During adiabatic acceleration, the spin follows the $\vec{h}$ field direction, which can significantly deviate from the longitudinal direction at the locations of the interference peaks of the coherent part of the resonance strength. However, this does not signify polarization loss, the beam polarization restores its longitudinal direction in places where $h_{sol} \gg w_{coh}$.

Let us present calculations of the spin dynamics during acceleration of protons and deuterons in the JLEIC ion collider ring made using a spin tracking code Zgoubi [14]. Figure 6 shows the longitudinal spin components in the ion collider ring during acceleration of 3 protons with $\Delta p/p = 0$ (green line), $\Delta p/p = 10^{-3}$ (red line) and $\Delta p/p = -10^{-3}$ (blue line). As one can see, the graphs of the longitudinal spin components practically do not differ from each other (the red line covers up the blue and green lines), i.e. the synchrotron energy modulation does not give a noticeable contribution to the ion spin motion when stabilizing the polarization by a weak solenoid in the JLEIC ion collider ring.

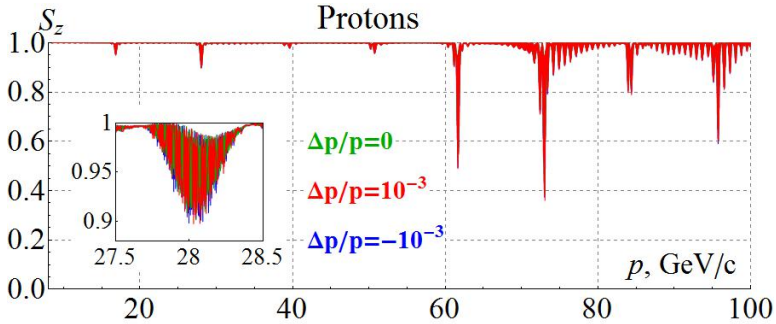

Figure 6: Longitudinal spin component during acceleration of three protons in the ion collider ring.

All particles were launched with the same initial conditions: $S_{z0} = 1$, $x_0 = 0.61$ mm, $x_0 = 0$ rad, $y_0 = 0.27$ mm, $y_0 = 0$ rad. The field ramp rate was ~3 T/min (the particles were accelerated in 8.3 million turns). During acceleration, the spin preserves its component along the spin field, which lies in the orbit plane and noticeably deviates from the longitudinal direction in the regions of the "interference" peaks of the coherent part of the resonance strength at momenta of about 60 GeV/c and 75 GeV/c, where the resonance strength becomes approximately equal to the size of the solenoid spin field. The spin tune induced by the solenoid during acceleration is 10^{-2}.

The simulation in Fig. 6 is done with a closed orbit excursion of 100 μm·rms. If needed the tolerances on alignment of the lattice elements can be relaxed. The strength of the stabilizing solenoid can be increased. One then has to account for the fact that the

solenoid itself gives a contribution to the spin resonance strength due to an angle between the distorted closed orbit and the solenoid axis. This results in a transverse magnetic field component, which has practically no effect on the orbital motion but can have a strong effect on the spin motion especially for a proton beam at high energies ($\gamma G \gg 1$). This contribution can be minimized either by a more precise alignment of the solenoid axis or by choosing such a collider lattice, which has a sufficiently small value of the spin response function at the solenoid location. The response function is the spin Green's function determined and controlled by the linear lattice. It describes the effect of the ring as a whole on the spin due to a δ-function-like radial field as described above [9]. Another option is to compensate the coherent part of the spin resonance strength at the experimental energy using a 3D spin rotator [9, 10].

Similar graphs of the longitudinal components of the deuteron spin are shown in Fig. 7. The initial conditions and the solenoid field strength during acceleration were chosen the same as in the proton case. In contrast to protons, the change in the deuteron longitudinal polarization during acceleration does not exceed $2 \cdot 10^{-5}$ even in the interference peak. This example demonstrates a high stability of the deuteron polarization in figure-8 rings, which can be used for high-precision experiments. To the contrary, in conventional accelerators with preferred periodic spin orientation, control of the deuteron polarization and its preservation during acceleration to 100 GeV/c is a practically unrealistic task.

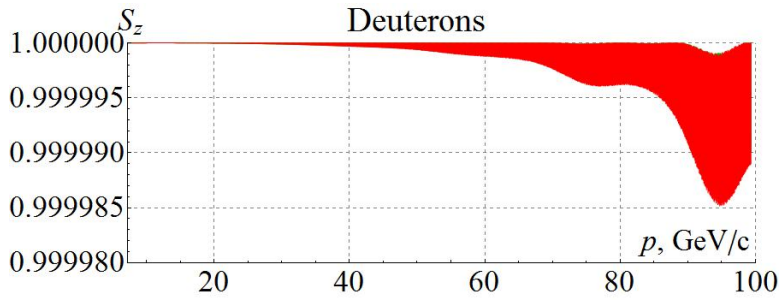

Figure 7: Longitudinal spin component during acceleration of three deuterons in the ion collider ring.

2.3.6.4 *3D spin rotator and polarization control in the JLEIC ion collider ring*

The beam polarization in the ion collider ring is controlled using 3D spin rotators. Each 3D spin rotator consists of three modules for control of the radial, vertical, and longitudinal beam polarization components. Figure 8(left) shows the module for control of the radial polarization component n_x, which consists of two pairs of opposite-field solenoids and three vertical-field dipoles producing a fixed orbit bump. The control module for the vertical polarization component n_y is the same as that for the radial component except that the vertical-field dipoles are replaced with radial-field ones (Fig. 8(center)). To keep the orbit bumps fixed, the fields of the vertical- and radial-field dipoles must be ramped proportionally to the beam momentum. The module for control of the longitudinal polarization component n_z consists of a single weak solenoid (Fig. 8(right)). There is a substantial flexibility in the placement and arrangement of these modules in the collider.

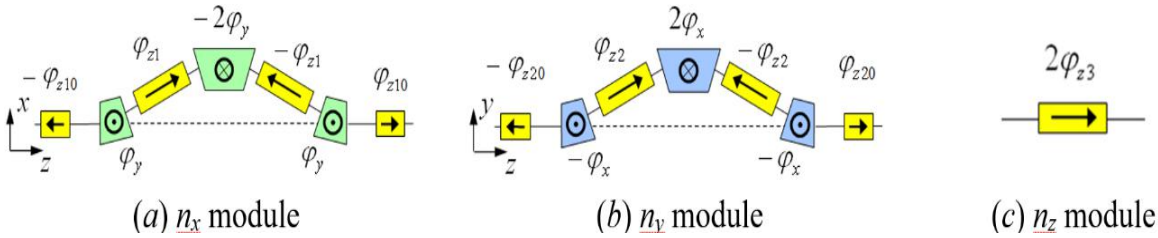

Figure 8: 3D spin rotator modules for control of the radial (left), vertical (center), and longitudinal (right) polarization components.

The formulae for calculation of the spin rotation angles φ_{zi} in the control solenoids for a given polarization direction at the 3D spin rotator location $n = (n_x, n_y, n_z)$ and a given value of the spin tune ν (linear approximation in ν) are:

$$n_x \text{ module: } \varphi_{z1} = \pi\nu\frac{n_x}{\sin\varphi_y}, \quad \varphi_{z10} = \frac{\pi\nu}{2}\frac{n_x}{\tan\varphi_y}, \quad \varphi_y = \gamma G\alpha_{orb},$$

$$n_y \text{ module: } \varphi_{z2} = \pi\nu\frac{n_y}{\sin\varphi_x}, \quad \varphi_{z20} = \frac{\pi\nu}{2}\frac{n_y}{\tan\varphi_x}, \quad \varphi_x = \gamma G\alpha_{orb}, \tag{2}$$

$$n_z \text{ module: } \varphi_{z3} = \pi\nu n_z.$$

The field B_{zi} of a control solenoid of length L_{zi} can be calculated using the formula:

$$B_{zi} = \frac{\varphi_{zi}}{(1+G)L_{zi}}. \tag{3}$$

Schematic placement of the 3D rotator elements in the collider ring's experimental straight is shown in Fig. 9 [9, 10]. The lattice quadrupoles are shown in black, the vertical-field dipoles are green, the radial-field dipoles are blue, and the control solenoids are yellow. With each module's length of ~7 m, the fixed orbit deviation in the bumps is ~15 mm in the whole momentum range of the collider. The 3D spin rotator can provide any desired polarization orientation at the interaction point. The maximum required dipole and solenoid magnetic field strengths are 3 and 3.6 T, respectively. Figure 10 shows placement of the 3D rotator magnetic elements in the ion collider ring with the following parameters: $L_x = L_y = 0.6$ m, $L_{zi} = 2$ m, $L_{zi0} = 1$ m, $\alpha_{orb} = 0.31°$.

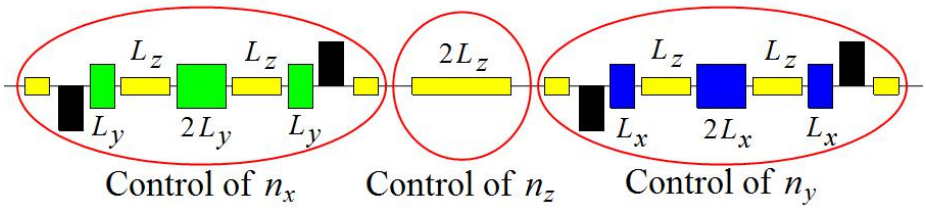

Figure 9: Schematic placement of the 3D spin rotator elements.

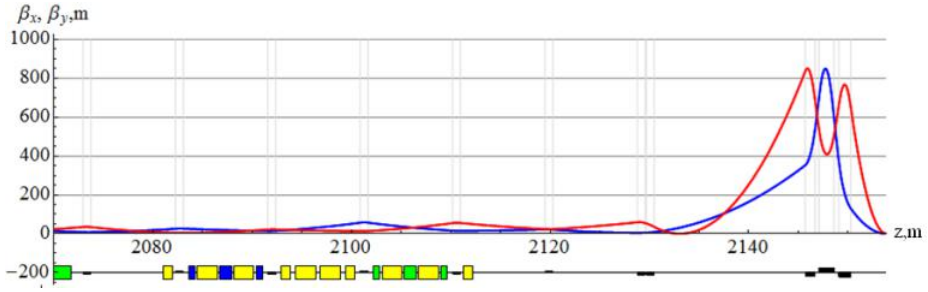

Figure 10: Placement of the 3D rotator in the ion collider lattice.

There are always errors in the strengths of the collider's magnetic lattice elements as well as errors in alignment of these elements along the collider's design orbit. These lattice imperfections lead to a change in the collider's closed orbit. As a result, particle spins experience additional coherent rotations caused by perturbing magnetic fields when the particles are moving along the distorted periodic closed orbit. The combined effect of these magnetic fields on the spin determines the coherent part of the resonance strength.

One of the main reasons for appearance of the coherent resonance strength component are random quadrupole shifts resulting in a change in the collider's closed orbit. Figures 11 show diagrams of random quadrupole shifts in the vertical and radial directions, respectively, which are used in calculations of the proton spin motion in the collider. The diagrams also indicate the locations of the control 3D rotator (1st 3D-rotator) and of the compensating 3D rotator (2nd 3D-rotator). The indicated quadrupole alignment errors result in a closed orbit distortion in the arcs of a few hundred μm (see Fig. 12).

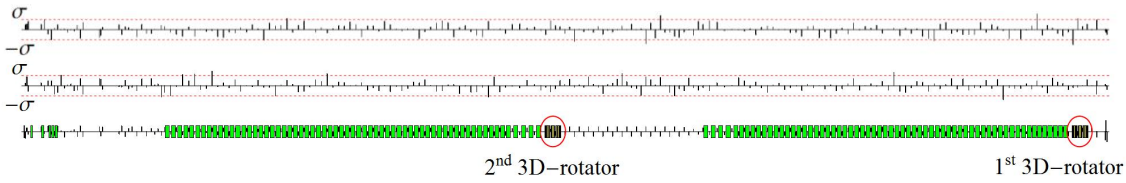

Figure 11: Diagrams of normally distributed radial (top) and vertical (bottom) quadrupole alignment errors in the ion collider ring.

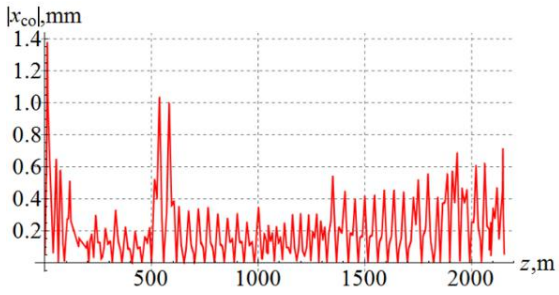

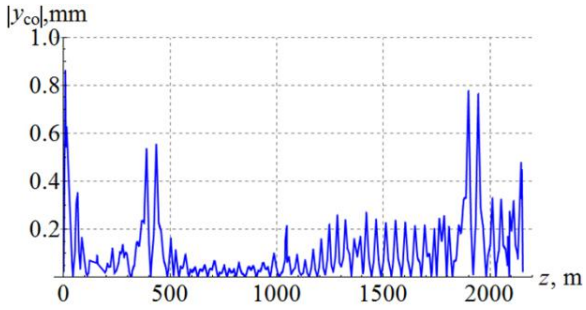

Figure 12: Radial (left) and vertical (right) orbit excursions with random misalignments of all quadrupoles in the ion collider ring according to the diagrams in Fig. 11.

Figure 4 shows that the coherent part of the proton resonance strength outside of the interference peaks reaches $w_{coh}^{prot} \approx 2.5 \cdot 10^{-3}$ in the ion collider ring. This means that using a 3D rotator with a spin tune of 10^{-2} to control the proton polarization already becomes, at least, inconvenient, since, during a spin manipulation process, one should always make a "correction" of the spin field for the coherent part of the resonance strength. Besides, the coherent part grows with increase in energy along with the fields required for its compensation. Nevertheless, the solenoid fields of the control 3D rotator can be left at the same level if one compensates the coherent part of the resonance strength using a second 3D rotator with static field located in the opposite straight (see Fig. 11).

The magnitude and direction of the spin field component associated with the coherent part of the zero-integer spin resonance strength can be determined experimentally and the parameters of the compensating 3D spin rotator can be set appropriately. Figure 13(left) shows a graph of the spin component evolution in a non-deal collider lattice when setting vertical proton polarization at the interaction point with compensation of the coherent part of the resonance strength. The parameters of the control 3D rotator are: $n_y = 1$ and $\nu = 0.01$. The beam momentum is 60 GeV/c. The particle is launched along the closed orbit with vertical spin. For comparison, Fig. 13(right) shows a similar graph without compensation of the coherent part of the resonance strength. The provided example shows that a non-ideal collider with compensation of the coherent part of the spin resonance strength becomes equivalent to an ideal one in terms of the polarization control.

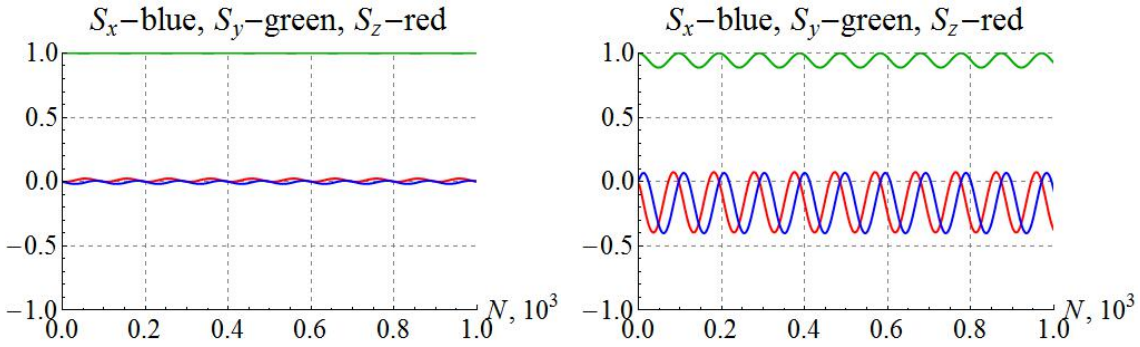

Figure 13: Setting vertical proton polarization in a non-ideal collider lattice with (left) and without (right) compensation of the coherent part of the resonance strength.

2.3.6.5 *Spin flipping in the JLEIC ion collider ring*

A 3D spin rotator allows one to make reversals of the particle spins during an experiment by slowly (adiabatically) changing the solenoid fields of the 3D spin rotator to rearrange the spin motion [15]. To preserve the polarization degree, one must meet the condition of adiabatic change in the spin direction, which has the following form for the number of particle turns N_{flip} necessary to flip the spin:

$$N_{flip} \gg 1/\nu\,. \tag{4}$$

We get a limit on the number of turns for a spin flip of $N_{flip}^{prot} \gg 10^2$ for protons and $N_{flip}^{deut} \gg 10^4$ for deuterons, which, in terms of the flip time, means $\tau_{flip}^{prot} \gg 1$ ms for protons and $\tau_{flip}^{deut} \gg 0.1$ s for deuterons. In practice, the adiabaticity condition is automatically satisfied, since the spin reversal time is limited by the field ramp rate in the super-conducting solenoids.

Let us illustrate proton spin reversals in the vertical (yz) plane of the collider. The pattern of how the spin field should change with the number of turns when making spin reversals is shown in Fig. 14. The number of turns is normalized to N_0, which is the number of turns for rotation of the spin from vertical to longitudinal direction. The vertical h_y (green line) and longitudinal h_z (red line) components of the spin field are set using the solenoids of the vertical n_y- and longitudinal n_z-modulesof the 3D spin rotator. The magnitude of the spin field sets the spin tune value. Change in the spin tune normalized to the maximum field h_{max} is shown in Fig. 15.

Figure 16 shows the proton spin components as a function of the number of turns for the indicated pattern of change in the spin field using the 3D rotator. Rotation from vertical to longitudinal direction and back is done in 50 thousand turns. The maximum spin tune value is 10^{-2}. The spin components then follow the shape of the spin field pattern practically everywhere, as it should be in case of adiabatic motion. Exceptions are small regions where the spin field pattern has sharp corners, in which the adiabaticity condition is violated. The spin starts directed vertically up. Then a spin rotation takes place in 50 thousand turns. As we can see, the spin undergoes sequential rotations from the vertical-up direction to the longitudinal direction along the particle velocity, then to the vertical-down direction and finally to the longitudinal direction opposite to the particle velocity. The presented calculations demonstrate the capability of spin-flipping using a 3D spin rotator. Thus, the figure-8 JLEIC ion collider provides a unique capability of doing high-precision experiments with polarized ion beams.

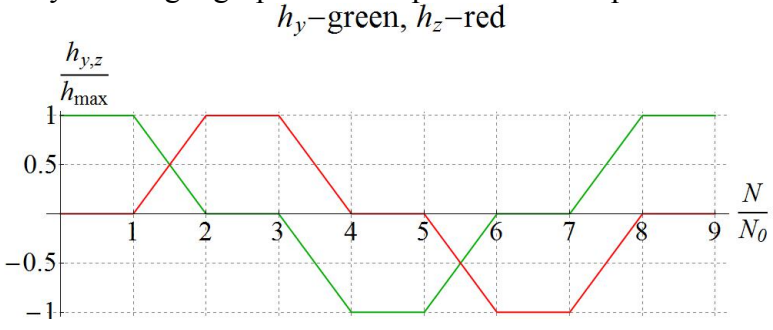

Figure 14: Pattern of change in the vertical h_y and longitudinal h_z spin field components when making spin reversals in the collider ring.

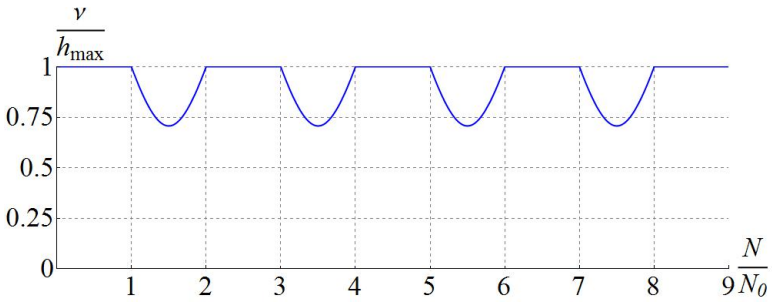

Figure 15: Change in the spin tune in units of the maximum spin field h_{max} when rotating the spin in the collider.

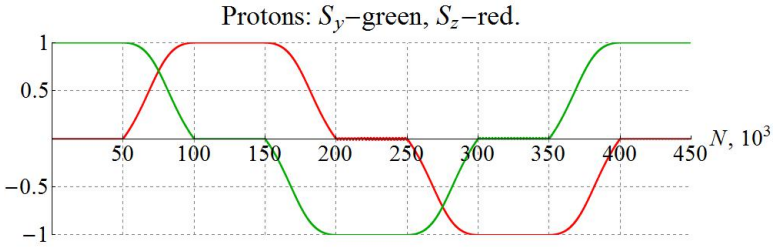

Figure 16: Change in the spin tune in units of the maximum spin field h_{max} when rotating the spin in the collider.

2.3.6.6 *References*

1. S.Y. Lee, Spin Dynamics and Snakes in Synchrotrons (World Scientific, Singapore, 1997).
2. F. Khiari et al., Phys. Rev. D 39, 45 (1989).
3. Ya. Derbenev and A. Kondratenko, Part. Accel. 8, 115 (1978).
4. H. Huang, in Proc. SPIN 2002, AIP Conf. Proc. 675 (2003), p. 122.
5. T. Roser, Handbook of Accelerator Physics and Engineering, 3rd edition, edited by A.W. Chao and M. Tigner (World Scientific, Singapore, 2006), p. 168.
6. V. Ptitsin and Y. Shatunov, NIM A398, 126 (1997).
7. V.S. Morozov et al., Phys. Rev. ST-Accel. Beams 7, 024002 (2004).
8. Ya.S. Derbenev, "The Twisted Spin Synchrotron", University of Michigan report, UM HE 96-05, 1996.
9. A.M. Kondratenko et al., "Ion Polarization Scheme for MEIC", arXiv:1604.05632 [physics.acc-ph], 2016.
10. Ya. S. Derbenev et al., Int. J. Mod. Phys. Conf. Ser. 40, 1660090 (2016).
11. A. M. Kondratenko et al., in Proc. IPAC'17, Copenhagen, Denmark, May 2017, paper WEPIK038, pp. 3014-3017.
12. V.S. Morozov et al., in Proc. IPAC'16, Busan, Korea, May 2016, paper WEPMW012, pp. 2445-2447.
13. Y. Nosochkov et al., in Proc. IPAC'15, Richmond, VA, USA, May 2015, paper TUPWI032, pp. 2311-2314.
14. F. Méot, Nucl. Instr. Meth A, vol. 427, pp. 353–356, 1999.

15. A.M. Kondratenko et al., in Proc. NAPAC'16, Chicago, IL, USA, October 2016, paper TUPOB30, pp. 558-560.

2.3.7 Electron Cooling and ERL Cooler

Steve Benson, He Zhang and Yuhong Zhang
Thomas Jefferson National Accelerator Facility, Newport News, Virginia, USA
Mail to: felman@jlab.org, hezhang@jlab.org, yzhang@jlab.org

2.3.7.1 *Multi-Stage Cooling Scheme*

For JLEIC protons or ion beams, there is no synchrotron radiation damping, therefore an efficient damping mechanism, namely, beam cooling, must be introduced in order to deliver high luminosity performance. Such beam cooling must enable a significant reduction of the proton and ion beam emittance, up to an order of magnitude in all directions, thus delivering a very short bunch with a very small beam spot at collision. It also must counteract the IBS induced emittance degradation during beam store, thus extending the luminosity lifetime.

The choice for the JLEIC design is conventional electron cooling, a proven technology. JLEIC also adopts a scheme of multi-phase cooling [1,2,3] which utilize electron cooling both during formation of the ion beam, particularly including an initial cooling at low energy, and during collision for enhancing the cooling efficiency. This scheme is based on a simple fact that the cooling time is proportional to ion beam emittance and beam energy. Therefore, electron cooling is much more efficient when the ion beam energy is low. At the collision energy, the cooling time also sees a reduction due to a much smaller emittance as a result of the initial cooling at low energy. Combining both cooling phases, it is expected the total cooling time should be orders of magnitude shorter than that of performing cooling only at high (collision) energy.

Table 1 summarizes the multiple cooling phases in JLEIC for a proton beam [4]. It can be seen that DC electron cooling is first utilized to maintain the proton beam emittance in the collider ring at injection energy during stacking of long bunches transferred from the booster ring. After stacking is completed, the proton beam emittance is reduced by DC cooling to the design values of collision. The protons then are boosted to collision energy and promptly cooled by a high energy bunched electron beam from an ERL circulator cooler for conditioning and maintaining the beam emittance. Figure 1 provides an illustration of the JLEIC proton beam formation process with electron cooling.

Table 1. Multi-phase electron cooling scheme for JLEIC proton beam

Ring	Functions	Kinetic energy (GeV/MeV)		Cooler type
		Proton	Cooling electron	
Booster	Injection and accumulation	0.285		
Collider	Maintain emittance during stacking	7.9	4.3	DC
	Pre-cooling for emittance reduction	7.9	4.3	
	Maintain emittance during collision	Up to 100	Up to 54.5	ERL

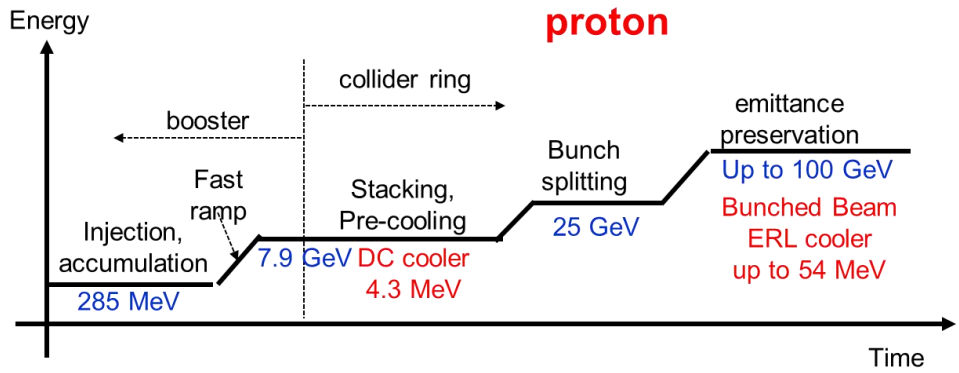

Figure 1: An illustration of JLEIC proton beam formation with electron cooling

The multi-phase cooling of JLEIC heavy ions is similar, nevertheless DC electron cooling is also utilized for assisting beam accumulation in the booster. As an example shown in Table 2 and Figure 2, partially stripped lead ions ($^{208}Pb^{32+}$) are injected from the pulsed warm/SRF ion linac into the booster and accumulated with assistance of low energy DC cooling to increase the beam intensity. The accumulated lead ion beam is boosted to 2 GeV, and transferred to the collider ring for stacking under a DC cooling protection of its emittance. Unlike a proton beam, pre-cooling of lead ions for emittance reduction is performed not at the injection energy (2 GeV) due to the space charge limit, rather after the lead beam energy is boosted to 7.9 GeV, to alleviate the space charge effect. The cooling scheme after that stage is basically same for proton and all ion beams.

Table 2. Multi-phase electron cooling scheme for JLEIC lead ion beam

Ring	Functions	Kinetic energy (GeV / MeV)		Cooler type
		Lead ion	Cooling electron	
Booster	Injection and accumulation	0.1	0.054	DC
Collider	Maintain emittance during stacking	2	1.1	DC
	Pre-cooling for emittance reduction	7.9	4.3	
	Maintain emittance during collision	Up to 40	Up to 54.5	ERL

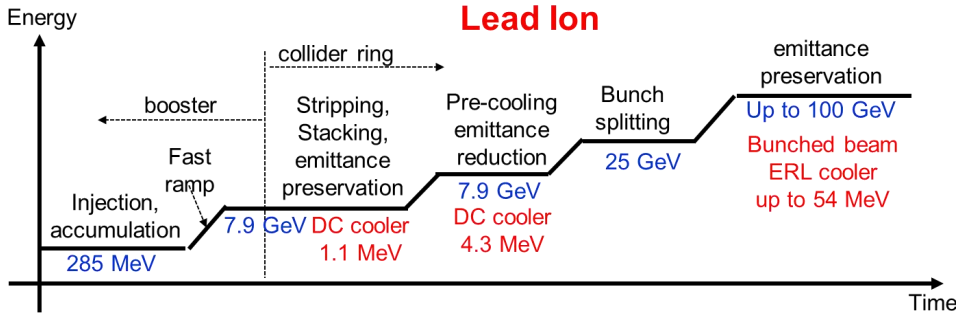

Figure 2: An illustration of JLEIC lead ion beam formation with electron cooling

Three electron coolers are required to implement the JLEIC cooling scheme. In the booster, a low voltage DC cooler with electron energy up to 55 keV is needed for cooling during ion accumulation. In the collider ring, a modest high voltage DC cooler with electron energy up to 4.3 MeV is needed to pre-cool proton and ion beams for emittance reduction. DC cooler is a matured technology. Two high voltage DC coolers, a non-magnetized 4.3 MeV cooler and a 2 MeV magnetized cooler have been constructed and operated at Recycler of Fermilab [5] and at COSY, Julish [6,7]. The JLEIC DC cooler will adopt the technology of these two coolers. In the JLEIC collider

ring, a high energy bunched beam cooler with electron energy up to 54 MeV is needed for cooling of ion beams during collision. This is ne critical accelerator R&D [8,9].

It should be pointed out one important design feature of the JLEIC electron coolers is magnetized electron beam. Cooling of ions by a magnetized electron beam has advantages in enhancement of cooling efficiency and in transport of electron beam in the circulator ring of the high energy ERL cooler.

2.3.7.2 *Simulation for Proton Beam Cooling*

JSPEC (Jlab Simulation Package for Electron Cooling) [10,11] is an open source numerical package for IBS effect and electron cooling process simulation developed at JLab. The goal of JSPEC is to enhance the simulation capability for electron cooling in JLEIC project. It will preferentially fulfil the needs of JLEIC design. The program simulates the evolution of the macroscopic beam parameters, such as emittances, momentum spread and bunch length, in different electron cooling scenarios with any combination of bunched or coasting ion beam with DC or bunched cooling electron beam. JSPEC has been thoroughly benchmarked with BETACOOL [12] for accuracy and efficiency. We have observed a large improvement of efficiency. For a typical simulation with both the IBS effect and electron cooling for JLEIC, JSPEC can be more than ten times faster than BETACOOL. JSPEC is actively used in our simulation study on electron cooling at JLab.

2.3.7.3 *Stacking and Pre-cooling in the Collider Ring*

No cooling is needed for the proton beam in the booster. The proton beam is injected from the booster to the collider at 7.9 GeV. Parameters of the proton beam at the beginning of the stacking are listed in Table 3. To study the necessity of cooling during the stacking process, the change of the proton beam due to the IBS effect is simulated for an hour, as shown in figure 3 (left). During the ~4 minutes of stacking, the increases of emittance and momentum spread are very limited.

The pre-cooling stage starts after the stacking of the proton beam in the collider ring. The DC cooler, 30 m long providing 3 A cooling electron beam, is used to reduce the normalized emittance to the desired value in collision. The pre-cooling process is simulated and the result is shown in Figure 2 (right). The equilibrium is reached within 15 minutes. The emittance is reduced below 0.5 mm·mrad and the momentum spread to 4×10^{-4}.

Table 3: Proton beam parameter for stacking in collider

Kinetic energy	*GeV*	*7.9*
Emittance	*mm·mrad*	*2.2/2.2*
Momentum spread	$\times 10^{-4}$	*6*
Particle number	$\times 10^{11}$	*6.58*
Bunch length	*M*	*7*

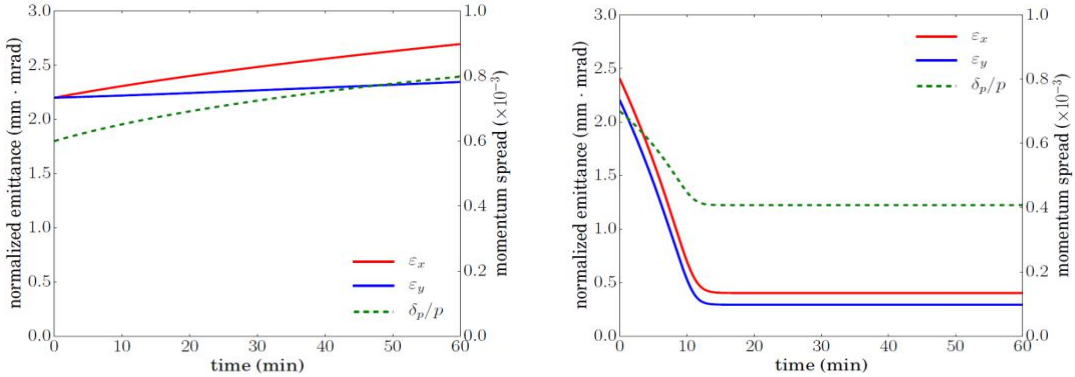

Figure 3: Expansion due to IBS (left) and pre-cooling (right) of the proton beam at 7.9 GeV.

2.3.7.4 *Cooling during collision*

After the pre-cooling, the proton beam is accelerated to the collision energy of 40 GeV to 100 GeV. Acceleration to the collision energy does not change the normalized emittance. After the beam splitting, the proton beam forms more than 3000 short bunches. IBS effect is very strong for the high intensity proton bunch, so the ERL based bunched beam cooler is used to mitigate the IBS effect and maintain the emittance of the proton beam during collision. This is the most challenging part of the JLEIC cooling scheme, due to the high energy and high density of the proton beam.

JLEIC covers a wide CM energy range from 21.9 GeV to 63.3 GeV. The property of the proton beam varies for different CM energies. In the following, we present preliminary simulation study on the cooling of the proton beam at 100 GeV energy for the two design points of 44.7 GeV and 63.3 GeV CM energies. The property of both the proton beams is listed in Table 3. Due to the absence of the vertical dispersion, the IBS effect in the vertical direction is much weaker than that in the horizontal direction. In both cases, the horizontal IBS expansion rate is tens of times larger than the vertical one. Assuming a bunched electron beam with 3.2 nC per bunch, the cooling in the vertical direction and the longitudinal direction is much stronger than the IBS effect, but in the horizontal direction the cooling is not strong enough to mitigate the IBS effect.

Table 4: Proton beam parameters for 44.7 & 66.3 GeV CM energy

Parameters	*Unit*	*44.7 GeV*	*66.3 GeV*
Kinetic energy	*GeV*	*100*	*100*
Emittance	*mm·mrad*	*0.5/0.1*	*0.9/0.18*
Momentum spread	$\times 10^{-4}$	*8*	*8*
Particle number	$\times 10^{10}$	*0.98*	*3.9*
Bunch length	*Cm*	*1*	*1*

Introducing proton beam dispersion at the cooler transfers the extra longitudinal cooling into the transverse direction. Introducing transverse coupling can translate the horizontal IBS effect into the vertical direction, which then can be mitigated by the extra vertical cooling. However, it is still very difficult to fully compensate the IBS effect with cooling even after introducing the dispersion and transverse coupling. In the following, two examples are presented in which the IBS effect and the electron cooling are in equilibrium or close to the equilibrium and the emittance of the proton beam is maintained. But in both examples, the proton beam property is slightly degenerated to reduce the IBS effect. Figure 3 (left) shows the cooling for the proton beam in the 44.7 GeV CM energy collision. The emittance remains constant. Momentum spread decreases very slowly. The current of the proton beam is 82% of the proposed value in Table 3, with 0.80×10^{10} protons per bunch. The emittance (0.5/0.15 mm·mrad) and the rms bunch length (1.5 cm) are also slightly larger than the proposed value. Transverse coupling of 40% is assumed. The luminosity with such a proton beam is 1.40×10^{34} $cm^{-2}s^{-1}$, lower than the proposed luminosity of $2.14 \times 10^{34} cm^{-2}s^{-1}$, but still above $10^{34} cm^{-2}s^{-1}$. Figure 3 (right) shows the cooling for the proton beam in the 66.3 GeV CM energy collision. The cooling and the IBS are in equilibrium and the emittance and the momentum spread remain constant. The current of the proton beam is 38% of the proposed value in Table 3, with 1.48×10^{10} protons per bunch. The emittance (1.25/0.38 mm · mrad) and the rms bunch length (2.5 cm) are also larger than the proposed value. Transverse coupling of around 40% is assumed. The luminosity with such a proton beam is 1.31×10^{33} $cm^{-2}s^{-1}$, lower than but in the same order with the proposed luminosity of $5.9 \times 10^{33} cm^{-2}s^{-1}$.

The proposed luminosity is considered achievable after deeper understanding and further optimization of the cooling process in future.

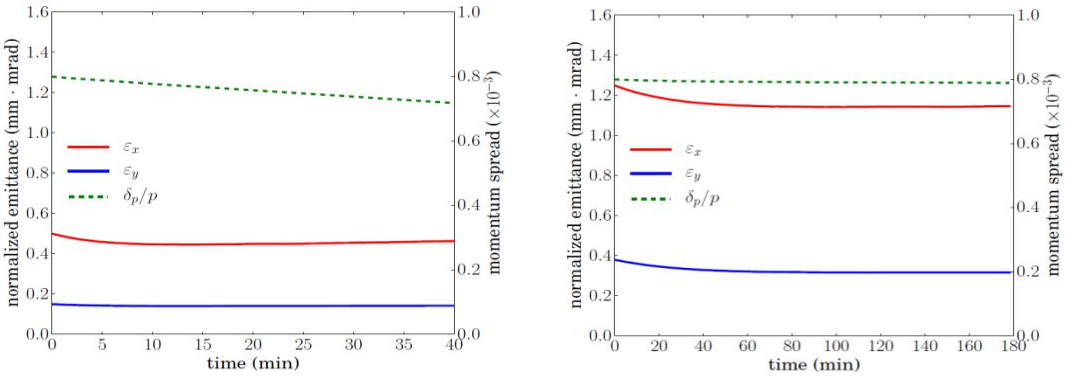

Figure 3: Proton beam cooling during collision for 44.7 GeV (left) and 63.5 GeV (right) CM energy.

2.3.7.5 *Simulation for heavy ion beam cooling*

2.3.7.5.1 DC Cooling for the heavy ion beam injection in the booster ring

Heavy ion beams are injected into the booster ring at 100 MeV/u. During the phase space painting injection process, electron cooling is needed to enhance the ion density in the booster ring. At this energy, traditional DC electron cooling is very efficient and is considered a mature technique.

2.3.7.5.2 Stacking and pre-cooling in the collider ring

In the following we present the simulations on the cooling of the lead ion, $^{208}Pb^{82+}$, as an epitome of heavy ions. The heavy ion beam is injected into the collider at 2.0 GeV/u. Parameters of the lead ion beam is listed in Table 4. First, we simulate the evolution of the beam in an hour without cooling. Due to the IBS effect, the emittances and the momentum spread grows very fast as shown in Fig. 4 (left). Even in ten minutes, the emittance increases to about 5.5 mm·mrad, about 3.6 times of the initial value. It will vitiate the luminosity and make the cooling in the following stage more difficult if the IBS effect is not mitigated. But the emittance should not be reduced at this stage to prevent large space charge tune shift. Simulations show that a DC cooling with 0.62 A electron beam can compensate the IBS effect and keep the emittance constant during the stacking as shown in Fig. 4 (middle).

After the stacking, the lead ion beam is accelerated to 7.9 GeV/u for pre-cooling. At this energy, the space charge tune shift is much smaller, which allows us to reduce the emittance. The same DC cooler for stacking is also used for pre-cooling, but with a higher current. Figure 4 (right) shows the pre-cooling process with a 2A electron beam. The equilibrium is reached within one minute. The emittance can be reduced below 0.5 mm·mrad, and the momentum spread to 4×10^{-4}. The cooler provides enough cooling strength to reduce the normalized emittance to the desired value in collisions.

Table 4: Lead ion beam parameter for stacking in collider

Kinetic energy	*GeV/u*	*2.0*
Emittance	*mm·mrad*	*1.5/1.5*
Momentum spread	$\times 10^{-4}$	*6*
Particle number	$\times 10^{9}$	*8.26*
Bunch length	*m*	*7*

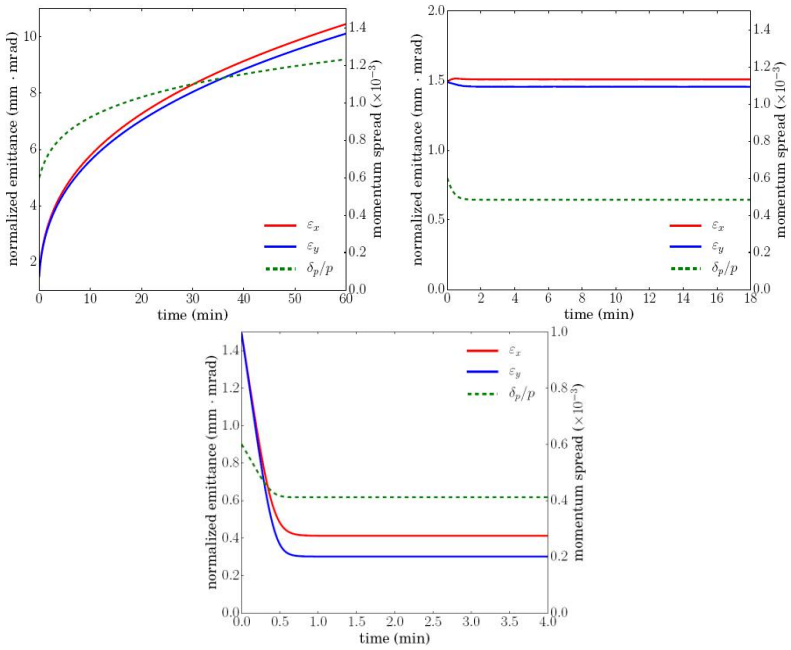

Figure 4: Lead ion beam stacking at 2.0 GeV without (left) or with (middle) cooling and pre-cooling (right).

2.3.7.5.3 Cooling during collision

The heavy ion beam is accelerated to 40 GeV/u for collision. Cooling by the ERL bunched beam cooler is also applied to maintain the emittance. Simulations show that cooling is much easier for the heavy ion beam than for the proton beam. Taking the lead ion, $^{208}Pb^{82+}$, as an example, the current is 0.75 A with design parameter listed in Table 5. As shown in Fig. 5, an electron beam of only 0.8 nC/bunch is used to cool the lead ion beam. Equilibrium is reached within two minutes and the emittance remains close to the proposed value consistently. The current of the cooling electron beam is only 25% of the current required for the proton beam. If needed, we could further reduce the lead ion beam emittance by increasing the cooling electron beam current. Comparing with the proton beam cooling, the technical risk of the heavy ion beam cooing is much lower.

Table 5: Lead ion beam parameter for collision

Kinetic energy	*GeV/u*	*40*
Emittance	*mm·mrad*	*0.5/0.3*
Momentum spread	$\times 10^{-4}$	*6*
Particle number	$\times 10^{8}$	*1.20*
Bunch length	*cm*	*1*

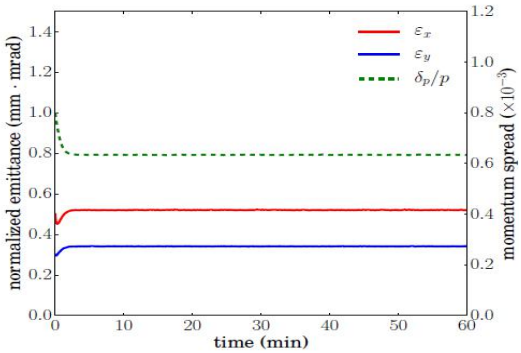

Figure 5: Lead ion beam cooling during collision.

2.3.7.6 *Bunched Beam Cooler Design*

If we assume a cooling electron beam with 3.2 nC of charge operating at the bunch repetition rate of 476.3 MHz, we need an electron beam of 1.52 A average beam current. At this time no electron source is available to provide such a large current. Storage rings have operated at this high current but not at such a low energy (20-55 MeV). Thus, neither a standard Energy Recovery Linac (ERL) or storage ring can provide the necessary cooling beam. To alleviate this situation, we have chosen a Circulating Collider Ring (CCR) [8.9] to boost the average current available from an ERL to the 1.52 A level. This is shown in Fig. 6.

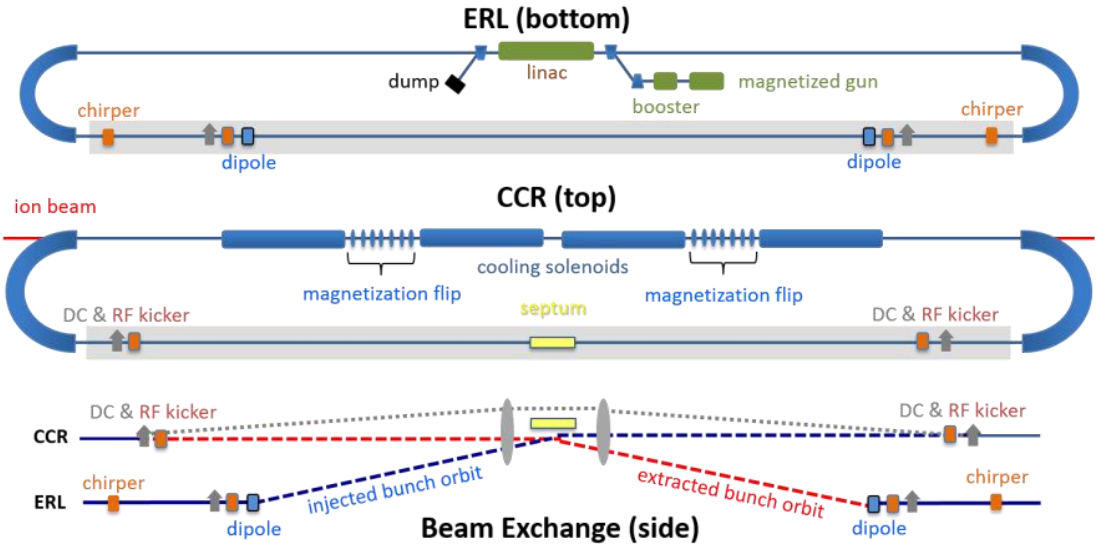

Figure 6: Electron cooler layout. See text for full description

In the proposed bunched beam cooler, high charge bunches are produced in a magnetized gun, accelerated to greater than 5 MeV, and merged into a linac that accelerates the electrons up to a speed that matches those of the protons or ions in the collider ring. The bunches are prepared to match the longitudinal phase space necessary for the cooling channel. They are then deflected upwards to a septum and kicker, which injects them into the Circulating Cooler Ring. Bunches are then circulated 11 times in the ring before being kicked out and energy recovered in the original linac structure. The concept is based on use of fast RF kickers to exchange bunches between the two sub-accelerators at a rate allowing substantial (order of magnitude) increase of cooling current beyond that reasonably available from the ERL alone. The cooler insertion itself consists of four 15-meter-long solenoids separated by matching and helicity swap segments. This allows the net effect of the solenoids on the spin of the proton beam to be zeroed out. The polarity of each solenoid is the opposite of the one upstream of it. One must have two helicity swap segments to make sure the helicity is correct on the next pass. The specifications for the cooler are shown in Table 6.

There are many challenges in such a system. Even with the CCR, the injector must provide over 140 mA of electron beam on a 24/7 basis. The beam must be magnetized and the magnetization must be preserved in the presence of strong space charge forces. We have found that this is possible and have derived a solution for an injector that produces 7 MeV electron bunches at 1.6 nC (half charge) with excellent magnetization and good slice emittance and energy spread. The bunches are not sufficiently uniform to suppress the effects of CSR and the beta functions are dependent on the position in the microbunch. Both of these effects can be alleviated by operating the injector at lower frequency and we are exploring that option.

The CCR is also challenging since the effects of CSR are quite large for a 3.2 nC bunch and the effects of microbunching accumulate over multiple passes, leading to an unacceptable increase in the energy spread. We have found one arc bend design that reduces the microbunching gain to less than unity for all wavelengths. This is shown in figure 7. The bend is not locally symmetric however, so the magnetization can degrade for high charge bunches. The degradation for half charge bunches looks reasonable. We are exploring designs that are locally symmetric that might be better for preserving the magnetization but they must also keep the microbunching gain below unity.

Table 6: Electron beam specifications for the electron cooler [9]

Energy	MeV	20-55
Charge	nC	3.2
CCR pulse frequency	MHz	476.3
Gun frequency	MHz	43.3
Bunch length (tophat)	Cm	2 (23°)
Thermal (Larmor) emittance	mm-mrad	<19
Cathode spot radius	mm	3.1
Cathode field	T	0.05
Normalized hor. drift emittance	mm-mrad	36
rms Energy spread (uncorr.)*		$3x10^{-4}$
Energy spread (p-p corr.)*		$<6x10^{-4}$
Solenoid field	T	1
Electron beta in cooler	Cm	37.6
Solenoid length	M	4x15
Bunch shape		beer can

*The uncorrelated energy spread is the *rms* energy spread at any point in the micropulse. The correlated energy spread is the peak-to-peak change in the mean energy in the micropulse.

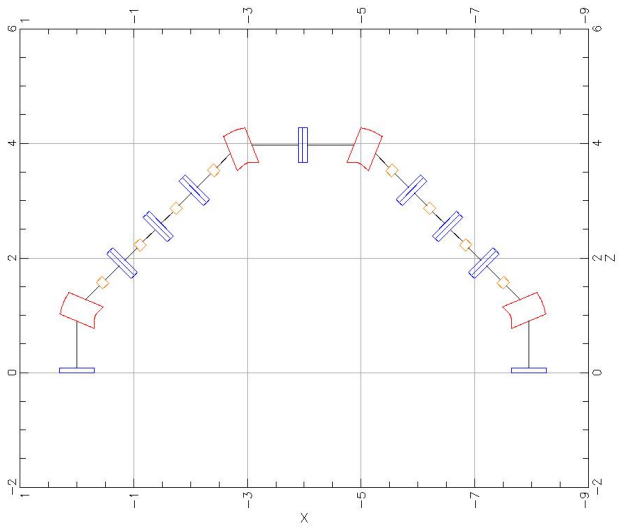

Figure 7: Layout of the CCR arc where red markers denote dipoles, blue markers denote quadrupoles and orange markers denote sextupoles.

Note that the desired bunch shape is a uniform solenoid. This provides slightly better cooling than a more typical Gaussian shape but more importantly reduces the effects of Coherent Synchrotron Radiation (CSR) and space charge on the core of the beam. There will still be an energy chirp and loss induced by the CSR and space charge but this can be compensated with a simple RF cavity.

The ERL to CCR beam exchange [9] is based on use of a fast RF kicker to deflect selected bunches, allowing them to betatron oscillate so as to evolve a displacement. This displacement insures the bunch of interest resides in the high field region of a septum magnet, which is used to bend the exchanged bunch into/out of the circulation beam line.

The basic concept of the exchange is presented in Figure 6. An incoming ERL bunch is de-chirped after bunch lengthening during transport through the linac-to-exchange recirculation arc. It is then bent upward by a vertical dipole, and brought parallel to the plane of the CCR by the field of the exchange septum. It is then focused toward the CCR backleg axis by the downstream transport, reaching an orbit node at an injection fast kicker. The kicker removes the angle, merging the injected bunch into the CCR bunch train. It is thereafter available for cooling.

An extracted bunch is deflected downward by fast kicker, generating an offset that directs the bunch into the septum, whereupon it is directed toward the plane of the ERL. A vertical bend brings the bunch orbit onto to the plane of the ERL; a re-chirper imposes a phase/energy correlation on the bunch, and the downstream exchange-to-linac recirculation arc compaction is used to recompress the bunch prior to reinjection and energy recovery with energy compression.

The sequence for recirculated beams is shown in Figure 8. After exiting the upstream CCR arc, the beam is matched to the exchange. After a DC kick upwards (DCK), the circulated bunch train traverses the EK at (nearly) zero kick. Bunches follow an upwardly offset orbit through the exchange, clear the septum, and return to the CCR axis at a downstream node (a half wavelength from the initial kick). A second DC kick – also upwards – flattens the orbit onto the CCR reference orbit; the beam

subsequently traverses the IK at (near) zero kick, cancelling any remnant EK-induced linear x'δt (or dp/pδx) correlation. The process is completed by a match back to the CCR.

Figure 8: Orbit configuration and beam handling sequence for recirculated beam. Beam motion is from left to right.

The sequence for injected beam and extracted beam are shown in Figure 9. The injected beam is matched from the ERL debunching/dechirping arc, given a DC kick upward (of the same magnitude as the kicks in the CCR), and traverses the PREK, receiving a compensatory downward kick, leaving the beam on the reference orbit (and precompensating any IK-induced angle/phase or energy/position correlations). It then propagates on the reference orbit through the vertical achromatic translation up to the plane of the CCR, crosses the septum, bending onto the CCR exchange region axis. The subsequent transport is on axis to the IK, where the beam receives a downward kick (and is correlation-corrected), and immediately kicked upward by the DCK, transversely merging it with the circulating beam. It is then matched to the CCR. The extracted beam undergoes the same process in reverse order.

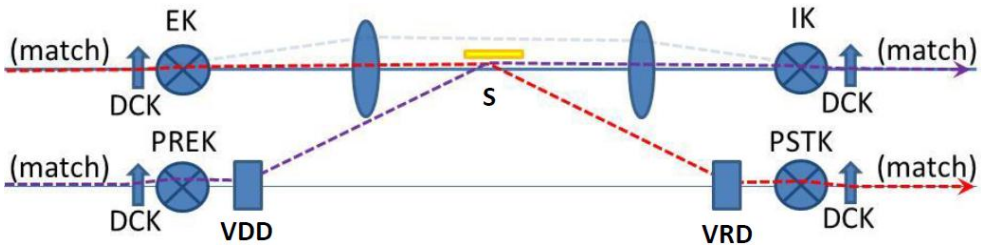

Figure 9: Orbit configuration and beam handling sequence for injected beam and extract beam. Each "match" in figures 8 and 9 is, as noted, generated using an eight-quad telescope.

We have run simulations of a 1.6 nC bunch circulating through the CCR for 11 orbits. The core of the beam is preserved but the ends of the bunch are accelerated relative to the core. This is shown in figure 10.

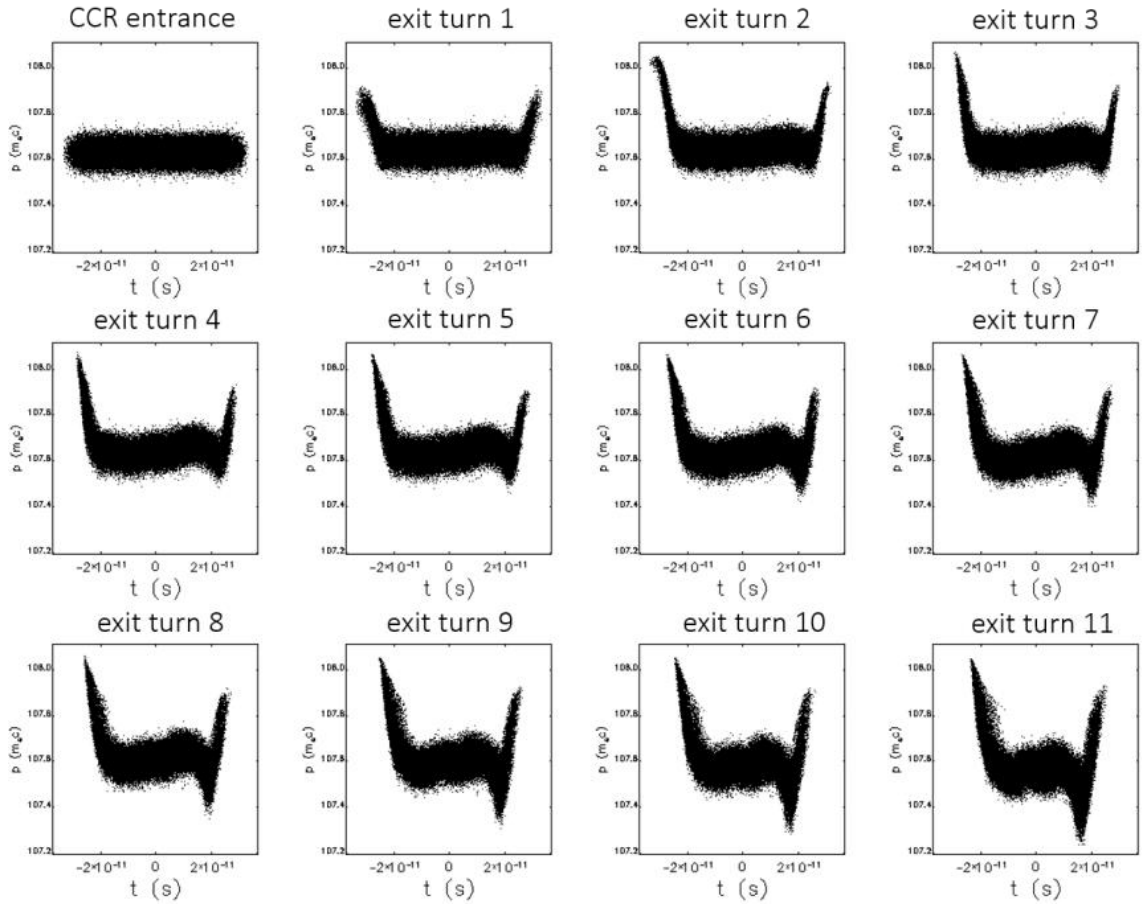

Figure 10: Longitudinal distributions for 11 passes through the CCR with CSR included but no CSR shielding or space charge. An RF cavity is used to compensate the energy loss and slope of the distributions. The initial distribution is an ideal superGaussian distribution with 2 cm full width and *rms* energy spread of 0.03%.

2.3.7.7 ***References***

[1] Ya. Derbenev, "Feasibility of Electron Cooling and Luminosity Potential in Collider", NIM A 532 (2004)

[2] Ya. Derbenev and Y. Zhang, "Electron Cooling for Electron-Ion Collider at JLab", Proc. of COOL09, Lanzhou, China (2009)

[3] Ya. Derbenev, *et al*. "Achieving High Luminosity in an Electron-Ion Collider." Proc. of HB2010 workshop, Morschach, Switzerland (2010).

[4] For the latest scheme, Y. Zhang, Presentation at JLEIC R&D Meeting, Sept. 9, 2017

[5] S. Nagaitsev, *et al.* "Antiproton cooling in the fermilab recycler ring." AIP Conference Proceedings. Vol. 821. No. 1. AIP, 2006.

[6] "COSY Electron Cooling Conceptual Design Report", BINP, Novosibirsk, 2009

[7] V. Kamerdzhiev, *et al.* "2MeV electron cooler for COSY and HESR–first results." (2014): MOPRI070.

[8] S.V. Benson *et al*., "Development of a Bunched-Beam Electron Cooler for the Jefferson Lab Electron-Ion Collider", IPAC'18, Vancouver, BC, Canada.

[9] S.V. Benson *et al*., "Progress Toward an ERL Driver for High Energy Bunched Beam Cooling in JLEIC" (JLAB-TN-17-009)

[10] H. Zhang, J. Chen, R. Li, Y. Zhang, H. Huang, and L. Luo. "Development of the electron cooling simulation program for JLEIC". In 7th Int. Particle Accelerator Conf.(IPAC'16), Bussan, Korea, 2016.
[11] JSPEC source code, https://github.com/zhanghe9704/electroncooling
[12] I. Meshkov, A. Sidorin, A. Smirnov, G. Trubnikov, and R. Pivin. BETACOOL Physics Guide. Dubna, 2007.

2.3.8 **Interaction Region Design**

Vasiliy Morozov and Markus Diefenthaler
Mail to: morozov@jlab.org, mdoefent@jlab.org
Thomas Jefferson National Accelerator Facility, Newport News, Virginia, USA

2.3.8.1 ***Introduction***

The basic physics process at the Electron-Ion Collider (EIC) is Deep Inelastic Scattering (DIS) [1], which is represented in Fig. 1. In the figure, an ion, composed of nucleons, in turn composed of partons (quarks and gluons), moves to the right and collides with an electron moving to the left. The electron collides with a parton within the ion in a hard collision.

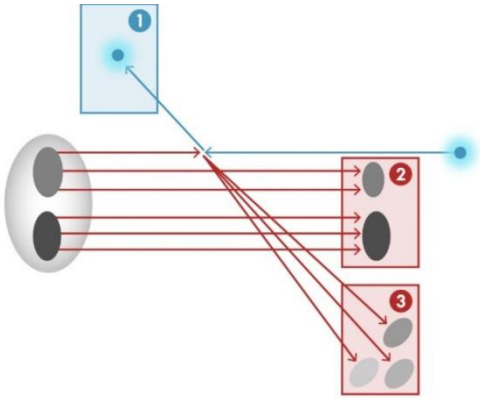

Figure 1: Classification of the final-state particles of a DIS process at the EIC: scattered electron (1), the particles associated with the initial state ion (2), and the struck parton (3).

We can, qualitatively, define three classes of particles in the final state.

1. The scattered electron.
2. Particles associated with the initial state ion.
3. Particles associated with the struck parton.

The aim of the EIC is the investigation of the QCD structure of hadrons including ions and nucleons. All three types of final state particles carry information about the ion. Therefore it is essential that the interaction region (IR) and the detector at the EIC are designed so that all three types of particles are measured at as close to 100% acceptance as possible and with the necessary resolutions. We define the concept of a total acceptance detector as one that achieves close to 100% acceptance for all three types of particles.

2.3.8.2 *IR-Detector Integration*

The luminosity of a collider to first order is inversely proportional to the distance between the last upstream and first downstream Final Focus Blocks (FFBs. Thus, the statistical uncertainty of measurements at the Central Detector scales as the distance between the FFBs. On the other hand, the closer the beam elements are to the IP, the more they obstruct the acceptance at shallow angles with respect to the beam axis and restrict the acceptance for forward particles.

From machine design and luminosity considerations, it is not desirable to leave a very large detector space free of beam focusing elements to allow the small-angle products to accumulate sufficient transverse separation from the incident beams. The solution is to let the small-angle particles pass through the nearest elements of the machine final-focusing system, which simultaneously perform the function of angle and momentum analyzer for the small angle reaction products. A significant challenge of this approach is that it has to consistently reconcile often contradictory detector and machine optics requirements. Taking these considerations into account as well as the asymmetric collisions at JLEIC, a central detector space of (-3.5 m / +7 m) has been chosen.

To achieve the required high luminosity of $10^{33} - 10^{34}$ $cm^{-2}s^{-1}$, the colliding beams are strongly focused to a small spot at the IP. Before and after focusing, the transverse beam sizes have to be greatly expanded in the upstream and downstream final focusing quadrupoles. These considerations already point towards a significant crossing angle of the two beams in order to have enough space for the necessary machine components. In order to accommodate the FFBs with large enough aperture, particularly in the ion-forward direction, and field strength consistent with the detector space of 12.5 m, we have chosen a crossing angle of 50 mrad. The crossing angle has the additional benefit of avoiding parasitic collisions.

The electron and ion detection regions extend 30-40 m in either direction from the central detector. The JLEIC full-acceptance detector is designed to meet the requirements for accessing the EIC physics [1] including a dedicated small-angle small-rigidity-offset high-resolution detection system [2, 3, 4]. From simple kinematics, the reaction products are biased towards small angles around the original ion beam. In particular, the detection of small-angle products requires acceptance to the recoiling target baryon (3D structure of the nucleon), hadrons produced from its breakup (target fragmentation), or all the possible remnants produced when using nuclear targets (including the tagging of spectator protons in polarized deuterium). The detection has to be done over a wide range of rigidities with respect to the original ion beam.

Figure 2 shows a schematic layout of the JLEIC interaction regions containing a full-acceptance detector [2, 3, 4]. The central detector is built around a 4 m long solenoid extending 2.4 m on the outgoing ion side and 1.6 m on the opposite side. The solenoid field is adjustable independently of the beam energies in order to optimize the detection for various processes. The maximum field is expected to be 3 T. As discussed above, the electron and ion beams cross at a relatively large angle of 50 mrad. The electron beam is aligned with the detector solenoid axis to avoid generation of the synchrotron radiation. The solenoid is surrounded by 2 m long detector end caps. Electrons scattered at small angles ($< 0.5°$) are detected in a low-Q^2 tagger consisting of a large-aperture electron FFB and a horizontally-bending dipole magnet followed by a drift space for momentum analysis.

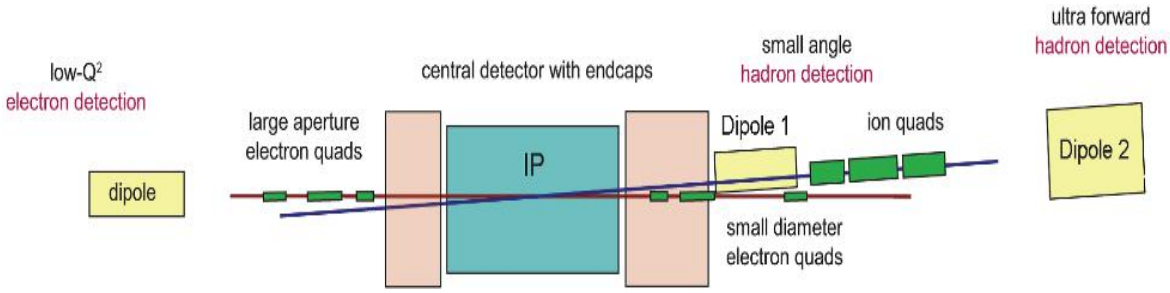

Figure 2: Classification of the final-state particles of a DIS process at the EIC: scattered electron (1), the particles associated with the initial state ion (2), and the struck parton (3).

In addition to momentum analysis provided by the large crossing angle in the solenoid, charged hadrons with scattering angles below $3-5^{\circ}$ with respect to the ion beam pass through a large-aperture 6 mrad dipole (Dipole 1) located before the ion FFB. The dipole is 1 m long and is followed by 1 m of drift space and detectors. Particles at very small angles ($< 0.5^{\circ}$) pass through the ion FFB quads and then, after a few meters of drift space, through a 56 mrad dipole (Dipole 2) for momentum analysis. Various detector elements are placed in the space between the final focus and Dipole 2 as well as beyond the dipole to provide complete angular and momentum coverage [2, 3, 4].

The beam optics of the interaction region has been optimized to maximize the detector's angular and momentum acceptance and resolution in the forward region as discussed below. Both the ion and electron beams are focused downstream of the forward final focus so that the small beam sizes at the focal points allow one to place the detectors closer to the beam centers. In combination with large dispersions at those points, this allows for detection of particles with small relative rigidity offsets $\Delta(B\rho)/(B\rho)$.

2.3.8.3 *Detector Regions*

The JLEIC IR and detector concept matched to the three types of particle as discussed above is shown in Fig. 3. The 50 mrad crossing moves the ion beam away from the electron beam elements and makes room for dipoles and FFBs located just downstream of the central detector area. The dipoles serve two purposes. First, they shape the ion beam orbit so that there is 1 m distance between the two beams 30 m away from the IP, making room for detectors. Second, the dipole systems allow momentum analysis of the particles with small transverse momentum with respect to the beams. The particles with large transverse momenta are analyzed using the solenoidal field in the central detector.

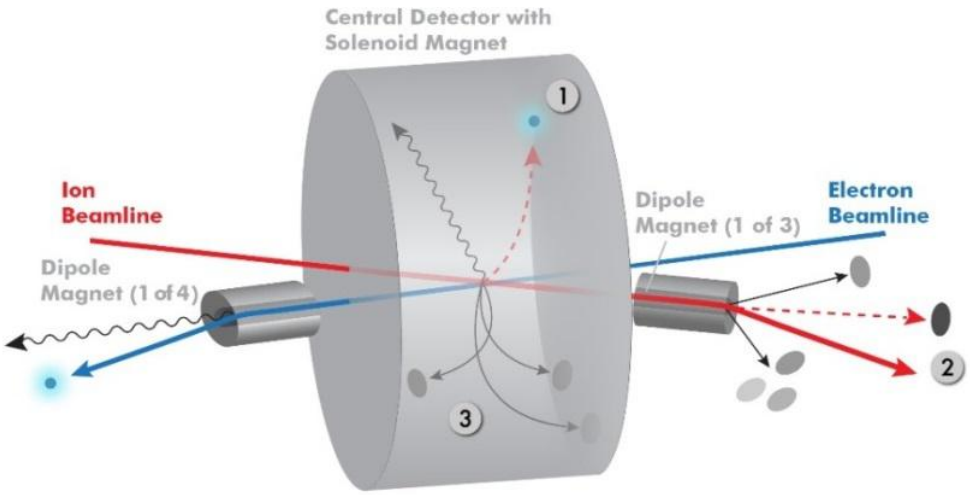

Figure 3: JLEIC IR and detector concept illustrating the crossing angle between the electron and ion beams and the dipole magnets downstream of the Central Detector.

The IR/detector area can be divided into three main components:

1. Central Region (-3.5 m, +7 m) around the IP. This is the region in which predominantly the final state particles from the hard collisions between the electron and the struck parton are measured (particles of type 1 and 2 in Fig. 1).
2. Far-Forward Hadron Region (+7m, +40m) downstream of IP in the ion direction. This is the region in which predominantly the particles associated with the initial ion is measured (particles of type 3 in Fig. 1).
3. Far-Forward Electron Region (-3.5m, -30m) downstream of IP in the electron direction. This is the region in which luminosity and polarization as well as tagger for electrons scattered at very small angles are detected.

The JLEIC design and the extended detector are shown in Fig. 4.

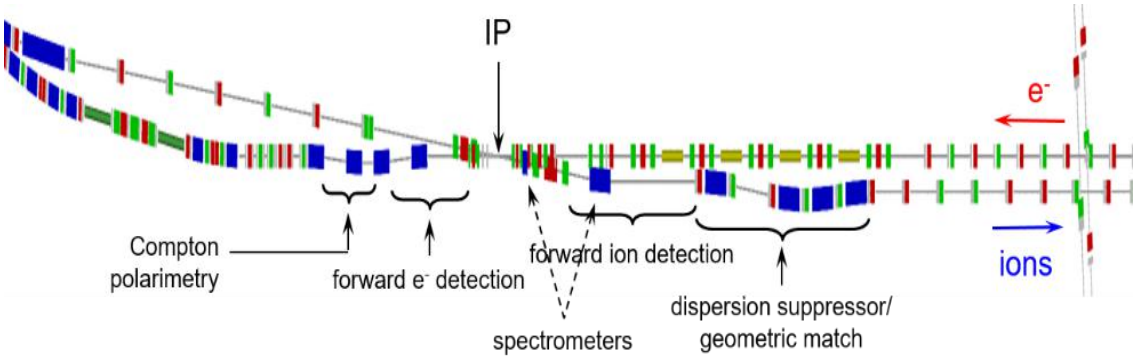

Figure 4: JLEIC design and extended detector: Accelerator elements in the IR and downstream the electron and ion beams are shown. The dark blue elements are dipoles whereas red and green elements are beam quadrupoles. The Central Detector is placed asymmetrically around the interaction point (IP). Forward electron (ion) detectors will be installed in the downstream electron (ion) area. The locations for the electron (labeled as Compton polarimetry) and ion polarimetry are also shown.

2.3.8.4 *Ion Interaction Region Optics*

In general, the optics of the interaction region must be flexible enough to allow for β -squeeze and optimization of the luminosity and detection in different collider configurations, e.g. different beam energies, ion species, and detector solenoid strengths. The ion interaction region optics designed with this in mind is shown in Fig. 5. Each ion FFB is a quadrupole triplet. We optimized parameters of the downstream final focusing quads including their strengths, length and positions for maximum acceptance to the forward scattered collision products. We adjusted the quadrupole strengths to fall off with the distance from the IP so that, with their pole-tip fields not exceeding 6 T at 100 GeV/c, their apertures form a cone with an opening angle of about $\pm$ 10 mrad.

As illustrated in Fig. 2, there is a 6 mrad spectrometer dipole, Dipole 1, before the downstream ion FFB and a 56 mrad spectrometer dipole, Dipole 2, after the FFB. Dipole 1 is used for momentum analysis of the forward scattered particles in the low-momentum-resolution region of the solenoid near its axis. Dipole 2 momentum-analyzes small-rigidity-offset particles that are moving very close to or within the ion beam. From the optics point of view, the dispersion generated by Dipole 1 is small and only acts a small perturbation of the dispersion generated by Dipole 2. Dipole 2 is followed by a 14.4 m long drift space instrumented with forward detectors. By the end of the drift, the horizontal dispersion reaches about 1 m making off-momentum collision products come out of the beam stay clear. To separate the small momentum offset products from the beam core even more and therefore improve the detector's momentum acceptance, the ion beam is focused towards the end of the drift space near the point of maximum dispersion as shown in Fig. 5 [2, 3, 4]. The horizontal and vertical β -functions are less than 0.6 m at the focal point. Implementation of the secondary focus leads to additional chromatic contribution but is necessary for forward detection. A combination of small beam size and large dispersion allow one to place Roman Pot detectors close to the beam and detect smaller momentum offset particles than without the secondary focus. Performance of this design from the forward detection point of view will be quantified below.

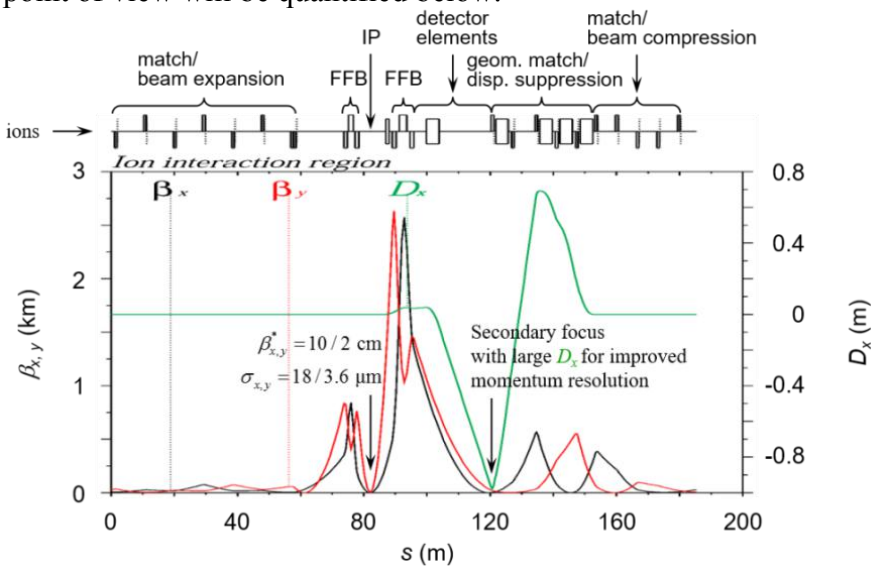

Figure 5: Beam optics of the ion detector region.

To keep the IR design modular, the dispersion generated by the spectrometer dipoles is suppressed by a section consisting of a number of dipoles and quadrupoles as shown

in Figs. 4 and 5. The geometry of the section is adjusted so that the ion beam exits it parallel to the electron beam and is transversely separated from it by 1.5 m. This provides the design with enough flexibility to allow changes in the geometry of the IR without affecting the geometry of the rest of the ring and simplifies optimization of the IR separately from the rest of the ring.

2.3.8.5 *Forward Acceptance*

For the optics design described above, we developed a complete G4beamline/ GEANT4 3D model [2, 3, 4, 5] of the detector region. The top view of the model is shown in Fig. 6. During the optics design and detector modeling, special attention is paid to sizes and positions of the detector region elements to avoid them interfering with each other and with the detector functionality. To provide a realistic solenoid field for particle tracking, the solenoid is modeled as a set of many infinitely-thin current sheets evenly spread in the radial direction with the solenoid fringe field penetrating into the nearby magnets. The remaining detector region elements, including dipoles and quadrupoles, are modeled as pure hard-edge multipoles.

The forward ion FFB is designed so that there is clear line of sight from the IP through the FFQ apertures within a cone with a ± 10 mrad opening angle. This determines the forward acceptance to neutral reaction products. Charged particle trajectories, however, are affected by the FFB's quadrupole fields. Therefore, understanding the forward acceptance to different angles and rigidities requires particle tracking.

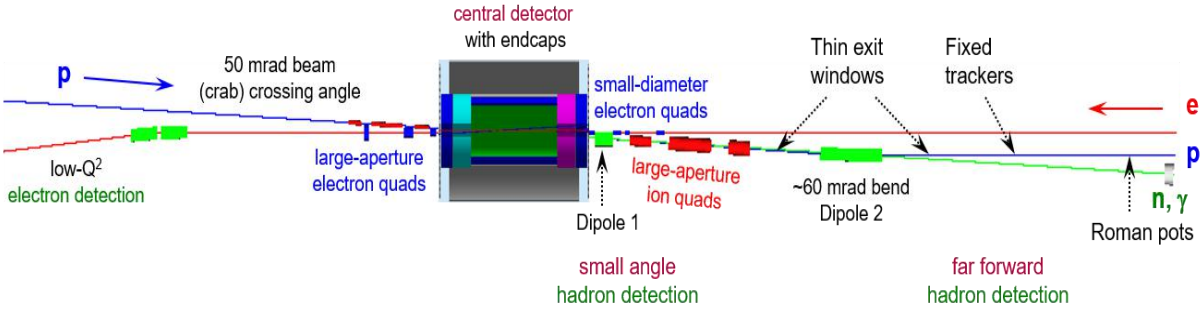

Figure 6: G4beamline/GEANT4 3D model of the JLEIC full-acceptance detector region.

Broadly speaking, there are two types of charged forward final state particles that need to be reconstructed. The first type of forward particles comes from interactions in which the beam particle receives a large transverse momentum kick and fragment into many parts. These particles typically retain a velocity similar in magnitude, but significantly different kinematics from that of the beam particle, and may have very different rigidities. Such particles will separate relatively rapidly from the beam. An example of such a particle is a forward proton from a deuteron-electron DIS. Measurements of such particles are important in understanding the nucleon-nucleon interactions in nuclei, as well as determining the structure of neutrons.

The second type is the (hadron) beam particle that stays intact during the collision and only loses a small fraction of their momentum and acquires a small transverse momentum (p_T). These particles are leading protons or ions in non-dissociative diffractive interactions and will have a trajectory that is close to the proton (or the ion) beam.

The focusing effect of the forward ion FFQs on collision products with different relative rigidities is illustrated in Fig. 7. It shows the trajectories of three sets of particles propagating in a cone from the IP and through the apertures of the FFQs. The three sets have different rigidities normalized to that of the ion beam: 0.5 (left, proton-rich nuclei, e.g. a spectator proton from a deuteron breakup), 1.0 (middle, the beam rigidity), and 1.5 (right, neutron-rich nuclei, e.g. a triton from an $N = Z$ nucleus). Obviously, the higher-rigidity particles are focused less and their trajectories are straighter, while the lower-rigidity particles are focused more and their trajectories are perturbed stronger.

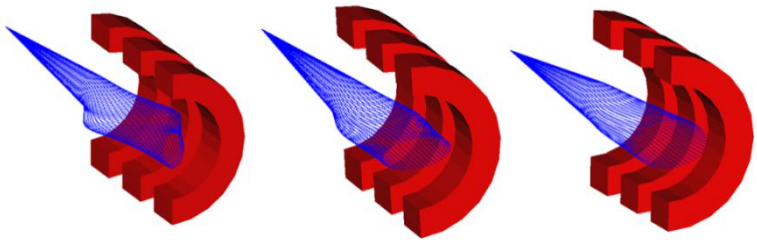

Figure 7: Trajectories of three sets of particles of different rigidities inside the FFQs. The relative rigidity values are 0.5 (left), 1.0 (middle), and 1.5 (right).

To study the forward acceptance to charged particles, we track multiple protons originating at the IP with different initial angles and momentum offsets with respect to a nominal 60 GeV/ c proton beam. We determine which particles pass through the apertures of the forward ion quads. The solenoid field is 4 T at the center, the first spectrometer dipole field is 1.2 T, and the FFB quadrupole gradients are adjusted to their 60 GeV/ c values. The quads are modeled as cylinders with their apertures determined by the assumed maximum pole-top field as $R_{inner} \equiv B_{pole-tip}/(\partial B_y / \partial x)_{100\ \mathrm{GeV}/c}$.

All particles that go outside of the apertures anywhere inside the quads are considered lost. Figure 8 shows the result of tracking 10^4 protons with their relative momentum (rigidity) offsets $\Delta p/p$ uniformly distributed within $\pm\, 0.7$ and their initial horizontal or vertical angles θ_x or θ_y uniformly distributed within $\pm\, 1°$ around a 60 GeV/c proton beam. The particles that clear the FFB are shown in blue. The study is done for the cases of 6, 9, and 12 T FFQ pole-tip fields as well as for a somewhat optimized case where the first two FFQs have 9 T pole-tip fields and the third one has a 7 T pole-tip field. The aperture of the third FFQ is reduced according to its pole-tip field because it does not limit the acceptance as shown in Fig. 8(d). The optimized case may be a good balance of aggressiveness in the forward acceptance and technical feasibility. The black box in Fig. 8 indicates the phase space area of interest for detection. For the optimized case in Fig. 8(d), the acceptance for the most part covers and even exceeds that area.

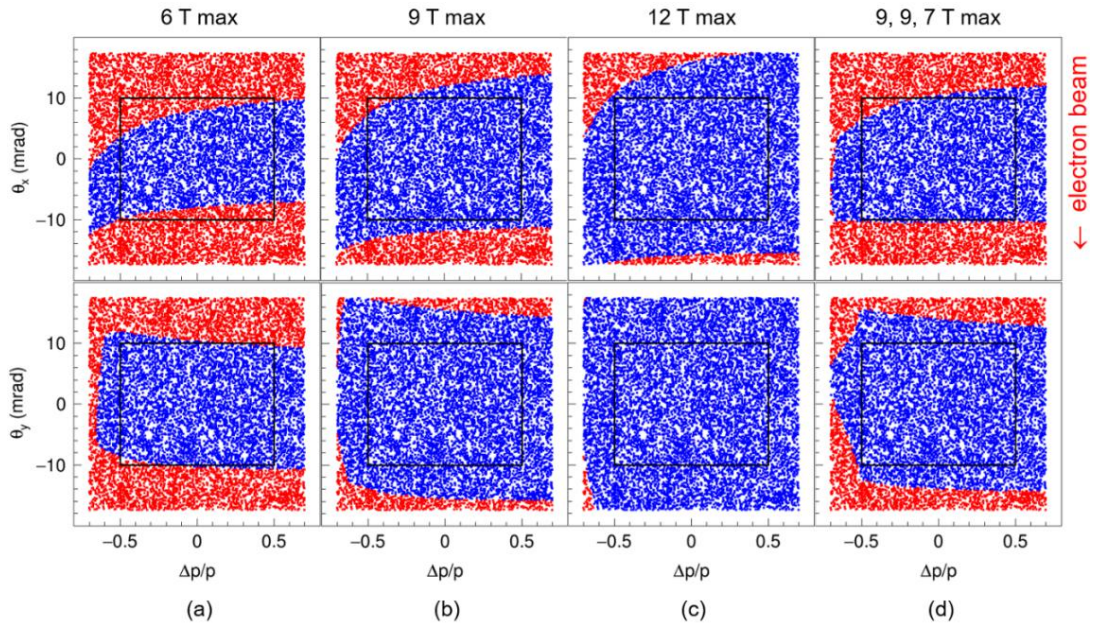

Figure 8: Acceptance (blue region) of the forward ion FFB in terms of the particle's relative momentum (magnetic rigidity) offset $\Delta p/p$ and its initial horizontal (θ_x, top) or vertical (θ_y, bottom) angle for the maximum FFQ pole-tip fields of 6 T (a), 9 T (b), 12 T (c) and optimized (d). The black box indicates the phase space area of interest for detection.

Figure 9 shows the acceptance for protons generated at the interaction point having momenta of $x_L \times 100$ GeV/c and having p_T of up to 1 GeV/c (i.e. the momentum range expected for leading protons in non-dissociative interaction at a proton beam momentum of 100 GeV/c). The acceptance is 100% in all of this area except for a diagonal region shadowed by the aperture of the FFQs. Even in this area, the acceptance is mostly above 50%. The lower right triangular area corresponds to the kinematics that will be measured in the high- resolution forward detection region. The large aperture of the FFQs also allows a large acceptance for zero-degree calorimeter placed at around 30 m downstream for neutron detection.

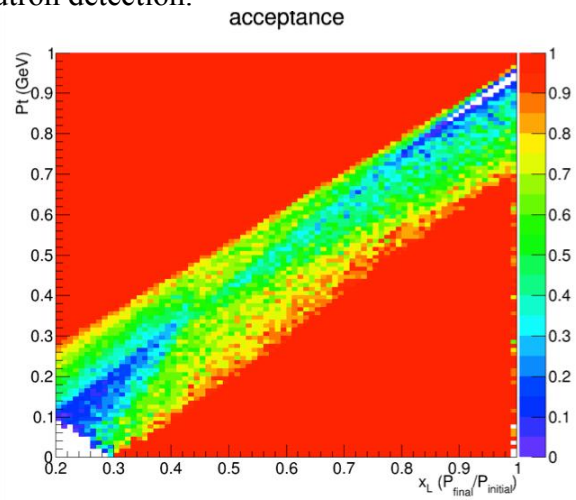

Figure 9: Simulated acceptance for far-forward protons from diffractive processes.

We then study the acceptance of the forward ion FFB to neutral particles in terms of their initial horizontal (θ_x) and vertical (θ_y) angles with respect to the ion beam at the IP.

The result is presented in Fig. 10. We track neutral particles with their θ_x and θ_y uniformly distributed within ± 17 mrad. We consider the cases where the FFQ apertures are determined by the maximum pole-tip fields of 6, 9, and 12 T. The transmitted particles are indicated in blue. The black circle outlines ± 9 mrad ($\pm 0.5°$) cone to guide the eye.

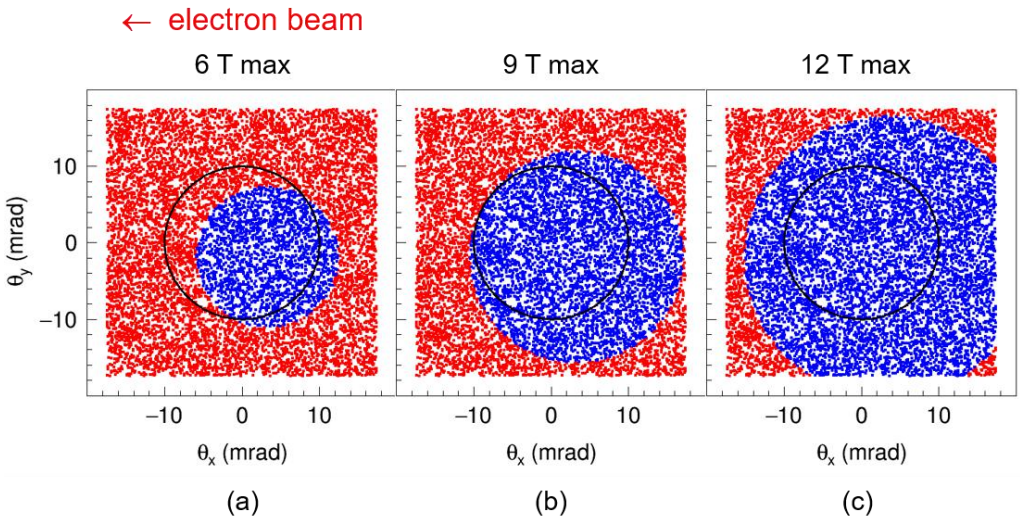

Figure 10: Acceptance (blue region) of the forward ion FFB to neutral particles in terms of their initial horizontal (θ_x) and vertical (θ_y) angles with respect to the ion beam at the IP for the maximum FFQ pole-tip fields of 6 T (a), 9 T (b), and 12 T (c). The black circle outlines ± 9 mrad cone to guide the eye.

For the optimized case shown in Fig. 8, we next study the acceptance of the forward ion FFB in terms of a particle's θ_x and θ_y angles for a characteristic set of the particle's relative momentum (rigidity) offsets $\Delta p/p$: -0.5 (e.g. a spectator protons from a deuteron breakup) (a), 0 (e.g. a beam particle) (b), and +0.5 (e.g. a triton from a $N = Z$ nucleus) (c) and that of neuteral particles (e.g. neutrons). In each case, the θ_x and θ_y angles of the test particles are uniformly distributed within ± 17 mrad. Figure 11 shows the simulated acceptance. The limitation imposed by each detector region element on the acceptance is indicated by a different color. This guides placement of the detectors at locations where the collision products can be detected before they are lost in the magnet apertures. The black circle indicated the outer size of the neutron cone. It is desirable to avoid blocking the neutron cone by any machine or detector elements. These estimates indicated that the detector acceptance meets or even exceeds the detection requirements.

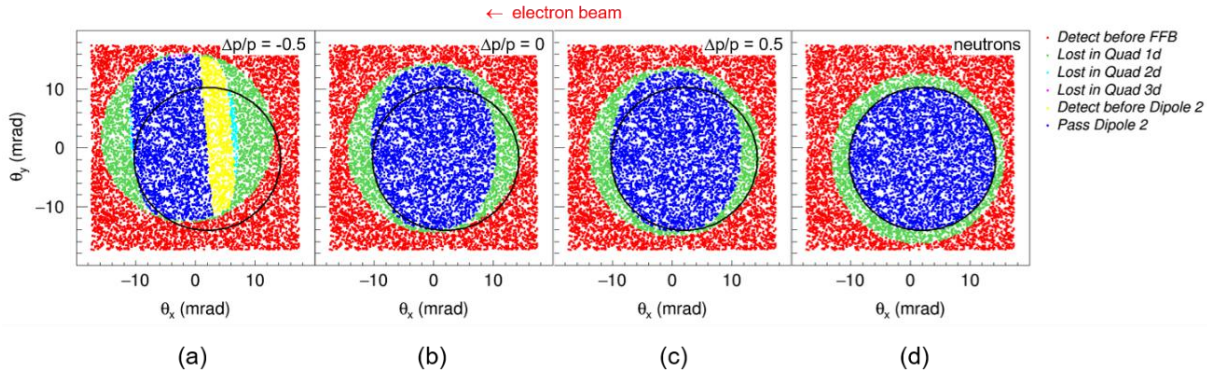

Figure 11: Acceptance (blue region) of the forward ion FFB in terms of the particle's initial horizontal (θ_x) and vertical (θ_y) angles for a characteristic set of relative momentum (rigidity) offsets $\Delta p/p$: -0.5 (e.g. a spectator protons from a deturon breakup) (a), 0 (e.g. a beam particle) (b), and +0.5 (e.g. a triton from a $N = Z$ nucleus) (c). Pane (d) shows acceptance to neutral particles such as neutrons. The different colors indicate the limitation imposed by each IR element on the acceptance. The black circle indicates the neutron cone.

Another importance characteristic of the detector performance is the detector resolution, i.e. the dependence of the particle's measured track on its initial parameters. We calculate the particle position at a few locations along the beam line as a function of its parameters at the IP. Figure 12 shows the particle's horizontal position at the beam focal point 16 m downstream of Dipole 2 as a function of the particle's $\Delta p/p$ for a number of different initial θ_x and θ_y angles. Note that no acceptance cuts are made in this study. The right graph in Fig. 12 is an expanded version of the left figure focusing on small values of $\Delta p/p$ and x. The red band indicates the nominal $\pm\, 10\sigma_x$ beam stay-clear region. A particle can be detected outside of that region. The points where the curves cross the red band boundaries determine the $\Delta p/p$ measurement limits, while the slopes of the curves determine the momentum measurement precision. The graph indicates, for example, that a particle initially moving along the beam, i.e. $\theta_{x,\,y} = 0$, can be detected as long as its $\Delta p/p$ is greater than $\sim 5{\cdot}10^{-3}$.

Similarly, we investigate the dependence of the particle's horizontal position on the initial θ_x and θ_y angles for a characteristic set of $\Delta p/p$ including 0, $\pm$ 0.01, $\pm$ 0.1, and $\pm$ 0.5. At the secondary focal point 16 m downstream of Dipole 2, to first order, there is no dependence of the particle's transverse position on its initial angle at the IP. Therefore, we move the observation point 4 m upstream to a location 12 m downstream of Dipole 2. Figure 13 shows the calculated dependence of the particle's radial deflection at that point as a function of the initial θ_x for the different $\Delta p/p$. Note that no acceptance cuts are used in this study. The graph on the right-hand side of Fig. 13 is a version of the left-hand side figure with a greatly expanded vertical scale. The red band is the nominal $\pm\, 10\sigma_x$ beam stay-clear area. A particle can be detected outside of this area. Figure 13 indicates that a particle of the same rigidity as the beam can be detected if its initial angle exceeds about $\pm$ 3 mrad.

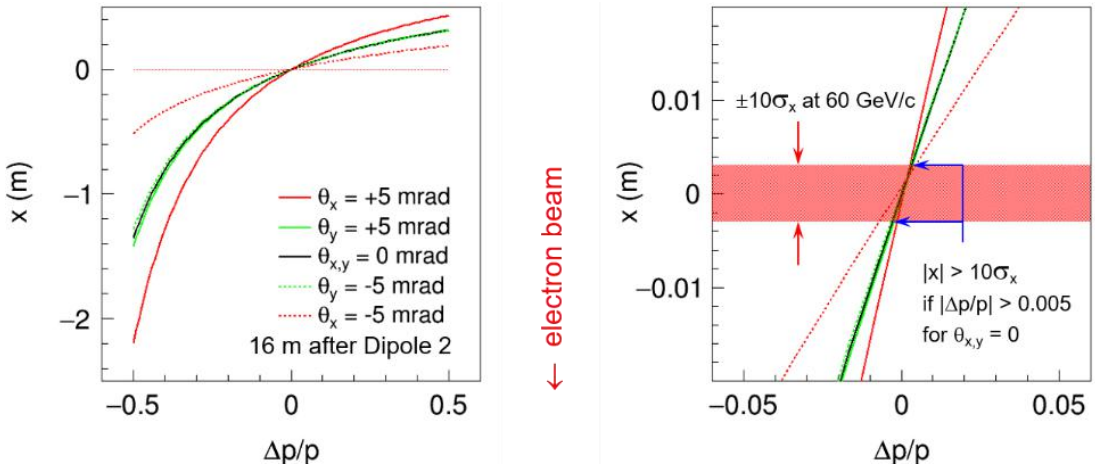

Figure 12: Detector momentum resolution: the particle's radial position 16 m downstream of Dipole 2 as a function of the particle's $\Delta p/p$ for a characteristic set of different initial θ_x and θ_y angles. The right plot is an expanded version of the left figure. The red band is the nominal $\pm\, 10\sigma_x$ beam stay-clear region.

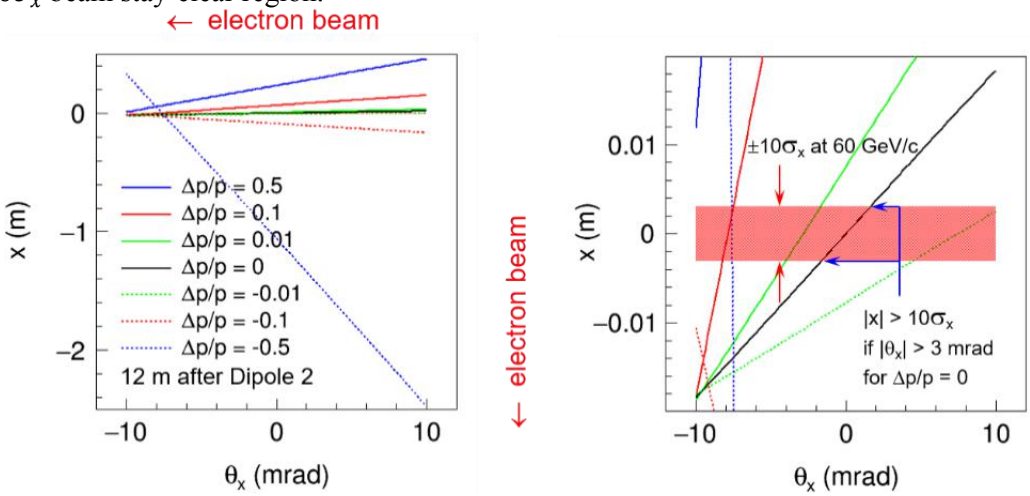

Figure 13: Detector angular resolution: the particle's radial deflection 12 m downstream of Dipole 2 as a function of the initial θ_x for a characteristic set of different $\Delta p/p$. The right plot is an expanded version of the left figure. The red band is the nominal $\pm\, 10\sigma_x$ beam stay-clear region.

Overall, the presented design demonstrates an excellent performance in terms of the detector acceptance and resolution and offers promising opportunities for nuclear physics studies.

2.3.8.6 *Electron beamline and far-forward electron detectors*

Measurements of particles down to the beam-line in the electron-beam direction are also needed. The detector/IR design is expanded in the forward electron direction to monitor the luminosity and polarization of the electron- beam as well as to significantly increase the low-Q^2 coverage of the detector.The detector region optics in the electron collider ring, shown in Fig. 14, is optimized to meet the detection requirements. Strengths, sizes and positions of the machine elements are optimized to reduce the technical challenge of the magnet design and to avoid them interfering with the ion detector region elements. The downstream final focusing quadrupoles (FFQs) are

designed with large apertures and are followed by spectrometer dipoles for forward low-Q^2 tagging as illustrated in Fig. 15. In addition, the electron beam is focused near the point of maximum dispersion to allow closer placement of the detectors at that location. Such a design enhances momentum resolution of the forward detectors. The dispersion generated by the spectrometer dipoles is suppressed by a simple dipole chicane structure whose parameters are chosen to avoid a significant impact on the electron equilibrium emittance.

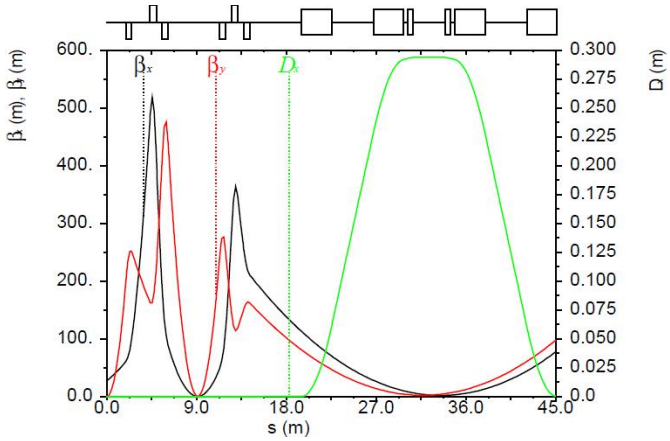

Figure 14: Electron collider ring detector region optics.

Electron-ion scattering where the electron is scattered through a very shallow angle corresponds to the case where the exchanged photon is almost real. Such photo-production processes are of interest in their own right; to characterize them, we would need to measure these electrons at shallow angles, which would be near the electron-beam. The first dipole separates the electron beam from the particles that move close to the electron beam. It serves as an analyzing magnet for small-angle electrons and allows the reconstruction of the low-Q^2 events whose scattering electrons cannot be detected in the central detector. A detector for off-momentum electrons is placed after the first dipole as shown in Fig. 15.

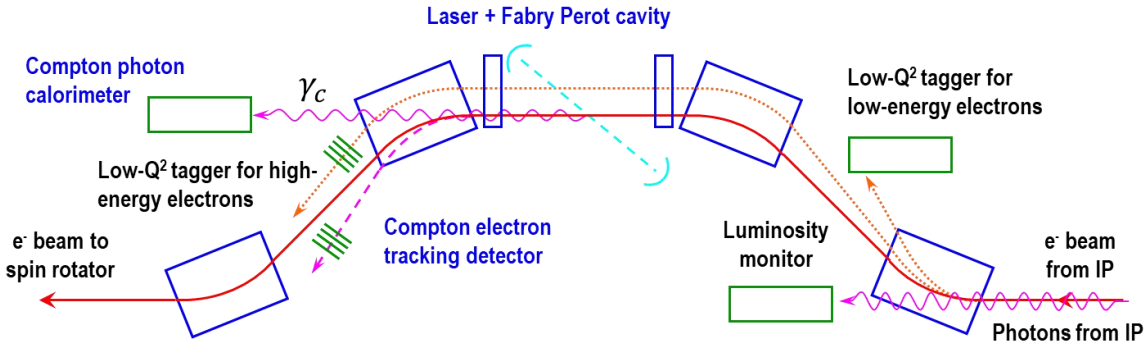

Figure 15: Schematic of the low-Q^2 tagger and electron polarimeter setup.

The minimum relative momentum offset, which makes particles come out of the beam stay clear, can be calculated using $(\Delta p/p)_{min} = 10\sigma_x/D_x$ where $\sigma_x = \sqrt{\beta_x \varepsilon_x + (D_x\,\Delta p/p)^2}$ is the rms value of the beam size and D_x is the horizontal dispersion. The minimum relative momentum offsets are 0.11 and 0.006 at the end of the first dipole and in the middle of the chicane, respectively.

The luminosity is measured via the Bethe-Heitler process. The same first dipole magnet separates the electron beam from the Bethe-Heitler photons that are travelling

along the beam. This allows for luminosity measurement using a photon detector after the dipole as shown in Fig. 15.

Three dipole magnets are installed after the first dipole magnet, as shown in Fig. 15 to bring the electron beam back into the ring and suppress the dispersion. This configuration is ideal for measuring the electron polarization, as shown in Fig. 15. The dipole magnets are identical, up to the direction of the field, so that their effects on the electron beam compensate each other. The polarization after the second dipole, up to the precision of the magnet parameters, is the polarization at the IP. This allows for measuring the beam polarization at a location of minimum background and with no space constraints. A laser system is installed in the straight section between the second and third dipole magnets. The third dipole magnet that bends the electron beam also separates the Compton photons from the Compton electrons. This allows for a combined analysis using both the Compton electrons and photons and will help to reduce the systematic uncertainties on the polarization measurement. The third dipole serves as an analyzing magnet for the Compton electrons. Because all dipoles in the chicane are identical, off momentum electrons that emerge from the central detector are constrained not to cross the beamline, and thus will not enter the Compton electron detector as background.

To mitigate the synchrotron radiation in the Compton detectors from the upstream dipoles in the chicane, two soft dipoles are placed in the middle of the chicane. Decreasing the solid angle acceptance of the detector and adding anti-chambers to absorb the synchrotron radiation photons further reduces the number of photos incident on the beam pipe and going through the pipe to hit the detectors.

2.3.8.7 *Compensation of nonlinear beam dynamics effects of the interaction region*

The large-β FFQs of the IR generate large chromatic effects on the beam dynamics. In addition to correcting the linear chromaticities, the chromatic kick of the FFBs must be locally compensated. Without such a local correction, the chromatic β perturbation propagates around the ring giving rise to large non-linear momentum dependence of the tune. A conventional solution to this problem is to use local sextupoles generating a chromatic beta wave opposite to the one from each FFB, so that they cancel each other. A separate local correction is needed on each side of the IP in order to avoid the chromatic beam smear at the IP. In case of JLEIC, the two FODO arcs are the only dispersive regions suitable for the chromaticity correcting sextupoles. The desired conditions at the sextupoles for an efficient correction are:

1. Large dispersion and β function to achieve compensation with a reasonable sextupole field;
2. $\sim n\pi$ phase advance between the FFB and the sextupoles (in the correcting plane);
3. Large β_x/β_y and β_y/β_x ratios at the x and y sextupoles, respectively, for orthogonal correction;
4. Minimal optics between the sextupoles and FFQ for minimal distortions due to chromaticity from other quadrupoles in this region.

The non-linear fields of sextupoles also generate 2nd and higher-order geometric (amplitude dependent) aberrations resulting in non-linear tune shift and excitation of 3rd and higher-order resonances. These effects can significantly limit the beam dynamic aperture (DA). A common way to compensate these aberrations is to use non-

interleaved pairs of identical sextupoles with $-I$ separation between them. As demonstrated at KEK-B [6], a pseudo $-I$ separation can also be used, which differs from $-I$ in that the matrix terms M_{21} and M_{43} are not zero. The latter adds flexibility to the sextupole optics.

Following the general strategy described above, we developed a non-linear chromaticity correction scheme for the JLEIC ion collider ring [7]. It is based on non-interleaved $-I$ sextupole pairs as illustrated in Fig. 16. Two pairs on each side of the IP correct the x and y nonlinear chromaticities of the respective FFB. In this case, we use a pseudo $-I$ separation between the sextupoles in each pair. We locally modify the optics of an arc section consisting of 13 FODO cells to create high β functions and large β ratios at these pairs as shown in Fig. 17. Only the quadrupole strengths are adjusted in this section. Its geometric layout does not change. β_x is adjusted to about 400 m at the x sextupole locations while β_y at the y sextupole locations is adjusted to a greater value of 800 m due to a smaller dispersion size at those locations. This section, called a Chromaticity Compensation Block (CCB), is matched to the regular FODO lattice on each side. Each CCB is placed in its arc as close as possible to the IP. The optics of the sections between a sextupole pair and the IP is adjusted to provide a betatron phase advance of exactly $n\pi + \pi/2$ in the correcting plane. The resulting setup is shown in Fig. 18. The CCBs correct about 55 and 75% of the horizontal and vertical natural chromaticities, respectively. The remaining linear chromaticity of the machine is canceled using two families of sextupoles in twelve 90° FODO cells of each arc. Note that the number of cells is chosen as a multiple of four. This provides compensation of second-order geometric and chromatic effects of the sextupoles [8].

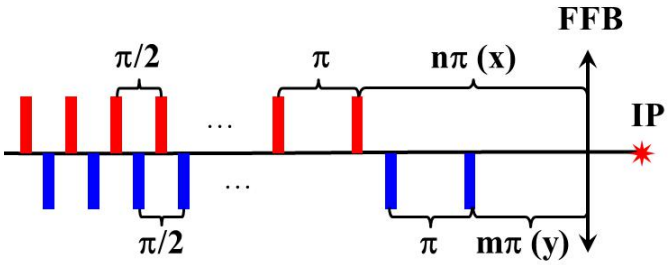

Figure 16: Schematic of a non-interleaved $-I$ sextupole pair setup for chromaticity compensation.

The correcting sextupole strengths are obtained using MAD-X [9]. First, the $-I$ sextupole strengths are set to cancel the chromatic β perturbation $\partial\beta/\partial\delta$ at the IP and minimize its amplitude in the rest of the ring. This way both the chromatic beam smear at the IP and the 2nd-order term of the chromatic tune shift are minimized. In MAD-X, we use the Montague W function as the objective function, since it is linearly proportional to $\partial\beta/\partial\delta$. The sextupoles downstream of the IP are stronger due to the higher FFB beta functions and additional optics on that side. Next, the two families of the periodic sextupoles are set to cancel the remaining linear chromaticity. The required sextupole strengths are quite modest even at the top proton energy (<0.4 T at 4 cm radius). Figure 19 shows the final W functions around the ring. One can clearly see the chromatic β waves excited by the sextupole pairs and their compensation of the chromatic kicks produced by the FFBs. The small bumps in the W functions are due to the chromatic kicks of the two periodic sextupole families. As one can see, these kicks cancel each other.

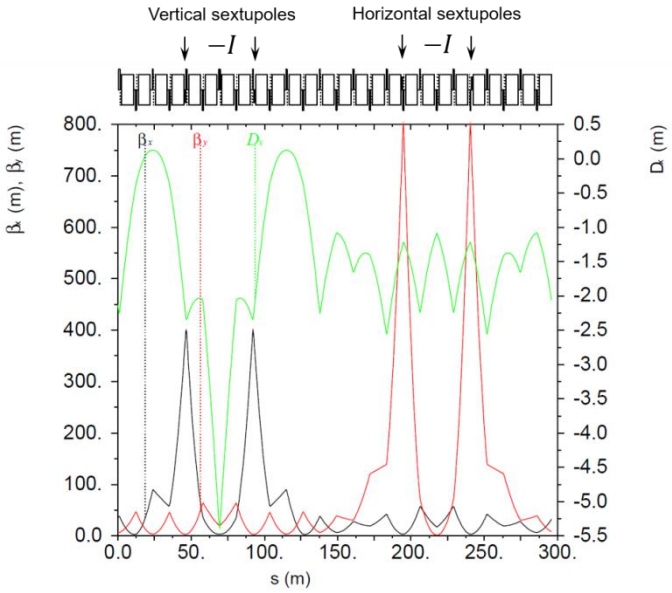

Figure 17: Optics of a Chromaticity Compensation Block (CCB) with the sextupoles locations indicated.

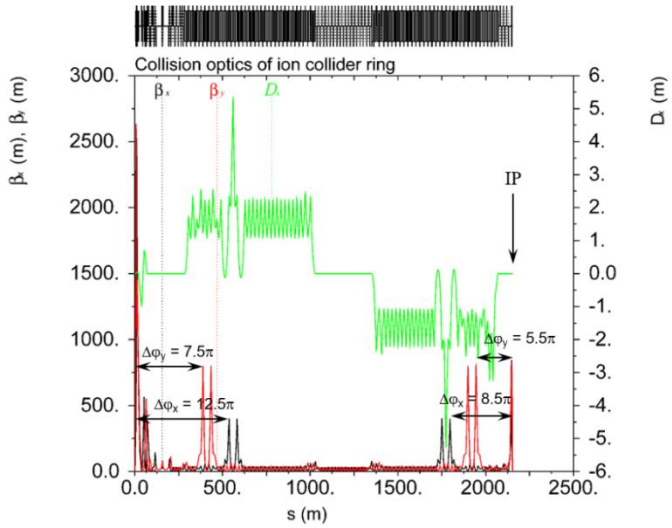

Figure 18: Complete optics of the ion collider ring including the CCBs with the betatron phase advance from the sextupole pairs to the IP indicated.

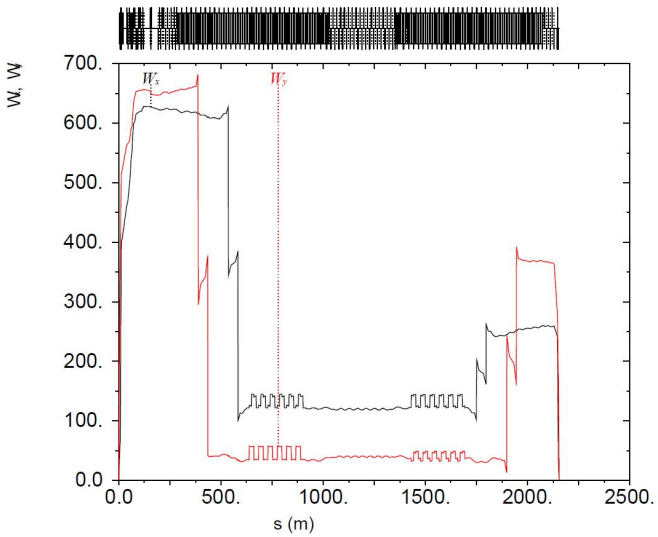

Figure 19: Montague W functions of the collider ring after chromatic compensation.

Figures 20(left) and 20(right) show the momentum dependencies of the betatron tunes $\nu_{x,y}$ and the IP β values $\beta^*_{x,y}$, respectively. They are sufficiently flat over a $\Delta p/p$ range of about $\pm$ 0.4%. Assuming an rms relative momentum spread $\sigma_{\Delta p/p}$ of $3{\cdot}10^{-4}$, this range corresponds to a momentum acceptance of $\pm 13\sigma$. The ν_x/ν_y betatron tunes are set to 24.22/23.16. The ξ_x/ξ_y linear chromaticities are both set to +1. The betatron tunes are chosen using the result of a dynamic aperture tune scan. The optimum dynamic aperture at the IP is shown in Fig. 21 for different $\Delta p/p$ values of up to $\pm$ 0.5%. This result is obtained for a ring without errors. The DA is plotted in units of the σ beam size at 100 GeV/c. However, the DA is sufficient even for the large beam size at the lowest collision momentum of 20 GeV/c. The momentum acceptance of $\pm$ 0.5% is also sufficient ($\pm 16\sigma_{\Delta p/p}$). Studies of error sensitivity and magnet multipole tolerances have also been completed [10, 11, 12, 13, 14]. They concluded that the magnet alignment, strength error and multipole requirements are within demonstrated ranges.

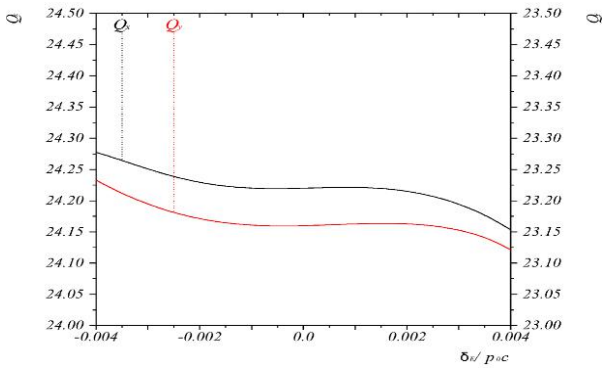

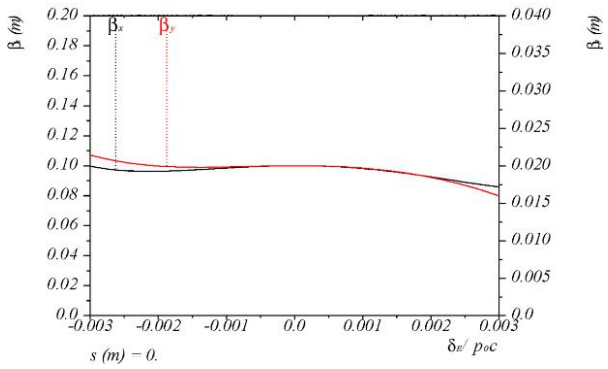

Figure 20: Momentum dependencies of $\nu_{x,y}$ (left) and $\beta_{x,y}$ (right) after chromatic compensation in the ion collider ring.

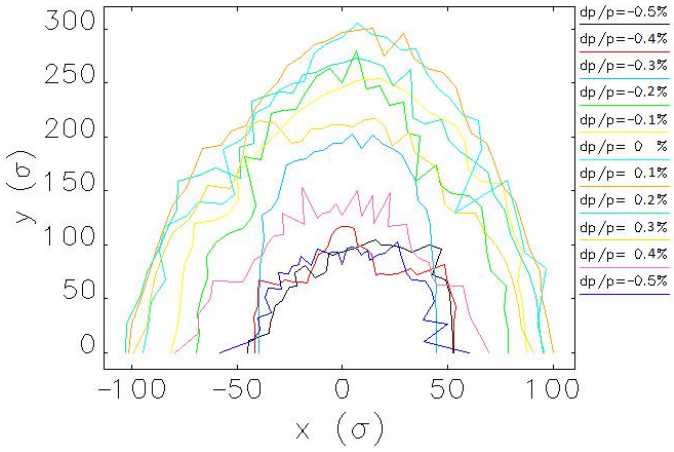

Figure 21: DA at the IP for different $\Delta p/p$ of up to $\pm 0.5\%$ obtained using a ring model without errors.

2.3.8.8 *References*

1. A. Accardi et al., "Ion Polarization Scheme for MEIC", arXiv:1212.1701 (2014).
2. V.S. Morozov et al., in Proc. IPAC'12, paper TUPPR080, pp. 2011-2013.
3. F. Lin et al., in Proc. PAC'13, paper TUPAC28, pp. 508-510.
4. V.S. Morozov et al., in Proc. IPAC'14, paper MOPRO005, pp. 71-73.
5. G4beamline, http://g4beamline.muonsinc.com
6. H. Koiso, K. Oide, "Lattice Design for KEKB Colliding Rings", in Proc. PAC'95, p. 2780, Dallas (1995).
7. Y. Nosochkov et al., in Proc. IPAC'15, paper TUPWI032, pp. 2311-2314.
8. K.L. Brown, "A Second-Order Magnetic Optical Achromat", SLAC-PUB-2257 (1979).
9. MAD-X, http://madx.web.cern.ch/madx/
10. G.H. Wei et al., in Proc. NAPAC'16, paper MOA4CO03, pp. 57-60.
11. G.H. Wei et al., in Proc. IPAC'16, paper WEPMW015, pp. 2454-2456.
12. G.H. Wei et al., in Proc. IPAC'16, paper THPMR053, pp. 3525-3527.
13. G.H. Wei et al., in Proc. IPAC'16, paper THPMR054, pp. 3528-3530.
14. G.H. Wei et al., in Proc. IPAC'17, paper THPAB084, pp. 3912-391

2.3.9 Interaction Region Magnets

Renuka Rajput-Ghoshal and Mark Wiseman
Thomas Jefferson National Accelerator Facility, Newport News, Virginia, USA
Mail to: renuka@jlab.org, wiseman@jlab.org

2.3.9.1 *Introduction*

The interaction region for JLEIC includes about 80 meters of the two collider rings. This section covers the 32 meter section of the ion and electron beam transport lines immediately surrounding the interaction point as shown in Figure 1. Magnets also included in this area are the detector solenoid and two detector dipoles in the ion beam line which were discussed in the detector section. Both the ion and electron line principally consist of three quadrupole magnets before and after the interaction point. Each line also includes two 'anti-solenoids' to compensate for the effects of the detector solenoid. Also included are a number of other skew and corrector magnets discussed below.The transport magnets will all be housed in three separate cryostats as indicated in the figure and operate around 4.5 K.

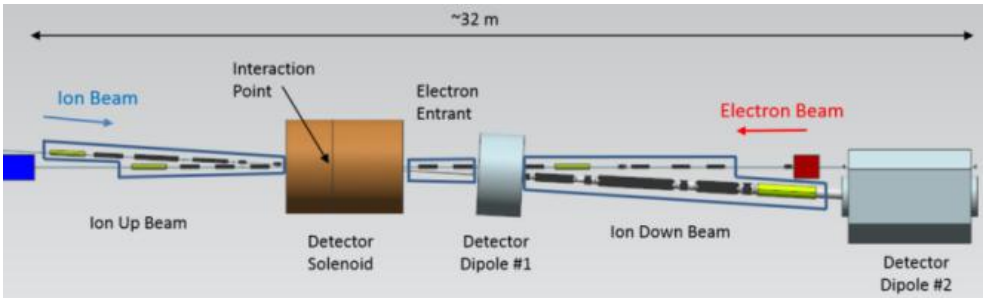

Figure 1: Interaction region detector and beam transport magnets. The beam transport cryostats are indicated as ion up beam, electron entrant and ion down beam.

2.3.9.2 *Interaction Region Magnet Requirements and Designs*

A preliminary design is done for all the quadrupole, skew quadrupole, correctors, solenoid and higher order multipole magnets. Some of these magnets are optimized to the first order and still need further optimization. The maximum peak field in the coils is 11.5 T, which is comparable to some of the LARP high gradient quadrupole magnets. The bore aperture of this magnet is bigger than the LARP magnet, but preliminary stress analysis shows that the peak stresses are not too high compared to LARP magnet designs (REF 1). The design summary for all the magnets is given in Table 1 and Table 2. The higher order multipole magnet is not included in these tables, as the requirements for these magnets are still being finalized. For the location of the principal magnets, see Figures 2 and 3.

Table 1: Requirements and design summary of the ion beam quadrupole and skew quadrupole magnets.

		Requirements					Design				
Magnet Location	Magnet Type	Magnet Strength (T, T/m, T/m^2)	Magnetic length (m)	Good field region radius (cm)	New Inner Radius (cm)	Outer radius (cm)	Inner radius (mm)	Coil inner radius (mm)	Coil width in radial direction (mm)	Coil outer radius (mm)	Peak field from VF (T)
Interaction Region Ion (IR)	Quadrupole QFFB3_US	-116	1	3	4	12	40	45.0	18	63.0	8.93
	QFFUS03S	-0.99	0.1		4	12		67.0	2	69.0	0.22
	Quadrupole QFFB2_US	149	1.5	3	4	12	40	45.0	30	75.0	8.0
	QFFUS02S	0.35	0.1		4	12		77.0	2	79.0	0.2
	Quadrupole QFFB1_US	-141	1.2	2	3	10	30	34.5	18	52.5	7.9
	QFFUS01S	-1.2	0.1		3	10		57.0	2	59.0	0.24
	QFFDS01S	8.6	0.1		8.5	17.1	85	90.8	10	100.8	1.6
	Quadrupole QFFB1	-88	1.2	4	8.5	17.1	85	90.8	43.6	134.4	11.5
	QFFDS02S	-3.7	0.1		12.6	24.7	126	133.4	10.0	143.4	1.8
	Quadrupole QFFB2	51	2.4	4	12.6	24.7	126	133.4	45.0	178.4	10.3
	QFFDS22S	-5.5	0.1		12.6	24.7	126	133.4	10.0	143.4	1.8
	Quadrupole QFFB3	-35	1.2	4	14.8	26.7	148	155.0	38.0	193.0	8.5
	QFFDS03S	4	0.1		14.8	26.7	148	155	10	165.0	1.84

Table 2: Requirements and design summary for the rest of the IR Magnets.

		Requirements					Design				
Magnet Location	Magnet Type	Magnet Strength (T, T/m, T/m^2)	Magnetic length (m)	Good field region radius	New Inner Radius (cm)	Outer radius (cm)	Inner radius (mm)	Coil inner radius (mm)	Coil width in radial direction (mm)	Coil outer radius (mm)	Peak field from VF (T)
Interaction Region Electron (IR)	Common Quad design based on new requirement January 2018, combined with Skew Quads	Quad 45 (varies from 13.63 to 44.78)	0.6	3.2	4.5	8	45	49.5	10	59.5	3.51
		Skew-Quad 9.5 (varies from 1.97 to 9.3)	0.6	3.2	4.5	8	45	61.5	3.25	64.8	1.248
Electron IR	Solenoid AASOLEUS	6	1.2		4		40	60	20	80.0	6
	Solenoid AASOLEDS	6	1.2		4		40	60	20	80.0	6
ION-IR	Solenoid AASOLEUS	6	1.2		4		40	60	20	80.0	6
	Solenoid AASOLEDS	3.6	2		17		170	190	12	202.0	3.614
Corrector	IPUSCORR1	-0.14 By -0.95 Bx	.2					34.5	9	43.5	3.06 in X coil 1.36 in Y coil (Both coils On)
	IPUSCORR2	0.15 By 1.55 Bx	.2					50	3	53	

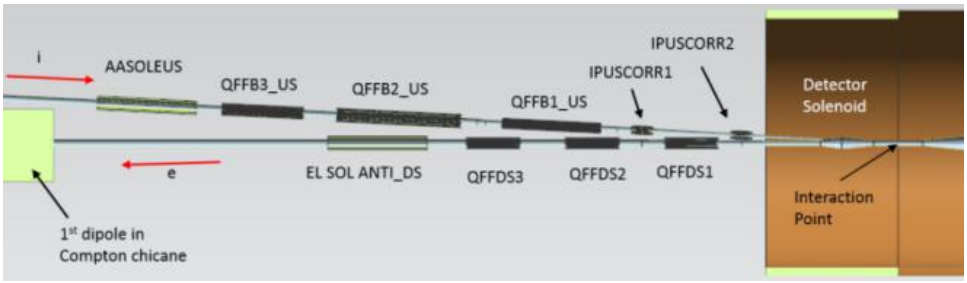

Figure 2: Interaction region detector and beam transport magnets shown in cross section. Nested skew quads and other correctors are not labelled.

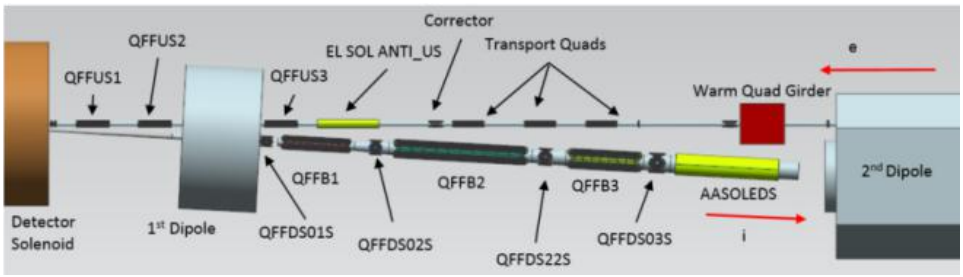

Figure 3: Interaction region detector and beam transport magnets. Nested skew quads and other correctors are not labelled.

The electron beam has six main quadrupoles, all these quadrupoles have the same magnetic length but need different gradients, varying from 13.7 T/m to 44.8 T/m. All these quadrupoles use the same coil design and operate at different current for the required gradient. The peak field in the coil at the highest design gradient is approximately 3.5 T. The coils will be operated at about 600 A of current and will use standard MRI NbTi conductor (e.g. 1.625 mm x 1 mm rectangular conductor). The calculated effective length of the magnet is 0.6 m vs the physical length of 0.629 m. The same coil design will also be used for the three transport quadrupoles shown in Figure 3. These quadrupoles are not fully optimized yet; and we still have to look at the mechanical analysis of these magnets. This is true for nearly all of the magnets at this point.

The ion beam has six main quadrupoles, three upstream and three downstream. The upstream quadrupoles have relatively smaller aperture compared to the downstream ones, but all the upstream quadrupole are stronger than the downstream ones. All these quadrupoles have different magnetic lengths and need different gradients, the required gradient varies from 35 T/m to 149 T/m.

The coil fields for all the ion beam IR quadrupoles are relatively high, all these magnets will use Nb3Sn conductor. The conductor is not fully designed for these magnets, but it will be stranded Nb3Sn cable with 20-30 strands per cable using 0.7 mm strands. The detailed conductor stability calculations will be done after further optimization of the coil cross section. All of these magnets will be operated between 5kA and 8kA of current. This Nb3Sn is also being used for LARP magnets, so it is a well established and well proven conductor.

All the upstream quadrupoles have a good field radius of 30 mm and the required beam aperture radius is 40 mm. In order to reduce the peak fields in the ion beam quadrupoles the magnets are based on a cold bore design. Allowing for the vacuum tube thickness and ground layer insulation, the coil inner radius is taken as 45 mm. The middle quadrupole in the upstream side QFFB2_US needs the highest gradient of 149

T/m. This coil design is optimized to the first order with peak fields in the coil approximately 8 T.

The first quadrupole in the downstream side QFFB1 needs the gradient of 88 T/m and the required beam aperture is 8.5 cm radius, the middle quadrupole QFFB2 needs the gradient of 51 T/m and has a beam aperture requirement of 12.6 cm radius. This coil design is optimized to the first order with peak fields in the coil of approximately 10.3 T (Figure 4). All of the quadrupoles in the ion beam line have peak fields below what has been demonstrated for the high luminosity LHC upgrade program. The three quadrupoles in the ion down beam do have larger apertures than what has been demonstrated in that program and require the most study.

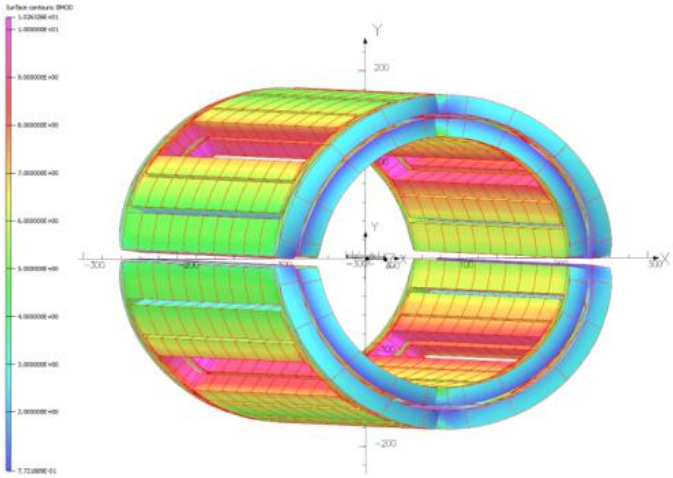

Figure 4: Coil fields for the QFFB2 ion beam transport magnet.

Preliminary stress analysis has been done only for the QFFB2 magnet, as this has a high gradient requirement and bigger aperture as well. ANSYS Maxwell is used to calculate the electromagnetic forces in the coils, the results from ANSYS Maxwell are compared with OPERA. The 1/16th FEA model is shown in Figure 5. Lorentz forces, strains and stresses in the coils are calculated using ANSYS Maxwell. For this preliminary analysis, isotropic material properties are used, the Key 1 and Key 2 are assumed of titanium and inner and outer keys are assumed to be made of G10 and titanium. Preliminary results indicate that the stresses are within the acceptable ranges for this conductor. More detailed analysis will continue as the designs evolve.

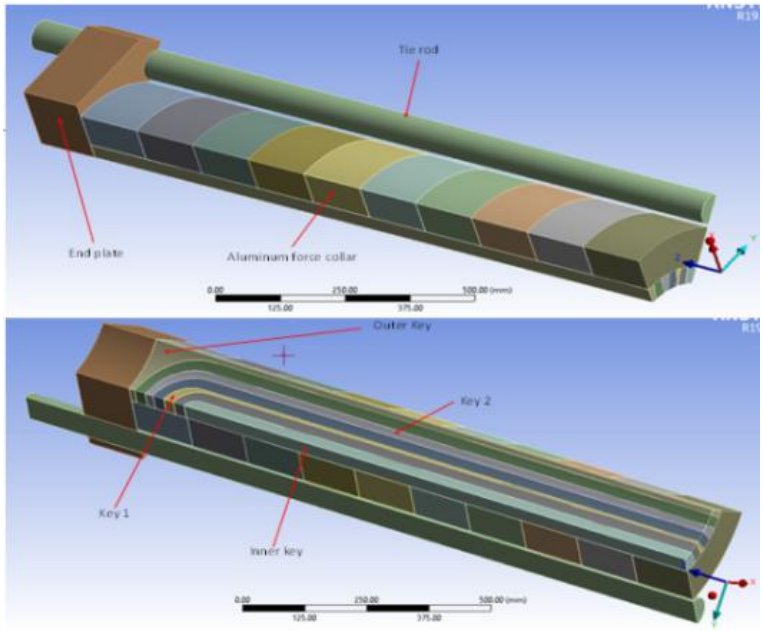

Figure 5: Interaction region detector and beam transport magnets.

All of the electron ring skew-quadrupoles are combined with the main quadrupoles. The ion ring upstream skew quadrupoles will be nested on top of the main quadrupoles, but the downstream skew-quadrupoles will be independent and are shown in Figure 3. The coil field in the skew quad, in presence of main quad field for the center quadrupole, is shown in Figure 6.

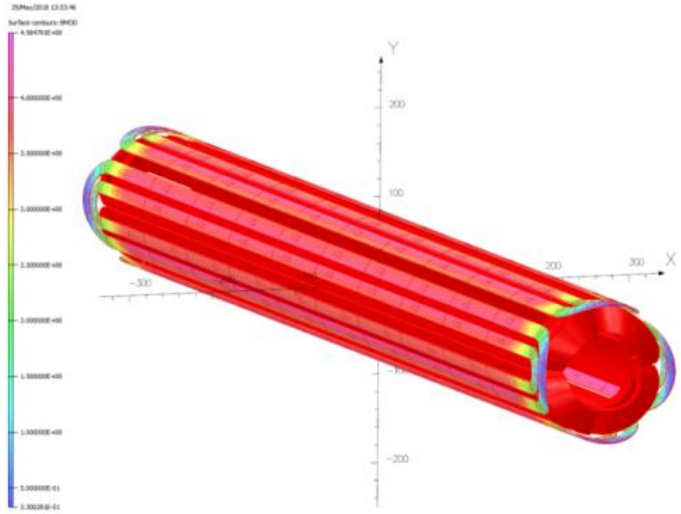

Figure 6: Nested skew quad field around the QFFB2_US magnet.

The coil fields in all the skew quadrupoles are relatively low to moderate. All these magnets will use NbTi conductor and will be operated at 4.5 K. The conductor is not fully designed for these magnets, but either it will be standard MRI rectangular conductor or standard round conductor.

All of the ion beam line quadrupoles will also need some higher order multipole magnets. The exact requirements for these correctors is not final but may include correction for both the principal and skew higher order terms. A preliminary look has been done that suggests these can be nested over the up beam quadrupoles as was done

for the skew quadrupoles. These correctors will be wound using 0.3 mm (bare)/0.33 mm (insulated) standard conductor, operating around 120 A. Because of the aperture size on the downstream magnets, a different design will be used but has not been explored.

There are four solenoid magnets in the interaction region, three of these (two for the electron beam and one for the upstream ion beam) will be identical magnets and the fourth (downstream ion beam) has a slightly lower central field but large bore. The small bore solenoids have a maximum central field of 6T; the coil inner radius is 60 mm. The larger bore solenoid has a central field of 3.6 T and the coil inner radius is 190 mm.

All these solenoids will be operated at 4.5 K and will be wound with NbTi conductor. The detail conductor design will be done after further optimization and after looking into the shielding requirements. The solenoid magnets will be operated at about 400 A of current and will use standard MRI NbTi conductor (e.g. 1.625 mm x 1 mm rectangular conductor).

The corrector magnets in the ion up beam line, IPUSCORR1 and IPUSCORR2, have slightly different field requirement, also IPUSCORR1 have both field components negative and IPUSCORR2 has both components positive. These magnets will be identical designs based on the IPUSCORR2 requirements.

There are more than 30 different magnets in the interaction region; these magnets are very close to each other and to the adjacent beam line. These magnets have some electromagnetic interaction with each other. In order to study the magnet-magnet interaction, the following sections are considered for the initial study (See Figures 2 and 3):

1. QFFDS2 and QFFB1_US
2. QFFUS1 with Ion beam line
3. QFFB2 with electron beam line
4. QFFB1, QFFUS3 and EL SOL_ANTI_US

A combination of passive and active shielding will be considered for each area with studies currently underway.

The beam transport magnets will be contained in three cryostats as shown in Figure 1 with approximate lengths of 2.6, 8.7 and 10.1 meters. These will house a minimum of four, eighteen, and fifteen magnets respectively. The final number of magnets will depend on the number of multipole corrector and shielding coils needed. The beamlines will all be cold bore with room for warm to cold transitions and RF shielded bellows included at each end of the cryostats. The ion up and down beam cryostats will include both beam lines. The electron entrant cryostat will only include the electron beam line. A preliminary look at the synchrotron radiation in the area indicates an acceptable amount of power will be distributed along the beamline from the final focusing quadrupoles. Beamline impedance calculations and vacuum system design are in progress. Work on the vacuum vessel, helium vessel, and support structure designs is underway.

2.3.9.3 *References*

1. “P. Ferracin, et. Al, “Magnet Design of the 150 mm Aperture Low-β Quadrupoles for the High Luminosity LHC”, CERN-ACC-2014-0031.

2.3.10 **Collective Effects**

Rui Li
Thomas Jefferson National Accelerator Facility, Newport News, Virginia
Mail to: lir@jlab.org

The JLEIC baseline parameters [1] are conceived based on the unique luminosity concept of the design, featuring small bunch emittances, relatively low bunch charge, and very high bunch repetition rate [2]. These features further determine the behaviour of collective instabilities in the collider rings during bunch collision. It implies moderate single-bunch instabilities; yet it poses strong requirements on the fast feedback systems to mitigate longitudinal and transverse coupled-bunch instabilities. For a complete design study, the collective effects need to be assessed for a wide range of beam energies and ion species, and also for the entire ion bunch formation process. For this presentation, we only focus on cases for a few selected collision energies.

Ideally, the wakefield induced beam instabilities can be analytically and numerically studied once the machine impedance budget is available. However, developing impedance budget and performing instability estimations are an iterative and gradually refining process. Presently, JLEIC design is still at its early phase and the engineering design has just begun. At this stage, a preliminary estimation of impedance thresholds, for various coherent instabilities, is necessary for the engineer design to make design choices so as to minimize machine impedances and ensure beam stability. In this section, we discuss the current status of the JLEIC impedance studies, and present our initial back-of-envelop estimations for the single and coupled bunch instabilities using the recent JLEIC baseline design parameters. The estimated impedance threshold will be compared with the expected machine impedances for the JLEIC collider rings, as inferred from the impedance budgets of some existing machines. We will also give preliminary discussions about the two-stream instabilities, i.e., the electron cloud effect in the ion ring and the ion effects in the electron ring.

2.3.10.1 ***Status of Impedance estimation***

In a storage ring, the electromagnetic response of the vacuum chamber to the beam current is characterized by the broadband and narrowband impedances, which could cause respectively the single-bunch and coupled-bunch collective instabilities. The narrowband impedances for the JLEIC electron and ion rings are discussed in Sec. 9.5.3. For broadband impedances, the estimation of the impedance budget requires engineer drawings of the vacuum chamber. Yet for JLEIC, presently the machine engineering design has just begun, hence no details are available except for the element counts for most of the impedance-generating components in both rings [3] (see Table 1). Without the actual component designs, at present we can only use the impedance budgets for some existing machines, such as PEPII, SUPERKEKB, or RHIC, as references [4-6]. One reason for using PEPII for reference is that there is consideration for the JLEIC e-ring to adopt the RF cavities, as well as the components for vacuum system and diagnostics, from PEPII HER. Another convenient feature is that the bunch length ($\sigma_z \approx 1.2$ cm) for JLEIC is comparable to that in PEPII, given that the effective impedances are bunch-length dependent. With the PEPII impedance budget and the JLEIC component counts in Table 1, and assuming these components are identical with

those used in the PEPII HER, we get the estimation for the JLEIC e-ring [7]: the inductance $L \approx 99.2$ nH , the effective longitudinal impedance $|Z_{\parallel}/n| \approx 0.09\ \Omega$, the loss factor $k_{\parallel} \approx 7.7$ V/pC , and the effective transverse impedance $|Z_{\perp}| \approx 0.03$ MΩ/m . If components in SUPERKEKB are used as reference, the JLEIC e-ring impedance estimation becomes [7] $L \approx 28.6$ nH , $|Z_{\parallel}/n| \approx 0.02\ \Omega$, $k_{\parallel} \approx 19$ V/pC , and $|Z_{\perp}| \approx 6.5$ kΩ/m , with the note that the smaller bunch length ($\sigma_z \approx 0.5$ cm) for beams in SUPERKEKB than that in JLEIC may cause underestimation of the effective impedances.

Table 1: Impedance-Generating Components in JLEIC

Elements	**e-Ring**	**ion-Ring**	**e-Cooler**
Flanges (pairs)	1215	*234*	104
BPMs	405	214	49
Vacuum ports	480	92	62
Bellows	480	559	74
Vacuum valves	23	14	-
Tapers	6	6	26
Collimators	16	16	-
Forks	0	0	4
Fast kickers	0	0	2
DIP screen slots	470	-	
Crab cavities	2	8	0
RF/SRF cavities	32	40	2
RF/SRF bellows	0	60	0
RF/SRF Valves	68	24	-
Feedback kicker	2	2	-
IR chamber	1	1	

For the JLEIC ion ring, the ion beam undergoes the bunch formation process including the injection, acceleration, bunch splitting, and finally collision. The bunch length varies through the whole process, and the short ion bunch ($\sigma_z \approx 1.2$ cm) at the collision state is made possible only by employing the envisioned high-energy electron cooling [8]. Since such short bunch length is unprecedented for the ion beams in existing ion rings, it is more appropriate [9] to use the PEPII rings rather than the existing ion rings for reference when estimating the JLEIC ion ring impedance budget. The ion-ring impedance at the collision scenario is thus estimated as [7]: $L \approx 97.6$ nH , $|Z_{\parallel}/n| \approx 0.08\ \Omega$, $k_{\parallel} \approx 8.6$ V/pC , and $|Z_{\perp}| \approx 0.04$ MΩ/m.

As the JLEIC design improves and getting more complete, the counts for certain elements in Table 1, such as the collimators, feedback kickers, and ion-clearing electrodes, will be further modified. In addition, some special components unique to the JLEIC design, such as the crab cavities and IR chamber, require detailed impedance modelling and cannot use reference of impedances from the existing machines. Accurate impedance budgets of both the electron and ion rings require careful

electromagnetic field calculations, which can generate the full impedance spectrum for each impedance-generating components.

2.3.10.2 ***Single Bunch Instability***

In this subsection, we discuss the beam stability at the collision scenarios for the electron beam at energies E_e=3, 5, 10 GeV and for the proton beam at E_p=100 GeV.

Longitudinal Microwave Instability (LMWI)

With the Boussard approximation, the LMWI instability threshold is given by the Keil-Schnell criterion:

$$\left|\frac{Z_{\parallel}(n)}{n}\right|^{\text{th}} \approx \frac{2\pi\beta^2|\eta|E\sigma_\delta^2}{eI_{\text{peak}}}$$

For JLEIC baseline parameters, the estimation of LMWI thresholds are listed in Table 2 and are compared with the expected machine impedances denoted by $\left|Z_{\parallel}/n\right|^{\text{ring}}$. It is interesting to note that unlike PEP-II LER, which is a separate ring and has different dipole configuration from that in HER, here the JLEIC e-ring uses the same dipole configuration for a wide range of beam energy, with both the dipole strength and the energy spread from synchrotron radiation scaling with the beam energy. As a result, the energy spread for beam at 3 GeV in the JLEIC e-ring is much smaller than that for the PEP-II LER beam, so the former is vulnerable to LMWI while the latter is not. This estimation indicates the necessity to apply suppression mechanisms against the microwave instability for the JLEIC e-ring at low energy. Examples of such mechanisms include use of an alternative dipole configuration or damping wigglers. For the ion ring, the machine impedance is expected to be much smaller than the threshold impedance, so the beam is safe from this instability. For the electron ring, detailed simulations are to be conducted to study the bunch lengthening due to potential-well distortion below the LMWI threshold, and the turbulent bunch lengthening and energy-spread increase beyond the instability threshold.

Transverse Mode-Coupling Instability TMCI

The impedance threshold for the transverse mode-coupling instability (TMCI) is roughly approximated by

$$\left|Z_{\perp}\right|^{\text{th}} \approx F\ \frac{E\ \nu_s}{e\langle\beta_{\perp}\rangle I_{\text{peak}}},$$

with F the bunch form factor ($F\ \ 2\pi$ for short bunches). The threshold results are shown in Table 2 for both the JLEIC electron and proton beams at selected collision energies, and are compared with the expected upper limits of the machine transverse impedances

denoted by $\left|Z_{\perp}\right|^{\text{ring}}$. These results show that the beams are stable with regard to TMCI. Here the machine impedances are estimated using impedance budgets of existing machines. Since there are uncertainties in both the machine transverse impedance and

the simple back-of-envelope formula, detailed studies of TMCI will be carried out when more accurate JLEIC impedance model becomes available. Such studies include solving the eigenvalue problem of the Vlasov equation [10] or macroparticle tracking that takes into account of potential-well distortion in the longitudinal phase space and many other effects [11]. Additionally, special attention needs to paid to the Christmas-tree-like equilibrium longitudinal charge distribution for the proton bunch under strong electron cooling, which has a very dense core with long tails [12]. Space-charge effects on TMCI will also be assessed, especially for the ion bunches during their formation process [13].

Table 2: Thresholds for Single Bunch Instabilities

	PEP-II (LER)	JLEIC e-Ring			JLEIC p-Ring
E [GeV]	3.1	3	5	10	100
I_p [A)]	113	59.0	59.4	50.6	15.6
η (10^{-3})	1.31	1.09	1.09	1.09	6.22
σ_δ (10^{-4})	7.7	2.78	4.55	9.28	3.0
ν_s (10^{-2})	3.7	0.88	1.46	2.51	5.3
$\langle\beta_\perp\rangle$ [m]	20	13	13	13	18
$\lvert Z_\parallel/n\rvert^{\text{ring}}$ [Ω]	~0.1	≤ 0.1 (expectation)			≤ 0.5
$\lvert Z_\parallel/n\rvert^{\text{th}}$ [Ω]	0.145	0.027	0.125	1.16	22.5
LMWI	stable	unstable		stable	stable
$\lvert Z_\perp\rvert^{\text{ring}}$ [MΩ/m]	< 0.1	≤ 0.1 (expectation)			≤ 5
$\lvert Z_\perp\rvert^{\text{th}}$ [MΩ/m]	0.28	0.22	0.60	2.4	119
TCMI	stable	stable			stable

2.3.10.3 *Coupled Bunch Instabilities*

Narrowband impedances from RF cavities can cause longitudinal or transverse coupled bunch instabilities (LCBI or TCBI). The JLEIC electron ring is expected to use the PEP-II RF cavities. For the JLEIC ion ring, an initial RF cavity design is recently developed, featuring low-cost 2-cell cavity with coaxial coupler for HOM damping. In the following, we present estimations of the growth rate for the coupled-bunch

instabilities under the assumption of even bunch filling pattern. This assumption gives an upper bound of the instability growth rate for general filling patterns. Since the growth rate is much faster than the natural damping rate, the design will rely on fast feedback systems (FBS) to mitigate the coupled-bunch instabilities. Consequently, we will assess the beam stability by comparing the instability growth time with the damping times (~ millisecond) of advanced fast feedback systems.

Table 3: Longitudinal HOM Parameters (p-Ring)

f [MHz]	R_s [Ω]	Q
940.8	7.98e06	2.98e06
1771.9	2.25e04	5643.9
1814.0	1.00e05	5265.5
2894.8	3.33e04	9172.4
3079.4	2.23e02	2.65e04

Table 4: Transverse HOM Parameters (p-Ring)

f [MHz]	Polarization	$R_\perp$ [kΩ / m]	Q
1169.8	V	17.9	82.2
1170.1	H	18.0	90.3
1183.8	H	28.1	91.3
1183.9	V	32.3	96.5
1286.7	H	110	501.6
1290.0	V	100	474.5
1315.5	H	357	697.9
1318.7	V	503	970.5
1390.0	H	1930	36348.4
1390.2	V	27700	539455
1572.7	H	1.20	64.2
1575.2	V	2.87	94.1
1627.6	H	1.96	51.2
1629.1	V	0.43	54.1
1865.1	V	3.54	84.7
2517.1	V	7.80	9707.1
2517.1	H	2.36	8531.8

With the JLEIC machine and beam parameters, together with the RF HOM parameters listed in Tables 1 and 2 of Ref. [14] for the electron ring and in Tables 3 and 4 here [15] for the ion ring, the growth rates for the coupled-bunch instabilities are obtained by ZAP [16] (using Sacherer-Zotter's formulas) as shown in Table 5. Here a nonzero chromaticity of $\xi = 1$ and a finite betatron tune spread of 3e-04 are assumed for the TCBI calculations for both the electron and the proton beams. Resistive-wall impedance has negligible effects on the LCBI growth rates for both of the JLEIC colliding beams. However, it plays a major role on the fast TCBI growth rate for the electron beam.

In Table 5, $\tau^{\parallel}_{a=1}$ and $\tau^{\parallel}_{a=2}$ are the growth time for the longitudinal dipole and quadruple modes respectively, and $\tau^{\perp}_{a=0}$ and $\tau^{\perp}_{a=1}$ correspond to the growth time for the transverse rigid and dipole modes. Here $\tau^{\parallel}_{\text{damp}}$ (or $\tau^{\perp}_{\text{damp}}$) for the e-ring represents the natural longitudinal (or transverse) damping time for the electron beam due to synchrotron radiation, while $\tau^{\parallel}_{\text{damp}}$ and $\tau^{\perp}_{\text{damp}}$ for the p-ring are the damping times for the proton beam due to the strong electron cooling [17] in the JLEIC design. Note that for the electron ring, the lowest energy beam (E_e =3 GeV) has the fastest growth time ($\tau^{\parallel}_{a=1}$ =2.9 ms) for LCBI, which is manageable by FBS as operated in modern electron storage rings. The fast growth times of $\tau^{\parallel}_{a=1}$ =6.0 ms for the proton beam require the longitudinal FBS in the proton ring to use much stronger kicker strength than those found in modern proton-ring FBS, implying higher broadband impedance due to the demand of more kicker cavities. Additional efforts are necessary for further improving the HOM damping for the p-ring RF cavities so as to alleviate these excessive demands on the kicker strength. More topics for CBI need to be addressed by computer modelling, such as (1) effects of realistic uneven bunch pattern (with injection/ejection gaps and/or ion clearing gaps), (2) the joint effects of HOMs from both the accelerating/focusing RF cavities and the crab cavities, (3) impact of the Christmas-tree-like equilibrium ion bunch distribution [12] on effective impedance as a result of strong electron cooling, and (4) the Landau damping effect on transverse coupled-bunch instability, from either the chromaticity or the beam-beam tune shift spread.

Table 5: Growth Time for the Coupled Bunch Instabilities in the JLEIC Design

	e-Ring			p-Ring
E (GeV)	3	5	10	100
$\tau^{\parallel}_{a=1}$ [ms]	2.9	4.1	72.8	6.0
$\tau^{\parallel}_{a=2}$ [ms]	31	43	466	6.0
$\tau^{\parallel}_{\text{damp}}$ [ms]	187.	40.5	5.1	> 30 min (e-cooling)
$\tau^{\perp}_{a=0}$ [ms]	1.6	2.7	64	23
$\tau^{\perp}_{a=1}$ [ms]	12.8	19.6	39.8	501
$\tau^{\perp}_{\text{damp}}$ [ms]	375	81	10	> 30 min (e-cooling)

2.3.10.4 *Electron Cloud in the Ion Ring*

In an ion ring, the ionization of residual gas and the beam-loss induced surface emission provide the source for the primary electrons, while the electron cloud build-up comes mainly from the secondary electron production [18]. For different stages of ion bunch formation, the build-up of electron cloud and its impact on the ion bunch stability can behave very differently. Unlike the trailing-edge effect of electron cloud for long ion bunches found in conventional ion rings, here the high rep rate and short bunches of the ion beam in JLEIC during collision render the electron cloud build-up process behaves similarly to those in positron rings of modern lepton colliders. For the proton beam at E_p =100 GeV, the electron cloud density rapidly rises up and then saturates at around the neutralization density of

$$\rho_{sat} = \frac{N_b}{\pi b^2 L_{sep}} = 2\times 10^{12}\ \mathrm{m}^{-3}$$

as modelled in Ref. [19] for a similar set of parameters. The threshold for the electron-cloud induced single-bunch transverse mode-coupling instability (TMCI) can be estimated using the two-particle model [20],

$$\rho_{th} = \frac{2\gamma Q_s}{\pi r_p C \langle \beta_y \rangle} = 1.7\times 10^{13}\ \mathrm{m}^{-3}.$$

With $\rho_{sat} < \rho_{th}$, the bunch is stable from the electron-cloud induced strong head-tail instability. The electron-cloud induced coupled-bunch instability for the JLEIC ion beam can cause more concern, which is yet to be studied by detailed simulations.

2.3.10.5 *Ion Effects in the Electron Ring*

The ionization scattering of the electron beam with residual gas molecules in the vacuum chamber can cause ion trapping in the electron ring. The trapped ions can cause many undesirable effects for the electron beam, such as emittance growth, tune shift, halo formation, and coherent coupled bunch instabilities. For symmetric bunch pattern, the critical ion mass for the ions to be trapped in either *x*-motion or *y*-motion is given by [21]

$$A_{x,y}^{trap} = \frac{r_p N_b L_{sep}}{2\sigma_{x,y}(\sigma_x + \sigma_y)}.$$

The critical ion masses for the JLEIC electron ring are listed in Table 6, which shows that all ion molecules ($A \geq 2$) will be trapped for even bunch fill. Here constant rms bunch sizes are assumed in the estimation.

Table 6: Critical Ion Mass for Trapped Ion

E_e[GeV]	3	5	10
L_{sep} [m]	0.63	0.63	2.52
σ_x[mm]	0.15	0.26	22.2
σ_y[mm]	0.07	0.12	0.51

A_x^{trap}	0.5	0.2	0.24
A_y^{trap}	1.1	0.4	0.4

Bunch clearing gaps in electron rings are often used to clear the ions so as to prevent them from accumulating turn after turn. Typically a gap in the bunch train, with a length of a few percent of the ring circumference, will help clear up the ions. However, even with the ions being cleared after each turn by a clearing gap (or gaps under multi-train operation), there is still the fast beam-ion instability (FBII) [23] that could cause coupled transverse dipole motion of the electron bunches, with the dipole amplitude increases in time and along the bunch train. Under the assumptions that (1) the force between the ion and electron beam is linear to their dipole offsets and (2) constant frequency for all ion oscillations, the FBII is characterized by the growth time

$$y_b(t) \propto \left(t/\tau_g\right)^{-1/4} e^{\sqrt{t/\tau_g}}$$

$$\tau_g^{-1}[s^{-1}] = 5\,p[Torr]\frac{N_b^{3/2} n_b^2 r_e r_p^{1/2} L_{sep}^{1/2} c}{\gamma \sigma_y^{3/2} (\sigma_x + \sigma_y)^{3/2} A^{1/2} \omega_\beta}\,.$$

For realistic beams, Landau damping is considered as a result of ion oscillation frequency spread due to bunch size variation. The dipole amplitude growth is then characterized by the e-folding time [24, 25]

$$y_b \propto e^{t/\tau_e},\quad \tau_e^{-1} \approx \tau_g^{-1} \frac{c}{4\sqrt{2\pi} L_{sep} n_b a_{bt} f_i}$$

for f_i being the coherent ion oscillation frequency, and a_{bt} the ion frequency variation. For the JLEIC electron ring, τ_g and τ_e are shown in Table 7 (for a_{bt} =0.5) for a single bunch train. Here for E_e=10 GeV, the growth time is comparable to its counterpart for the PEPII HER beam. However, for E_e=3-5 GeV, the growth time is one or two orders of magnitude faster and is consequently a serious concern for the electron beam stability. Possible mitigation methods include using chromaticity to Landau damp the FBII, or using multiple bunch trains to reduce the growth amplitude. Comprehensive numerical modelling of FBII and its the mitigation schemes in JLEIC will be performed, along with its joint effect with the beam-beam induced tune spread and the coupled-bunch beam-beam instability in the gear-change collision arrangements [26].

Table 7. Growth time of FBII for JLEIC e-Ring

E_e [GeV]	3	5	10
τ_c [μs]	0.01	0.11	13.9
τ_e [ms]	0.02	0.1	3.2

2.3.10.6 ***Conclusions***

In this section, we present the status of our initial back-of-envelope estimations for the JLEIC beam stability for a set of selected collision energies. Our estimation shows that for the current design, the low-energy electron beam is vulnerable to the longitudinal single bunch instability, and mitigation measures need to be explored. As for the coupled bunch instabilities, both the electron and proton beams require the state-of-art longitudinal and transverse fast feedback systems---as strong as those used in PEP-II or modern storage-ring light sources. As the engineering design progresses and when more details of impedance budget are available for the JLEIC collider rings, a more in-depth modeling will be conducted for the impedance-induced single and coupled bunch instabilities. Moreover, we need to model the electron-cloud buildup and its effect on the ion beam stability, in particular the e-cloud induced coupled bunch instability, as well as the effects of chromaticity and multi-bunch train on the mitigation of fast beam-ion instability for the electron beam. The ion effects for the ERL-based high-energy electron cooling system also require careful studies

2.3.10.7 ***References***

[1] Y. Zhang, "JLEIC Baseline Update and New Parame-ters", https://www.jlab.org/indico/event/210/ (2017).
[2] Ya. Derbenev *et al.,* "Achieving High Luminosity in an Electron-Ion Collider", proceedings of HB2010 Workshop (2010).
[3] T. Michalski, private communication (2017).
[4] "PEP-II an Asymmetric B Factory", Conceptual Design Report, SLAC-418 (1993).
[5] D. Zhou, SuperKEKB mini optics meeting (2015).
[6] S. Pegg and W. W. MacKay (editors), "Collective Instabilities in RHIC", RHIC/AP/36 (1994).
[7] K. Dietrick, private communication (2018).
[8] S. Benson, Cool17 Workshop (2017).
[9] A. Hutton, private communication (2018).
[10] Y.H. Chin, MOSES 2.0, CERN/LEP-TH/88-05 (1988).
[11] M. Blaskiewicz, "The TRANFT User's Manual version 1.0", private communication (2017).
[12] A. Sidorin *et al.,* THAP01, Proceedings of COOL 2007 (2007).
[13] A. Burov, Phys. Rev. ST Accel. Beams 12, 044202 (2009); Erratum Phys. Rev. ST Accel. Beams 12, 109901 (2009).
[14] R. Rimmer *et al.,* "PEP-II RF Cavity Revisited", CBP Tech Note 197, LCC-0032 (1999).
[15] F. Marhauser, private communication (2017).
[16] M. Zisman, S. Chattopadhyay, J.J. Bisognano, "ZAP USER'S MANUAL" LBL-21270 (1986)
[17] H. Zhang, "Cooling Simulation Studies", https://www.jlab.org/indico/event/210/ (2017).
[18] K. Ohmi *et al.*, PRSTAB 5, 114402 (2002).
[19]] S. Ahmed *et al.*, "Computational Modeling of Electron Cloud for MEIC", Proc. of IPAC12 (2012).
[20] K. Ohmi, F. Zimmermann, PRL 85, p. 3821 (2000).
[21] Y. Baconnier, G. Brianti, CERN/SPS/80-2 (1980).
[22] M. Q. Baron, NIMA 243, 278 (1986).

[23] T.O. Raubenheimer and F. Zimmermann, Phys. Rev. E, Vol. 52, 5487 (1995).
[24] G. Stupakov, T.Raubenheimer, and F. Zimmermann, PRE, Vol. 52, 5499 (1995).
[25] F. Zimmermann *et al.,* SLAC-PUB-7617 (1997).
[26] V. S. Morozov *et al.,* "Study of Beam Synchronization at JLEIC", arXiv: 1606.09117 (2016).

2.3.11 **Beam-Beam Effects in JLEIC**

Yves Roblin
Thomas Jefferson National Accelerator Facility, Newport News, Virginia, USA
Balsa Terzić
Old Dominion University, Norfolk, Virginia, USA
Mail to: roblin@jlab.org

2.3.11.1 ***Introduction***

The Jefferson Lab Electron Ion Collider (JLEIC) presents a number of unique scenarios for which beam-beam effects have to be considered. It will feature an ion beam that can range from 20 to 250 GeV/c, whereas the electron beam will be varying from 3 to 10 GeV/c.

2.3.11.2 ***JLEIC parameter range and lattice design***

2.3.11.2.1 Nominal lattice design

JLEIC is designed to meet the requirements laid out by the white paper on the science program [1]. It is a ring-ring electron-ion collider. It departs from traditional colliders by adopting a figure-8 layout in order to preserve the beam polarization, allowing it to remain above 70% for both electrons and ion beams and longitudinal at the interaction points by means of energy-independent spin rotators, a consequence of the figure-8 design.

The electron ring will permit accumulating and colliding with electrons ranging from 5 to 12 GeV. It is a based on warm magnet technology to allow for reaching higher synchrotron radiation loads. The ion collider is based on super-conducting super-ferric magnets and will enable the use of ion species ranging from proton, deuteron, all the way to lead. Details of the design can be found in [2].

2.3.11.2.2 Kinematical ranges

There are essentially three broad kinematic ranges in terms of center of mass energy that are considered, all having different implications in terms of the beam-beam effects.

2.3.11.2.3 Beam-beam challenges

The low energy range ($\sqrt{s}$=21.9 GeV) is limited by space-charge and requires a longer bunch length to be able to stay within a reasonable range for the Lasslett tune shift. This in turn gives raise to stronger geometric hourglass effects. It is also challenging in terms of beam synchronization for some of the kinematics where the ion momentum is low [3].

The middle energy range ($\sqrt{s}$=44.7 GeV), where the luminosity peak is limited by the beam-beam effect, and finally the high energy range ($\sqrt{s}$=63.3 GeV) which is

restricted by the maximum synchrotron radiation load tolerable in the electron ring. These values are currently being revisited as we are moving towards higher $\sqrt{s}$ (near 100 GeV).

We concentrated the initial beam-beam studies on the middle kinematic range which is where the beam-beam effects are prevalent.

2.3.11.2.3.1 Determination of the initial working point

We employed a variety of techniques to perform the initial searches for the working points. In these studies, we make use of BeamBeam3D [1], a beam-beam simulation code which uses a self-consistent approach based on a shifted integrated Green function method to solve the Poisson equation on a grid surrounding the beam bunches. It is a massively parallel code that can run on a large number of processors. We used it both at the Jefferson Lab High Performance Computing farm and at NERSC.

The search for an optimal working point was first carried out by performing tune scans with a linear lattice model for both the electron and proton ring. Figure 1 shows an example of such a weak-strong tune scan. We obtained a few candidates working points and selected ν_x=0.53, ν_y=0.567 for the electron beam for further studies. The proton ring working point, we initially selected to be ν_x=0.23, ν_y=0.14 as a result of previous studies [2].

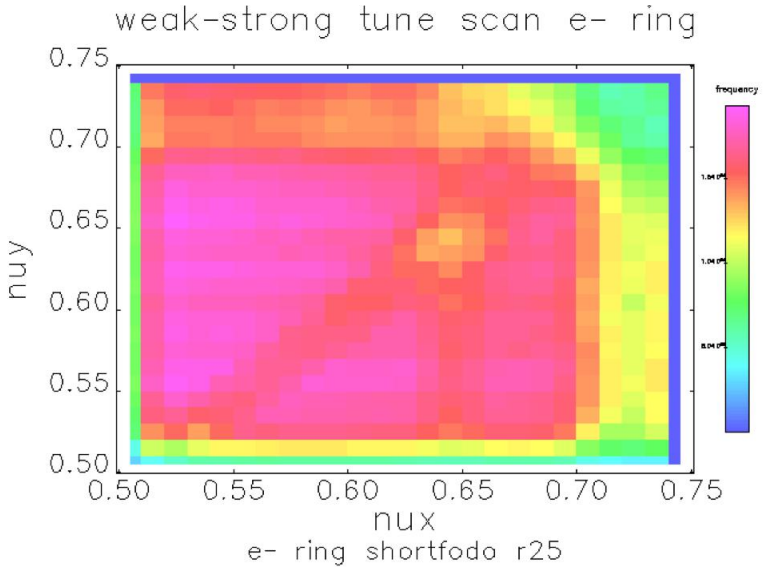

Figure 1: Weak-Strong scan for the electron ring

The head-on collision simulations showed adequate initial behaviour. The current JLEIC design relies upon short bunches and high repetition rates to achieve the desired luminosity unlike most ion colliders which rely on longer bunches with higher space charge. This design choice implies that one has relatively strong longitudinal focusing. Given that the JLEIC design also has a half crossing-angle of 25 mrad, it is important to check for synchro-betatron resonances.

2.3.11.2.3.2 Strong longitudinal focusing and synchro-betatron

The design calls for a proton bunch length of around 1 cm, corresponding to a longitudinal tune ranging from $\upsilon_s = 0.045$ ($\sigma_z = 1.4cm$) to $\upsilon_s = 0.058$ ($\sigma_z = 1.1cm$). Stronger values yielding to a smaller bunch length are possible but require a costly

increase of RF cavity power. We scanned the synchrotron tune between these values and examined the tune footprint of the proton bunch in the first 1024 turns.

As can be clearly seen in Figure 2, there is a synchro-betatron resonance. Scanning the longitudinal tune produces similar results with the resonance moving to other areas of the tune space.

2.3.11.2.3.3 Search for an alternate working point

This prompted us to consider another working point in the lower quadrant, namely ν_x=0.08, ν_y=0.14. Further optimizations for the higher order resonances ultimately resulted in converging to ν_x=0.078, ν_y=0.132. The tune diagram is shown in Figure 3.

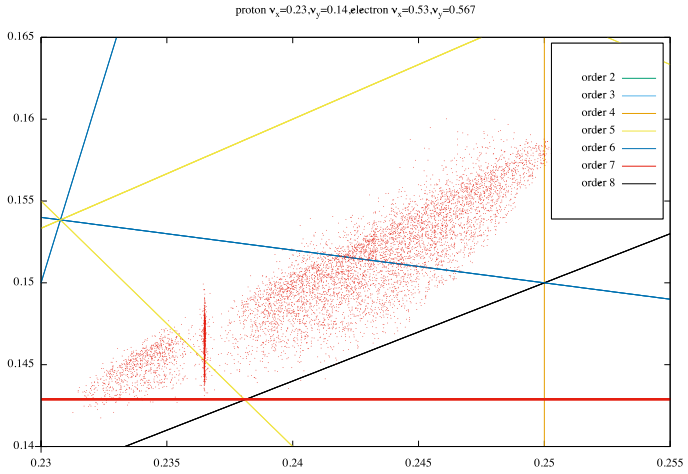

Figure 2: Tune footprint for proton with initial working point.

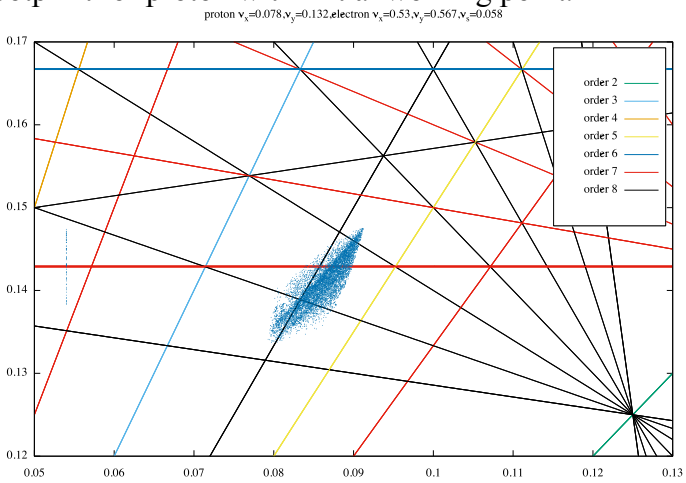

Figure 3: Tune diagram up to 8th order for proton.

2.3.11.2.3.4 Head on simulation results after optimizations

The optimized design for head-on collisions easily reaches the design luminosity of 2.1×10^{34} $cm^{-2}s^{-1}$.

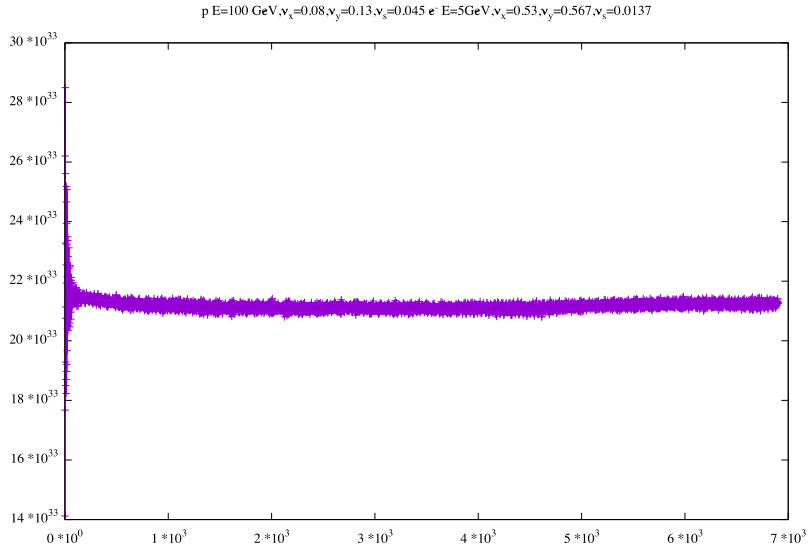

Figure 4: Head-on luminosity after optimizations.

2.3.11.2.4 The effect of crabbing

The JLEIC design features a crossing angle of 50 mrad leading to a Piwinsky angle of 13.8 which would result in an unacceptable loss of luminosity due to the beam-beam kicks generating synchro-betatron resonances.

Therefore, we adopted a crab-crossing scheme similar to what has been used elsewhere already [4]. Inherent to this scheme is the fact that since crab cavities provide transverse kicks that are dependent on the longitudinal position in the bunch, they will themselves generate synchro-betatron resonances although at a more manageable level.

2.3.11.2.4.1 Crabbing implementation

We made use of the BB3D implementation which models the crab cavities as thin-lens kicks in the *x*-*z* plane. One such cavity is placed on each side of the IP for both the proton and ion beam. The actual implementation will utilize several cavities to make up for the required gradient of 20.1 MV for a half-crossing angle of 25 mrad.

The location at which these cavities are placed in the lattice is still being under consideration. For the subsequent studies we assumed that they would be in a dispersion free region with a β_c=600 m.

The frequency was chosen to be 952 MHz in order to produce compact crab cavities. We note that since the bunch length of the ion and electron beam is small (of the order of 1 cm) compared to the RF wavelength of the crab cavities, there is no significant degradation of the longitudinal bunch phase space. We calculated the nominal crabbing voltage as $= \frac{c \tan \theta/2}{2\pi q \sqrt{\beta_c \beta_I}}$.

2.3.11.2.4.2 Initial studies and synchro-betatron crabbing mode

The initial calculation showed that with nominal crabbing voltage we have a slow decline of the luminosity over time (Figure 5).

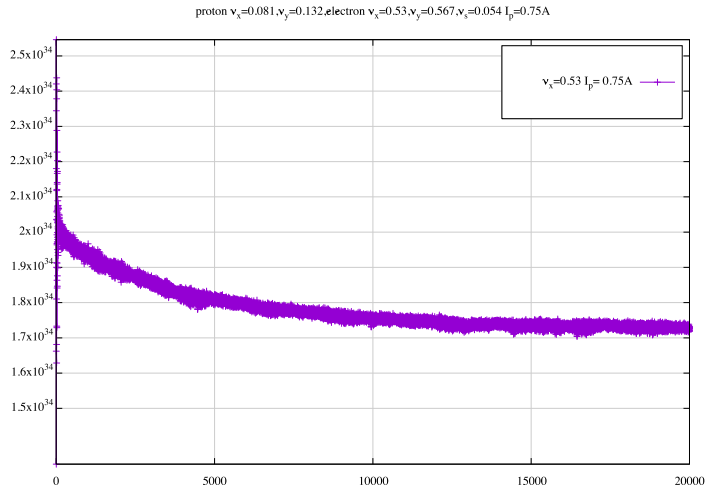

Figure 5: Luminosity reduction when crabbing.

In order to cure it, we performed longitudinal tune scans of the electron beam until we found a setting which adequately pushed the resonances away from the tune footprint.

2.3.11.2.4.3 Luminosity after optimization

After adjusting the synchrotron tune to θ_s=0.02, we were able to eliminate the loss and increase the proton beam current pushing for higher luminosity (Figure 6) which shows values well above our design goal of 2.11×10^{34} $cm^{-2}s^{-1}$.

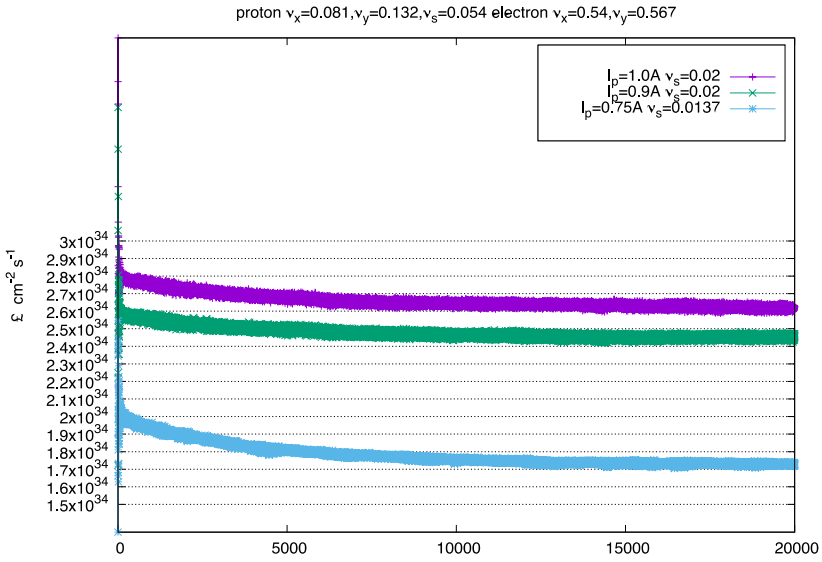

Figure 6: Luminosity versus current after optimization

We did not observe any beam-beam limit within the range of the proton currents we investigated. The upper limit for the proton current was given by limiting the Lasslett tune shift to keep the space-charge effects in the ion ring under control.

Future work in this direction will consider the effect of dispersion leakage at the location of the crab cavities as well as the tolerances required on the cavity white noise, voltage stability and higher order field components. Some of these effects can be compensated via a transverse feedback system.

2.3.11.2.5 Beam synchronization and Gear Changing

In the JLEIC design for an electron-ion collider, broad adjustments in the momentum of the ion beam are required to span the appropriate kinematical range. Consequently, because of the non-relativistic nature of the ion beam at low momentum, one has to adjust the relative timing between the relativistic electron beam and non-relativistic ion beam. This can be accomplished by adjusting the RF frequency, ring sizes or harmonic numbers of either or both rings at the same time. The latter method is attractive because it alleviates the needs for expensive hardware adjustments (moving magnets to change the path length). However, it has dynamical issues for the beam-beam interaction that have to be carefully evaluated. Namely, this "gear changing" scheme will generate a large number of additional resonances due to the uneven collision pattern which results in each bunch colliding with every other bunch in a repeating pattern giving rise to dipole moments as well as higher order moments potentially reducing the lifetime drastically.

The problem was examined in [5] by treating it in a simplified 4D framework. We propose to carry out more detailed studies using full 6D tracking with a greater number of bunches. Dedicated software, the GPU-optimized High Order Symplectic Tracker (GHOST) is being developed to do a large scale many-bunch beam-beam tracking [6,7]. It is implemented to take advantage of modern high-performance computing infrastructure using Graphical Processing Units (GPU).

2.3.11.2.6 Initial results for gear changing

Each beam is simulated by a set of point particles, sampling their initial distributions. Beam-beam effects of one beam on the other are simulated using the generalized Bassetti-Erskine approximation [8]. This treatment, which is valid for an infinitesimally short bunch, is generalized to beams of finite size by considering a number of slices. In between the consecutive collisions, the beams are transported through the rings using symplectic maps which can be of any order.

For purposes of testing and benchmarking of the new beam-beam code, we use the baseline parameters shown in Figure 1 and performed a strong-strong simulation.

Figure 7 shows the 1x1 result in red which is to be compared with the BB3D result in Figure 4. Subsequent runs with uneven number of bunches were carried out. It shows a drop in luminosity when the bunch number increases. This is expected since N1 bunches will produce an array of resonances separated by 1/N1 and is similar to what was shown in [5] using a simple beam-beam model.

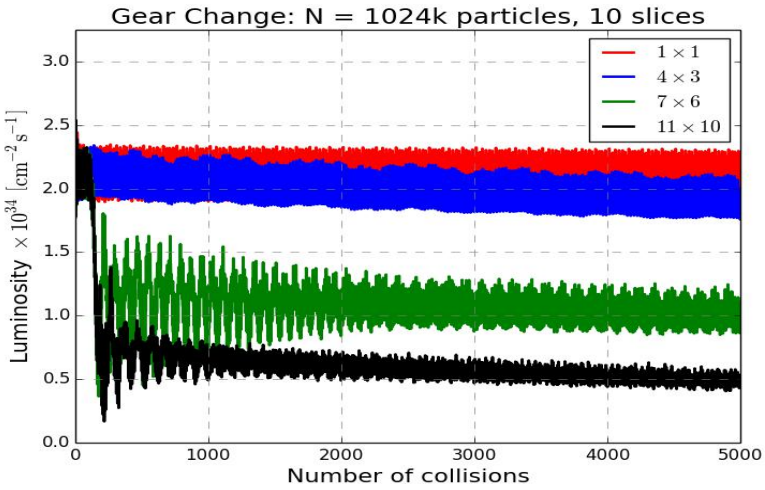

Figure 7: Initial tests of gear changing with

Future work will carefully examine the characteristics of the resonance pattern and its dependency on bunch number and beam-beam parameters for increasing values of bunches. As a reminder, the JLEIC design feature 3416 bunches. Some of the kinematics with a low momentum ion or proton will be synchronized by dropping this number by one or more units, thus running in gear change mode. In order to damp the dipole moment kicks coming from the resulting resonances, we are going to investigate using a state of the art feedback system. We expect to damp the higher moments by making use of non-linearities in the lattices as well as running with increasing Landau damping via altering the chromaticities and/or using damping wigglers.

2.3.11.3 *References*

1 S. Abeyratne et al., “Science requirements and conceptual design for a polarized medium energy electron-ion collider at Jefferson lab”, edited by Y. Zhang and J. Bisognano, arXiv:1209.0757 (2012)

2 S. Abeyratne et al, “MEIC Design Summary”, arXiv:1504:0.7961 (2015)

3 V.S. Morozov et al, “Study of Beam Synchronization at JLEIC”, arXiv:1606:0.9117 (2015)

4 T. Abe et al.,” Compensation of the Crossing Angle with Crab Cavities at KEKB”, arXiv:0706.3248

5 Y. Hao et al., “Beam Beam Effects of Gear Changing in Ring-Ring Colliders”, arXiv:1309.1739v1 (2013)

6 K. Arumugam et al., "GPU-Accelerated High-Fidelity Simulation of Beam-Beam Effects in Particle Colliders, 2017, Proceedings of the *Summer Computer Simulation Conference*, article 5.

7 R. Majeti “Multi-GPU Accelerated High-Fidelity Simulations of Beam-Beam Effects in Particle Colliders”, Masters Thesis, Old Dominion University, 2017.

8 Bassetti, M., and G. Erskine. 1980. Technical report, CERN Report No. CERN-ISR-TH/80-06.

3 Workshop and Conference Reports

3.1 9th InternaAdvanced LinEar collider study GROup workshop 2018, ALEGRO2018

Roman Walczak , John Adams Institute & Department of Physics,
University of Oxford, UK.
Andrei Seryi, Jefferson Lab, USA
Brigitte Cros, CNRS, LPGP Université Paris Sud, Orsay, France
Patric Muggli, MPP, Germany and CERN, Switzerland
Mail to: roman.walczak@physics.ox.ac.uk

The ALEGRO2018 workshop was held from March 25 to 28, 2018 at the JAI in Oxford. The Advanced LinEar collider study GROup (ALEGRO) has been set up following the ANAR 2017 workshop to co-ordinate the preparation of a proposal for an Advanced Linear Collider in the multi-TeV energy range. In the short term, the first objective of ALEGRO will be to provide input towards the update of the European Strategy for Particle Physics Update 2018.

Organized at the initiative of the ICFA panel for Advanced and Novel Accelerators (http://www.lpgp.u-psud.fr/icfaana), the ALEGRO2018 workshop brought together about 80 participants to discuss the issues to be addressed in the near future to be in a position to identify promising technologies for future advanced accelerators, and to propose some input for the European Strategy for Particle Physics Update.

Figure 1: Participants of the ALEGRO2018 workshop

Several challenges must be addressed before proposing a technical design for an Advanced Linear International Collider (ALIC), requiring the sustained efforts of a diverse community that currently includes more than 62 laboratories in more than 20 countries. The key challenges are either related to fundamental components of ANAs -- such as the injectors, accelerating structures, staging of components and their reliability -- or to beam dynamics at high energy and to the preservation of energy spread and emittance and to reaching high efficiency.

The first task of ALEGRO is to prepare and deliver, by the end of 2018, a document detailing the international roadmap and strategy of advanced novel accelerators (ANAs) with clear priorities as input for the European Strategy Group, as well as input to ICFA.

The workshop was organized around the four Advanced and Novel Accelerators (ANAs) concepts that have already reached, or hold the promise to reach an accelerating gradient larger than 1 GeV/m: the laser wakefield accelerator (LWFA), in which an intense laser pulse drives a plasma wake; the plasma wakefield accelerator (PWFA), in which a particle bunch drives a plasma wake; the structure wakefield accelerator (SWA), in which a particle bunch drives wakefields in dielectric or metallic structures; and the dielectric laser accelerator (DLA), in which a laser pulse drives wakefields in a periodic dielectric structure. The program of the workshop is available http://www.physics.ox.ac.uk/confs/alegro2018/index.asp

In addition to four working groups (WG) related to the ANA concepts, additional WGs on the physics, simulations, and machine design and a sub WG on positron acceleration were formed and worked to identify main advantages and challenges for ALIC. Overview talks of the first day were followed by discussion sessions to draw in more details the scientific roadmap previously proposed during the ANAR workshop and to more precisely define priorities for the 5-10 years time scale.

The workshop discussions can be summarized as follows:

- Long term and ambitious goals for HEP will give a new impulse to ANA development. Coordinated efforts and increased funding are needed in order to achieve faster progress
- ANAs are still partly in the exploratory/discovery phase
- Mid-term milestones have been identified and their achievement is associated with the construction of specific dedicated facilities (e.g. EuPRAXIA, kBella, FACET II, …) in order
    - to validate the reliability of ANAs
    - to demonstrate their capability to achieve higher average power
    - to develop compact positron sources
- The ALEGRO collaboration should grow and contributions from the accelerator and HEP communities are strongly encouraged

The next ALEGRO workshop will take place at CERN, March 26-29, 2019. It will be organized according to colliders systems: physics case, acceleration (plasma, dielectrics), power sources (drive beam, laser, etc), luminosity delivery (beam sources, beam cooling, tolerances, stabilization, focusing), detector (machine detector interface).

The workshop is open to contributions from the beam dynamics community in order to make more rapid progress towards a collider design.

3.2 Future Circular Collider (FCC) Week 2018

P. Charitos, F. Zimmermann
CERN, BE Department, 1211 Geneva 23, Switzerland
Mail to: frank.zimmermann@cern.ch

Almost 500 scientists and engineers from around the globe gathered at the 2018 FCC collaboration week in Amsterdam. During intense discussions from 9 to 13 April 2018, this group of world experts identified the key contents and objectives for the FCC Conceptual Design Report (CDR), which shall be delivered by the end of this year. The FCC CDR will be an input to the next update of the European Strategy for Particle Physics in 2019/20. Major advances in theoretical studies and detector techniques, presented in Amsterdam, demonstrate that with the machines explored by the FCC study one could efficiently address several of the most compelling issues in post-LHC particle physics, while at the same time driving a major program in training, technology and industrial development.

More specifically, the FCC Week 2018 reviewed the design status and technology progress of the various Future Circular Collider options – 100 TeV hadron collider (FCC-hh), highest-luminosity high-energy electron positron collider for the 90-365 GeV energy range (FCC-ee), lepton-hadron collider (FCC-eh), and an energy doubler in the LHC tunnel (High Energy LHC, HE-LHC). Coherent baseline designs and a solid physics case exist for the FCC-hh, FCC-ee, and FCC-eh. At the time of the FCC Week still several options were under investigation for the HE-LHC, which, due to its smaller tunnel cross section and constraints from the existing infrastructure, faces additional challenges. Enormous progress was reported from the technological R&D. For example, excellent gradients and Q values recently achieved with Nb/Cu cavities, and energy-efficient arc magnet systems both bode well for the FCC-ee. Enhancing the performance of Nb_3Sn superconductor through the creation of artificial pinning centers could be the key to success for the hadron colliders FCC-hh and HE-LHC. No beam dynamics showstoppers were identified for any of the collider options.

The FCC Week 2018 featured 285 oral presentations, an industrial partnership program with exhibition, and an innovation session with 80 posters. The scientific program consisted of plenary sessions on Monday and Friday and up to five parallel sessions on Tuesday, Wednesday and Thursday. A special plenary session on Thursday evening put the spotlight on the potential Dutch contributions for such a visionary project.

A snapshot from the opening of the FCC Week 2018 is shown in Fig. X1. At this opening, Jose van Dijck, President of the Royal Netherlands Academy of Arts and Sciences, asked “What is the origin of the universe?” before she observed “This very simple question lies at the heart of all your work and forms the basis of the ambitions for the Future Circular Collider study.” Figure X2 presents the geographical origins and Fig. X3 the age distribution of the FCC Week 2018 participants. The 465 participants hailed from 147 institutes in 27 countries. More than 30% of the participants were younger than 35 years. It is this young generation which will most benefit from the FCC.

During the event, CERN Director General Fabiola Gianotti remarked “I cannot see a more natural and better place than CERN to host future circular colliders of the complexity of the FCC, given CERN’s demonstrated expertise in building and operating high-energy accelerators, the existing powerful accelerator complex, and the available infrastructure that we continue to upgrade”. Indeed, the laboratory’s long history and strong expertise in all the necessary technical domains, as well as its ability to foster international collaborations which amplify the impact of such large-scale projects, provides the ideal base from which to mount the post-Higgs adventure.

More details and all the presentations give can be found on the indico web site of the FCC Week 2018, at https://indico.cern.ch/event/656491/ .

The FCC concept was born in the frame of the EU co-founded EuCARD and EuCARD-2 projects in the 2010-2014 time period. The H2020 project ARIES continues the historical support of this activity, along with the targeted H2020 programs EuroCirCol and EasiTrain.

Figure X1: Photograph showing Sijbrand de Jong, the President of the CERN Council, opening the FCC Week 2018 in Amsterdam (credit: FCC Study Office | Hucopix).

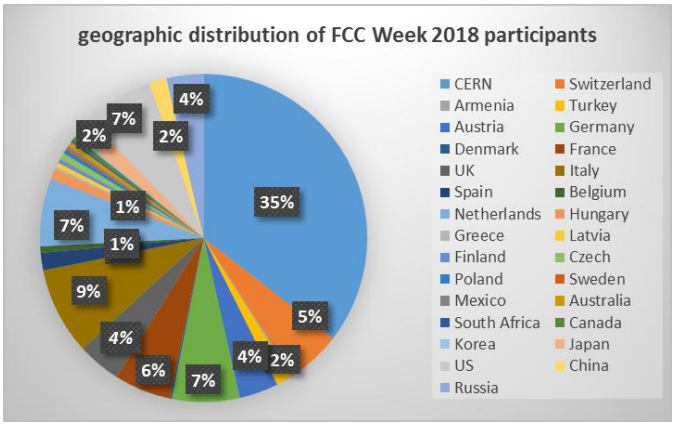

Figure X2: Geographical distribution of the FCC Week 2018 participants.

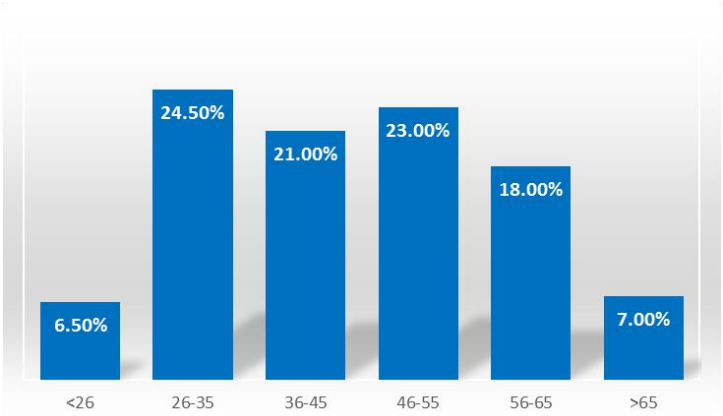

Figure X3: Age distribution (in years) of the FCC Week 2018 participants.

3.3 International Particle Accelerator Conference, IPAC'18

Shane Koscielniak
Mail to: shane@triumf.ca
TRIUMF, 4004 Wesbrook Mall, Vancouver, B.C. Canada V6T2A3

3.3.1 Introduction

The ninth International Particle Accelerator Conference, IPAC'18, took place at the J.W. Marriott Parq Hotel, Vancouver, British Columbia, Canada from Sunday to Friday, April 29 to May 04, 2018. IPAC'18 was attended by 1,276 delegates from 31 countries on all continents. The tally includes 125 industry delegates, but excludes the 88 exhibitor registrations. Hosted by the TRIUMF Laboratory, the conference was organized under the auspices of the Institute of Electrical and Electronics Engineers (IEEE), and the American Physical Society Division of Physics of Beams (APS-DPB). Established in 1968 in Vancouver, TRIUMF is Canada's particle accelerator centre. Delegates and Exhibitors were supported by a 26-member Local Organizing Committee (LOC) volunteered by TRIUMF.

3.3.2 Scientific Program

The conference was opened by Shane Koscielniak (TRIUMF), Chair of the Organizing Committee (OC), Kate Young, Federal Parliamentary Secretary for Science, and Bruce Ralston, Minister of Jobs, Trade and Technology, Government of British Columbia, who all made welcoming remarks.

Yukiyoshi Ohnishi (KEK) and Jonathon Bagger (TRIUMF) opened the scientific program with presentations, respectively, on *SuperKEKB Phase 2 Commissioning* and *TRIUMF in the ARIEL Era*. The other plenary talks on Monday morning were presented by Frank Gerigk (CERN), John Galayda (SLAC) and Sergei Nagaitsev (FNAL), respectively, *on Status and Future of Microwave Sources for Accelerators*, *LCLS-II a High-Power Upgrade for LCLS* and *The Path to Long Baseline Neutrino Factory.*

Inspiring closing presentations were delivered by Junko Yano (LBNL), *Review of FEL Science*; Bruce Carlsten (LANL,) *Applications of Compact Accelerators in Space for National Security*; and Stefania Gori (Univ. of Cincinnati), *Hidden Sectors: from Cosmos to Accelerators*.

62 invited and 63 contributed oral presentations of very high quality were made during the week. Given the recent prominence of ring- and linac-based light sources, the program was adjusted to emphasize these machines. The regional distribution of talks was 22% from Asia, 34% from Europe, and 44% from the Americas. The gender ratio for oral presentations was 84% male and 16% female.

The scientific program was developed by the 16-member IPAC'18 Scientific Program Committee (SPC) comprising 8 leads from the Americas and 4 deputies each from Asia and Europe under the leadership of Tor Raubenheimer (SLAC). Valued suggestions for invited talks were contributed by the 200-member Scientific Advisory Board (SAB) representing every accelerator laboratory world-wide. Oral sessions and poster sessions were grouped according to the eight IPAC Main Classes. The conference program spanned four and a half days, with plenary talks on Monday and Friday mornings, and additional plenary sessions on Wednesday afternoon for the Industry Panel and the Entertainment talk and on Thursday afternoon for the Accelerator Awards Ceremony. All other sessions were composed of three invited or contributed talks in parallel.

3.3.3 **Poster Sessions**

Seven Poster Sessions were held: Monday afternoon, and morning and afternoon Tuesday through Thursday – during which 1581 posters from 233 institutions were scheduled for presentation. 144 students from 83 institutions, representing 20 countries, participated in the successful Sunday afternoon student poster session, now a firm tradition of the IPAC series.

3.3.4 **Special Sessions & Events**

The scientific program was supplemented by a variety of special sessions and events.

The IEEE Women In Science and Engineering (WISE) reception, a feature of IPAC in the Americas region, was held Tuesday evening and focused on best practices for the retention, tenure, and promotion of WISE. The format was a keynote address by Grace Wong-Sneddon (Univ. of Victoria) followed by a dinner during which panelists rotated between tables to facilitate discussion on the theme topics. 109 women and men plus 10 panelists participated in the reception.

The Industry Panel Session was held on Wednesday. Panelists Alberto Degiovanni (ADAM SA), Morgan Dehnel (Buckley Systems Ltd), Michelle Shinn (US Department of Energy) and Nikolaj Zangenberg (Danish Technical Institute), moderated by Kathryn Hayashi (TRIUMF), shared their experiences and opinions on the theme *Moving from Lab to Market: Global Models of Knowledge Translation and Commercialization in the Particle Accelerator Community*.

The industry panel was followed by the entertainment talk *The Kilogram Redefined* by Alan Steele (Director General of Canada's NRC Measurement Science and Standards) wherein the System International kilogram artefact is to be replaced by a

combination of fundamental physical constants. After a brief historical introduction to the SI, Steele charted the motivation and conceptual framework for this momentous change, and the technologies being developed for its introduction.

The Industrial Exhibition took place during the first three days of the conference. Industrial exhibitors (90 companies) occupied 79 booths and 5 tables, at which they presented their high technology products and services to the delegates in an excellent atmosphere conducive to discussions wherein exhibits and posters were inter-mingled. It must be acknowledged that the conference would not be possible in its present format without the generous support of the IPAC industry exhibitors and sponsors. 12 learned societies exhibited at desks during the same 3-day period.

With the younger delegates in mind, the APS offered a *breakfast and learn* tutorial for aspiring authors and referees on Tuesday morning. This was very well attended, about 160 participants. Also oriented toward students, the conference was preceded by a one and half day program of student tutorials organized by Alyson Gold (SLAC) and Oliver Kester (TRIUMF); 51 students attended.

IPAC'18 hosted 30 official satellite meetings ranging from SPC meetings of LINAC'18 and IPAC'19, through business meetings of IEEE-NPSS, APS-DPB, EPS-AG, ICFA, IUPAP and PRAB to the 125th anniversary celebration of APS Physical Review (journal) to vendor-sponsored receptions and to French and Spanish delegations.

3.3.5 **Accelerator Awards Session**

During the Accelerator Awards Session, the prizes for best student posters were awarded to Alysson Gold (SLAC) for "A 2D Steady-State Space Charge Solver for Azimuthally Symmetric Problems of Arbitrary Degree"; and Yaoshuo Yuan (GSI): "Space charge limitations for bunch compression in synchrotrons"; and Mario Beck (CERN) for "Studies of horizontal instabilities in the CERN-SPS".

The APS Robert R. Wilson Prize, recognizing and encouraging outstanding achievement in the physics of particle accelerators was awarded to Alexander Wu Chao (SLAC) "For insightful, fundamental and broad ranging contributions to accelerator physics."

The IEEE Particle Accelerator Science and Technology (PAST) awards are granted at each Particle Accelerator Conference held in the Americas to two individuals who have made outstanding contributions to the development of particle accelerator science and technology. Hermann Grunder (Director Emeritus ANL) received the IEEE-NPSS PAST 2018 award "For far-reaching contributions to accelerator science and technology" while Sandra Biedron (Univ. of New Mexico) received the PAST 2018 award "For broad impact in accelerator science and technology".

The IEEE Nuclear and Plasma Sciences Society awards the PAST Doctoral Student Award to individuals who made significant and innovative contributions to accelerator science and technology in a student doctoral thesis. Martina Martinello (FNAL) received the 2018 IEEE-NPSS PAST Doctoral Student Award "For contributions to the physical understanding of limiting factors in SRF cavities".

The APS Division of Particle Beams Thesis Award recognizes doctoral thesis research of outstanding quality and achievement in beam physics and engineering. The 2017 recipient is Spencer Gessner (SLAC) "For an original theoretical treatment and experimental demonstration of accelerating positrons in a hollow channel plasma wakefield accelerator". The 2018 recipient is Sergey Antipov (CERN & FNAL) "For

experimental studies and analysis of electron cloud build-up and corresponding instability in accelerators with combined function magnets…"

3.3.6 **Student Support**

214 young scientists from all over the globe attended the conference. 99 of these students received travel grants thanks to the sponsorship of societies, institutes and laboratories worldwide. The Americas region sponsors are: APS, NSF and TRIUMF. The Asia region sponsors are: ANSTO, IHEP, RIKEN, KEK, SSRF and PAL. The Europe region sponsors are: CEA, CELLS, CERN, Cockcroft, DESY, Diamond, ELETTRA, ESRF, ESS, GANIL, GSI, HZB, INFN, in2p3, KIT, MAXIV, PIS, SOLEIL, STFC. The IPAC'18 budget contributed $20,000 student grants to each region. The organizers of IPAC'18 are grateful to all sponsors for their valued support of students.

3.3.7 **Proceedings**

The proceedings of IPAC'18 are published on the JACoW site (www.jacow.org). The proceedings contain the reports of 1502 total contributions. The regional breakdown is 24% Asia, 35% Americas and 41% Europe. The breakdown by Main Class is as follows: MC1 Circular and Linear Colliders, 112 contributions; MC2 Photon Sources and Electron Accelerators, 279 contributions; MC3 Novel Particle Sources and Acceleration Technologies, 108 contributions; MC4 Hadron Accelerators, 167 contributions; MC5 Beam Dynamics and EM Fields, 230 contributions; MC6 Beam Instrumentation, Controls, Feedback, and Operational Aspects, 233 contributions; MC7 Accelerator Technology, 318 contributions; MC8 Applications of Accelerators, Tech Transfer and Industrial Relations, 55 contributions.

The processing of the electronic manuscripts was achieved on-site by the 30-strong JACoW team prior to, during and immediately after the conference. The team, led by Todd Satogata (JLAB), Jana Thomson (TRIUMF) and Volker Schaa (GSI), includes "seasoned experts" who also trained less experienced volunteers. The JACoW Collaboration is formed of electronic publishing experts and technicians volunteered by laboratories worldwide. Tasks performed by the proceedings office include: author reception, processing of contributions and transparencies, checking that references are formatted to journal standards, and cross-checking of titles and authors. Setting up the computers and internet network, presentations management and poster session management were a collaborative effort between the LOC and JACoW. Thanks to the work of this dedicated team, a pre-press version with almost 1500 contributions was published on the last day of the conference. The final version was published at the JACoW site just weeks after the conference. This is yet another impressive record set by the JACoW Collaboration, which is sincerely grateful to the supervisors of each of the team members for releasing them from their usual duties.

A new feature of IPAC, introduced on a trial basis at IPAC'17, is light peer review of a limited number of papers for publication in a volume of an Institute of Physics conference proceedings. A white paper defining the review criteria and process was developed by Koscielniak & Bogacz. Papers are reviewed by the SAB, while the SPC under the leadership of the Scientific Publication Board chair, Alex Bogacz (JLAB), performed the function of editorial board. Candidate papers were submitted two weeks in advance of the normal deadline to allow a cycle or review, revision, and

final review. 190 papers were submitted, many were revised, and 177 were approved. Todd Satogata managed the review process within the JACoW database.

3.3.8 **Acknowledgments**

The success of IPAC'18 was due in great part to the truly excellent collaboration between the international teams of the OC and the SPC, and the LOC. Membership of the LOC, under the leadership of Shane Koscielniak included the following TRIUMF staff:

Cornelia Hoehr and Marco Marchetto: LOC Co-chairs
Silke Bruckner: Conference Secretary
Jana Thomson: Proceedings Office Coordinator and Deputy Chief Editor
Aurelia Laxdal: Industry Exhibits & Sponsors Liaison
Yetvart Hosepyan: Booths and Posters Logistics
Francis Pau: Accountant
Cynthia Reis: Hotel liaison, On-site registration, Visas, Events and companions
Oliver Kester: Student Grants & Student Posters
Geoff Hodgson: Audio-Visual Coordinator
Angela Hoiem & Nic Zdunich: Laboratory Tour
Kathryn Hayashi: Industry Panel Coordinator
Anna Kiatkowski: WISE Reception
Dana Giasson: Website Support
Diana Castaneda: Graphic Design
Davis Swan: IT Management
Bob Chow: JACoW IT Support
Hassan Tahir: Cell-phone App
Valentine Wu: MIS Registration
Steve McDonald: Wireless Internet
Yuri Bylinsky and Mindy Hapke: Signage
Spencer Kiy: Poster Police Coordinator
Laura Lambert: Photographer
Nancy Breedveld (Simon Fraser Univ.): Website Development and IPAC Marketing Assistant
Thu-Anh Vu (Simon Fraser Univ.): Conference Management Assistant.

The invaluable assistance of the following are also gratefully acknowledged:

Tor Raubenheimer (SLAC): Scientific Program Chair
Todd Satogata (JLAB): Scientific Secretary
Volker Schaa (GSI): Chief Editor
Alex Bogacz (JLAB): Scientific Publication Board Chair
Geoffrey Krafft (JLAB) & Hari Areti (JLAB): US Student Grants Administration.

3.3.9 **Conclusion**

The high levels of participation and enthusiasm shown at IPAC'18 clearly confirm the strong mandate for the International Particle Accelerator Conference series from the worldwide accelerator community. May future events be even more successful

than this one! The tenth IPAC will return to the Asia super-region that includes Australia, and will take place in Melbourne, Victoria, Australia, hosted by Australian Synchrotron-ANSTO and the Univ. of Melbourne.

We are convinced that the collaboration among the three regions, steadily enhanced in recent years, will continue to grow to the benefit of IPAC and the accelerator community worldwide.

3.4 The 6th Electron-Cloud Workshop, ECLOUD'18.

Roberto Cimino, LNF-INFN
Mail to: Roberto.cimino@lnf.infn.it

Electron cloud phenomena generate a lot of interest in the accelerator and other communities as the recent 6th electron-cloud workshop, ECLOUD'18 (ECLOUD'18, https://agenda.infn.it/conferenceDisplay.py?confId=13351) has demonstrated. The workshop was held at La Biodola (Isola d'Elba) Italy, from 3 to 7 June, 2018 and was attended by more than 60 participants representing institutions from Asia, Europe and USA.

The scientific program of the workshop was set up by the International Advisory Committee, chaired by F Zimmermann (CERN) and Roberto Cimino (LNF-INFN). The workshop was hosted by Istituto Nazionale di Fisica Nucleare (INFN), its Organizing Committee was chaired by R. Cimino and included Marco Angelucci, (INFN – LNF) Maria Giuseppina Bisogni, (University of Pisa and INFN Pisa), Maria Rita Ferrazza, (INFN – LNF), Lucia Lilli, (INFN Pisa), Riccardo Paoletti, (University of Siena, and INFN Pisa), Giovanni Rumolo, (CERN).

Electron clouds – abundantly generated in accelerator vacuum chambers by residual-gas ionization, photoemission and secondary emission – can affect the operation and performance of hadron and lepton accelerators in a variety of ways. They can induce increases in vacuum pressure, beam instabilities, beam losses, emittance growth, reductions in the beam lifetime, or additional heat loads on a (cold) chamber wall.
More than 60 physicists and engineers from around the world gathered at La Biodola, Elba, on 3-7 June, to discuss the state of the art and review recent electron-cloud experience. Not only scientists active in accelerator studies were present at the workshop, but also some international experts working on plasma research, space charging and satellite communication radio frequency issues, Gabor lenses and even in astrochemistry shared common experimental and theoretical issues in a very dense three days workshop with about 60 talks.

The first day was devoted to reports on the many electron-cloud signatures which have been recorded and analysed not only at the LHC at CERN in Geneva, but also at the SuperKEKB in Japan, at CESR Damping Ring Test Accelerator (CesrTA) at Cornell, at DAFNE in Frascati Italy, at the Relativistic Heavy Ion Collider (RICH) and

FERMILAB in USA, at the Japan Proton Research Complex (J-PARC), PETRA III at DESY Germany etc.
These machines all serve as valuable test beds for simulations of electron-cloud build up, instabilities and heat load, as well as for new diagnostics methods. These latter include measurements of synchronous phase-shift and cryo effects at the LHC, as well as coded-aperture images and time-resolved shielded pick-ups at CesrTA. The impressive resemblance between simulation and measurement suggests that the existing electron-cloud models correctly describe the phenomenon. The workshop also analysed potential electron-cloud effects on proposed future machines, such as the High-Luminosity LHC, the Future circular colliders (FCC), the China Spallation Neutron Source (CSNS), the Circular Electron Positron Collider (CEPC) in China, etc.

The second day was devoted to present and discuss the laboratory studies performed worldwide to study material and surface properties governing the phenomena. Secondary Electron Yield (SEY), Photoelectron Yield (PY), Photo Reflectivity (R), are all experimental properties necessary to simulate the e-cloud effects in accelerators, but also governs performances of: satellites under the influence of sunlight or when moving across electron clouds in outer space in space; high-power microwave devices on space satellites; Hall Thruster propulsion in plasma physics, etc.
A section was devoted to discuss other properties, low impedance and vacuum performance and stability among others, required to a material to be compliant with its use in accelerators, Radio Frequency antennas, etc. Any mechanism proposed to mitigate e$^-$cloud effects needs to be validated to fulfil all the different material requirements, so interplay between different communities studying different material properties is strongly recommended.

The third day was devoted to analyse the huge progress in simulations not only at CERN with PyECLOUD but also for SYNRAD3D from Cornell for photon tracking, including surface properties and 3D geometries. Also, studies to simulate SEY from basic material properties as done in Trento and in Toulouse were presented and recognized to be potentially very useful to device applications.
Finally, a section presenting the solutions proposed to mitigate such e-cloud related detrimental effects was of great interest and triggered a lot of passionate discussion. Future directions and common activities were also discussed.
The participants also enjoyed a 1-hour soccer match between experimental and theoretical electron-cloud experts, as well as post-dinner discussions until well after midnight.

ECLOUD18 could not solve all of the puzzles and open questions remain. Therefore, it has been proposed to reconvene in Elba in 2021 for the next edition of this topical workshop. A major request was to extend it to a five-days meeting to broaden up the

interested audience, the various interdisciplinary contributions and to leave more time for open discussion.

For the workshops organizers, the request from the community to repeat the event in the same place, for a larger audience and for a longer time is of great satisfaction.
The workshop was dedicated to the memory of the late Francesco Ruggiero, former leader of the accelerator physics group at CERN, who launched an important remedial electron-cloud crash programme for the LHC in 1997.

The detail program and talks are available via the workshop website. The workshop proceedings will be published as CERN "Yellow Book" and should be available by 2019.

Figure 1: ECLOUD'18 Workshop poster.

Figure 2: Participants of the ECLOUD'18 Workshop.

3.5 The 61st ICFA Advanced Beam Dynamics Workshop on High-Intensity and High-Brightness Hadron Beams, HB2018

Dong-O Jeon
Mail to: jeond@ibs.re.kr
Institute for Basic Science, Daejeon, S. Korea

The 61st ICFA Advanced Beam Dynamics Workshop on High-Intensity and High-Brightness Hadron Beams (HB2018, http://hb2018.ibs.re.kr) was held in Daejeon, S. Korea from June 17 to June 22, 2018 and was attended by 157 participants from 12 countries representing Asia, Europe and the USA. HB2018 was the 9th workshop in the series of international workshops covering the high-intensity and high-bright hadron beam dynamics and accelerators.

The scientific program was formulated by five working groups which were set up by the International Organizing Committee, chaired by Y.H. Chin (KEK). The workshop was hosted by the Institute for Basic Science in Korea, and its Local Organizing Committee was chaired by D. Jeon (IBS) and included J.H. Jang (IBS), I.S. Hong (IBS), H. Jin (IBS), D.E. Kim (PAL), E.H. Lee (PAL), B.S. Lee (KBSI), M.S. Won (KBSI), M. Chung (UNIST), E.S. Kim (Korea Univ), S.H. Park (Korea Univ), B.S. Joo (IBS), J. Cho (IBS).

102 talks were presented during the plenary sessions and parallel working group (WG) sessions. Five working groups covered a wide range of topics. WG-A was dedicated to beam dynamics in rings and 26 talks were presented. WG-A was convened by Y.H. Chin (KEK), G. Franchetti (GSI), and V. Lebedev (FNAL). WG-B focused on beam dynamics in linacs and 26 talks were presented. WG-B was convened by P. Ostroumov (FRIB), P.A.P. Nghiem (CEA), and H. Zhao (IMP). WG-C addressed accelerator systems and 15 talks were presented. WG-C was convened by F. Garcia (FNAL), N. Pichoff (CEA), and M. Chung (UNIST). WG-D covered commissioning and operations, and 14 talks were presented. WG-D was convened by H. Hideaki (JAEA), Y. Papaphilippou (CERN), and D. Raparia (BNL). WG-E was dedicated to instruments and beam interactions, and 12 talks were presented. WG-E was convened by P. Forck (GSI), M. Minty (BNL), and H.S. Lee (PAL).

There was one poster session on Wednesday afternoon and 28 posters were presented. Thursday evening there was a banquet and the Korean traditional music and dance performance were presented. On Friday there were summary sessions of each working group followed by an invited talk titled “Summary of the laser plasma acceleration researches in Korea” which was presented by H. Suk (GIST).

The detailed workshop program and workshop photos are available via the workshop website. The workshop pre-proceeding was published on the closing of the workshop at http://hb2018.vrws.de. Thanks go to the JACoW team.

Figure 1: HB2018 Workshop poster.

Figure 2: HB2018 Workshop group photo.

3.6 Muon Collider Workshop 2018

M. Zanetti[1)], F. Zimmermann[2)]

[1)] INFN and U. Padova, Italy
[2)] CERN, BE Department, 1211 Geneva 23, Switzerland
Mail to: frank.zimmermann@cern.ch

On 2-3 July 2018 a muon collider workshop at the University of Padua attracted 78 experts from Europe and the US, as illustrated in Figs. Y1 and Y2. This exciting and forward-looking workshop was the second event organized in the frame of the EU co-funded ARIES work package 6.6, after the Photon Beams workshop in 2017 (https://indico.cern.ch/event/668097/).

Setting the stage, Carlo Rubbia, from CERN and INFN, the recipient of the 1984 Nobel Prize for Physics and a lifelong Member of the Senate of the Italian Republic, called for an initial cooling experiment to demonstrate muon cooling and the particular merits of parametric ionization cooling. He pointed out that the first muon facility would comprise a ring at the scale of the PS, and hinted at the ESS as being the ideal place for a muon-beam facility in Europe. Recognizing the muon collider as a project of reasonable cost and of reasonably fast construction, he admonished the audience to focus on scientific work instead of "PowerPoint studies".

BNL's Mark Palmer summarized the results of the past MAP studies n the US. He reported the designs of the facilities NuSTORM, and NuMAX, which are short and long baseline options, respectively, with remarkably attractive capabilities for precision physics. A later multi-TeV muon collider would fit on the FNAL site. Mark also discussed alternative options for a muon collider in the LHC tunnel. The MAP study had considered 10 T dipoles, or about 1000 turns decay time. Echoeing Carlo Rubbia, Mark's recommended strategy was to build NuSTORM and to pursue an advanced cooling demonstration. The full physics performance and achievable resolution need to be further analyzed. The preferred scenario is a programme which culminates in a muon collider and which does do exciting science all along the way.

Ken Long from Imperial College London reported the excellent results of the MICE cooling experiment. A novel emittance measurement technique, which had to be developed for MICE, achieved a percent level precision.

At the workshop a general consensus emerged that the steps forward should include the design and implementation of a 6D cooling experiment, and the establishment of a particle-physics programme based on high-intensity, high-energy muon beam, e.g. NuSTORM, presented in detail by Jaroslav Pasternak, also from Imperial College. Scott Berg of BNL pointed out that the matching problem for multiple cooling cells still ought to be addressed.

In addition to the classical muon production approach where high-intensity proton beams are shot on a target for pion generation, with subsequent muon ionization cooling, three alternative novel schemes are recently being explored, under the names "Gamma Factory", "muon photocathode" and "LEMMA".

Witek Krasny, from LPNHE Paris and CERN, introduced the "Gamma Factory," where partially stripped heavy ion beams at high energy are collided with laser or FEL pulse. He highlighted three specific scenarios for producing polarized leptons (muons or positrons) using the Gamma Factory concept, and the associated ongoing SPS experiments. A breakthrough scheme with Pb^{+79} ions avoids the double excitation of electrons into the continuum.

Camilla Curatolo, from INFN Padova discussed a "muon photocathode", which could be realized in Hadron Photon Collisions using an FEL. To study such a scheme she developed a dedicated event generator. For an FCC-based example, the normalized emittance would be less than 1 micron. The proton-gamma luminosity could be $10^{38}/cm^2/s$. Muon accumulation and muon polarization are to be considered.

Manuela Boscolo from INFN Frascati presented the LEMMA scheme, which she had first proposed together with Pantaleo Raimondi (ESRF) and Mario Antonelli (INFN). At LEMMA, 45 GeV positrons circulating in a storage ring annihilate on a thin internal target, resulting in muon production. The positron beam loses several tens of MW energy passing through the target, made e.g. from beryllium, carbon, or hydrogen. About 200 kW of this power is deposited inside the target. Target survival is an open question. Liquid targets or rotating targets are among the options proposed. The workshop participants agreed on the need for experimental target tests. Oscar Blanco from INFN-LNF reported on the LEMMA muon accumulator ring. He pointed out that the muon beam emittance is limited by multiple scattering in the annihilation target. Citing Daniel Schulte of CERN, he also showed that for a 3 mm Be target the minimum normalized emittance is 600 nm, significantly larger than the 40 nm emittance previously assumed. Simone Liuzzo of ESRF explained that, for LEMMA, more than 120 MW of synchrotron radiation are emitted in a 6.2 km positron ring. For a 27 km

ring the synchrotron-radiation power drops below 30 MW. Frank Zimmermann of CERN highlighted that this power becomes even lower if the 100 km FCC-ee ring is employed, which serendipitously, thanks to its Z-pole running mode, already offers the right beam energy. Intriguingly, Francesco Collamati, from INFN Roma, showed that the abundant bremsstrahlung photons which are equally emitted from the target can be used to generate more positrons, leading to a self-amplification of the positron beam, which could solve the challenge of generating positrons at the rate required for LEMMA. Susanna Guiducci from INFN-LNF reviewed the state of the art in positron sources, which would be an integral part of LEMMA.

Daniel Schulte of CERN discussed the potential use for muon-collider R&D of an experimental programme using electron beams from the CERN SPS, with a CLIC like injector. He underlined that plasma acceleration is a perfect match for muons, which typically are of low intensity and fairly large emittance. He argued that "if it is not suitable here, plasma acceleration probably cannot be used for any other type of collider".

Scott Berg of BNL and Alex Bogacz from JLAB discussed options for muon acceleration, including the FFA accelerator prototype CBETA under construction at Cornell (see also the recent first ever experimental demonstration of muon radiofrequency acceleration at J-PARC, CERN Courier 9 July 2018; https://cerncourier.com/muons-accelerated-in-japan/).

In an exceptional remote presentation of this workshop, David Neuffer of FNAL, presented the fascinating option of a 14 TeV muon collider in LHC tunnel, which could be a cost-effective approach for reaching the ten-TeV scale in lepton collisions. The proposal is illustrated in Fig. Y3. Upon request, he also detailed the three fundamental laws of beam physics.

Daniel Kaplan of IIT reviewed limits from neutrino radiation. Concerning the next steps, he recalled that "you don't get tenure by saving government money".

Frank Zimmermann, of CERN, sketched a possible upgrade of the FCC lepton and hadron-collider complex to a high-energy muon collider, using a combination of Gamma Factory and LEMMA concepts – Fig. Y4. He showed that for various reasons and in view of the scaling laws – which call for ring of large circumference and with high magnetic field – the FCC appears to be the ideal basis for constructing a future 100 TeV muon collider.

CERN's Jean-Pierre Delahaye compared the performance of proposed future colliders, introducing two figures of merit, the luminosity per construction cost and the luminosity power electrical power. He showed that the FCC-ee was the best of all options, while the figures of the muon collider extended all across the figure-of-merit plane from the worst (muon Higgs factory) to the best (multi-TeV muon collider) – see Fig. Y5.

Alain Blondel from the University of Geneva pointed out that luminosity measurement techniques for muon colliders need to be worked out. Mario Greco from Roma Tre highlighted the importance of QED radiative eff ects for a precision study of the Higgs pole line shape and the signal-to-background ration, both at a Higgs factory muon collider and at the FCC-ee.

At the end of the workshop, Nadia Pastrone, from INFN Torino, the coordinator of the European muon collider study group, drew some enthusiastic conclusions and discussed the muon-collider input to the European Strategy Update.

More details and all presentations can be found on the indico web site of the muon collider workshop, at https://indico.cern.ch/event/719240 .

Figure Y1: Some participants of the ARIES WP6 workshop on Muon Colliders.

Figure Y2: A few snapshots from the ARIES muon collider workshop in Padua, showing – among others – Carlo Rubbia, Mark Palmer, Witek Krasny, Alex Bogacz, Marco Zanetti, Manuela Boscolo, Susanna Guiducci, Rol Johnson, Pantaleo Raimondi, and Jean-Pierre Delahaye.

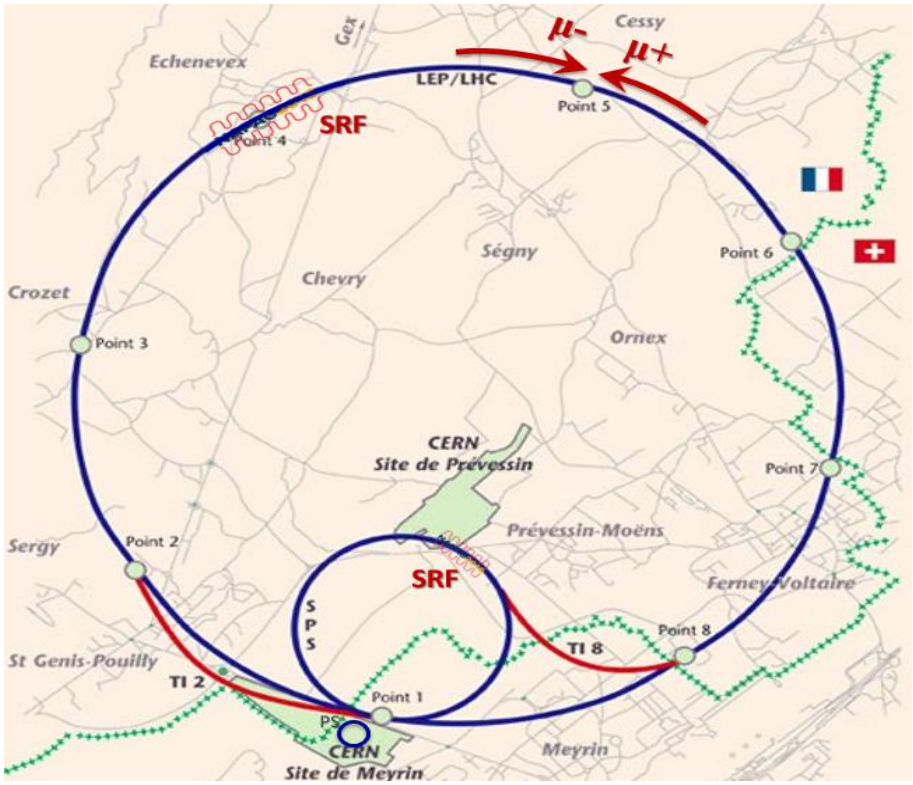

Figure Y3: A 14 TeV muon collider in the LHC tunnel (D. Neuffer and V. Shiltsev).

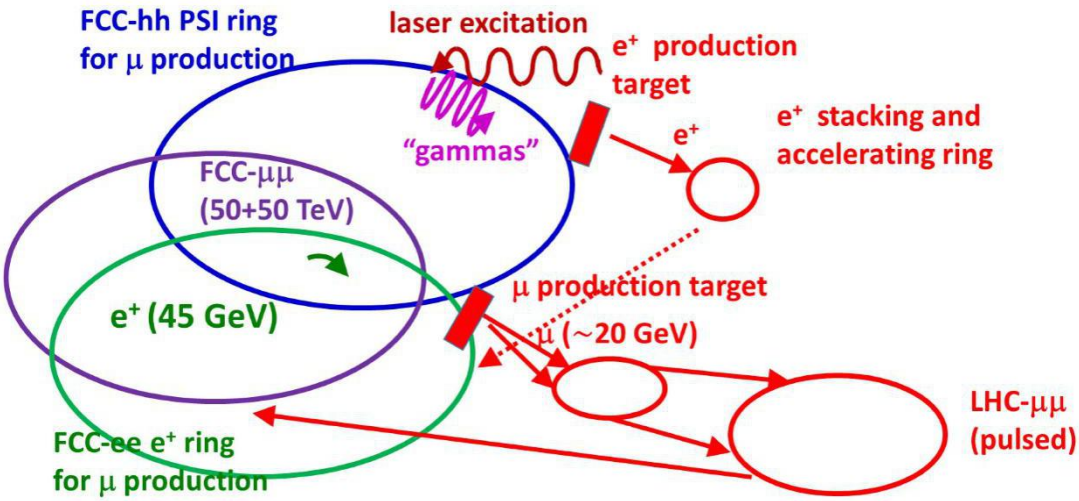

Figure Y4: A 100 TeV muon collider, "FCC-μμ", in one of the FCC-hh rings, with e^+ production from a Gamma Factory using partially stripped ion beams circulating in the other FCC-hh ring, and with LEMMA type muon production from a positron beam stored in one of the 45 GeV FCC-ee rings (Frank Zimmermann).

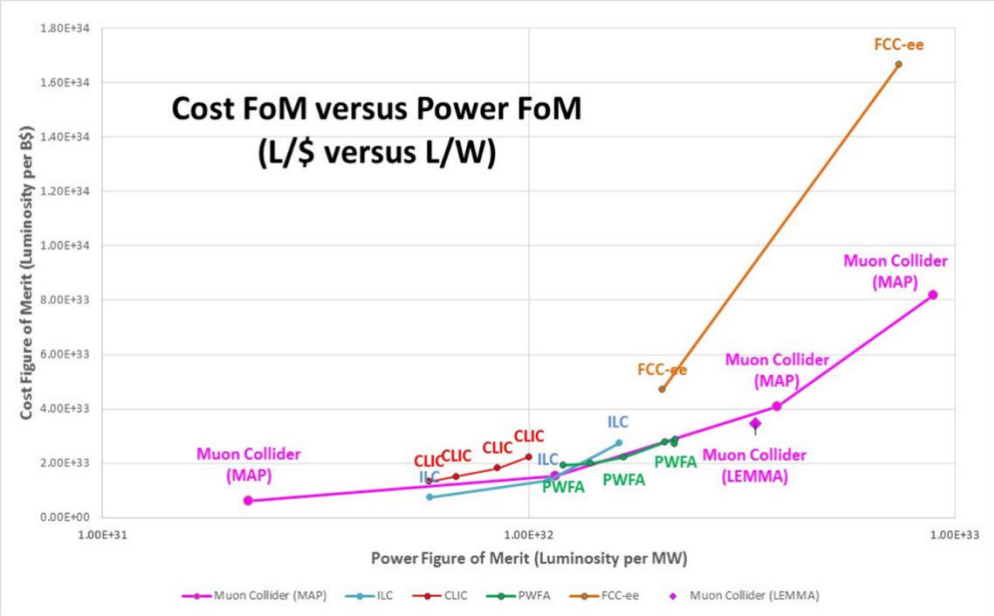

Figure Y5: Cost-figure-of-merit versus power-figure-of-merit for future lepton colliders (Jean-Pierre Delahaye).

4 Recent Doctorial Theses

4.1 Circular Electron Positron Collider Booster Lattice Design and Nonlinear Beam Dynamics Optimization

Tian Jian Bian
IHEP, CAS, 100049, Beijing, China
Mail to: biantj@ihep.ac.cn

Graduation date: 8 May 2018
Institutions: Institute of High Energy Physics, CAS, China
Supervisors: Prof. Jie Gao (IHEP)

Abstract
In this thesis, we have studied the key physics problems in beam dynamic of CEPC booster. Booster do not have low beta section and low emittance requirement, so in most of the boosters with small circumference, the nonlinear beam dynamic is not the keystone of research. The circumference of CEPC booster is 100 kilometres, some nonlinear beam dynamic phenomena will limit the lattice design at this length scale.

The main contents of this thesis is as follows:
First, we analyzed the linear motion of spring oscillator with Lie algebra as an example, then we talked about the nonlinear behaviors of charged particle in accelerator. The first, second, third order nonlinear map of the most commonest magnet elements are derived. This part is the theoretic basis of our work.

Second, accelerator design study of 50 kilometres scheme (including normal bend scheme and wiggler bend scheme) and 100 kilometres scheme are presented. Because of the disturbance of the geomagnetic field, orbit correction is implemented.
Third, the key point of optimization of FODO structure is analyzed analytically. An optimized FODO lattice is proposed for CEPC booster. Theoretical analysis and numerical simulation are agree well with each other.
Fourth, getting rid of background of the CEPC booster design, the optimization method of common FODO lattice is studied. A FODO lattice scheme with cancellation effect of first and second order energy spread nonlinear resonance terms is proposed. Comparing with the FODO lattice of arc region in CEPC collider, the new FODO lattice scheme in this thesis show better performance in nonlinear beam dynamics.
Fifth, development of C++ open source library of beam dynamics simulation and optimization. The library is named Moola (Modular&parallel Optics Optimization for LAttice). After benchmarking, Moola is used for simulation and optimization of CEPC booster lattice and new FODO lattice scheme.

The innovation points of the thesis include:
1. The first, second, third order nonlinear map of the drift, bend and sextupole are derived.
2. Preliminary design of CEPC booster lattice.
3. The key point of optimization of FODO structure is analyzed analytically. The optimization method is used for lattice design of CEPC booster.
4. A FODO lattice scheme with cancellation effect of first and second order energy spread nonlinear resonance terms is proposed. The optimization result of the new scheme is verified by numerical simulation.
5. Development of C++ open source library of beam dynamics simulation and optimization.

4.2 Coupling Impedance Measurement and Analysis of Critical Vacuum Chamber Components for the Advanced Photon Source (APS) Upgrade

Medani Sangroula
The Advanced Photon Source at Argonne National Laboratory, Argonne, IL, USA
Illinois Institute of Technology, Chicago, IL, USA
Mail to: msangrou@hawk.iit.edu

Graduation date: 11 May 2018
Institutions: The Advanced Photon Source at Argonne National Laboratory, Argonne, IL, USA Illinois Institute of Technology, Chicago, IL, USA
Supervisors: Prof. Dr. Carlo Segre (Illinois Institute of Technology), Dr. Ryan Lindberg (APS, ANL)

Abstract
The Advanced Photon Source is in the design phase of a major upgrade that will increase the x-ray brightness by two to three orders of magnitude. Stably storing such

an intense beam requires very strong magnets that demand narrow gap vacuum chamber. These narrow gap chambers and the associated small aperture vacuum components must be designed with minimal coupling impedance so as to minimize potential rfheating and to avoid deleterious collective instabilities of the electron beam. This thesis focuses on impedance measurements, simulations, and analysis of critical vacuum chamber components for the APS Upgrade (APS-U), using both the traditional coaxial wire method and the novel Goubau line (G-line) method. Impedance measurements of accelerator components have traditionally been done with the coaxial wire method, which is based on the fact that the fundamental TM mode can mimic the field of a particle beam. We describe how a similar field profile can be exploited to measure impedance with a G-line, which is essentially a transmission line designed to propagate Sommerfeld-like surface waves. We describe in detail the measurement procedure that we have developed for the G-line, including the measurement setup and proper definition of a reference, measurement procedure and advantages, and our experience regarding how to reduce systematic experimental error that we learned over the course of the measurements. After describing the measurement and simulation techniques, we then turn to our results. Since there has been some controversy regarding the impedance cost of NEG, we first present impedance measurements of APS-U NEG-coated copper chambers based on the traditional coaxial wire method. We then discuss the impedance analysis of APS-U vacuum chamber components using the G-line, starting with our initial suite of measurements and simulations designed to benchmark and validate the novel G-line based measurement technique. We then present the measured results for the beam position monitor (BPM)-bellows assembly, gate valve liner, rf-flanges, pumping cross etc., along with some simulated results and associated analysis. The measured results of the NEG-coated chamber show that the effect of impedance due to the 1.5- micron thick NEG coating on copper is mostly negligible up to 21 GHz, as predicted by simulations. In 28-29 GHz range, the NEG-coated chamber exhibited a slightly higher ($\leq$ 1 dB) transmission, which is unexplained but of little impact to APS-U design. In addition, the measured results of the APS-U BPM-bellows assembly, gate valve liner and the pumping cross have been properly designed and manufactured to specifications, with no observable resonance peaks. On the other hand, impedance evaluations of several flange designs have displayed resonances that we subsequently attributed to improper machining and/or poor tolerance control, and we have worked to insure future designs can be made to specifications. Finally, we show that the G-line is relatively simple and in our opinion better way to measure the impedance over a broad frequency range.

5 Forthcoming Beam Dynamics Events

5.1 Workshop on Accelerator Operations (WAO2018)

The 11th workshop in this series is will take place on Long Island in Stony Brook, New York, USA, from September 30 to October 5, 2018. WAO 2018 is hosted by the Relativistic Heavy Ion Collider (RHIC) and National Synchrotron Light Source II (NSLS-II) facilities at Brookhaven National Laboratory (BNL).

Since its inception in 1996, the Workshop on Accelerator Operations has taken place every 2-3 years at a variety of venues alternating between North America, Europe, and Asia. Operations staff and other professionals from around the world gather to collaborate and discuss topics related to accelerator operations, such as this year's agenda:

- Adapting to Change
- Aging Accelerators
- Beam Diagnostics
- Designing and Building a Control Room
- Commissioning new Accelerators
- Compact Facilities
- How We Do Business
- Involving Operators in Accelerator Physics
- New Technologies
- Operator Interface to Controls
- Operator Roles Outside Operations
- Operator Tools and Software
- Operator Training Programs

In addition to presentations, there will be a poster session and software demonstrations, and periods of open discussion for additional topics. A tour of BNL facilities is also scheduled at the end of the workshop.

The Workshop will be held in the Wang Center at Stony Brook University. Short travel to nearby villages offer fine dining, entertainment, and pleasant ocean views of the Long Island Sound from the north shore of the island. Further travel south and east offer Atlantic Ocean beaches, wineries, and other interesting and historic destinations. To the west, past more historic landmarks dining and entertainment, New York City remains 1.5-2 hours away by train or car, with major airports available for international travel.

The International Program Committee's preliminary workshop agenda is now published online:

https://www.bnl.gov/wao18/

The website also includes information on registration, travel and directions, accommodations, abstract submissions, and other local information.

Gregory Marr, International Program Committee Chair WAO 2018

5.2 DAFNE as Open Accelerator Test Facility in year 2020 ICFA Mini-Workshop (DAFNE-TF)

The workshop will take place on December 17th, 2018 at the Frascati Laboratory of INFN, Italy. It is intended to discuss the interest from scientists to access the DAFNE e+ e- complex, which will conclude its physics program as collider by the end of 2020.

An infrastructure almost unique, that could open to the international community for studies of accelerator technologies, beam physics, for small experiments, and to be used as a test bed for enterprises in the sector of instrumentation for accelerators.

The workshop website will be setup soon to include the latest information and will appear on:

www.lnf.infn.it

Pierluigi Campana, DAFNE-TF ICFA Mini-Workshop Chair

6 Announcements of the Beam Dynamics Panel

6.1 ICFA Beam Dynamics Newsletter

6.1.1 Aim of the Newsletter

The ICFA Beam Dynamics Newsletter is intended as a channel for describing unsolved problems and highlighting important ongoing works, and not as a substitute for journal articles and conference proceedings that usually describe completed work. It is published by the ICFA Beam Dynamics Panel, one of whose missions is to encourage international collaboration in beam dynamics.

Normally it is published every April, August and December. The deadlines are 15 March, 15 July and 15 November, respectively.

6.1.2 Categories of Articles

The categories of articles in the newsletter are the following:

1. Announcements from the panel.

Reports of beam dynamics activity of a group.

Reports on workshops, meetings and other events related to beam dynamics.

Announcements of future beam dynamics-related international workshops and meetings.

Those who want to use newsletter to announce their workshops are welcome to do so. Articles should typically fit within half a page and include descriptions of the subject, date, place, Web site and other contact information.

Review of beam dynamics problems: This is a place to bring attention to unsolved problems and should not be used to report completed work. Clear and short highlights on the problem are encouraged.

Letters to the editor: a forum open to everyone. Anybody can express his/her opinion on the beam dynamics and related activities, by sending it to one of the editors. The editors reserve the right to reject contributions they judge to be inappropriate, although they have rarely had cause to do so.

The editors may request an article following a recommendation by panel members. However anyone who wishes to submit an article is strongly encouraged to contact any Beam Dynamics Panel member before starting to write.

6.1.3 How to Prepare a Manuscript

Before starting to write, authors should download the template in Microsoft Word format from the Beam Dynamics Panel web site:

http://icfa-bd.kek.jp/icfabd/news.html

It will be much easier to guarantee acceptance of the article if the template is used

and the instructions included in it are respected. The template and instructions are expected to evolve with time so please make sure always to use the latest versions.

The final Microsoft Word file should be sent to one of the editors, preferably the issue editor, by email.

The editors regret that LaTeX files can no longer be accepted: a majority of contributors now prefer Word and we simply do not have the resources to make the conversions that would be needed. Contributions received in LaTeX will now be returned to the authors for re-formatting.

In cases where an article is composed entirely of straightforward prose (no equations, figures, tables, special symbols, etc.) contributions received in the form of plain text files may be accepted at the discretion of the issue editor.

Each article should include the title, authors' names, affiliations and e-mail addresses.

6.1.4 **Distribution**

A complete archive of issues of this newsletter from 1995 to the latest issue is available at

http://icfa-usa.jlab.org/archive/newsletter.shtml.

Readers are encouraged to sign-up for electronic mailing list to ensure that they will hear immediately when a new issue is published.

The Panel's Web site provides access to the Newsletters, information about future and past workshops, and other information useful to accelerator physicists. There are links to pages of information of local interest for each of the three ICFA areas.

Printed copies of the ICFA Beam Dynamics Newsletters are also distributed (generally some time after the Web edition appears) through the following distributors:

John Byrd	jmbyrd@lbl.gov	North and South Americas
Rainer Wanzenberg	rainer.wanzenberg@desy.de	Europe++ and Africa
Toshiyuki Okugi	toshiyuki.okugi@kek.jp	Asia**and Pacific

++ Including former Soviet Union.

** For Mainland China, Jiu-Qing Wang (wangjq@mail.ihep.ac.cn) takes care of the distribution with Ms. Su Ping, Secretariat of PASC, P.O. Box 918, Beijing 100039, China.

To keep costs down (remember that the Panel has no budget of its own) readers are encouraged to use the Web as much as possible. In particular, if you receive a paper copy that you no longer require, please inform the appropriate distributor.

6.1.5 **Regular Correspondents**

The Beam Dynamics Newsletter particularly encourages contributions from smaller institutions and countries where the accelerator physics community is small. Since it is impossible for the editors and panel members to survey all beam dynamics activity worldwide, we have some Regular Correspondents. They are expected to find interesting activities and appropriate persons to report them and/or report them by themselves. We hope that we will have a "compact and complete" list covering all over the world eventually. The present Regular Correspondents are as follows:

Liu Lin *Liu@ns.lnls.br* *LNLS Brazil*
Sameen Ahmed Khan Rohelakan@yahoo.com SCOT, Middle East and Africa

We are calling for more volunteers as Regular Correspondents.

6.2 ICFA Beam Dynamics Panel Members

Name	eMail	Institution
Rick Baartman	baartman@lin12.triumf.ca	TRIUMF, 4004 Wesbrook Mall, Vancouver, BC, V6T 2A3, Canada
Marica Biagini	marica.biagini@lnf.infn.it	INFN-LNF, Via E. Fermi 40, C.P. 13, Frascati, Italy
John Byrd	jbyrd@anl.gov	Accelerator Systems Division Argonne National Laboratory 9700 S. Cass Ave Building 401-C4263, Argonne, IL 60439, U.S.A.
Yunhai Cai	yunhai@slac.stanford.edu	SLAC, 2575 Sand Hill Road, MS 26 Menlo Park, CA 94025, U.S.A.
Yong Ho Chin	yongho.chin@kek.jp	KEK, 1-1 Oho, Tsukuba-shi, Ibaraki-ken, 305-0801, Japan
Jie Gao	gaoj@ihep.ac.cn	Institute for High Energy Physics, P.O. Box 918, Beijing 100039, China
Ajay Ghodke	ghodke@cat.ernet.in	RRCAT, ADL Bldg. Indore, Madhya Pradesh, 452 013, India
Eliana Gianfelice-Wendt	eliana@fnal.gov	Fermilab, Mail Station 312, PO Box 500, Batavia IL 60510-5011, U.S.A.
Ingo Hofmann	i.hofmann@gsi.de	High Current Beam Physics, GSI Darmstadt, Planckstr. 1, 64291 Darmstadt, Germany
Sergei Ivanov	sergey.ivanov@ihep.ru	Institute for High Energy Physics, Protvino, Moscow Region, 142281 Russia
In Soo Ko	isko@postech.ac.kr	Pohang Accelerator Lab, San 31, Hyoja-Dong, Pohang 790-784, South Korea
Elias Metral	elias.metral@cern.ch	CERN, CH-1211, Geneva 23, Switzerland
Peter Ostroumov	Ostroumov@frib.msu.edu	FRIB, National Superconducting Cyclotron Laboratory, Michigan State University, 640 S. Shaw Lane East Lansing, Michigan 48824, U.S.A.
Mark Palmer	mpalmer@bnl.gov	Brookhaven National Lab, Upton, NY 11973, U.S.A.
Chris Prior	chris.prior@stfc.ac.uk	ASTeC Intense Beams Group, STFC RAL, Chilton, Didcot, Oxon OX11 0QX, U.K.
Ji Qiang	jqiang@lbl.gov	Lawrence Berkeley National Laboratory (LBNL), MS 71J-100a, One Cyclotron Road, Berkeley, California, CA 94720-8211 USA
Yuri Shatunov	Yu.M.Shatunov@inp.nsk.su	Acad. Lavrentiev, Prospect 11, 630090 Novosibirsk, Russia
Yoshihiro Shobuda	yoshihiro.shobuda@j-parc.jp	Japan Proton Accelerator Research Complex (J-PARC), Shirakata-Shirane 2-4, J - Tokai-Mura, Naka-Gun, Ibaraki-Ken 319-1195
Jiu-Qing Wang	wangjq@ihep.ac.cn	Institute for High Energy Physics, P.O. Box 918, 9-1, Beijing 100039, China
Rainer Wanzenberg	rainer.wanzenberg@desy.de	DESY, Notkestrasse 85, 22603 Hamburg, Germany
Zhentang Zhao	zhaozhentang@sinap.ac.cn	SINAP, Jiading campus: 2019 Jia Luo Road, Jiading district, Shanghai 201800, P. R. China Zhangjiang campus: 239 Zhang Heng Road, Pudong New District, Shanghai 201203, P. R. China

The views expressed in this newsletter do not necessarily coincide with those of the editors. The individual authors are responsible for their text.